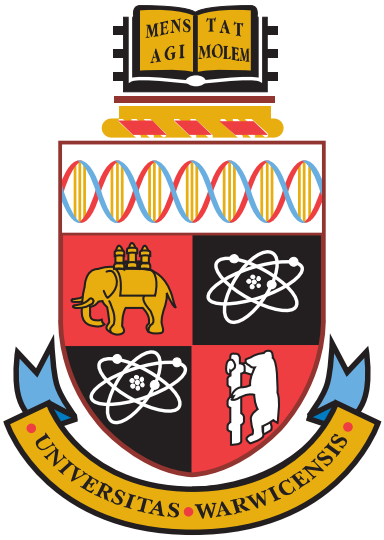

Identification and Characterisation of Point Defects in CVD Diamond

by

Enrik Nako

Thesis

Submitted to the University of Warwick

for the degree of

Doctor of Philosophy

Department of Physics

January 2020

Contents

List of Tables

List of Figures

Acknowledgements

Whilst there is only one author credited for this thesis, the undertaking of such a project has only been possible with the support of many individuals to whom I am sincerely grateful.

First and foremost I would like to thank Prof. Mark Newton for his supervision, guidance and patience during the course of this PhD, and for providing support during all my time in diamond research, which also contained some of life's unexpected surprises. I would also like to thank Dr Ben Green for being very generous with his time and experience, and in particular the countless discussions on group theory and unixial stress which make up a considerable portion of this thesis.

I must thank the team at De Beers Technologies in Maidenhead for their financial and technical support. In particular, I would like to thank Dr Philip Martineau and Dr David Fisher for encouragement and thoughtful discussions; and Dr Brad Cann and Dr Matthew Dale for their help with preparing a number of stress samples, which I am sure involved contributions from other members of the team to whom I am also thankful.

The number of people in the Warwick Diamond and EPR group has dramatically increased since I joined; I am grateful to all members, past and present, and especially Angelo, Anton, BenOne, BenTwo, Claudio, Colin, Guy, Jenny, Lewis, Luke, Matt, Phil, and Sinead. During this PhD, they all have provided engrossing discussion and education in all manner of subjects, from how to conduct diamond research, to the nuances of political developments, and perhaps most importantly, learning to appreciate good coffee. My unreserved thanks goes out to them all.

It would be remiss to not thank all the students and staff, and in particular Cohort 1, of the Diamond Science and Technology Centre for Doctoral Training (DST CDT), where I began my journey in diamond research, for their support and encouragement during the challenging MSc year.

My participation in the University of Warwick Archery Club has contributed immensely to making my time at Warwick an incredibly fulfilling and enjoyable experience. I give my profound thanks to all members for the opportunity to indulge in this wonderful sport (irrespective of what I may have said in the past!) which, at times, has provided a much needed escape from my studies and research. It has been a significant part of my life and I am grateful for all the shared experiences.

This PhD could not have been completed without Sophie and I am more thankful than she will ever know for her constant love and support that was crucial all throughout this trialling and sometimes tumultuous adventure.

Finally, I thank my parents and sister, to whom I am forever grateful for their great love and belief in me: it is to them that I proudly dedicate this thesis.

Më në fund, falënderoj prindërit dhe motrën time, të cilëve u jam përgjithmonë mirënjohës për dashurinë dhe besimin e madh te tyre tek unë: jam krenar që jua dedikoj atyre këtë tezë.

Declaration and published work

I declare that the work presented in this thesis is my own except where stated otherwise, and was carried out entirely at the University of Warwick, during the period of January 2016 to January 2020, under the supervision of Prof. Mark Newton. The research reported here has not been submitted, either wholly or in part, in this or any other academic institution for admission to a higher degree.

Some parts of the work reported in this thesis have been published, as listed below. It is anticipated that further parts of this work will be submitted for publication in due course.

Published papers

1. B. L. Green, M. W. Doherty, E. Nako, N. B. Manson, U. F. D'Haenens-Johansson, S. D. Williams, D. J. Twitchen, M. E. Newton, *Physical Review B* **99**, 161112 (2019)

Conference presentations

1. 69th Diamond Conference, University of Warwick, oral presentation 'Identification of hydrogen-related defects in diamond'
2. 69th Diamond Conference, University of Warwick, poster presentation 'Production of diamond samples for nitrogen vacancy based ensemble magnetometry'

3. 68th Diamond Conference, University of Warwick, poster presentation 'Identification of hydrogen-related defects in diamond'

4. 67th Diamond Conference, University of Warwick, poster presentation 'Identification of hydrogen-related defects in diamond'

Abstract

This thesis reports research on the identification and characterisation of point defects in chemical vapour deposition (CVD) grown synthetic diamond. Investigation has been facilitated by a number of techniques, including electron paramagnetic resonance (EPR), infrared (IR) and ultraviolet-visible (UV-Vis) absorption, and photoluminescence (PL) spectroscopies. The perturbing effect of uniaxial stress on the symmetry of defects has also been utilised in conjunction with IR absorption and PL spectroscopies.

The electronic structure of the neutral silicon vacancy centre (SiV^0), and in particular the 946 nm zero-phonon line (ZPL) transition, is investigated. Through PL measurements with uniaxial stress, the 946 nm ZPL is assigned to a ${}^3E_u \leftrightarrow {}^3A_{2g}$ transition where the ${}^3E_u$ excited state is coupled to a ${}^3A_{2u}$ shelving state 6.8 meV lower in energy. The symmetry-forbidden transition between the ${}^3A_{2g}$ ground state and ${}^3A_{2u}$ shelving state is observed (at approximately 951 nm) upon applied stress that lowers the $\mathscr{D}_{3d}$ symmetry of SiV^0, and a scheme is proposed for spin-dependent initialisation and readout of the spin states. A pseudo-local vibrational mode (pLVM) of the SiV^0 centre is identified at 976 nm.

IR absorption and PL measurements of nitrogen-doped CVD diamond will often observe a hydrogen-related line at 7354 cm^{-1}/1360 nm, and a suite of diamonds containing this feature are studied. The 7354 cm^{-1} centre is observed to exhibit preferential orientation relative to the growth direction when grown on {0 0 1}- and {1 1 0}-oriented substrates, which is subsequently lost upon annealing at a temperature of at least 1000 °C. Upon thermal treatment the 7354 cm^{-1} line will charge transfer and increase in intensity, given a sufficient concentration of acceptors are also present. The excited state of the 7354 cm^{-1} transition is determined to be degenerate through thermalisation experiments, whilst under applied stress, with a purpose-built PL spectrometer equipped with 1064 nm excitation. Previous results allow for the 7354 cm^{-1} line to be assigned to (at least) an $E \leftrightarrow E$ transition, but the exact symmetry of the defect responsible for the transition cannot be confidently determined.

An annealing study of two brown-coloured boron-doped CVD diamonds is also reported. Upon annealing between 1000–1500 °C, the brown-colouration is progressively annealed-out along with a number of unidentified features in the UV-Vis absorption spectra; simultaneously, IR absorption measurements observe a progressive increase in the uncompensated boron concentration. A large number of unreported features are also observed with IR absorption measurements, which show negligible change in intensity from annealing and charge transfer treatment. However, most are 100% preferentially orientated either parallel or perpendicular to the growth direction of the diamond. It is also the case with PL measurements that many unidentified ZPLs are observed. The nature of the majority of spectroscopic features observed in these boron-doped diamonds is currently unknown.

Abbreviations

Definitions

[X]	Concentration of X
CT	Charge transfer
CVD	Chemical vapour deposition
CWEPR	Continuous wave electron paramagnetic resonance
DFT	Density functional theory
EM	Electromagnetic
EPR	Electron paramagnetic resonance
FTIR	Fourier transform infrared
FWHM	Full width at half maximum
HPHT	High pressure high temperature
IR	Infrared
ISC	Intersystem crossing
λ	Wavelength of light
LVM	Local vibrational mode
MIR	Mid-infrared
MO	Molecular orbital
MPCVD	Microwave plasma chemical vapour deposition
NIR	Near-infrared
ODMR	Optically detected magnetic resonance

PBS	Phonon sideband
ppb	Parts per billion atomic density
ppm	Parts per million atomic density
PL	Photoluminescence
PO	Preferential orientation
pLVM	Pseudo-local vibrational mode
r_f	Ramp factor
RPEPR	Rapid passage electron paramagnetic resonance
RT	Room temperature
SIMS	Secondary ion mass spectrometry
UV-Vis	Ultraviolet-visible
ZFS	Zero-field splitting
ZPL	Zero-phonon line

Crystalographic notation

$[h\,k\,l]$	A specific hkl direction
$\langle h\,k\,l\rangle$	A general hkl direction
$(h\,k\,l)$	A specific hkl plane
$\{h\,k\,l\}$	A general hkl plane

1

Introduction

Carbon, the sixth element, is an abundant and uniquely versatile element. Organic chemistry and life on Earth showcase the ability of carbon to readily form bonds with itself and other elements. Even when bonding with itself, carbon forms a diverse range of allotropes with unique and often extreme properties [1]; graphite, graphene [2], fullerenes [3, 4], and diamond—the carbon allotrope of interest in this thesis—are currently some of the most researched carbon allotropes.

Carbon-12 (^{12}C) is the most naturally abundant stable isotope of carbon (98.9% ^{12}C relative to 1.1% ^{13}C [5]) and comprises of six protons, neutrons, and electrons. The ground state electronic configuration is $1s^2 2s^2 2p^2$; the $2p$ electrons are split between the $2p_x$ and $2p_y$ orbitals whilst the $2p_z$ orbital is empty. Diamond forms when an electron is excited from the $2s$ orbital into the $2p_z$ orbital, which creates four unpaired electrons. This excited state reconfigures into the lowest energy state of four equivalent bonds such that all the orbitals in the second electronic shell hybridise into four sp^3 orbitals [6]. The energy required to excite the electron is easily provided from the energy released during bonding. Since this is the lowest energy excited state configuration, it is unsurprising that diamond is a metastable allotrope of carbon and therefore will, given enough energy and time to overcome the (large) activation energy barrier, return to graphite. Graphite—much like other carbon allotropes—consists of three hybridised sp^2 orbitals, with the final $2p$ orbital part of a π-bond [7].

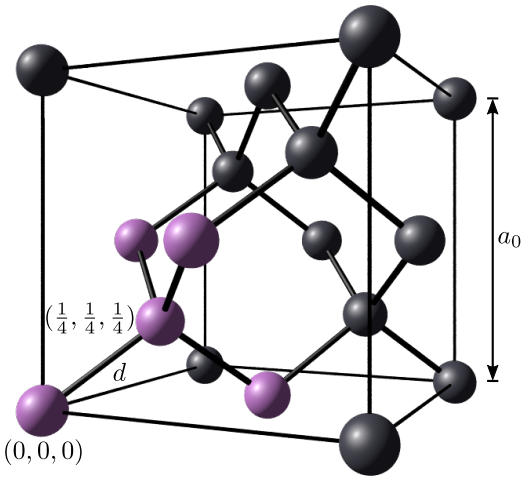

Figure 1-1 The diamond unit cell, viewed off-axis, with cell length of $a_0 = 3.57\,\text{Å}$ and nearest-neighbout C–C bond length of $d = 1.54\,\text{Å}$ [5]. The two-point basis of the FCC Bravais lattice is indicated by the atoms at positions $(0, 0, 0)$ and $(\frac{1}{4}, \frac{1}{4}, \frac{1}{4})$ [6]. The highlighted spheres represent one tetrahedral unit of the diamond lattice.

1.1 Structure and properties

The structure of diamond is shown in Figure 1-1. This homonuclear, cubic crystal has a face-centred cubic (FCC) Bravais lattice with a two atom basis of $(0, 0, 0)$ and $(\frac{1}{4}, \frac{1}{4}, \frac{1}{4})$. This structure is shared with other group IV elements such as silicon and germanium. For diamond, the lattice constant $a_0 = 3.57\,\text{Å}$, and the sp^3 bond length $d = 1.54\,\text{Å}$ [5], which is very short compared to the bond lengths of crystal silicon and germanium: $d = 2.33\,\text{Å}$ and $d = 2.41\,\text{Å}$, respectively [8]. Consequently, diamond has the highest atomic density of any solid at $1.76 \times 10^{23}\,\text{cm}^{-3}$ [9]. This bonding structure facilitates the variety of extreme properties of diamond.

The thermal conductivity of diamond is the highest of any material at room temperature [10], thereby making it an attractive heat spreader material [11]. The 5.47 eV band gap allows diamond to be optically transparent between a large range of wavelengths from 225 nm–3 µm [12]. Diamond is chemically and biologically inert [13, 14], and radiation hard [15]. These properties make diamond a prime material for applications in harsh environments where other materials are unsuitable, such as optical windows [16] and sensors [17]. Mechanically, diamond is used as an abrasive tool for cutting, drilling and polishing [18, 19] due to being the hardest natural material, registering a 10 on the Mohs scale of hardness [6].

1.2 Classification and defects

The first diamond classification system was developed by Robertson *et al.* [20], through the utilisation of infrared (IR) absorption spectroscopy. They noted that the majority of diamonds contained a particular set of absorption lines; the diamonds containing that specific set of absorption lines were classified as type I and those without were classified type II. More knowledge about these types of diamond was acquired throughout the following decades and the classification system is still commonly used, albeit with further subcategories added as shown in Figure 1-2.

The absorption lines in type I diamonds were related to nitrogen [21] and corresponded with a variety of yellow-to-brown coloured diamonds. Type Ia diamond mostly comprises of aggregated nitrogen (i.e. two or more substitutional nitrogen atoms bonded together), whilst type Ib diamond mostly contains single substitution nitrogen with relatively few aggregates [22]; type Ib diamonds are therefore typically a deeper yellow/brown colour. Relative to other types of nitrogen aggregation, type IaA diamond contains mostly A centres (two nearest-neighbour substitutional nitrogen atoms) [23] whilst type IaB diamond contains mostly B centres (a vacancy with all four nearest-neighbour sites containing a substitutional nitrogen atom) [24]. Type IaA/B diamond contains comparable concentrations of both A and B centres.

Type II diamond, which has no observable IR absorption from nitrogen, only has two subcategories: type IIa diamond which also has no observable IR absorption from boron, and type IIb diamond which does exhibits IR absorption from boron [25]. The concentration of boron in type IIb diamond can alter the colour from blue (low concentration) to black (high concentration).

The defects used to classify diamonds are all examples of point defects, which are localised to only one or a few lattice sites in the diamond crystal. Extended defects, such as dislocation and inclusions, are much larger and can span significant sections of any given crystal. No diamond crystal (natural or synthetic) is entirely perfect so it will invariably contain some defects [26]. The focus of this thesis is on

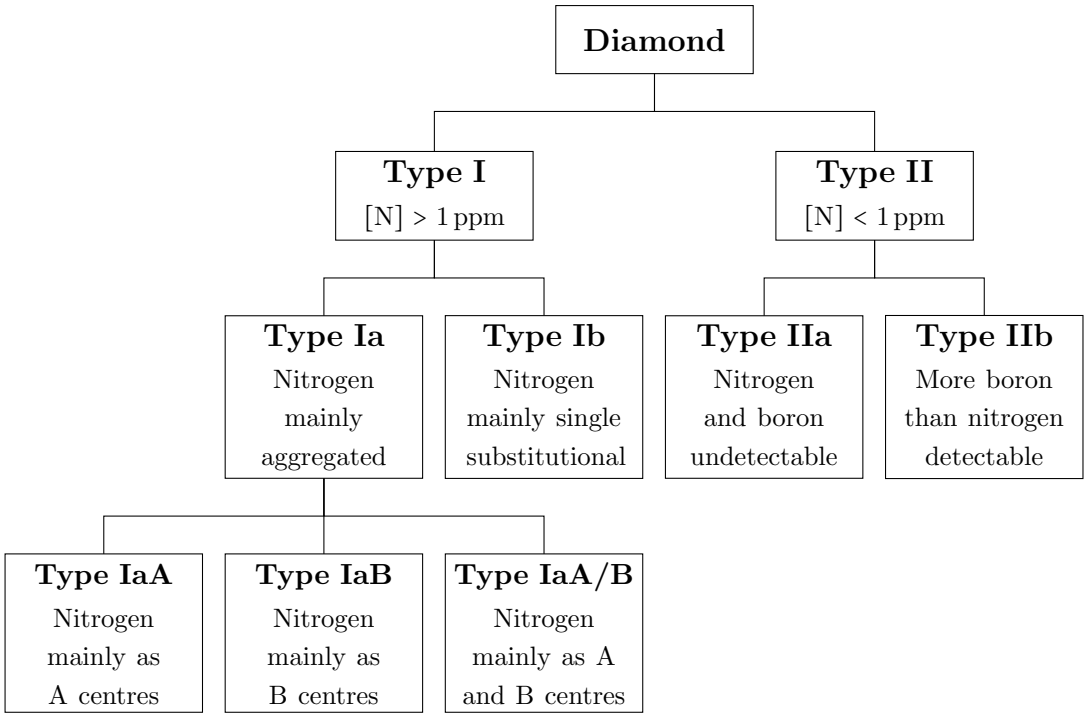

Figure 1-2 Classification of diamond based on detectable concentrations of various point defects from IR spectroscopy.

the study of the properties of point defects in diamond grown by chemical vapour deposition (CVD). Point defects that are pertinent to this thesis are reviewed in Chapter 2.

The incorporation or *doping* of substitutional nitrogen and boron impurities into the diamond lattice during growth can produce yellow and blue colouration, respectively, as the classification system describes. Other colours such as green, pink and red can also be produced in diamond via the formation of a variety of other defects—common defects and the colour (or lack thereof) they produce in diamond is provided by Shingley and Breeding [27]. The less-desirable coloured diamonds, such as brown, can have their colour modified to something more desirable or even removed entirely via post-growth treatment [28, 29]. As colour is an important attribute of gem diamond, the ability to engineer the colour of synthetic diamond during growth and alter the colour of both natural and synthetic diamond after growth, is of significant importance to the gemmological market.

The properties of point defects in diamond can even expand the already vast array of applications of diamond. Whilst diamond is typically an insulator, heavy

doping with boron facilitates electrical conduction in diamond and has led to electrochemical applications of diamond [30]. Diamond is also an excellent host material for defects with attributes that are applicable for quantum information processing, such as the negatively charged nitrogen vacancy centre (NV^-) [31] and the negatively charged silicon vacancy centre (SiV^-) [32].

1.3 Motivation for study

Whilst historically diamond was once solely viewed as a high-value gem, the knowledge acquired about its properties and their near endless fields of application makes diamond one of the most useful and exciting materials available. Point defects in diamond can increase the scope of applications further, however this research is far from complete. Hundreds of point defects are known to incorporate into diamond, as they can be observed spectroscopically, but relatively few are thoroughly understood for direct application despite decades of scientific research.

The motivation of this thesis is therefore to expand on the fundamental understanding of the properties of point defects in CVD diamond and where possible learn about their incorporation, formation, and migration. A variety of spectroscopic techniques are applied in tandem with symmetry-distorting uniaxial stress and an annealing study in order to identify and characterise the defects.

1.4 Structure of thesis

The structure of the remainder of this thesis is as follows:

- Chapter 2 reviews the literature on CVD synthesis of diamond and on the point defects relevant to the characterisation studies reported in this thesis.
- Chapter 3 provides the theory underpinning the experimental techniques employed in this thesis.
- Chapter 4 details the experimental techniques and bespoke apparatus utilised in this thesis.
- Chapter 5 presents photoluminescence measurements, whilst under uniaxial

stress, of the SiV^0 centre and provides an explanation of the origin of a related feature at 976 nm.

- Chapter 6 contains optical absorption and photoluminescence measurements, whilst under uniaxial stress, of a feature at 7354 cm^{-1}/1360 nm that is commonly observed in nitrogen-doped CVD diamond.
- Chapter 7 reports an annealing study on two brown-coloured boron-doped CVD diamonds, which are characterised by a variety of techniques.
- Chapter 8 is a summary of the work presented in this thesis.

References

1. E. H. Falcao, F. Wudl, *Journal of Chemical Technology & Biotechnology* **82**, 524–531 (2007).
2. K. S. Novoselov, *Science* **306**, 666–669 (2004).
3. S. Iijima, *Journal of Crystal Growth* **50**, 675–683 (1980).
4. A. Astefanei, O. Núñez, M. T. Galceran, *Analytica Chimica Acta* **882**, 1–21 (2015).
5. H. Holloway *et al.*, *Physical Review B* **44**, 7123–7126 (1991).
6. J. E. Field, *The Properties of Diamond* (Academic Press, London, 1979).
7. F. P. Bundy *et al.*, *Carbon* **34**, 141–153 (1996).
8. R. R. Reeber, K. Wang, *Materials Chemistry and Physics* **46**, 259–264 (1996).
9. V. V. Brazhkin *et al.*, *Physics-Uspekhi* **52**, 369–376 (2009).
10. J. E. Field, *Reports on Progress in Physics* **75**, 126505 (2012).
11. O. A. Voronov, G. S. Tompa, V. Veress, *MRS Proceedings* **956**, 195–200 (2007).
12. C. D. Clark, P. J. Dean, P. V. Harris, *Proceedings of the Royal Society of London. Series A. Mathematical and Physical Sciences* **277**, 312–329 (1964).
13. R. J. Narayan, R. D. Boehm, A. V. Sumant, *Materials Today* **14**, 154–163 (2011).
14. P. A. Nistor, P. W. May, *Journal of the Royal Society Interface* **14**, 20170382 (2017).
15. W. Adam *et al.*, *Nuclear Instruments and Methods in Physics Research Section A: Accelerators, Spectrometers, Detectors and Associated Equipment* **565**, 278–283 (2006).
16. C. A. Klein, *Diamond and Related Materials* **2**, 1024–1032 (1993).
17. G. Samudrala, S. Moore, Y. Vohra, *Materials* **8**, 2054–2061 (2015).
18. D. Belnap, A. Griffo, *Diamond and Related Materials* **13**, 1914–1922 (2004).
19. V. I. Lavrinenko, *Journal of Superhard Materials* **40**, 348–354 (2018).

20. R. Robertson, J. J. Fox, A. E. Martin, *Philosophical Transactions of the Royal Society of London. Series A, Containing Papers of a Mathematical or Physical Character* **232**, 463–535 (1933).
21. W. Kaiser, W. L. Bond, *Physical Review* **115**, 857–863 (1959).
22. H. B. Dyer *et al.*, *Philosophical Magazine* **11**, 763–774 (1965).
23. G. Davies, *Journal of Physics C: Solid State Physics* **5**, 2534–2542 (1972).
24. R. Jones, P. R. Briddon, S. Öberg, *Philosophical Magazine Letters* **66**, 67–74 (1992).
25. R. M. Chrenko, H. M. Strong, R. E. Tuft, *Philosophical Magazine* **23**, 313–318 (1971).
26. M. D. McCluskey, E. E. Haller, *Dopants and Defects in Semiconductors* (CRC, Boca Raton, 2012).
27. J. E. Shigley, C. M. Breeding, *Gems & Gemology* **49**, 107 (2013).
28. D. Fisher, *Lithos* **112**, 619–624 (2009).
29. C. B. Hartland, PhD thesis, The University of Warwick, 2014.
30. J. V. Macpherson, *Physical Chemistry Chemical Physics* **17**, 2935–2949 (2015).
31. M. W. Doherty *et al.*, *Physics Reports* **528**, 1–45 (2013).
32. L. J. Rogers *et al.*, *Nature Communications* **5**, 4739 (2014).

2

Point defects in CVD diamond

This chapter provides a brief summary of the point defects in chemical vapour deposition (CVD) diamond that are pertinent to the experimental results presented in this thesis. An outline of diamond synthesis (with a focus on the CVD technique) will be provided, followed by an introduction of defects intrinsic to diamond. Hundreds of extrinsic point defects in diamond have been catalogued by Zaitsev [1] and Dischler [2], although few are well understood with regards to their structure and properties. Consequently, a review is only provided for relevant substitutional, vacancy-related, and hydrogen-related point defects that are investigated in this thesis.

2.1 Synthesis of (CVD) diamond

Reproducible diamond synthesis was first realised in 1955 by Bundy *et al.* [3], by successfully replicating the thermodynamic conditions where diamond is the stable form of carbon in the carbon phase-space [4, 5] (Figure 2-1). Appropriate conditions are found above the graphite-diamond transition line (known as the Berman-Simon line [6, 7]). The method employed by Bundy *et al.* [3] is known as high pressure, high temperature (HPHT) synthesis and aims to effectively mimic the diamond growth conditions experienced in the Earth's mantle [8], whereby the carbon source (e.g. graphite) is converted into diamond. HPHT diamond of various sizes and structures can be grown, including single crystal (i.e. monocrys-

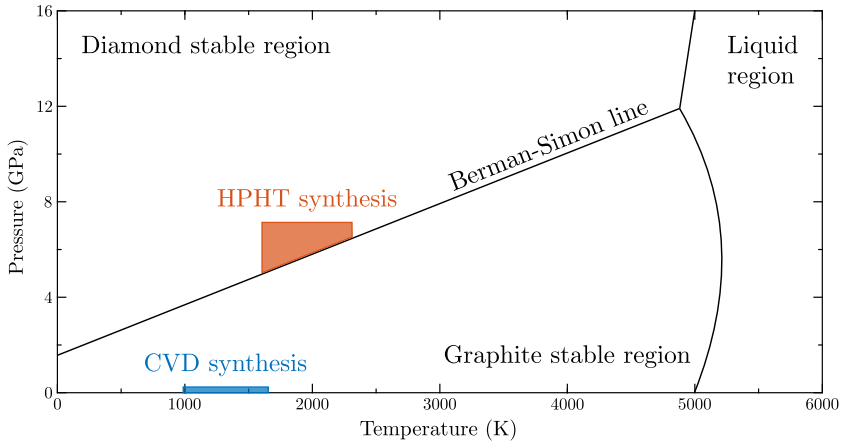

Figure 2-1 The relevant section of the carbon phase diagram that includes the diamond and graphite stable regions where HPHT and CVD synthesis occur, respectively. The Berman-Simon line [6, 7] marks the transition between the diamond and graphite regions. The pressures indicated for CVD synthesis have been exaggerated for clarity. Figure adapted from [4, 5]

talline) [9], polycrystalline [10] and nano-polycrystalline [11] diamond.

During HPHT synthesis, high pressures aid in stabilising diamond over graphite as the stable form of carbon, whilst high temperatures address the chemical kinetic energy required to break sp^2 and form sp^3 carbon bonds [12, 13]. Typically, metallic additives (e.g. iron, cobalt, nickel) are utilised to reduce the requirement of prohibitively high pressures and temperatures, such that typical "catalytic" HPHT growth conditions are approximately between 1200–1500 °C and 5–6 GPa [14, 15]. The presence of impurities in the carbon source cell can result in their incorporation into the diamond crystal, with nitrogen [16] and boron [17] being examples of readily incorporated impurities; intentional inclusion of impurities (e.g. nitrogen, boron) is known as doping. The technical details of how these conditions are met, the growth process, and the HPHT press systems are beyond the scope of this thesis; the reader is instead directed to several reviews on HPHT synthesis of diamond [13, 18, 19].

Also during the 1950s, Eversole was developing the CVD synthesis technique that later became patented in 1962 [20, 21]. Contrary to HPHT growth, CVD growth of diamond operates below the Berman-Simon line in the graphite stable region of the carbon phase diagram (Figure 2-1), and utilises chemical kinetics to form metastable diamond [22]. Hence, whilst diamond is thermodynamically unstable

at CVD growth conditions relative to the phase diagram, it does not readily convert to graphite as the breaking of sp^3 diamond bonds provides a large kinetic barrier, and thus is kinetically stable.

CVD growth occurs via epitaxial deposition of gas-phase carbon onto a substrate [23]. Input gases are fed into a reaction chamber, with a typical mixture being methane (CH_4, the carbon source) and molecular hydrogen (H_2). Typically, a significant concentration of H_2 is required such that $[H_2] \gg [CH_4]$, as the activation and dissociation of H_2 into hydrogen radicals ($H^\bullet$) facilitates the CVD growth process. The hydrogen radicals are primarily responsible for reacting with CH_4 to create methyl radicals ($CH_3^\bullet$); reacting with surface bonded hydrogen atoms on the hydrogen-terminated substrate to create a reactive site that $CH_3^\bullet$ can bond to; and reacting with hydrogen atoms on neighbour surface bonded CH_3 species, to create surface bonded $CH_2^\bullet$ species that reconstruct to form sp^3 carbon bonds. Crucially, hydrogen radicals also preferentially etch graphitic sp^2 carbon (and any long hydrocarbons that may form in the chamber) over diamond sp^3 carbon, which results in the net growth of diamond on the substrate surface [22–24].

A variety of reaction chamber types and methods for activating the reactants exist [25]. Relatively simple and inexpensive systems include hot-filament (typically tungsten filament) reactors which directly heat the reactants. However, these reactors suffer from limited growth rates and undesired contamination from the filament into the diamond being grown [26, 27]. If high purity and high quality diamond is desired, then microwave plasma CVD (MPCVD) reactors are typically utilised [28–31].

Within the MPCVD growth method, there are several parameters that significantly affect diamond growth: concentration of reactants and impurities, substrate material, temperature, plasma shape and its power density, and chamber pressure are examples of variables that require consideration [25, 32]. The parameters chosen often represent a compromise between growth rate and diamond crystal quality [33]. MPCVD growth rates may vary between 1–150 $\mu m\,h^{-1}$ [29, 34, 35], but higher growth rates generally produce lower quality diamond [36]. Nevertheless, high quality diamond (with low dislocation densities and low birefringence)

grown at a rate of up to 100 µm h^{-1} has been reported [37].

Similar to HPHT diamond, CVD diamond may also be grown as single crystal or polycrystalline—this is typically determined by the choice of substrate material. Single crystal CVD diamond is usually achieved by homoepitaxial growth on diamond substrates, but heteroepitaxial growth on carefully engineered non-diamond substrates may also grow single crystal diamond [38]. An advantage of heteroepitaxial growth has been demonstrated in the synthesis of single crystal diamond wafers with diameters approaching 100 mm [39, 40]. Homoepitaxial growth of large-area single crystal diamond has also been reported [41], with the current largest area of growth reported as 40×60 mm on a substrate mosaic of 24 cloned 10×10 mm single crystal CVD plates [42]. Polycrystalline CVD diamond is typically produced by heteroepitaxial growth on non-diamond substrates (when no effort is made to grown single crystal diamond) [43–45]. The samples studied in this thesis are all single crystal CVD diamond.

For homoepitaxy, the orientation of the diamond substrate also directly affects the growth rate, impurity incorporation, and morphology of the resultant diamond crystal [46, 47]. Crystallographic imperfections on the substrate surface will be replicated into the diamond during growth, which can result in dislocations propagating along the growth direction [31, 48, 49]. Consequently, substrate surface preparation is a key area of consideration for CVD growth, with etching and chemical mechanical polishing [50–52] utilised to improve the diamond growth quality. The {0 0 1} plane of diamond is relatively soft and easy to polish through traditional polishing techniques [53] and plasma etch pre-growth in the CVD reactor [51], hence it is the commonly chosen surface for homoepitaxial CVD growth. However, equally low surface roughness of the harder {1 1 1} surface has been demonstrated through silica based chemical mechanical polishing [54].

An introduction of dopants (e.g. nitrogen, boron, silicon) into the input gases may also affect the morphology and properties of CVD diamond. Nitrogen is a common impurity amongst natural, HPHT and CVD diamond and is known to modify the morphology and increase the CVD growth rate [34, 35, 55, 56]. Nitrogen-doped CVD diamond exhibits step-flow growth, such that the layer-by-layer process of

CVD diamond growth involves steps and risers that result in observable striations throughout the final material that highlight different impurity incorporation [57, 58]. Boron-doping may also change the morphology of the CVD diamond, but at the cost of lowering the CVD growth rate [29, 59]. The high incorporation efficiency of boron enables diamond to be heavily doped with boron, which can give rise to new metallic and superconducting properties [60, 61].

Unintentional doping in CVD diamond is also observed. Silicon-containing components of the CVD reactor (such as quartz windows) are etched by the plasma, and silicon impurities may become incorporated in the diamond [62, 63]. The silicon vacancy centre is a common manifestation of silicon incorporation in CVD diamond [64, 65]; substitutional silicon, however, has yet to be conclusively identified. Similarly, unintentional hydrogen incorporation also occurs as it is the main constituent of the gas phase plasma, and incorporation of up to 1 atomic percent in polycrystalline diamond has been reported [66].

The incorporation of nitrogen, boron, silicon, and hydrogen provide the basis for a variety of defects in CVD diamond, several of which are reviewed later in this chapter.

2.2 Intrinsic defects

All diamonds, irrespective of their origin, contain defects. Chapter 1 introduced the idea of point defects, which are localised to a few lattice points, and extended defects, which span beyond the diamond unit cell. Defects may be further categorised by their relation to the host crystal: in the case of diamond, a defect that contains only carbon atoms or the absence of any atom (known as a vacancy) is an intrinsic defect; incorporation of any non-carbon atom is an extrinsic defect. Whilst the entirety of the defects characterised in this thesis are extrinsic, a brief introduction to intrinsic defects will be provided in order to appreciate the spectrum of defects in diamond.

The vacancy (V) point defect is the absence of any atom at a lattice site. As vacancies are not stable at diamond growth temperatures, any significant concentration

in any type of diamond is usually produced by irradiation [67, 68]. Neutral and negative vacancies (V^0 and V^-, respectively) may be identified by their absorption features [69–71]. Electron paramagnetic resonance (EPR) is also detectable from an excited state of V^0 when illuminated with ultraviolet light [72] (the ground state is diamagnetic and therefore EPR-inactive), and the ground state of V^- [73]. Whilst stable at room temperature, vacancy mobility increases rapidly with temperature before beginning to anneal-out at ~600 °C [74]. The vacancy is not explicitly characterised in this thesis, but it may combine with various impurities to form a multitude of complexes [75], some of which are discussed later in this chapter.

Other types of intrinsic point defects that typically form in irradiated diamond are the carbon-related interstitials. A carbon interstitial forms when two carbon atoms share the same lattice site and aggregates of carbon interstitials are also possible. Whilst the vacancy has the same tetrahedral ($\mathscr{T}_\mathrm{d}$) symmetry as bulk diamond, carbon interstitials (and most other defects) are a lower class of symmetry. Examples of carbon-related interstitials include the R1 and R2 defects that were identified via EPR in electron irradiated type IIa diamond [76]. Both defects have been identified, with R1 as the (aggregated) di-$\langle 0\,0\,1\rangle$-split interstitial with $\mathscr{C}_\mathrm{1h}$ symmetry [77], and R2 as the neutral $\langle 0\,0\,1\rangle$-split self interstitial ($\mathrm{C}^0_{\mathrm{I}_{001}}$) with $\mathscr{D}_\mathrm{2d}$ symmetry [78]. The R2 defect is observable in optical absorption [79, 80], but no optical absorption line has been identified for the R1 defect.

Intrinsic defects may also be extended, with notable examples in single crystal diamond being twinning, stacking faults, and dislocations. Twinning is observed as a mirror image twin of the diamond crystal, typically rotated by 180° about the $\langle 1\,1\,1\rangle$ crystal axis, that is bonded to itself [81]. Stacking faults are typically in a $\{1\,1\,1\}$ plane, and involve the absence or inclusion of a carbon layer, such that an irregular section of the crystal is formed [82]. Whilst growth errors that lead to stacking faults are rare in CVD diamond, they can be of concern when high quality CVD diamond is attempted to be grown on HPHT substrates that contain stacking faults, since they tend to induce dislocations in the CVD diamond [31]. Low dislocation density ($< 10^5$–$10^6\,\mathrm{cm}^{-2}$) CVD diamond may be grown on

moderate dislocation density type IIa HPHT substrates [83].

In general, control of dislocation density is important as low dislocation densities are typically desired for several application of CVD diamond. For example, dislocations pose a challenge to increasing the size and power of diamond-based power electronic devices [84], and in diamond-based optical elements they increase the birefringence of the diamond which inhibits the ability to preserve polarisation and increases losses [85].

2.3 Extrinsic point defects

Impurities by definition form extrinsic point defects, and may produce centres that are attractive for application due to possessing exploitable properties. Consequently, the characterisation details of extrinsic point defects of interest in this thesis are presented (along with their related complexes).

A tabulated characterisation summary of the symmetry, spin, and optical lines of the defects reviewed in this section is given in §2.3.6; Table 2-1.

2.3.1 Substitutional nitrogen

Nitrogen is one of the most common impurities in natural and synthetic diamond [86, 87]. The neutral substitutional nitrogen (N_S^0) centre was initially observed by EPR measurements (with a ground state spin of $S = 1/2$) [88]—it is often referred to as the P1 centre in the context of its EPR signal, and sometimes the C centre in the context of its IR absorption lines. Further investigation revealed N_S^0 has $\mathscr{C}_{3v}$ symmetry due to an elongation of one of its four N–C bonds along $\langle 1\,1\,1 \rangle$, caused by the fifth electron occupying an anti-bonding orbital [89, 90]. Consequently, N_S^0 may donate the anti-bonding electron such that the centre acts as a deep donor approximately 1.7 eV below the conduction band [91, 92].

N_S^0 may be quantified by EPR spectroscopy; infrared (IR) absorption at 1130 cm^{-1} [93, 94]; and ultraviolet-visible (UV-Vis) absorption at 270 nm [93]. A sharp peak at 1344 cm^{-1} is also observed in IR absorption and is associated with a local vibrational mode (LVM) of N_S^0 [95].

When N_S^0 donates an electron to a nearby defect in the lattice, it becomes the positive substitutional nitrogen (N_S^+) centre. The loss of an electron results in a diamagnetic, EPR-inactive defect that may still be quantified by its IR absorption with peaks at 950 cm^{-1}, 1046 cm^{-1} and 1332 cm^{-1} [96]. Reliable quantification occurs primarily with the two lower energy absorption features, as the 1332 cm^{-1} peak contains a high density of phonon states, and therefore can originate from absorption at many different defects [96]. Whilst not experimentally verified, the N_S^+ centre is expected to have $\mathscr{T}_d$ symmetry as it is isoelectronic with carbon in the diamond lattice [97, 98]. Upon donating the anti-bonding electron that causes the elongation of one N–C bond, the nitrogen atom should relax to the lattice point such that all N^+–C bonds are the same length [97, 98].

The negative substitutional nitrogen (N_S^-) centre has been reported in ultrafast spectroscopy measurements (with a short lifetime of ~10 ns), whereby N_S^0 accepts an electron from another nearby N_S^0 [99]. Simultaneously, an unknown IR absorption feature at 1349 cm^{-1} is observed during measurements and is thought to be the LVM of N_S^- [99].

In addition to substitutional nitrogen, it is possible to find aggregated forms such as the A centre (N_{2S}, a pair of nearest-neighbour substitutional nitrogen atoms) [100, 101], and the B centre (a vacancy surrounded by four nearest-neighbour substitutional nitrogen atoms, discussed in §2.3.3.1) [102], in natural and HPHT treated synthetic diamond. The A centre has $\mathscr{C}_{3v}$ symmetry [101] and a diamagnetic ground state, but does give rise to a broad range of IR absorption lines, with the most notable at 1282 cm^{-1} [103].

2.3.2 Substitutional boron

Neutral uncompensated substitutional boron (B_S^0) is a shallow acceptor in diamond at approximately 0.37 eV above the valence band [104]. Quantification of B_S^0 in this thesis is primarily achieved through the IR absorptions features at 1288 cm^{-1} and 2802 cm^{-1} (amongst several other boron-related features) [105–108]. In total, up to 30 boron-related (temperature dependant) IR absorption features can be resolved in boron-doped diamond, with the ground state having a 2.1 meV splitting

between a lower four-fold degenerate state and a higher two-fold degenerate state [109, 110]. The linewidth of boron IR absorption features is observed to increase with an increase of boron concentration [111, 112].

The B_S^0 centre is EPR-active ($S = 3/2$), however quantification of B_S^0 via EPR is not routinely performed, as both liquid helium temperatures and uniaxial stress are typically required to detect a sufficiently sharp signal [113]. Internal strain will lower the degeneracy of the ground state levels which in turn broadens the EPR signals [113, 114], and likely also affects the linewidth of the boron IR absorption features.

Boron quantification may also be achieved by cathodoluminescence spectroscopy [115], secondary ion mass spectrometry (SIMS) [116], and Hall effect measurements [105].

Similar to N_S^0, the inability of B_S^0 to solely form four covalent bonds with neighbour carbon atoms is predicted to result in a distortion of a B–C bond, and thus $\mathscr{C}_{3v}$ symmetry [75, 117, 118]. By extension (and analogously opposite to N_S^+), it is also expected that once B_S^0 accepts an electron to become B_S^-, it is isoelectronic with carbon such that four equivalent B^-–C bonds are formed and the boron atom can relax to the lattice point such that the centre has $\mathscr{T}_d$ symmetry [75, 117, 118].

2.3.3 Impurity-vacancy complexes

Impurities are typically observed to trap vacancies in both as-grown and annealed diamond. Several types of impurity-vacancy complexes have been investigated [75] but only nitrogen- and silicon-related vacancy complexes will be discussed here.

2.3.3.1 Nitrogen-related

A family of (multi-)nitrogen-vacancy defects, of the form N_nV ($n = 1, 2, 3, 4$), are observed in diamond, and their models are presented in Figure 2-2.

The nitrogen vacancy (NV) defect

The nitrogen vacancy (NV) centre (Figure 2-2a) in its negative charge state (NV^-), has received a significant amount of attention from the scientific community. Single

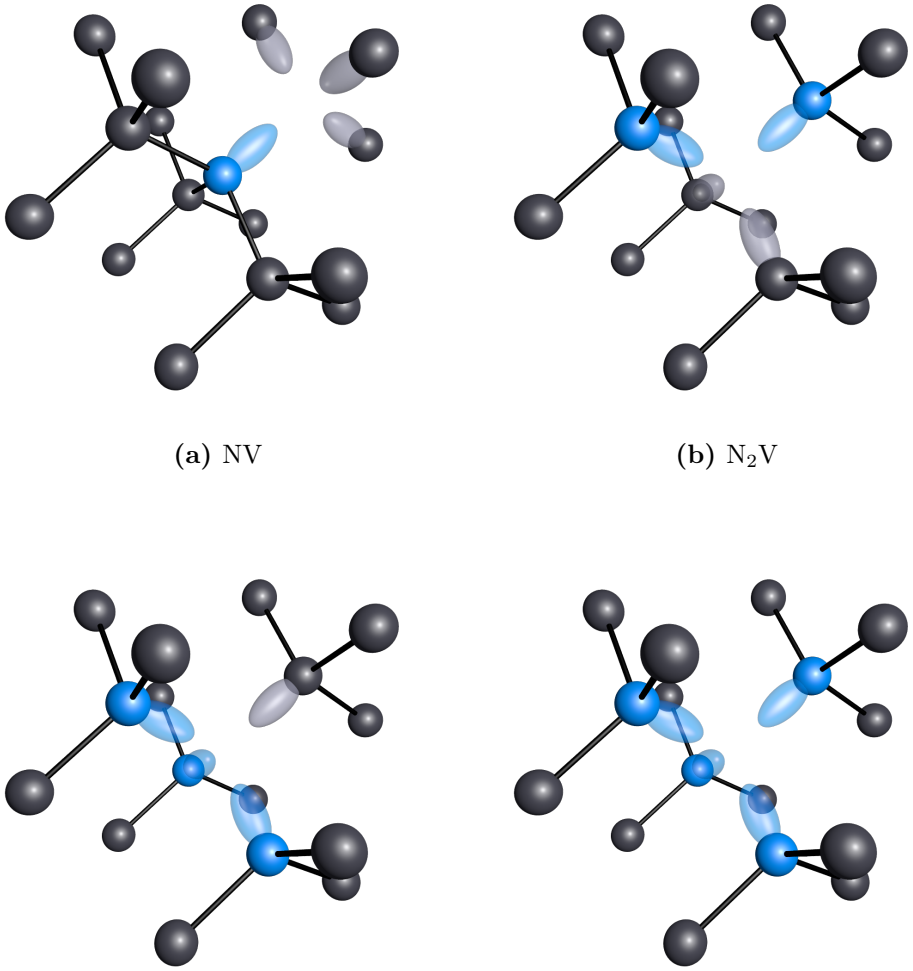

(a) NV **(b)** N_2V

(c) N_3V **(d)** N_4V

Figure 2-2 Models of (multi-)nitrogen-vacancy defects of the form N_nV (n = $1, 2, 3, 4$). Nitrogen (carbon) atoms are indicated in blue (black) and lone pairs (dangling bonds) are indicated by blue (grey) lobes.

NV^- defects can be detected by optically detected magnetic resonance (ODMR), resulting in a resource that may be utilised for applications in quantum information processing and sensing [119]. This review is focused on the characterisation properties of NV^- (and the neutral charge state NV^0); for an extensive discussion of NV^- properties and its quantum technology based applications, the reader is directed to several review articles [120–123]. In Chapter 5, a comparative discussion is provided on the respective quantum application properties of NV^- and the negative and neutral charge states of the silicon vacancy centre (SiV^- and SiV^0, respectively).

The NV^- centre may be detected by its zero phonon line (ZPL) transition at approximately 637 nm (1.945 eV) in absorption and photoluminescence spectroscopy [124]. The ZPL was determined to occur between the A ground state and E excited state at a trigonal centre [124], and subsequent EPR measurements observing an $S = 1$ ground state defect with a zero-field splitting of 2.88 GHz and $\mathscr{C}_{3v}$ symmetry [114] were eventually assigned to the NV^- centre [125, 126].

The 637 nm emission of the NV^- centre is the radiative decay from the ^3E excited state to the $^3A_2$ ground state, but non-radiative decay from the ^3E excited state is also possible [127, 128]. In this instance, a ZPL at 1042 nm (1.190 eV) may be observed from a $^1A_1$ state (populated by the non-radiative decay) to a ^1E state [127, 128]. Further non-radiative decay from the ^1E state preferentially decays into the $m_s = 0$ state of the 637 nm ZPL $^3A_2$ ground state, thereby enabling spin polarisation and efficient ODMR [129]. Potential improvements in the magnetic sensitivity of broadband magnetometry with the NV^- centre, that utilises the IR absorption of the 1042 nm transition, has been demonstrated [130].

The NV^0 centre also has $\mathscr{C}_{3v}$ symmetry and its ZPL emission at 575 nm (2.156 eV) is between a ^2A excited state and ^2E ground state [120, 131]. Whilst NV^0 has an $S = 0$ ground state, an EPR signal is not observed as dynamic Jahn-Teller effects are believed to broaden the EPR signal and therefore reduce the detection sensitivity [132]. However, upon optical excitation and population of a $^4A_2$ excited state ($S = 3/2$) in NV^0, an EPR signal may be recorded [132]. Charge transfer between NV^0 and NV^- is routinely observed and facilitated by the N_S^0 donor [133].

The N_2V, N_3V, and N_4V defects

The di-nitrogen vacancy (N_2V) centre is depicted in Figure 2-2b. The neutral charge state (N_2V^0, the H3 defect) is observed with a ZPL at 503 nm (2.463 eV), whilst the negative charge state (N_2V^-, the H2 defect) is observed with a ZPL at 986 nm (1.257 eV) [74, 124]. Both charge states have rhombic $\mathscr{C}_{2v}$ symmetry but only N_2V^- has a paramagnetic $S = 1/2$ ground state and is therefore detectable with EPR [134]. However, as with NV^0, an EPR signal may be record upon optical excitation and population of a $^3B_1$ excited state ($S = 1$) in N_2V^0 [135]. Also,

similar to the NV centre charge states, charge transfer between the two charge states of the N_2V centre is easily observed [136].

The tri-nitrogen vacancy (N_3V) centre is depicted in Figure 2-2c with $\mathscr{C}_{3v}$ symmetry and has only been observed in its neutral charge state (N_3V^0, the N3 defect) with a ZPL at 415 nm (2.985 eV) [137]. The ground state of N_3V^0 has $S = 1/2$, from which an EPR signal (referred to as P2) has been detected [138, 139]. Whilst the centre is observed in as-grown natural diamond, it only forms in synthetic diamond upon HPHT annealing [140].

The final centre comprising of four nearest-neighbour nitrogen atoms around a vacancy (N_4V) is depicted in Figure 2-2d with $\mathscr{T}_d$ symmetry. Again, only the diamagnetic neutral charge state (N_4V^0, the B centre) is observed with a characteristic broad IR absorption, where the largest peak is at approximately 1170 cm^{-1} [102]. It is possible for a B centre to capture a vacancy and form N_4V_2 (the H4 defect), with a ZPL at 496 nm (2.499 eV) [140, 141]. The H4 defect is less stable than the H3 defect, which may provide an explanation for why H4 is rarely observed in natural diamond, even when B centres are also present [140].

2.3.3.2 Silicon-related

The silicon (split-)vacancy (SiV) centre is frequently observed in CVD diamond (with neutral and negative charge states) and is depicted in Figure 2-3. The relatively large size of the silicon atom means that it is positioned between two lattice sites along a $\langle 1\,1\,1 \rangle$ direction, resulting in $\mathscr{D}_{3d}$ symmetry [142, 143].

In the neutral state of SiV^0, a ZPL at 946 nm (1.31 eV) is observed [144] along with a pseudo-LVM at 976 nm (1.27 eV) that arises from the oscillation of the silicon atom in the di-vacancy (see Chapter 5 for more information) [145]. Characterisation is also possible via EPR with the $S = 1$ ground state (originally labelled KUL1) [146, 147]. The electronic structure of SiV^0 is further discussed in Chapter 5.

The negative silicon vacancy (SiV^-) has a ZPL at approximately 737 nm (1.68 eV) [64, 148]. The ZPL may be resolved as a doublet at temperatures of 77 K, and may be further resolved as a quartet at temperatures of 4 K [64]. Theoretically,

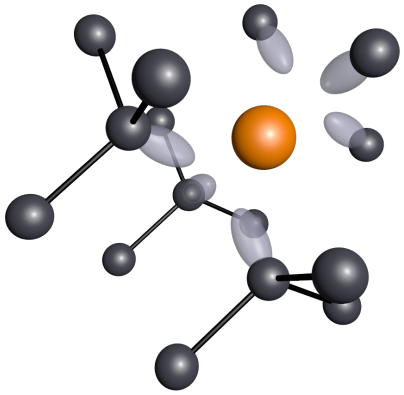

Figure 2-3 Model of the silicon (split-)vacancy defect (SiV). The silicon atom (orange) is positioned equidistant from adjacent lattice-vacancy sites; dangling bonds are highlighted by lobes (grey) on the six nearest-neighbour carbon atoms (black).

the ground state is expected to have an effective spin of $S = 1/2$ [148, 149], however no EPR signal related to SiV^- has been identified. It is possible that (similar to NV^0) Jahn-Teller effects are broadening the EPR signal to below detectable levels [150]. Nevertheless, a scheme to perform on-resonant ODMR has been realised for the SiV^- centre [151].

Charge transfer between SiV^0 and SiV^- is observed, and was utilised to estimate calibration constants for the relative absorptions of the centres (under the assumption no other charge states of SiV were involved) [144]. However, the double negatively charged silicon vacancy (SiV^{2-}) is believed to form in diamond, with theoretical and experimental evidence for its existence increasing [152, 153]. If SiV^{2-} is unambiguously identified, then the calibration constants will require recalculating in order to account for simultaneous charge transfer between all three charge states of SiV. Theoretically, it should be possible to create the positively and double-positively charged silicon vacancy centres [152], but there are currently no reported observations of these centres.

Similar to NV^-, both SiV^0 [154, 155] and SiV^- [156] exhibit properties which are attractive for quantum technology applications. As mentioned previously, Chapter 5 provides a comparative discussion on the respective quantum application properties of NV^-, SiV^-, and SiV^0.

No other complexes involving only silicon and vacancies have been unambiguously identified, but silicon-vacancy-hydrogen-related defects are discussed in §2.3.4.2. Silicon-vacancy defects should, however, be efficient traps for other vacancies, and therefore the silicon di-vacanacy (SiV_2) is expected to form in annealed diamonds that contain large concentration of silicon and vacancies [149]. The negative charge state (SiV_2^-) is expected to have a paramagnetic $S = 1/2$ ground state [149].

2.3.4 Impurity-vacancy-hydrogen complexes

Hydrogen is typically observed to passivate dangling bonds in vacancy-related complexes. Several of the nitrogen- and silicon-related impurity vacancy complexes have been observed to incorporate hydrogen in their structure.

2.3.4.1 Nitrogen-related

A family of (multi-)nitrogen-vacancy-hydrogen defects of the form N_nVH ($n = 1, 2, 3$) are observed in diamond, and their models are presented in Figure 2-4. An HPHT annealing study on CVD diamonds performed by Hartland [157] has shown the aggregation path NVH → N_2VH → N_3VH. Subsequent aggregation of $N_3VH + N$ to form N_4VH is not expected, as there are no dangling bonds to facilitate a bond with a hydrogen atom.

The NVH defect

The nitrogen vacancy hydrogen (NVH) defect presents the first observed case of a hydrogen atom rapidly reorientating between the three nearest-neighbour carbon radicals (Figure 2-4a), such that the time-averaged symmetry is $\mathscr{C}_{3v}$. The neutral charge state (NVH^0) has an IR absorption feature at 3123 cm^{-1} (sometimes reported in literature as 3124 cm^{-1}) [158], but an EPR-inactive diamagnetic ground state. Uniaxial stress experiments with IR absorption on NVH^0 determined the centre has $\mathscr{C}_{1h}$ symmetry [159]. The negative charge state (NVH^-) has no known optical transitions but may be quantified by EPR ($S = 1/2$ ground state) [160], and was determined to possess $\mathscr{C}_{3v}$ symmetry.

The apparent contradiction of the defect symmetry may be explained by the hy-

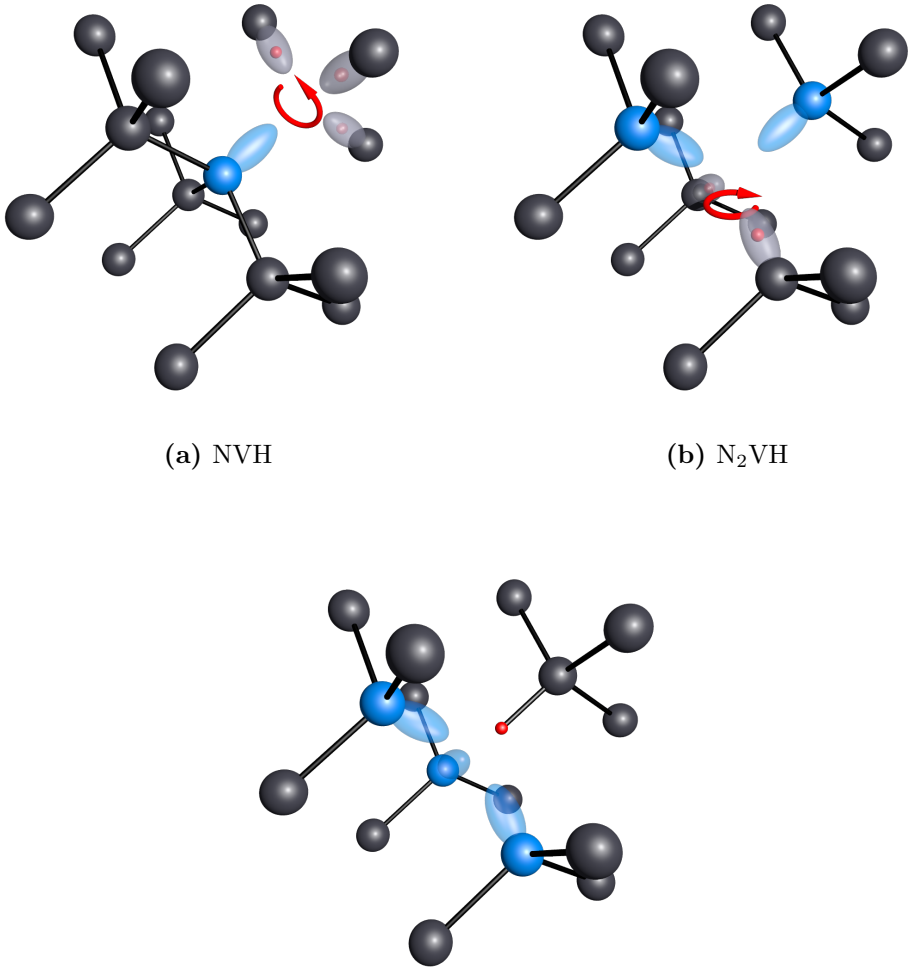

(a) NVH **(b)** N_2VH

(c) N_3VH

Figure 2-4 Models of (multi-)nitrogen-vacancy-hydrogen defects of the form N_nVH (n = 1, 2, 3). Nitrogen (carbon) atoms are indicated in blue (black), and lone pairs (dangling bonds) are indicated by blue (grey) lobes. A circular red arrow indicates the red hydrogen atom is rapidly reorientating between carbon dangling bonds.

drogen rapidly reorientating between equivalent carbon radicals on a time scale that is fast compared to EPR (such that EPR observes the time-average position), but slow compared to optical absorption (such that IR absorption observes the static position of the hydrogen only bonded to one carbon). It could also be argued the hydrogen is instead in a quantum superposition [161], but this would not explain why the IR and EPR unixial stress experiments provide different symmetry results for the same defect. Theoretical studies support the rapid

reorientation description [162, 163], and thus is the prevailing understanding of the system. Observation of hydrogen reorientating in one defect implies it may be worth considering similar hydrogen behaviour in other hydrogen-related defects.

The N_2VH defect

An EPR signal (S = 1), that involves a hydrogen and two nitrogen atoms, was assigned to the N_2VH^0 defect by Hartland [157]. HPHT annealing on samples with as-grown concentrations of NVH saw the defect anneal-in at 1800 °C and begin to anneal-out at 2200 °C [157]. Furthermore, an IR absorption doublet at 1375 cm^{-1} and 1378 cm^{-1} was observed to correlate in intensity to the EPR signal of N_2VH^0—the energies of the doublet are within 3% error of theoretical estimates [164].

The model of the N_2VH defect is presented in Figure 2-4b, which also includes a rapidly reorientating hydrogen atom between the two carbon radicals such that the defects has a time-averaged $\mathscr{C}_{2v}$ symmetry (as indicated by the EPR). The static hydrogen position in this defect is believed to result in $\mathscr{C}_{1h}$ symmetry [164, 165].

The N_3VH defect

The strong 3107 cm^{-1} IR absorption feature (and accompanying bend mode at 1405 cm^{-1}) has been routinely observed in natural diamonds [166] and synthetic diamonds that have been HPHT annealed at temperatures over 1700 °C [57, 157, 167]. Uniaxial stress measurements revealed the 3107 cm^{-1} line has $\mathscr{C}_{3v}$ symmetry and comprises of an $A \leftrightarrow A$ transition [97, 159]. With the aid of theoretical modelling [168], these absorption features have been assigned to the neutral charge N_3VH^0 centre, that is depicted in Figure 2-4c. No other optical features have been identified and the centre has a diamagnetic ground state.

2.3.4.2 Silicon-related

Hydrogenation of the silicon vacancy defect has also been observed, in the form of silicon vacancy hydrogen (SiVH) as depicted in Figure 2-5a. The EPR signal (S = ½) was originally labelled KUL3 [146, 147] and was unambiguously assigned to

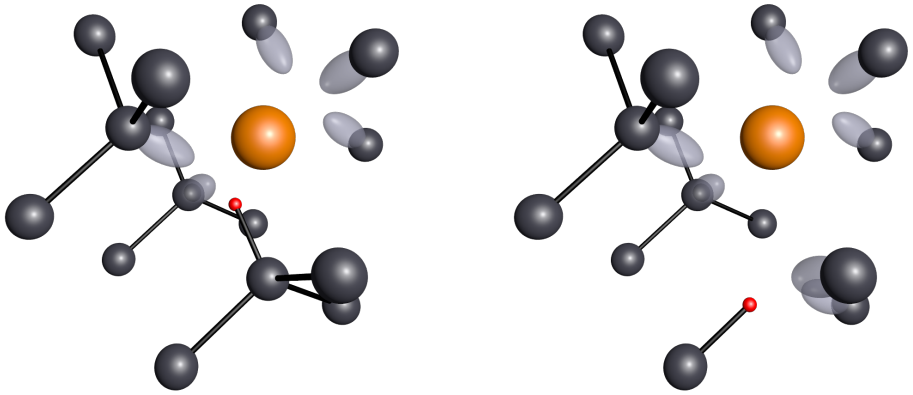

(a) SiVH **(b)** SiV_2H

Figure 2-5 Models of silicon-(multi-)vacancy-hydrogen defects of the form SiV_nH ($n = 1, 2$) defects. The silicon atom (orange) is positioned equidistant from adjacent lattice-vacancy sites; dangling bonds are highlighted by lobes (grey) on the six nearest-neighbour carbon atoms (black). Hydrogen atoms are indicated in red.

the neutral charge state ($SiVH^0$) by the agreement between experimental [143] and theoretically calculated [149] hyperfine parameters of ^{29}Si and ^{1}H. The hydrogen is statically bonded, therefore the centre has $\mathscr{C}_{1h}$ symmetry [143]. No optical transitions have been assigned to the $SiVH^0$ centre.

Additionally, whilst the predicted silicon di-vacancy [149] has yet to be observed, the silicon di-vacancy hydrogen (SiV_2H) has been identified and is depicted in Figure 2-5b. This centre was identified by its EPR signal ($S = 1/2$) called WAR3, which was assigned to the neutral charge state of the centre (SiV_2H^0) by the agreement between experimentally [169] and theoretically calculated [149] hyperfine parameters. The hydrogen is located in the vacancy furthest away from the silicon atom, such that the centre has $\mathscr{C}_{1h}$ symmetry.

2.3.5 Other hydrogen-related defects

Given the prevalence of hydrogen in the gas phase during CVD growth, it is somewhat surprising how relatively few hydrogen-related point defects have been identified in diamond. It is likely that other hydrogen-related defects in diamond have yet to be identified, as indicated by annealing studies where the hydrogen

assay concentration significantly varies between anneals [157]. Several theoretical studies have been performed on the stability of various hydrogen-related defects [170–172] but clearly there is more work to be done in understanding the incorporation of hydrogen in point defects in diamond.

A few more examples of predicted and observed hydrogen-related defects will be discussed in the remainder of this chapter. Further consideration of hydrogen-related defects is provided in Chapter 6, which is concerned with investigating the hydrogen-related feature at 7354 cm^{-1} that is often observed to dominate the IR absorption spectrum of nitrogen-doped diamond [57, 167, 173–175].

2.3.5.1 The N:H–C defect

A commonly observed feature in the IR absorption of CVD diamond is the 3324 cm^{-1} line (sometimes reported in literature at 3323 cm^{-1}). The defect responsible is observed to anneal-out at above 1100 °C and optical uniaxial stress measurements revealed the defect has $\mathscr{C}_{3v}$ symmetry [159]. Further investigation identified the line involves a C–H stretch, as suggested by isotopic substitution of $^{1}H \rightarrow {}^{2}D$, but no shift was observed with the substitution of $^{14}N \rightarrow {}^{15}N$ [97]. In conjunction with simulations [171], the line was assigned to a C–H stretch where the hydrogen is bonded to the unique carbon in the N_S^0 centre—in other words, the hydrogen-decorated substitutional nitrogen (N_S:H–C), as presented in Figure 2-6.

2.3.5.2 Vacancy hydrogen and di-vacancy hydrogen

A hydrogen-related defect was reported from an EPR signal ($S = 1$), with a small hydrogen hyperfine that presents $\mathscr{C}_{3v}$ symmetry, by Glover *et al.* [160]. The model proposed by Glover *et al.* (Figure 2-7a) involves a hydrogen atom statically bonded to a carbon radical in the vacancy (VH); the defect is believed to be negatively charged (i.e. VH^-).

However, Shaw *et al.* [176] performed theoretical calculations of the hydrogen hyperfine parameters which disagree with those experimentally observed by Glover *et al.* [160]. Furthermore, the general concept of a statically bonded hydrogen in the presence of effectively identical carbon radicals was argued against, such that

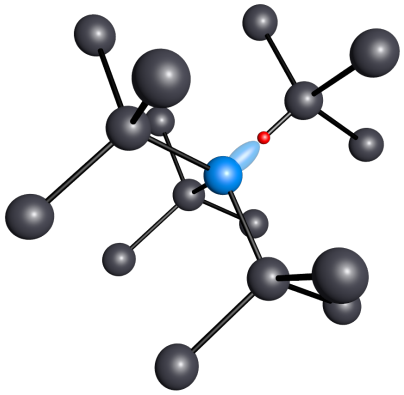

Figure 2-6 Model of the hydrogen-decorated substitutional nitrogen (N_S:H–C) defect. Nitrogen (carbon) atoms are indicated in blue (black) and the lone pair is indicated by the blue lobe. The hydrogen atom is indicated in red and has passivated the dangling bond on the carbon atom opposite the nitrogen lone pair.

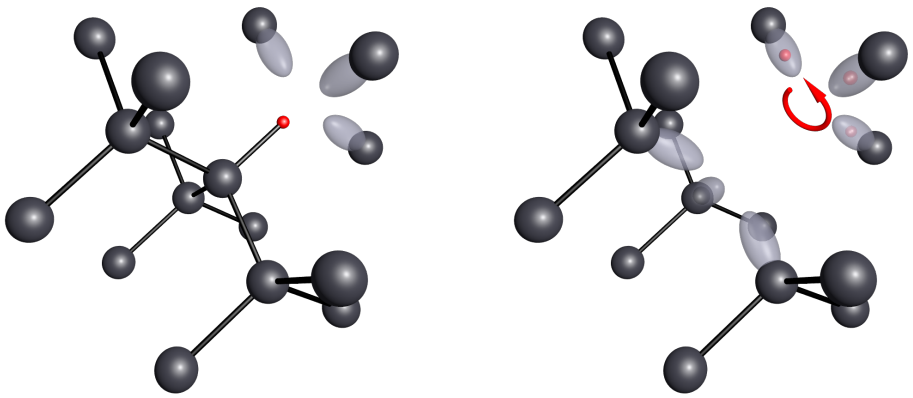

(a) VH **(b)** V_2H

Figure 2-7 Models of (multi-)vacancy-hydrogen defects of the form V_nH (n = 1, 2). Carbon atoms are indicated in black and dangling bonds are indicated by grey lobes. The hydrogen atoms is indicated in red. A circular red arrow indicates the red hydrogen atom is rapidly reorientating between carbon dangling bonds.

all vacancy-hydrogen type defects with more than one carbon radical (for example, NVH and N_2VH) should experience reorientation of the hydrogen atom between the carbon radicals.

Subsequently, a different model (Figure 2-7b) was proposed that involves a di-vacancy with the hydrogen atom quantum tunnelling between three carbon radi-

cals in one vacancy (V_2H) [176]. This defect is also in the negative charge state (V_2H^-) in order to have a ground state with $S = 1$.

To date, the structure of the EPR signal has not been unambiguously assigned to either VH^- or V_2H^-. If V_2H^- is demonstrated to be the correct model, then questions will still remain about why VH defects remain unobserved, as several of the charge state variants of VH are expected to be stable, EPR-active, and have observable absorption features [164, 177].

2.3.5.3 Isolated interstitial hydrogen

There is currently no experimental data showing the existence of isolated interstitial hydrogen in diamond, unlike other semiconductors (including other group IV elements) where it is reported [178]. The closest defect in terms of structure to interstitial hydrogen, that has been observed in diamond, is N_S:H–C (§2.3.5.1).

Nevertheless, theoretical calculations have been performed to investigate the stability and properties of interstitial hydrogen sites in diamond (Figure 2-8) [170, 171]. Of the various sites investigated, the results predict the bond-centred (BC) isolated interstitial site (H_{BC}) as the lowest energy position of hydrogen. With regards to the different charge states, $H_{BC}{}^+$ is the most mobile charge state, becoming mobile at ~400 °C, and as a result would be quickly lost to defects or the surface during CVD growth, thereby making direct observation difficult. $H_{BC}{}^0$ should be detectable by EPR, but is IR inactive, and $H_{BC}{}^-$ should be IR active.

Whilst there is no experimental data for isolated interstitial hydrogen, there is experimental muonium data generated from muon spin resonance (μSR) [179]. Muonium may be considered a light isotope of hydrogen (one ninth the mass of hydrogen) and are composed of a positive muon and an electron. In μSR, a muon with known polarisation is fired towards the sample and combines with an electron to become muonium which decays with a half-life of 2.2 µs. The muonium decay into a positron (and neutrino) is detected by positron detectors around the sample, and the direction of the positron emission informs about the magnetic field of the muonium and therefore its original position in the sample.

Muonium in diamond was initially proposed by Cox and Symons [180] to exist

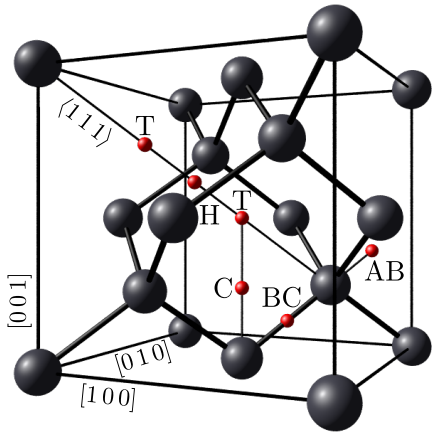

Figure 2-8 Possible interstitial hydrogen sites in diamond. T - tetrahedral, H - hexagonal, BC - bond-centred, AB - antibonding and C - midpoint of T-site and atom site. Figure adapted from [171].

in the BC configuration as the lowest energy state. Two types of muonium have since been discovered in diamond, along with their hyperfine parameters: Mu (normal muonium) is on a tetrahedral site and Mu* (anomalous muonium) is on the bond-centred site [181–183]. Thermally, Mu is stable below 350 K and between 350–800 K Mu thermally converts into Mu*; above 800 K only Mu* is present [184]. The ability for muonium to form in diamond supports arguments for the extremely similar isolated interstitial hydrogen to also form in diamond.

2.3.6 Summary of defect characterisation

Table 2-1 provides a summary of defect characterisation across several spectroscopic techniques. Photoluminescence (PL) spectroscopy is the only non-quantitative technique (on bulk diamond) in the table. Electron paramagnetic resonance (EPR), and fourier transform infrared (FTIR) and ultraviolet-visible (UV-Vis) absorption spectroscopy allow for quantitative measurements, given sufficient information about the defect. Further details of the spectroscopic techniques are given in Chapters 3 and 4.

Defect	Common moniker	Symmetry	EPR (S)	FTIR (cm^{-1})	UV-Vis (nm)	PL (nm)
N_S^0	P1, C centre	$\mathscr{C}_{3v}$	1/2	1130, 1344†	270	—
N_S^+		$[\mathscr{T}_d]$	0	950, 1046, 1332†	—	—
N_{2S}	A centre	$\mathscr{C}_{3v}$	0	1282 (broad), and others	—	—
B_S^0		$[\mathscr{C}_{3v}]$	3/2	1288†, 2802, and others	—	—
NV^0		$\mathscr{C}_{3v}$	[GS:1/2], ES:3/2	—	575	575
NV^-		$\mathscr{C}_{3v}$	1	—	637	637, 1042
N_2V^0	H3	$\mathscr{C}_{2v}$	GS:0, ES:1	—	503	503
N_2V^-	H2	$\mathscr{C}_{2v}$	1/2	—	986	986
N_3V^0	P2, N3	$\mathscr{C}_{3v}$	1/2	—	415	415
N_4V	B centre	$\mathscr{T}_d$	0	1170 (broad), and others	—	—
SiV^0	KUL1	$\mathscr{D}_{3d}$	1	—	946, 976‡	946, 976‡
SiV^-		$\mathscr{D}_{3d}$	[1/2]	—	737	737
VH^- or V_2H^-		$\mathscr{C}_{3v}$	1	—	—	—
N_S:H–C^0		$\mathscr{C}_{3v}$	0	3324† (or 3323)	—	—
NVH^0		$\mathscr{C}_{1h}$, $\mathscr{C}_{3v}^{\diamond}$	0	3123† (or 3124)	—	—
NVH^-		$\mathscr{C}_{1h}$, $\mathscr{C}_{3v}^{\diamond}$	1/2	—	—	—
N_2VH^0		$\mathscr{C}_{1h}$, $\mathscr{C}_{2v}^{\diamond}$	1/2	—	—	—
N_3VH^0		$\mathscr{C}_{3v}$	0	1405, 3107†	—	—
$SiVH^0$	KUL3	$\mathscr{C}_{1h}$	1/2	—	—	—
SiV_2H^0	WAR3	$\mathscr{C}_{1h}$	1/2	—	—	—

Table 2-1 Summary of defect characterisation across several spectroscopic techniques. All spin (S) values are given for the ground state (GS), unless an excited state (ES) spin is otherwise indicated. [Symmetry] indicates theoretical but unconfirmed symmetry. [S] indicates the EPR signal is unobserved despite being paramagnetic. — indicates no identification of the defect has been observed with the spectroscopic technique. † = local vibrational mode, ‡ = pseudo-local vibrational mode, $\diamond$ = time-average symmetry from reorientating hydrogen.

References

1. A. M. Zaitsev, *Optical Properties of Diamond* (Springer, Berlin, Heidelberg, Berlin, 2001).
2. B. Dischler, *Handbook of Spectral Lines in Diamond* (Springer, Berlin, Heidelberg, 2012).
3. F. P. Bundy *et al.*, *Nature* **176**, 51–55 (1955).
4. F. P. Bundy *et al.*, *Carbon* **34**, 141–153 (1996).
5. R. S. Balmer *et al.*, *Journal of Physics: Condensed Matter* **21**, 364221 (2009).
6. R. Berman, S. F. Simon, *Zeitschrift für Elektrochemie* **59**, 333–338 (1955).
7. R. Berman, J. Thewlis, *Nature* **176**, 834–836 (1955).
8. S. B. Shirey, J. E. Shigley, *Gems & Gemology* **49**, 188 (2013).
9. V. V. Lysakovskyi *et al.*, *Journal of Superhard Materials* **40**, 315–324 (2018).
10. H. Katzman, W. F. Libby, *Science* **172**, 1132–1134 (1971).
11. H. Sumiya, *SEI Technical Review* **74**, 15 (2012).
12. G. Davies, T. Evans, *Proceedings of the Royal Society of London. A. Mathematical and Physical Sciences* **328**, 413–427 (1972).
13. R. C. Burns, G. J. Davies, in *The Properties of Natural and Synthetic Diamond*, ed. by J. E. Field (Academic Press, London, 1992), pp. 395–422.
14. H. Kanda, T. Sekine, in *Properties, Growth and Applications of Diamond*, ed. by M. H. Nazaré, A. J. Neves (INSPEC, London, 2001), chap. B1.1.
15. D. Borse *et al.*, WO 2013/135785 Al (2013).
16. C. V. H. Strömann *et al.*, WO 2006/061672 Al (2006).
17. R. H. Wentorf, H. P. Bovenkerk, *The Journal of Chemical Physics* **36**, 1987 (1962).
18. K. Schmetzer, *The Journal of Gemmology* **32**, 52 (2010).
19. E. Ito, in *Treatise on Geophysics* (Elsevier, Oxford, 2015), pp. 233–261.
20. W. G. Eversole, US3030187A (1962).
21. W. G. Eversole, US3030188A (1962).
22. J. C. Angus, H. A. Will, W. S. Stanko, *Journal of Applied Physics* **39**, 2915 (1968).

23. P. W. May, *Philosophical Transactions of the Royal Society of London. Series A: Mathematical, Physical and Engineering Sciences* **358**, ed. by J. M. T. Thompson, 473–495 (2000).
24. J. J. Lander, J. Morrison, *Surface Science* **4**, 241–246 (1966).
25. M. Schwander, K. Partes, *Diamond and Related Materials* **20**, 1287–1301 (2011).
26. G. Lai *et al.*, *Journal of Research of the National Institute of Standards and Technology* **100**, 43 (1995).
27. F. Mendoza *et al.*, in *Chemical Vapor Deposition - Recent Advances and Applications in Optical, Solar Cells and Solid State Devices*, ed. by S. Neralla (InTech, London, 2016), chap. 4.
28. M. Kamo *et al.*, *Journal of Crystal Growth* **62**, 642–644 (1983).
29. H. Okushi, *Diamond and Related Materials* **10**, 281–288 (2001).
30. J. E. Butler *et al.*, *Journal of Physics: Condensed Matter* **21**, 364201 (2009).
31. P. M. Martineau *et al.*, *Journal of Physics: Condensed Matter* **21**, 364205 (2009).
32. A. Tallaire *et al.*, *Comptes Rendus Physique* **14**, 169–184 (2013).
33. C. Johnston, C. F. Ayres, P. R. Chalker, *Le Journal de Physique IV* **02**, C2–915–C2–921 (1991).
34. C.-S. Yan *et al.*, *Proceedings of the National Academy of Sciences of the United States of America* **99**, 12523–5 (2002).
35. J. Achard *et al.*, *Diamond and Related Materials* **16**, 685–689 (2007).
36. B. A. Reshi *et al.*, *Materials Research Express* **6**, 046407 (2019).
37. Q. Liang *et al.*, *Diamond and Related Materials* **18**, 698–703 (2009).
38. M. Schreck *et al.*, *MRS Bulletin* **39**, 504–510 (2014).
39. M. Fischer *et al.*, *Diamond and Related Materials* **17**, 1035–1038 (2008).
40. M. Schreck *et al.*, *Scientific Reports* **7**, 44462 (2017).
41. H. Yamada *et al.*, *Applied Physics Express* **3**, 051301 (2010).
42. H. Yamada *et al.*, *Applied Physics Letters* **104**, 102110 (2014).
43. X. Jiang, C. P. Klages, *Diamond and Related Materials* **2**, 1112–1113 (1993).
44. R. S. Sussmann *et al.*, *Diamond and Related Materials* **3**, 303–312 (1994).

45. I. Kratochvilova, in *Polycrystalline Diamond Thin Films for Advanced Applications*, ed. by A. M. Silva, S. A. Carabineiro (IntechOpen, London, 2016), chap. 8.
46. L. F. Sutcu *et al.*, *Journal of Applied Physics* **71**, 5930–5940 (1992).
47. R. E. Rawles, W. G. Morris, M. P. D'Evelyn, *MRS Proceedings* **416**, 13 (1995).
48. H. Pinto, R. Jones, *Journal of Physics: Condensed Matter* **21**, 364220 (2009).
49. P. Martineau *et al.*, *physica status solidi (c)* **6**, 1953–1957 (2009).
50. G. M. R. Sirineni *et al.*, *Journal of the Arkansas Academy of Science* **49**, 37 (1995).
51. A. P. Malshe *et al.*, *Diamond and Related Materials* **8**, 1198–1213 (1999).
52. N. Tatsumi *et al.*, *Japanese Journal of Applied Physics* **57**, 105503 (2018).
53. M. S. Couto, W. J. P. van Enckevort, M. Seal, *Philosophical Magazine B* **69**, 621–641 (1994).
54. E. L. H. Thomas *et al.*, *Science and Technology of Advanced Materials* **15**, 035013 (2014).
55. R. Samlenski *et al.*, *Applied Physics Letters* **67**, 2798 (1995).
56. S. Dunst, H. Sternschulte, M. Schreck, *Applied Physics Letters* **94**, 224101 (2009).
57. P. M. Martineau *et al.*, *Gems & Gemology* **40**, 2–25 (2004).
58. N. Davies *et al.*, *Journal of Physics: Conference Series* **281**, 012026 (2011).
59. X. Wang *et al.*, *Diamond and Related Materials* **1**, 828–835 (1992).
60. T. Yokoya *et al.*, *Nature* **438**, 647–650 (2005).
61. K. Muzyka *et al.*, *Analytical Methods* **11**, 397–414 (2019).
62. L. H. Robins *et al.*, *Physical Review B* **39**, 13367 (1989).
63. J. Barjon *et al.*, *physica status solidi (a)* **202**, 2177–2181 (2005).
64. C. D. Clark *et al.*, *Physical Review B* **51**, 16681–16688 (1995).
65. C. M. Breeding, W. Wang, *Diamond and Related Materials* **17**, 1335–1344 (2008).
66. B. Dischler *et al.*, *Physica B: Condensed Matter* **185**, 217–221 (1993).

67. C. D. Clark, R. W. Ditchburn, H. B. Dyer, *Proceedings of the Royal Society of London. Series A, Mathematical and Physical Sciences* **234**, 363–381 (1956).
68. C. D. Clark, R. W. Ditchburn, H. B. Dyer, *Proceedings of the Royal Society of London. Series A, Mathematical and Physical Sciences* **237**, 75–89 (1956).
69. C. I. A. Coulson, M. J. Kearsley, *Proceedings of the Royal Society of London. Series A, Mathematical and Physical Sciences* **241**, 433–454 (1957).
70. J. E. Lowther, *Physical Review B* **48**, 11592 (1993).
71. G. Davies, *Nature* **269**, 498–500 (1977).
72. J. A. Van Wyk *et al.*, *Physical Review B* **52**, 12657–12667 (1995).
73. J. Isoya *et al.*, *Physical Review B* **45**, 1436–1439 (1992).
74. S. Lawson *et al.*, *Journal of Physics: Condensed Matter* **4**, L125–L131 (1992).
75. J. P. Goss *et al.*, *Physical Review B* **72**, 035214 (2005).
76. E. A. Faulkner, J. N. Lomer, *Philosophical Magazine* **7**, 1995–2002 (1962).
77. D. J. Twitchen *et al.*, *Physical Review B* **54**, 6988–6998 (1996).
78. D. C. Hunt *et al.*, *Physical Review B* **61**, 3863–3876 (2000).
79. J. Walker, *Journal of Physics C: Solid State Physics* **10**, 3867–3876 (1977).
80. G. Davies, H. Smith, H. Kanda, *Physical Review B* **62**, 1528–1531 (2000).
81. J. T. Glass, M. Sunkara, *Journal of Materials Research* **7**, 3001–3009 (1992).
82. W. Zhu, A. R. Badzian, R. Messier, *Journal of Materials Research* **4**, 659–663 (1989).
83. A. Tallaire *et al.*, *Diamond and Related Materials* **77**, 146–152 (2017).
84. H. Umezawa, Y. Kato, S.-I. Shikata, *Applied Physics Express* **6**, 011302 (2013).
85. I. Friel *et al.*, *Diamond and Related Materials* **18**, 808–815 (2009).
86. T. Evans, Z. Qi, *Proceedings of the Royal Society of London. A. Mathematical and Physical Sciences* **381**, 159–178 (1982).
87. K. M. McNamara, *Applied Physics Letters* **83**, 1325–1327 (2003).
88. W. V. Smith *et al.*, *Physical Review* **115**, 1546–1552 (1959).
89. P. Briddon, R. Jones, *Physica B: Condensed Matter* **185**, 179–189 (1993).

90. A. Cox, M. E. Newton, J. M. Baker, *Journal of Physics: Condensed Matter* **6**, 551–563 (1994).
91. R. G. Farrer, *Solid State Communications* **7**, 685–688 (1969).
92. M. H. Nazaré, in *Properties and Growth of Diamond*, ed. by G. Davies (INSPEC, London, 1994), chap. 3.2.
93. R. M. Chrenko, H. M. Strong, R. E. Tuft, *Philosophical Magazine* **23**, 313 (1971).
94. G. S. Woods, J. A. Van Wyk, A. T. Collins, *Philosophical Magazine B* **62**, 589–595 (1990).
95. A. T. Collins, M. Stanley, G. S. Woods, *Journal of Physics D: Applied Physics* **20**, 969–974 (1987).
96. S. C. Lawson *et al.*, *Journal of Physics: Condensed Matter* **10**, 6171–6180 (1998).
97. S. Liggins, PhD thesis, The University of Warwick, 2010.
98. M. K. B. Atumi, PhD thesis, Newcastle University, 2014.
99. R. Ulbricht *et al.*, *Physical Review B* **84**, 165202 (2011).
100. G. Davies, *Journal of Physics C: Solid State Physics* **9**, L537–L542 (1976).
101. O. D. Tucker, M. E. Newton, J. M. Baker, *Physical Review B* **50**, 15586–15596 (1994).
102. A. T. Collins, *The Journal of Gemmology* **27**, 341–359 (2001).
103. G. B. B. M. Sutherland, D. E. Blackwell, W. G. Simeral, *Nature* **174**, 901–904 (1954).
104. A. T. Collins, *Philosophical Transactions: Physical Sciences and Engineering* **342**, 233–244 (1993).
105. A. T. Collins, A. W. S. Williams, *Journal of Physics C: Solid State Physics* **4**, 1789–1800 (1971).
106. J. Mort, M. A. Machonkin, K. Okumura, *Applied Physics Letters* **58**, 1908–1910 (1991).
107. S. J. Breuer, P. R. Briddon, *Physical Review B* **49**, 10332–10336 (1994).
108. E. Gheeraert, A. Deneuville, J. Mambou, *Diamond and Related Materials* **7**, 1509–1512 (1998).
109. K. Thonke, *Semiconductor Science and Technology* **18**, S20–S26 (2003).

110. J. Walker, *Reports on Progress in Physics* **42**, 1605–1659 (1979).

111. A. T. Collins *et al.*, *Physical Review* **140**, A1272–A1274 (1965).

112. R. Burns *et al.*, *Journal of Crystal Growth* **104**, 257–279 (1990).

113. C. A. J. Ammerlaan, R. van Kemp, *Journal of Physics C: Solid State Physics* **18**, 2623–2629 (1985).

114. J. H. N. Loubser, J. A. van Wyk, *Reports on Progress in Physics* **41**, 1201–1248 (1978).

115. F. Omnès *et al.*, *Diamond and Related Materials* **20**, 912–916 (2011).

116. M.-A. Pinault-Thaury *et al.*, *Applied Surface Science* **410**, 464–469 (2017).

117. J. P. Goss *et al.*, *Physical Review B* **68**, 235209 (2003).

118. J. P. Goss, P. R. Briddon, *Physical Review B* **73**, 085204 (2006).

119. A. Gruber *et al.*, *Science* **276**, 2012–2014 (1997).

120. M. W. Doherty *et al.*, *Physics Reports* **528**, 1–45 (2013).

121. L. Childress, R. Hanson, *MRS Bulletin* **38**, 134–138 (2013).

122. R. Schirhagl *et al.*, *Annual Review of Physical Chemistry* **65**, 83–105 (2014).

123. F. Casola, T. van der Sar, A. Yacoby, *Nature Reviews Materials* **3**, 17088 (2018).

124. G. Davies, M. F. Hamer, *Proceedings of the Royal Society of London. Series A, Mathematical and Physical Sciences* **348**, 285–298 (1976).

125. N. R. Reddy, N. B. Manson, E. R. Krausz, *Journal of Luminescence* **38**, 46–47 (1987).

126. D. A. Redman *et al.*, *Physical Review Letters* **67**, 3420–3423 (1991).

127. M. W. Doherty *et al.*, *New Journal of Physics* **13**, 025019 (2011).

128. P. Kehayias *et al.*, *Physical Review B* **88**, 165202 (2013).

129. M. L. Goldman *et al.*, *Physical Review B* **91**, 165201 (2015).

130. V. M. Acosta *et al.*, *Applied Physics Letters* **97**, 174104 (2010).

131. G. Davies, *Journal of Physics C: Solid State Physics* **12**, 2551–2566 (1979).

132. S. Felton *et al.*, *Physical Review B* **77**, 081201 (2008).

133. N. B. Manson, J. P. Harrison, *Diamond and Related Materials* **14**, 1705–1710 (2005).

134. B. L. Green *et al.*, *Physical Review B* **92**, 165204 (2015).

135. J. A. Van Wyk, G. S. Woods, *Journal of Physics: Condensed Matter* **7**, 5901–5911 (1995).
136. Y. Mita *et al.*, *Journal of Physics: Condensed Matter* **2**, 8567–8574 (1990).
137. M. F. Thomaz, G. Davies, *Proceedings of the Royal Society of London. Series A, Mathematical and Physical Sciences* **362**, 405–419 (1978).
138. J. A. van Wyk, *Journal of Physics C: Solid State Physics* **15**, L981–L983 (1982).
139. B. L. Green, PhD thesis, The University of Warwick, 2013.
140. A. T. Collins *et al.*, *Journal of Applied Physics* **97**, 083517 (2005).
141. E. S. De Sa, G. Davies, *Proceedings of the Royal Society of London. Series A, Mathematical and Physical Sciences* **357**, 231–251 (1977).
142. H. Sternschulte *et al.*, *Diamond and Related Materials* **4**, 1189–1192 (1995).
143. A. M. Edmonds *et al.*, *Physical Review B* **77**, 245205 (2008).
144. U. F. S. D'Haenens-Johansson *et al.*, *Physical Review B* **84**, 245208 (2011).
145. B. L. Green *et al.*, *Physical Review B* **99**, 161112 (2019).
146. K. Iakoubovskii, A. Stesmans, *physica status solidi (a)* **186**, 199–206 (2001).
147. K. Iakoubovskii *et al.*, *Diamond and Related Materials* **12**, 511–515 (2003).
148. J. P. Goss *et al.*, *Physical Review Letters* **77**, 3041–3044 (1996).
149. J. P. Goss, P. R. Briddon, M. J. Shaw, *Physical Review B* **76**, 075204 (2007).
150. A. M. Edmonds, PhD thesis, The University of Warwick, 2008.
151. B. Pingault *et al.*, *Nature Communications* **8**, 15579 (2017).
152. A. Gali, J. R. Maze, *Physical Review B* **88**, 235205 (2013).
153. S. Häußler *et al.*, *New Journal of Physics* **19**, 063036 (2017).
154. B. L. Green *et al.*, *Physical Review Letters* **119**, 096402 (2017).
155. B. C. Rose *et al.*, *Science* **361**, 60–63 (2018).
156. C. Hepp *et al.*, *Physical Review Letters* **112**, 036405 (2014).
157. C. B. Hartland, PhD thesis, The University of Warwick, 2014.
158. R. U. A. Khan *et al.*, *Journal of Physics: Condensed Matter* **21**, 364214 (2009).
159. R. Cruddace, PhD thesis, The University of Warwick, 2007.
160. C. Glover, PhD thesis, The University of Warwick, 2003.

161. P. W. Atkins, R. S. Friedman, *Molecular Quantum Mechanics* (Oxford University Press, Oxford, 5th, 2012).

162. J. P. Goss *et al.*, *Journal of Physics: Condensed Matter* **15**, S2903–S2911 (2003).

163. A. Kerridge, A. H. Harker, A. M. Stoneham, *Journal of Physics: Condensed Matter* **16**, 8743–8751 (2004).

164. C. V. Peaker, PhD thesis, Newcastle University, 2018.

165. C. V. Peaker *et al.*, *physica status solidi (a)* **212**, 2616–2620 (2015).

166. R. M. Chrenko, R. S. McDonald, K. A. Darrow, *Nature* **213**, 474–476 (1967).

167. S. J. Charles *et al.*, *physica status solidi (a)* **201**, 2473–2485 (2004).

168. J. P. Goss *et al.*, *Journal of Physics: Condensed Matter* **26**, 145801 (2014).

169. U. F. S. D'Haenens-Johansson, PhD thesis, The University of Warwick, 2011.

170. J. P. Goss *et al.*, *Physical Review B* **65**, 115207 (2002).

171. J. P. Goss, *Journal of Physics: Condensed Matter* **15**, R551–R580 (2003).

172. S. Mehandru, A. B. Anderson, J. C. Angus, *Journal of Materials Research* **7**, 689–695 (1992).

173. F. Fuchs *et al.*, *Applied Physics Letters* **66**, 177–179 (1995).

174. F. Fuchs *et al.*, *Diamond and Related Materials* **4**, 652–656 (1995).

175. W. Wang *et al.*, *Gems & Gemology* **39**, 268–283 (2003).

176. M. J. Shaw *et al.*, *Physical Review Letters* **95**, 105502 (2005).

177. C. V. Peaker *et al.*, *physica status solidi (a)* **212**, 2431–2436 (2015).

178. V. Kolkovsky *et al.*, *Physica B: Condensed Matter* **404**, 5080–5084 (2009).

179. M. D. McCluskey, E. E. Haller, *Dopants and Defects in Semiconductors* (CRC, Boca Raton, 2012).

180. S. F. J. Cox, M. C. R. Symons, *Chemical Physics Letters* **126**, 516–525 (1986).

181. T. L. Estle, S. Estreicher, D. S. Marynick, *Physical Review Letters* **58**, 1547–1550 (1987).

182. E. Holzschuh *et al.*, *Physical Review A* **25**, 1272–1286 (1982).

183. W. Odermatt *et al.*, **32**, 583–588 (1986).

184. B. D. Patterson *et al.*, *Hyperfine Interactions* **18**, 605–610 (1984).

3

Theory

As discussed in Chapter 2, several characterisation techniques are required to identify and investigate the variety of defects that form in diamond. For the techniques that have been utilised in the experimental work of this thesis, an overview to their theoretical principles is provided in order to complement the experimental results.

3.1 Electron paramagnetic resonance (EPR)

Electron paramagnetic resonance (EPR) is a quantitative technique performed on systems which contain (one or more) unpaired electrons, such that they are paramagnetic with a non-zero net electron spin ($S \neq 0$). The intensity of an EPR signal represents the number of spins in the system, which enables the quantification of the defects producing that specific signal. Information about the energy levels, symmetry, constituents, and environment of a paramagnetic defect may also be acquired. EPR is therefore routinely employed to investigate and characterise the many known and unknown paramagnetic defects in diamond. As only a modest introduction to the theory of EPR is presented here, the reader is made aware of several other resources that are more comprehensive [1–3].

3.1.1 The spin Hamiltonian

The various interactions an unpaired electron experiences may be described by the spin Hamiltonian $\hat{\mathscr{H}}$ of the form

$$\hat{\mathscr{H}} = \underbrace{\mu_B \boldsymbol{B}^T \cdot \boldsymbol{g} \cdot \hat{\boldsymbol{S}}}_{\text{Zeeman}} + \underbrace{\hat{\boldsymbol{S}}^T \cdot \boldsymbol{D} \cdot \hat{\boldsymbol{S}}}_{\text{zero-field}} + \sum_i^n \Big[\underbrace{\hat{\boldsymbol{S}}^T \cdot \boldsymbol{A}_i \cdot \hat{\boldsymbol{I}}_i}_{\text{hyperfine}} + \underbrace{\hat{\boldsymbol{I}}_i^T \cdot \boldsymbol{P}_i \cdot \hat{\boldsymbol{I}}_i}_{\text{quadrupole}} - \underbrace{\mu_N g_{n_i} \boldsymbol{B}^T \cdot \hat{\boldsymbol{I}}_i}_{\text{nuclear Zeeman}} \Big], \tag{3-1}$$

where $\hat{\boldsymbol{S}}$ and $\hat{\boldsymbol{I}}$ represent the electron and nuclear spin operators, respectively, and the sum is over the n nearby nuclei. A discussion of each individual interaction now follows.

3.1.1.1 Electronic Zeeman interaction

The electronic Zeeman interaction describes the energy of an unpaired electron with magnetic dipole $\hat{\boldsymbol{\mu}}$ in a magnetic field $\boldsymbol{B}$ as

$$\hat{\mathscr{H}}_{\text{EZ}} = E = -\hat{\boldsymbol{\mu}} \cdot \boldsymbol{B} \,. \tag{3-2}$$

The magnetic dipole may be defined in terms of the orbital angular momentum $\hat{\boldsymbol{L}}$ and spin $\hat{\boldsymbol{S}}$ of the electron:

$$\hat{\boldsymbol{\mu}} = -\mu_B \left(\hat{\boldsymbol{L}} + g_e \hat{\boldsymbol{S}} \right) , \tag{3-3}$$

where, μ_B is the Bohr magneton ($\mu_B = {}^{e\hbar}/_{2m}$), and g_e is the dimensionless electron g-factor constant. Upon application of a magnetic field aligned along z such that $\boldsymbol{B}^T = (0, 0, B)$, and assuming an isotropic g-factor, the electron Zeeman interaction becomes

$$\hat{\mathscr{H}}_{\text{EZ}} = -\hat{\boldsymbol{\mu}} \cdot \boldsymbol{B}^T = g\mu_B \boldsymbol{B}^T \cdot \hat{\boldsymbol{S}} = g\mu_B B \hat{S}_z \,. \tag{3-4}$$

Quantum mechanics prescribes that the spin of an electron quantised along z, has a spin quantum number $m_s = \pm {}^1/_2$. In general, for spin S and spin multiplicity $2S + 1$, $m_s = -S, -S + 1, ...S$. Consequently, an applied magnetic field will remove the energy degeneracy of the two spin states, with the energy difference between the states given as

$$\Delta E = h\nu = g\mu_B B \Delta m_s \,, \tag{3-5}$$

where a photon with frequency ν may match the resonance condition and induce a magnetic dipole transition between the two states, assuming the selection rule

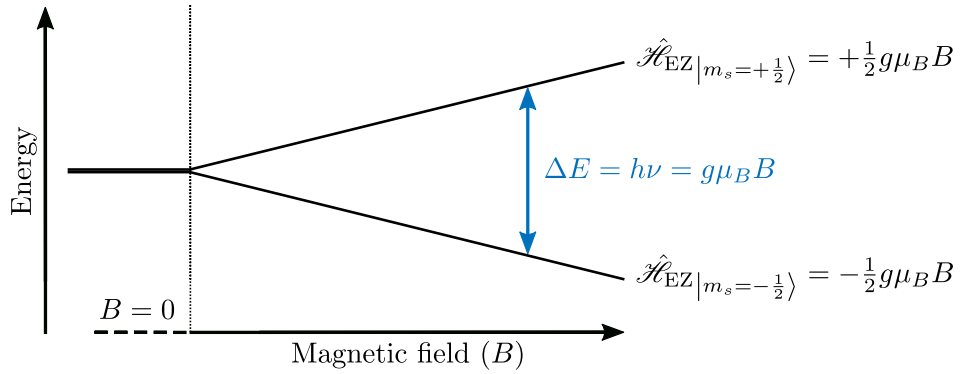

Figure 3-1 Electronic Zeeman interaction for an electron with spin $S = 1/2$. The degeneracy of the spin-up ($m_s = +1/2$) and spin-down ($m_s = -1/2$) spins states is remove upon application of a magnetic field. A resonance transition may occur with a photon of energy $h\nu$.

$\Delta m_s = \pm 1$ is satisfied (Figure 3-1). Alternatively, the electromagnetic (EM) radiation frequency may be kept constant, and the strength of the magnetic field is instead varied to match the energy separation of the states to $h\nu$.

In reality the Zeeman interaction is susceptible to anisotropy, which arises from spin-orbit coupling mixing of excited states with the ground state. The resulting interaction can be written as

$$\hat{\mathscr{H}}_{\mathrm{EZ}} = \mu_B \boldsymbol{B}^T \cdot \boldsymbol{g} \cdot \hat{\boldsymbol{S}}\,, \tag{3-6}$$

where $\boldsymbol{g}$ is a tensor.

3.1.1.2 Zero-field interaction

The zero-field interaction is applicable only to defects that contain two or more unpaired electrons ($S \geq 1$). In such systems, local fields that arise from spin-orbit coupling and dipole-dipole interactions may lift the degeneracy of the spin states without requiring an external magnetic field. The zero-field interaction is described by the traceless tensor $\boldsymbol{D}$ with the Hamiltonian equation:

$$\hat{\mathscr{H}}_{\mathrm{ZF}} = \hat{\boldsymbol{S}}^T \cdot \boldsymbol{D} \cdot \hat{\boldsymbol{S}}\,, \tag{3-7}$$

which is typically given in terms of the principal axes of the interaction:

$$\hat{\mathscr{H}}_{\mathrm{ZF}} = D\left(S_z^2 - \frac{1}{3}S\left(S+1\right)\right) + E\left(S_x^2 - S_y^2\right)\,, \tag{3-8}$$

where, $D = 3/2 D_z$ and $E = 1/2\left(D_x - D_y\right)$ describes the rhombicity of the system for values of $E \neq 0$, otherwise the symmetry is axial.

3.1.1.3 Hyperfine interaction

The hyperfine interaction describes the coupling of an unpaired electron to a local non-zero nuclear spin I, which produces additional splitting in the EPR spectrum. This sensitivity to the local environment proves a powerful tool of EPR spectroscopy as the hyperfine interaction informs about the constituent atoms of a defect, as well as the symmetry and spin localisation of the electron spin probability density.

The general rule for the number of EPR lines observed, for defects with a hyperfine interaction, is $2nI + 1$ where n is the number of equivalent nuclei and I is the nuclear spin of one of these atoms. Common isotopes that give rise to hyperfine interactions in diamond are ^{1}H, ^{13}C, ^{14}N, ^{15}N, and ^{29}Si.

There are two components of the hyperfine interaction:

- The Fermi contact interaction, which is a product of the non-zero unpaired electron probability density at the nucleus. Only s-shell electrons contribute to this component, and thus their spherically symmetric nature results in the interaction being isotropic.
- The dipole-dipole coupling interaction between the electron and the nucleus, which results in an anisotropic interaction field. The anisotropy of this interaction informs about the distribution of the unpaired electron probability density, and by extension the geometrical configuration of the defect.

The hyperfine interaction is not directly utilised in this thesis and therefore the related Hamiltonian:

$$\hat{\mathscr{H}}_{\mathrm{HF}} = \hat{\boldsymbol{S}}^{T} \cdot \boldsymbol{A}_i \cdot \hat{\boldsymbol{I}}_i \,, \tag{3-9}$$

where $\hat{\boldsymbol{I}}_i$ is the i^{th} coupled nucleus and $\boldsymbol{A}_i$ is its associated hyperfine coupling tensor, will not be derived.

3.1.1.4 Quadrupole interaction

For a nucleus of spin $I \geq 1$, there is a non-spherical charge distribution internally, which allows for an interaction between the nuclear quadrupole moment and an electric field gradient that is generated by the anisotropic distribution of charge

at the defect. The quadrupole interaction is only applicable to nuclei that are not localised at a site with perfect cubic symmetry ($\mathscr{T}_\mathrm{d}$ for diamond).

The quadrupole interaction is described by the tensor $\boldsymbol{P}$ with the Hamiltonian equation:

$$\hat{\mathscr{H}}_\mathrm{Q} = \hat{\boldsymbol{I}}_i^T \cdot \boldsymbol{P} \cdot \hat{\boldsymbol{I}}_i \,, \tag{3-10}$$

and like the zero-field interaction (c.f. equation (3-8)), may also be written in terms of the principal axes of the interactions:

$$\hat{\mathscr{H}}_\mathrm{Q} = P_\parallel \left(I_z^2 - \frac{1}{3} I \left(I + 1 \right) \right) + \frac{1}{3} \eta \left(I_x^2 - I_y^2 \right) . \tag{3-11}$$

Again, similar to the zero-field interaction, $P_\parallel = {}^3\!/_2 P_z$ and $\eta = \left(P_x - P_y \right) / P_z$ also describes the rhombicity of the system. Usually, $\boldsymbol{P}$ is traceless as an isotropic component would cause an equal shift to all energy levels.

3.1.1.5 Nuclear Zeeman interaction

The nuclear Zeeman interaction is analogous to the electronic Zeeman interaction, and is applicable to non-zero nuclear magnetic moment nuclei. The corresponding Hamiltonian is similar to equation (3-4), except that g and μ_B are substituted for g_N and μ_N, respectively:

$$\hat{\mathscr{H}}_\mathrm{NZ} = -\mu_N g_{N_i} \boldsymbol{B}^T \cdot \hat{\boldsymbol{I}}_i \,. \tag{3-12}$$

As the mass of a proton is much larger than an electron (${}^{m_p}\!/_{m_e} \approx 1836$), then $\mu_N \ll \mu_B$, which typically results in this interaction providing a small contribution to the overall energy shift.

3.1.2 Transition probability

During an EPR experiment, a transition between energy levels is driven by the time-dependent magnetic component of the microwave field $\boldsymbol{B}_1(t)$. The Hamiltonian describing the interaction of this magnetic field componont with magnetic moment $\hat{\boldsymbol{\mu}}$ is given by

$$\hat{\mathscr{H}}_\mathrm{\mu w} = -\hat{\boldsymbol{\mu}} \cdot \boldsymbol{B}_1(t) \,. \tag{3-13}$$

From which, the transition probability between states u and v is given as being proportional to

$$\left|\langle v|\,\hat{\mathscr{H}}_{\text{lw}}\,|u\rangle\right|^2. \tag{3-14}$$

3.2 Optical absorption spectroscopy

Optical absorption spectroscopy concerns the attenuation, by absorption mechanisms, of an EM wave propagating through a material. Scattering mechanisms may also attenuate the EM wave, but for the energies utilised to investigate the absorption of single crystal diamond, the attenuation caused by scattering may be considered negligible. The optical absorption energies are often subcategorised by wavelength into three regions: $< 400\,\text{nm}$ refers to ultraviolet (UV) absorption; between 400 nm and 700 nm refers to visible (Vis) absorption; and $> 700\,\text{nm}$ refers to infrared (IR) absorption.

Optical absorption in diamond may be considered as intrinsic absorption when an EM wave interacts with the diamond lattice, whilst extrinsic absorption concerns interaction with defects. Absorption spectroscopy is quantitative (assuming the transition is not saturated) and hence is used to quantify defect concentrations, along with informing about properties such as symmetry and preferential orientation (when the polarisation of light in considered).

In principle, optical absorption spectroscopy is a simple comparison of the EM light before and after propagating through the material. An overview of the theory relevant to this thesis will be provided here, although more extensive resources are offered by other authors [4, 5].

The Beer-Lambert law describes the absorption of an EM wave, with angular frequency ω, propagating in one dimension z through a medium, by the intensity $I(z,\omega)$:

$$I(z,\omega) = I_{0,\omega}e^{-\alpha(\omega)z}, \tag{3-15}$$

where, $I_{0,\omega}$ is the initial intensity at $z = 0$, and $\alpha(\omega)$ is the frequency-dependent absorption coefficient of the material. After propagating through a medium of thickness t, the intensity of the EM wave is given as $I_t(\omega)$, and the absorption

interaction may be expressed as an absorbance $A(\omega)$, such that (with surface reflections neglected):

$$A(\omega) = -\log_{10}\left(\frac{I_t(\omega)}{I_{0,\omega}}\right). \tag{3-16}$$

From this, the absorption coefficient may be expressed by a linear dependence to the measured absorbance:

$$\alpha(\omega) = \frac{\ln(10)}{t} A(\omega). \tag{3-17}$$

The absorption coefficient allows for the defect concentration of an extrinsic absorption to be calculated if the calibration constant—which correlates the integrated area of absorption to the number density of the absorbing defect—is known.

In reality, surface reflections may be significant for optical absorption in diamond if the absorption intensity is low and/or the sample is relatively thin (i.e. $< 1\,\text{mm}$ thick). For a given refractive index n and wavenumber of light k, the total transmitted intensity is given by [4]

$$I = \frac{I_{0,\omega}\,(1-R)^2\,e^{-\alpha t}}{1 + R^2 e^{-2\alpha t} - 2Re^{-\alpha t}\cos(2knt)}, \tag{3-18}$$

where R is the Fresnel reflection at the air-material interface. The period term representing interference may manifest itself experimentally as a periodic beating in the absorption spectrum of a thin diamond sample. However, as the beating is at a fixed frequency, it may be effectively removed with a band block fast Fourier transform (FTT).

3.2.1 Intrinsic absorption

Any perfect, tetrahedral, homonuclear lattice cannot absorb light in the one-phonon region as a consequence of possessing inversion symmetry [6]. The maximum frequency vibration that is allowed to propagate through a perfect diamond lattice is $1332\,\text{cm}^{-1}$, which is the characteristic Raman frequency for diamond. Whilst one-phonon optical absorption is nominally forbidden, multi-phonon absorption is allowed such that intrinsic diamond two- and three-phonon absorption is observed between approximately 1600–3850 cm^{-1}. However, the introduction of extrinsic defects or lattice defects lowers the local symmetry, such that one-phonon absorption can be locally allowed and observed with several common impurities in diamond [7].

In general, the large indirect diamond band gap of 5.47 eV (227 nm) [8], results in diamond being transparent to wavelengths longer than 227 nm (notwithstanding multi-phonon absorption). For wavelengths shorter than 227 nm, such that the energy equal to or greater than the band gap, then intrinsic band-band absorption may occur between the valence band and conduction band.

3.2.2 Extrinsic absorption

Defects and impurities may give rise to energy states in the band gap of diamond. A transition between one of these states and the conduction or valence band will produce a broad absorption continuum. However, if a defect produces as least two energy states in the band gap, then characteristic (allowed) transitions between these localised levels may be observed.

The characteristic transitions often comprise of two features: the zero-phonon line (ZPL) and the phonon sideband (PBS). The ZPL transition is almost entirely electronic and its energy exactly corresponds to the energy separation between the ground and excited states of the defect (Figure 3-2a). In diamond, it is possible to discriminate between individual ZPL energies with meV resolution.

Electron-phonon coupling introduces additional levels to the energy states, creating a vibronic structure. In a simplified model, the energy separation between the vibronic levels is $\hbar\omega$, where ω is the frequency of the impurity atom in the diamond lattice that may be calculated using a simple diatomic model [9]. In reality there are likely multiple phonon vibrations involved in the coupling. Consequently, a range of transition energies are possible between the two levels, which gives rise to a PBS that is mostly lower wavelength/higher energy than the ZPL (Figure 3-2b).

In general, analytical spectroscopy is interested in the intensity and linewidth of the ZPL. A defect will possess a native ratio of its ZPL intensity in comparison to the PSB—this is known as the Debye-Waller factor and is dependent on temperature. The Debye-Waller factor may be temporarily increased (values are between zero and unity, with higher values implying more photons are at the ZPL energy) by reducing the temperature of the diamond to 77 K (or colder). As the occupation levels of higher energy vibrational states are reduced with temperature, intensity

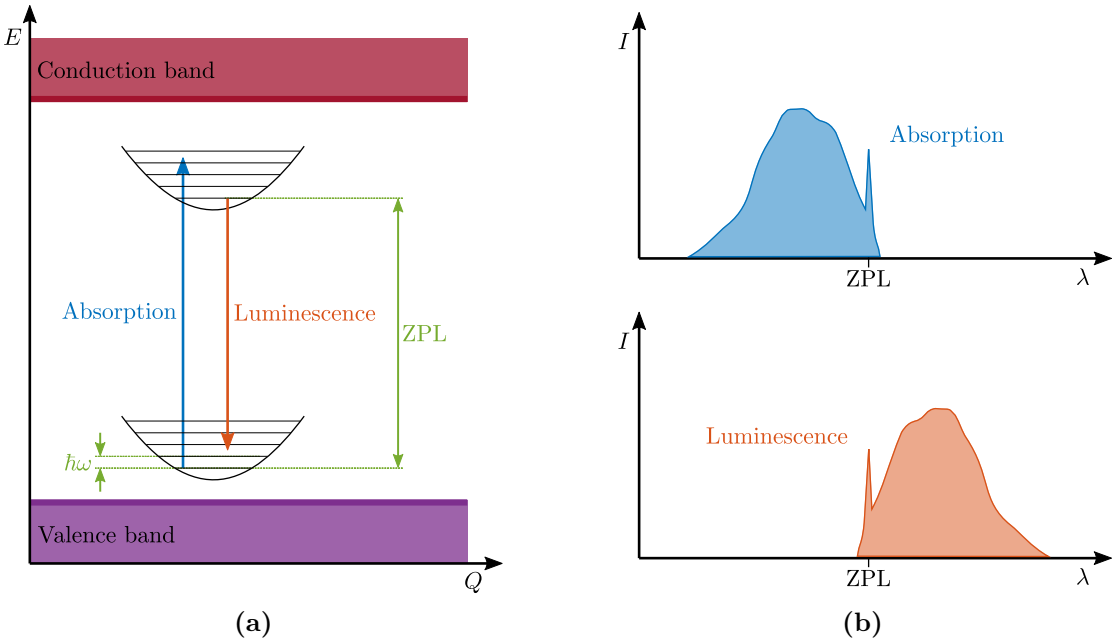

Figure 3-2 (a) Absorption and luminescence transitions between the vibronic structure of the ground and excited state levels (in the band gap) of a defect. The ZPL is indicated between the lowest vibronic energies in each state, and the vibrational energy separation is given as $\hbar\omega$. Energy (E) and configuration coordinate (Q) are noted as the axes of the transitions. (b) Typical spectroscopic envelopes of absorption and luminescence, from the in-gap states of a defect. Intensity (I) and wavelength (λ) are noted as the axes of the spectra. Figure adapted from [5].

is transferred from the PBS to the ZPL; the linewidth of the ZPL is narrowed; and the spectroscopic sensitivity is improved. Hence, spectra of diamond are often recorded at cryogenic temperatures, which is also the case for many of the spectra reported in this thesis.

Impurities heavier than carbon typically produce a vibrational frequency lower than the Raman frequency, and by lowering the local symmetry, their absorption features are observed in the one-phonon region. An example of these heavy-impurity vibrational modes is substitutional nitrogen and its aggregates [10]. Conversely, impurities lighter than carbon (or those highly strained) produce a vibrational frequency higher than the Raman frequency. As propagation through the lattice is not allowed, the vibration is localised in both frequency and space, and may be observed as a sharp features known as a local vibrational mode (LVM). LVMs provide another key characteristic feature of impurities which aids the identification of defects.

3.3 Photoluminescence (PL) spectroscopy

Photoluminescence (PL) spectroscopy is analogous to absorption spectroscopy, except that it observes the emission, or luminescence, from a defect rather than the absorption (Figure 3-2a). Specifically, PL is observed after an electronic dipole has absorbed an incident photon and consequently transitions into the excited state of the defect, from which it may relax by emitting a photon of equal or lower energy than the incident photon. The radiative lifetime in diamond is typically a few tens of nanoseconds [11].

Whilst the ZPL energy of a defect is the same in absorption and luminescence, the PSB of a PL spectrum is on the higher wavelength/lower energy side of the ZPL (Figure 3-2b). The PBS of absorption and luminescence are illustrated as mirror images of each other in Figure 3-2b, but this is not necessarily the case as the electron-phonon coupling in ground and excited states may be different and lead to different PSB structures.

PL spectroscopy is very sensitive and may detect sub ppb (parts per billion) concentrations of defects. However, PL spectroscopy is not considered a quantitative method for bulk measurements since the excited state of a defect may also relax via non-radiative processes (through phonon emission), which greatly complicates the analysis of PL spectra and makes quantitative analysis unreliable. However, the sensitivity of PL spectroscopy allows for single centre detection with confocal microscopy [12], from which a quantitative measurement may be made on a very small area by counting the individual centres.

A delayed luminescence effect, known as phosphorescence, may also occur in diamond. Rather than emitting some nanoseconds after absorption, the excited state performs intersystem crossing (ISC) to a metastable state with a different spin multiplicity. Subsequent relaxation from this metastable state often requires forbidden transitions which occur at a slower rate than PL, such that phosphorescence lifetimes are in the order of seconds (or even longer in some cases) [13].

3.4 Charge transfer

Charge transfer is the reversible transfer of charge between defects, often via the conduction or valence band, and is facilitated by thermo- and photo-chromic processes [14]. Thermo-chromic charge transfer involves a thermal treatment process whereby the sample is heated in an environment unexposed to visible light (i.e. the dark); photo-chromic charge transfer involves an optical illumination treatment process, whereby the sample is directly illuminated with light. In CVD diamond the dominant donor is typically N_S^0, which often results in charge transfer with other defects accepting electrons from N_S^0 centres. The charge transfer process in such a diamond, with an acceptor X, generally behaves as the following equation:

$$X^0 + N_S^0 \underset{\text{Optical}}{\overset{\text{Thermal}}{\rightleftharpoons}} X^- + N_S^+ \,. \tag{3-19}$$

Thermal treatment is expected to drive the transfer of charge (usually one electron) from the N_S^0 donor to the deeper X^0 acceptor, such that the resultant centres are N_S^+ and X^-. Optical treatment can reverse the charge transfer effect of thermal treatment and restore both the donor and acceptor to their neutral charge states.

The thermo-chromic charge transfer process is outlined in the example shown in Figure 3-3a. Thermal treatment provides sufficient energy to electrons in the valence band such that they are excited to acceptor states (X_1^0 and X_2^0). The process results in the production of holes in the valence band, which travel through the valence band and are captured by N_S^0.

Similarly, the photo-chromic charge transfer process is outline in Figure 3-3b. Optical illumination treatment of sufficient energy excites an electron from the acceptor states (now X_1^- and X_2^- after thermal treatment) to the conduction band. Analogous to holes in the valence band, the electrons travel through the conduction band and are captured by N_S^+ centres, thereby reversing the charge transfer process.

The processes outlined in Figure 3-3, involving the N_S^0 donor level at approximately 1.7 eV below the conduction band, require the majority of acceptor states to be closer than 1.7 eV above the valence band. In the event that relatively few acceptor states are sufficiently close to the valence band, thermal treatment at 1.7 eV may

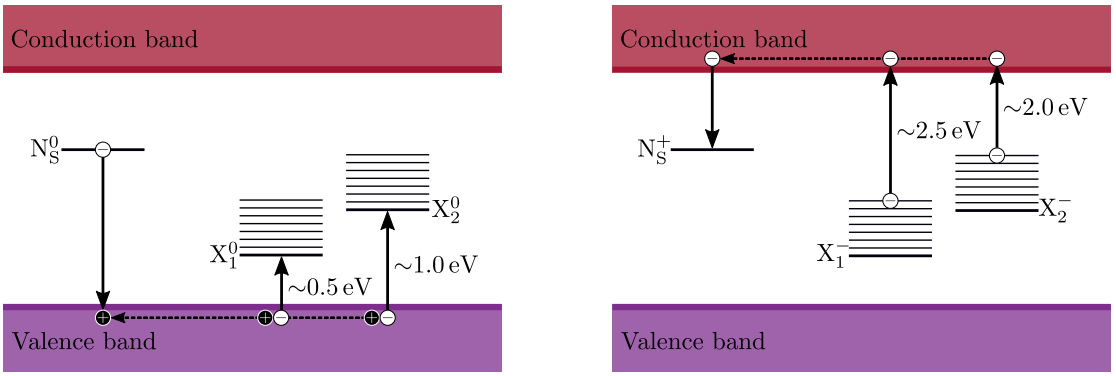

(a) Thermo-chromic charge transfer

(b) Photo-chromic charge transfer

Figure 3-3 The reversible thermo- and photo-chromic charge transfer processes are demonstrated with N_S^0 as an example donor. (a) The thermo-chromic process involves thermal electron excitation from the valence band to acceptor states in the band gap. Holes in the valence band—produced as a result of electron excitation—travel along the valence band and are captured by N_S^0. (b) The photo-chromic process involves optical electron excitation from the acceptor states to the conduction band. The excited electrons travel through the conduction band and are captured by N_S^+. Figure adapted from [14, 15].

ionise the N_S^0 centres and excite electrons into the conduction band. These excited electrons travel through the conduction band and may be captured by mid-gap acceptor states, which are further than 1.7 eV from both the conduction band and valence band.

Furthermore, the relatively large ~5.5 eV band gap of diamond effectively removes the ability to predict the charge state of defects based on their position in the gap relative to the Fermi level [16]. In other semiconductors such as silicon (band gap of ~1.1 eV), a simple interpretation would suggest that all states below the Fermi level have accepted electrons, whilst all those above have donated electrons. However, in diamond the position of the Fermi level is not locally well defined, and instead it is the spatial proximity of donors and acceptors that predominately dictates the charge of the defects.

For example, using the N_S donor and the B_S acceptor (0.37 eV above the valence band) as an example, if $[N_S] \gg [B_S]$ (e.g. $[N_S] = 100[B_S]$) then most B_S^0 centres are likely to accept an electron to become B_S^-, as they likely have an N_S^0 centre spatially nearby. If $[N_S] \approx [B_S]$, then whilst it is still theoretically possible to charge transfer most B_S^0 centres to B_S^-, it is unlikely that an N_S^0 centre will be

spatial nearby most B_S^0 centres, so only a fraction of B_S^0 will charge transfer to B_S^-. Similar concentrations of donors and acceptors result in unstable charges which may be easily manipulated by thermal and/or optical treatment.

The dependence on spatial proximity rather than the Fermi level also provides an explanation for why more than one charge state of the same defect may be simultaneously observed in the same diamond [16] (e.g. N_S^0/N_S^+, NVH^0/NVH^-, NV^0/NV^-, SiV^0/SiV^-).

3.5 Symmetry and point groups

Diamond is a cubic crystal system, and may be further classified by its crystal class, or point group, symmetry as tetrahedral or $\mathscr{T}_d$ (in Schöenflies notation). The $\mathscr{T}_d$ point group is invariant under a total of 24 geometric symmetry operations, and by Neumann's principle this invariance extends to any physical property, such as the atoms, of a $\mathscr{T}_d$ lattice [17]. Therefore, any atom positioned exactly on a lattice site in diamond also possesses $\mathscr{T}_d$ point group symmetry, and is symmetrically indistinguishable from any other identical and equivalently positioned atom. The majority of $\mathscr{T}_d$ lattice sites in diamond are necessarily occupied by carbon, but impurities may also occupy a lattice site (or several lattice sites) and also possess $\mathscr{T}_d$ symmetry (e.g. N_S^+, N_4V).

Any atom that is offset from the diamond lattice, or combination of atoms and/or vacancies that do not form a structure invariant to the 24 symmetry operations of $\mathscr{T}_d$, possess a lower point group symmetry that is a subgroup of $\mathscr{T}_d$. By extension, as the number of symmetrically invariant operations reduce from 24, the orientational degeneracy also reduces and several symmetry-related orientation sites become distinguishable. Table 3-1 presents all the $\mathscr{T}_d$ subgroups and the number of orientation sites of each point group, that have been observed in diamond.

Symmetry and point groups derive from group theory and allow for the physical properties of a system to be related to its symmetry. In particular, information about the electronic orbital symmetry of a particular defect may be acquired from group theory and is typically tabulated in a character table. The work in this

Crystal system	Point group	Orientation sites
Tetrahedral	$\mathscr{T}_\mathrm{d}$	1
Tetragonal	$\mathscr{D}_\mathrm{2d}$	3
Trigonal	$\mathscr{C}_\mathrm{3v}$, $\mathscr{D}_\mathrm{3d}$	4
Rhombic	$\mathscr{C}_\mathrm{2v}$	6
Monoclinic	$\mathscr{C}_\mathrm{2h}$, $\mathscr{C}_\mathrm{1h}$, $\mathscr{C}_2$	12
Triclinic	$\mathscr{C}_1$	24

Table 3-1 The crystal system and point group (in Schöenflies notation) symmetries observed in diamond, along with the number of symmetry-related orientation sites of each symmetry.

$\mathscr{D}_\mathrm{3d}$	E	$2\mathrm{C}_3$	$3\mathrm{C}_2$	i	$2\mathrm{S}_6$	$3\sigma_d$	
A_1g	1	1	1	1	1	1	
A_2g	1	1	-1	1	1	-1	
E_g	2	-1	0	2	-1	0	
A_1u	1	1	1	-1	-1	-1	
A_2u	1	1	-1	-1	-1	1	z
E_u	2	-1	0	-2	1	0	(x, y)

Table 3-2 The character table of the $\mathscr{D}_\mathrm{3d}$ point group [23]. The first row contains the geometrical symmetry operations, and the first column contains all the possible symmetry species of the point group. The table is filled with the characters (i.e. the matrix trace) of the operation for each symmetry species. Also noted are the symmetry species of the dipole operators relative to the point group axes (x, y, z).

thesis concerns the application of character tables, and therefore the derivation of the tables through group theory is omitted. However, a general introduction to the group theory of molecular orbitals is provided by Atkins and Friedman [18], whilst the derivation of character tables for defects in diamond has been addressed in various PhD theses [19–22].

As an example, the character table for the $\mathscr{D}_\mathrm{3d}$ point group [23] is given in Table 3-2 and provides a wealth of information about the point group. Along the first row is the point group symbol, and the relevant symmetry operations under which the point group is invariant. Whilst specific operations are not particularly relevant here, the principal axis—defined as the axis of rotation with the largest (unique) n, where C_n is an n-fold rotation of angle $^{2\pi}/_n$—may be obtained from the table. The C_3 rotation axis, and therefore the principal axis, is located along the $\langle 1\,1\,1 \rangle$ directional bonds of the diamond lattice.

Along the first column are the irreducible representations of the symmetry species given in Mulliken symbols. The symmetry species correspond to energy levels that a defect with this particular point group symmetry may form. A and E refer to one- and two-dimensional (i.e. singly and doubly degenerate) states, respectively, and A is also symmetric about the principal axis. Note that the identity symmetry operation E should not be confused with the doubly degenerate E state. The 1 and 2 subscripts identify whether a species is symmetric or antisymmetric with regards to rotation about a secondary axis, respectively. The g (*gerade*, even) and u (*ungerade*, uneven) subscripts identify whether a species is symmetric or antisymmetric with regards to inversion, respectively. Other Mulliken symbols and subscripts may be required to describe other point groups [23]. The table is filled with characters which summarise the result of an operation on the symmetry species basis; no further consideration to characters is given in this thesis.

Finally, the character table also provides the symmetry species of the electronic dipole operator(s) in the Cartesian basis (x, y, z). This knowledge enables the ability to calculate if a transition between two states is forbidden by symmetry (i.e. a symmetry selection rule), and therefore greatly reduces the number of possibilities that need considering. An electronic transition is allowed if the direct product of the two states contains either (or both) of the dipole operator symmetry species. The direct products of point group symmetry species are also typically tabulated [23]; Table 3-3 provides the $\mathscr{D}_{3d}$ point group product table. From this, the allowed electronic dipole transitions may be calculated from any ground state symmetry species Γ_{GS} to excited state symmetry species Γ_{ES}, as presented in Table 3-4. Additionally, the possible energy levels of the defect may also be determined from the product table if the molecular orbital configuration is know, as demonstrated for SiV^0 in Chapter 5.

As noted in the diagonal of Table 3-3, a direct product between two identical symmetry species always produces the totally symmetric irreducible representation, which for the $\mathscr{D}_{3d}$ point group is A_{1g}. Thus, if a transition is allowed, the direct product of the ground and excited state symmetry species must contain at least one of the electronic dipole symmetry species, which would result in the

$\otimes$	A_{1g}	A_{2g}	E_g	A_{1u}	A_{2u}	E_u
A_{1g}	A_{1g}	A_{2g}	E_g	A_{1u}	A_{2u}	E_u
A_{2g}		A_{1g}	E_g	A_{2u}	A_{1u}	E_u
E_g			$A_{1g} + [A_{2g}] + E_g$	E_u	E_u	$A_{1u} + [A_{2u}] + E_u$
A_{1u}				A_{1g}	A_{2g}	E_g
A_{2u}					A_{1g}	E_g
E_u						$A_{1g} + [A_{2g}] + E_g$

Table 3-3 The direct product table for the $\mathscr{D}_{3d}$ point group. A state inside square brackets will have the highest spin multiplicity $(2S + 1)$ allowed.

Γ_{GS}		A_{1g}	A_{2g}	E_g	A_{1u}	A_{2u}	E_u
Γ_{ES}	z	A_{2u}	A_{1u}	E_u	A_{2g}	A_{1g}	E_g
	(x, y)	E_u	E_u	A_{1u}, A_{2u}, E_u	E_g	E_g	A_{1g}, A_{2g}, E_g

Table 3-4 The allowed electronic dipole transitions of the $\mathscr{D}_{3d}$ point group. For a given ground state symmetry species Γ_{GS}, an electric dipole transition with a z or (x, y) dipole operator, is only allowed to a specific excited state symmetry species Γ_{ES}.

direct product of all three species containing the totally symmetric irreducible representation. The symmetry selection rule may therefore be formulated as

$$\Gamma_{GS} \otimes \Gamma_{Dipole} \otimes \Gamma_{ES} \supset \Gamma_{Sym}\,, \tag{3-20}$$

where, Γ_{Dipole} is the irreducible representation of the dipole operator, and Γ_{Sym} is the totally symmetric irreducible representation that is typically denoted as A, A_1, A_{1g}, A_g, or A' depending on the point group. The advantage of considering the symmetry selection rule in this manner also allows for vibronic transition to be considered via the inclusion of the irreducible representation of an LVM (Γ_{LVM}):

$$\Gamma_{GS} \otimes \Gamma_{Dipole} \otimes \Gamma_{ES} \otimes \Gamma_{LVM} \supset \Gamma_{Sym}\,. \tag{3-21}$$

Group theory is therefore an extremely useful tool that places restrictions on the electronic and vibronic behaviour of a defect, simply from knowing the symmetry. However, group theory does not inform about the relative energies of the energy levels, nor which symmetry species are involved in any particular transition. Further spectroscopic investigation, often aided by the symmetry-lowering technique of unixial stress (discussed in the next section), are typically required to answer these questions.

3.6 Uniaxial stress

The uniaxial stress technique is utilised to reduce electronic and orientational degeneracy that a defect may possess. Stress is applied to a sample along a single axis whilst a spectroscopic technique—such as EPR, optical absorption, or PL—observes the stress-induced shifting and splitting of the spectral features of a defect. The seminal work by Kaplyanskii describes the effect of uniaxial stress on cubic crystals and defects with cubic or lower symmetry [24, 25]. Several other authors have further developed the theory and technical application of uniaxial stress for a variety of symmetries and defects [26–31].

In order to illustrate how the electronic and orientational degeneracy of a defect may be lifted by uniaxial stress lowering the symmetry, an $E \leftrightarrow A$ (orbital doublet-to-singlet) transition at trigonal centre will be considered. Uniaxial stress will shift the energy of all states, but electronic degeneracy may only be lifted from orbitally degenerate transition states (i.e. a doubly degenerate E state, or higher degeneracy state). Figure 3-4a illustrates the possible splitting of the excited E state upon applied stress, such that two different energy absorption transitions may now occur with the ground A state. Spectroscopically, the single peak at zero stress is observed to split into two peaks upon applied stress, which shift in energy in opposite directions relative to the initial peak (Figure 3-4b).

The orientational degeneracy of a defect is dependent on the number of equivalent symmetry-related orientations its point group possesses. A trigonal defect has four equivalent orientations (Table 3-1), with the principal axis of each orientations along a $\langle 1\,1\,1 \rangle$ direction: $[1\,1\,1]$, $[\bar{1}\,\bar{1}\,1]$, $[1\,\bar{1}\,\bar{1}]$, and $[\bar{1}\,1\,\bar{1}]$. The principal axis is typically defined as the Z axis of the defect, such that the $[1\,1\,1]$ principal axis has corresponding X and Y axes of $[1\,\bar{1}\,0]$ and $[1\,1\,\bar{2}]$, respectively. As shown in Figure 3-5a, these trigonal defect axes must not be confused with the crystal axes of x, y, and z that are along different directions.

Orientational degeneracy of any defect may be lifted if the applied stress direction (conventionally along $\langle 0\,0\,1 \rangle$, $\langle 1\,1\,1 \rangle$, or $\langle 1\,1\,0 \rangle$) forms different angles with different principal axis directions. In the case of $\boldsymbol{\sigma} \parallel \langle 0\,0\,1 \rangle$, a common angle is made with

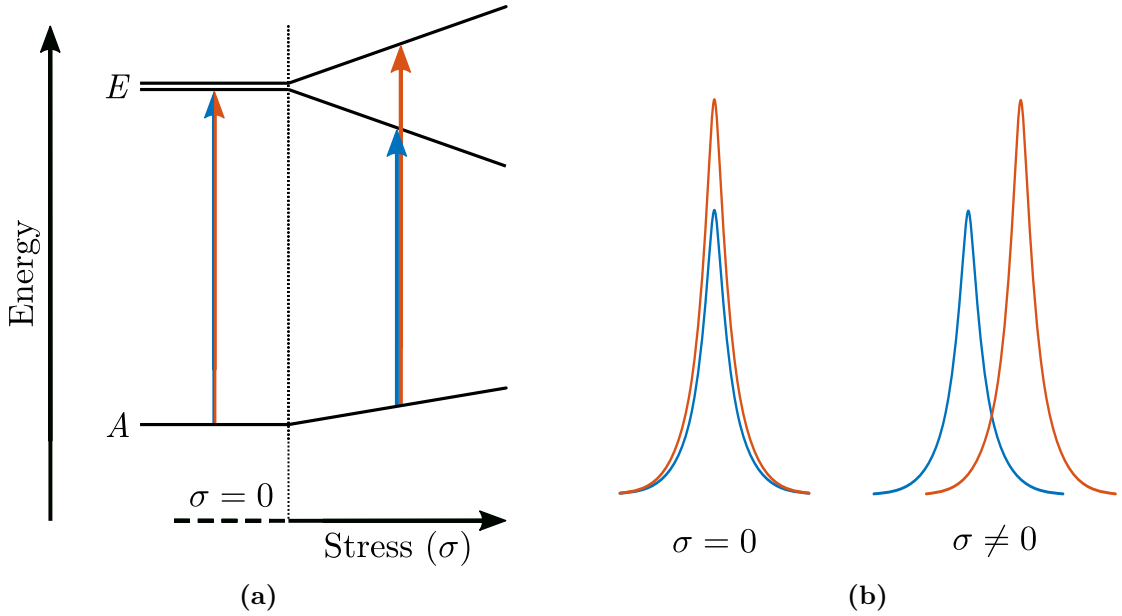

Figure 3-4 An illustration of applied uniaxial stress breaking the electronic degeneracy of an $E \leftrightarrow A$ optical absorption transition. (a) With increasing stress (σ), the orbitally non-degenerate state A will only shift in energy, whilst the orbitally doubly degenerate E state will both shift in energy and simultaneously split into two energy levels. (b) A schematic of the potential absorption spectrum of this transition under zero applied stress (left) and non-zero applied stress (right) where two distinguishable transitions are now observed.

all four principal axis orientations of the trigonal defect, and therefore there is no change to the orientational degeneracy (Figure 3-5b). However, $\boldsymbol{\sigma} \parallel \langle 1\,1\,1 \rangle$ and $\boldsymbol{\sigma} \parallel \langle 1\,1\,0 \rangle$ both form two unique sets of angles with the principal axes, such that the two classes of orientation become distinguishable under applied stress (Figures 3-5c and 3-5d).

The breaking (or lack thereof) of the electronic and orientational degeneracy of a defect informs about the symmetry of the states between which the transition occurs, as it is possible to predict the behaviour of a defect with any given symmetry and (allowed) transition. In particular, the number of transitions and their intensities may be compared to extensive tabulations of splittings and intensities for the relevant point group symmetry [22, 26, 30]. The tables are generated by considering the stress Hamiltonian, for which only a brief description will be provided here, but detailed deviations of splitting and intensity tables for various point group symmetries and transitions may be found in other PhD theses [20, 22, 31, 33].

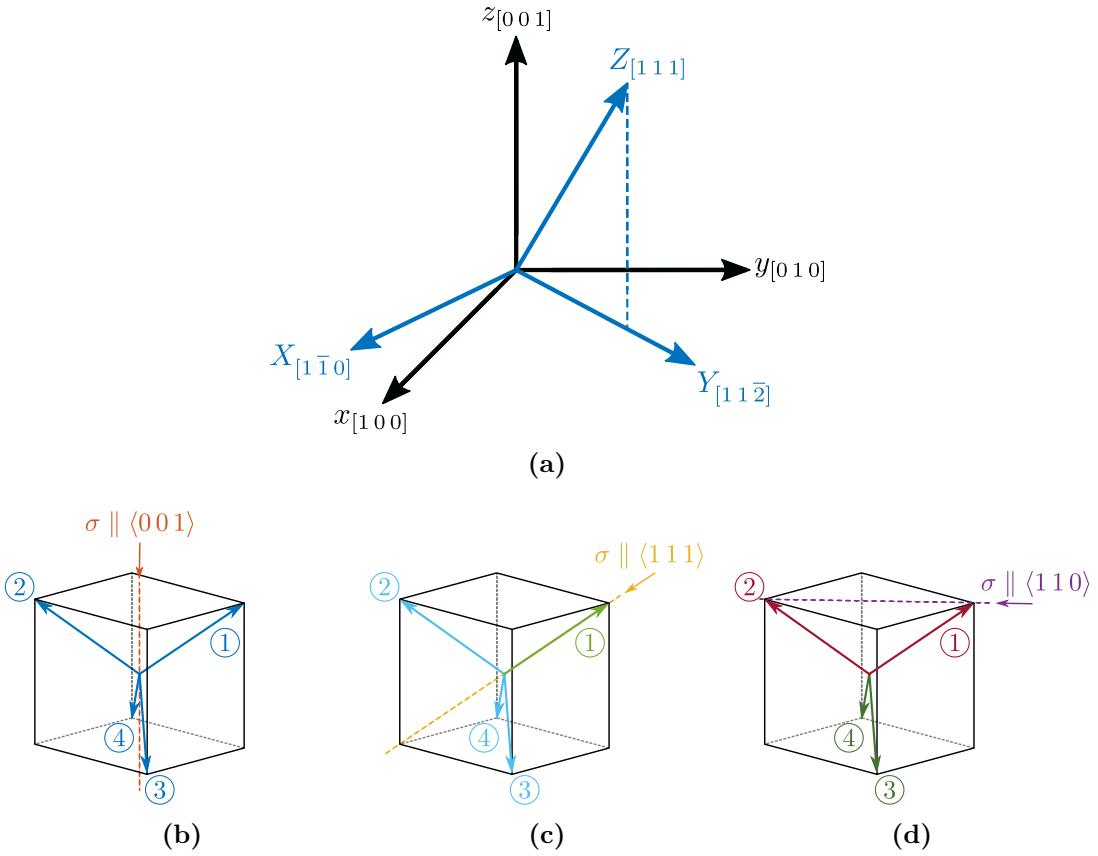

Figure 3-5 (a) The axes of a trigonal centre (X, Y, Z) in blue, relative to the crystal axes (x, y, z) in black. The orientational degeneracy of a trigonal centre is probed by comparing the angle between the stress axis and each principal axis (labelled ①, ②, ③, and ④). Stress applied along (b) $\langle 0\,0\,1 \rangle$ results in the same angle with all orientations and no change in degeneracy, whilst (c) $\langle 1\,1\,1 \rangle$, and (d) $\langle 1\,1\,0 \rangle$ both result in two unique sets of angles such that two classes of orientation may be observed. Figure adapted from [32].

First, the stress tensor $\boldsymbol{\sigma}_{ij}$ is considered:

$$\boldsymbol{\sigma}_{ij} = \sigma \cos(\theta_i) \cos(\theta_j) = \begin{pmatrix} \sigma_{xx} & \sigma_{xy} & \sigma_{xz} \\ \sigma_{yx} & \sigma_{yy} & \sigma_{yz} \\ \sigma_{zx} & \sigma_{zy} & \sigma_{zz} \end{pmatrix}, \tag{3-22}$$

where, σ is the applied magnitude of stress, and θ_i and θ_j represent the angle between the stress axis and the i^{th} and j^{th} crystal axis (x, y, or z). The stress tensor is symmetric ($\sigma_{ij} = \sigma_{ji}$) due to the structure of diamond. Compressive stress occurs if $i = j$ (i.e. $\boldsymbol{\sigma} \parallel \langle 0\,0\,1 \rangle$), whereas shear stress occurs if $i \neq j$ (i.e. $\boldsymbol{\sigma} \parallel \langle 1\,1\,1 \rangle$); $\boldsymbol{\sigma} \parallel \langle 1\,1\,0 \rangle$ comprises of both compressive and shear stress.

Defect	Symmetry	Substrate orientation
NV	$\mathscr{C}_{3v}$	{0 0 1} [34], {1 1 0} [35], {1 1 1} [36], {1 1 3} [37]
SiV	$\mathscr{D}_{3d}$	{1 1 0} [38]
SiVH	$\mathscr{C}_{1h}$	{1 1 0} [39]
SiV_2H	$\mathscr{C}_{1h}$	{1 1 0} [40]
WAR2	$\mathscr{C}_2$ or $\mathscr{C}_{2v}$	{0 0 1} [41]
7354 cm^{-1}	$\mathscr{C}_{3v}$ or $\mathscr{D}_{3d}$	{0 0 1}, {1 1 0} (see Chapter 6)

Table 3-5 Preferential orientation of defects in CVD diamond. Non-equilibrium populations are observed in diamonds grown on specific substrate orientations.

The perturbation caused by stress V may then be considered:

$$V = \sum_{i,j} a_{ij}\sigma_{ij} \,, \tag{3-23}$$

where, σ_{ij} are the elements of the stress tensor in equation (3-22), and a_{ij} are the electronic operators [24–26]. Finally, the full Hamiltonian $\mathscr{H}$ may be constructed:

$$\mathscr{H} = \mathscr{H}_0 + V \,, \tag{3-24}$$

where, $\mathscr{H}_0$ is the unperturbed Hamiltonian.

It is important to note that the relative intensity tables assume equilibrium populations of all possible orientations of the given point group. However, this is not always the case as several defects have been observed to grow with preferential orientation (i.e. non-equilibrium populations) in CVD diamond, as summarised in Table 3-5. For such defects, it is necessary to recalculate the intensity tables in order to match the preferential orientation populations observed.

References

1. G. R. Eaton *et al.*, *Quantitative EPR* (Springer, Vienna, 2010).
2. J. A. Weil, J. R. Bolton, *Electron Paramagnetic Resonance* (John Wiley & Sons inc., Hoboken, NJ, 2nd, 2007).
3. A. Abragam, B. Bleaney, *Electron Paramagnetic Resonance of Transition Ions* (Oxford University Press, Oxford, 1980).
4. G. Davies, in *Semiconductors and Semimetals*, ed. by M. Stavola (Academic Press, 1999), vol. 51 Part B, chap. 1, pp. 1–92.
5. M. Fox, *Optical Properties of Solids* (Oxford University Press, Oxford, 2nd, 2010).
6. R. P. Mildren, in *Optical Engineering of Diamond*, ed. by R. P. Mildren, J. R. Rabeau (John Wiley & Sons, Ltd, 2013), chap. 1, pp. 1–34.
7. C. D. Clark, S. T. Davey, *Journal of Physics C: Solid State Physics* **17**, L399–L403 (1984).
8. C. D. Clark, P. J. Dean, P. V. Harris, *Proceedings of the Royal Society of London. Series A. Mathematical and Physical Sciences* **277**, 312–329 (1964).
9. M. D. McCluskey, *Journal of Applied Physics* **87**, 3593–3617 (2000).
10. J. Walker, *Reports on Progress in Physics* **42**, 1605–1659 (1979).
11. G. Davies *et al.*, *Physical Review B* **46**, 13157–13170 (1992).
12. A. Gruber *et al.*, *Science* **276**, 2012–2014 (1997).
13. J. Custers, *Physica* **18**, 489–496 (1952).
14. R. U. A. Khan *et al.*, *Journal of Physics: Condensed Matter* **21**, 364214 (2009).
15. C. B. Hartland, PhD thesis, The University of Warwick, 2014.
16. A. T. Collins, *Journal of Physics: Condensed Matter* **14**, 3743–3750 (2002).
17. S. Bhagavantam, P. V. Pantulu, *Proceedings of the Indian Academy of Sciences - Section A* **66**, 33–39 (1967).
18. P. W. Atkins, R. S. Friedman, *Molecular Quantum Mechanics* (Oxford University Press, Oxford, 5th, 2012).
19. H. E. Smith, PhD thesis, King's College London, 2004.
20. S. Liggins, PhD thesis, The University of Warwick, 2010.

21. U. F. S. D'Haenens-Johansson, PhD thesis, The University of Warwick, 2011.
22. B. L. Green, PhD thesis, The University of Warwick, 2013.
23. P. W. Atkins, M. S. Child, C. S. G. Phillips, *Tables for Group Theory* (Oxford University Press, Oxford, 1970).
24. A. A. Kaplyanskii, *Optics and Spectroscopy* **16**, 329 (1964).
25. A. A. Kaplyanskii, *Optics and Spectroscopy* **16**, 557 (1964).
26. A. E. Hughes, W. A. Runciman, *Proceedings of the Physical Society* **90**, 827–838 (1967).
27. I. K. Ludlow, *Journal of Physics C: Solid State Physics* **1**, 307 (1968).
28. G. Davies, *Journal of Physics C: Solid State Physics* **12**, 2551–2566 (1979).
29. G. Davies, M. H. Nazaré, *Journal of Physics C: Solid State Physics* **13**, 4127–4136 (1980).
30. K. Mohammed, G. Davies, A. T. Collins, *Journal of Physics C: Solid State Physics* **15**, 2779–2788 (1982).
31. K. Mohammed, PhD thesis, King's College London, 1982.
32. L. J. Rogers *et al.*, *New Journal of Physics* **17**, 013048 (2015).
33. R. Cruddace, PhD thesis, The University of Warwick, 2007.
34. L. M. Pham *et al.*, *Physical Review B* **86**, 121202 (2012).
35. A. M. Edmonds *et al.*, *Physical Review B* **86**, 35201 (2012).
36. J. Michl *et al.*, *Applied Physics Letters* **104**, 102407 (2014).
37. M. Lesik *et al.*, *Diamond and Related Materials* **56**, 47–53 (2015).
38. U. F. S. D'Haenens-Johansson *et al.*, *Physical Review B* **84**, 245208 (2011).
39. A. M. Edmonds, PhD thesis, The University of Warwick, 2008.
40. U. F. S. D'Haenens-Johansson *et al.*, *Physical Review B* **82**, 155205 (2010).
41. B. L. Cann, PhD thesis, The University of Warwick, 2009.

4

Experimental techniques

This chapter provides technical details of the experimental techniques utilised in this thesis. The theory relevant to these techniques may be found in Chapter 3.

4.1 Quantitative EPR

Quantitative electron paramagnetic resonance (EPR) is a powerful and sensitive technique which has been utilised to measure the concentration of several paramagnetic defects in this thesis.

A simple schematic of the main components of an EPR spectrometer [1] is presented in Figure 4-1. The microwave bridge is responsible for generating microwaves, which are transmitted to the cavity (which contains a sample) via a waveguide; and for recording the signal reflected from the cavity when resonance occurs (typically stored on the controlling computer). The cavity is positioned in an iron core electromagnet that creates a magnetic field, and is controlled with feedback from a Hall probe that measures the field. By tuning the cavity waveguide coupling structure to match the impedance with the waveguide—such that the system is critically coupled and no power is reflected—any absorption of microwaves by a defect at resonance causes a small change in impedance that results in microwaves reflected back via the bridge to the detector. The modulation coils assist in improving sensitivity by modulating the magnetic field at typically 100 kHz, and by extension the EPR signal, which a lock-in amplifier later utilises

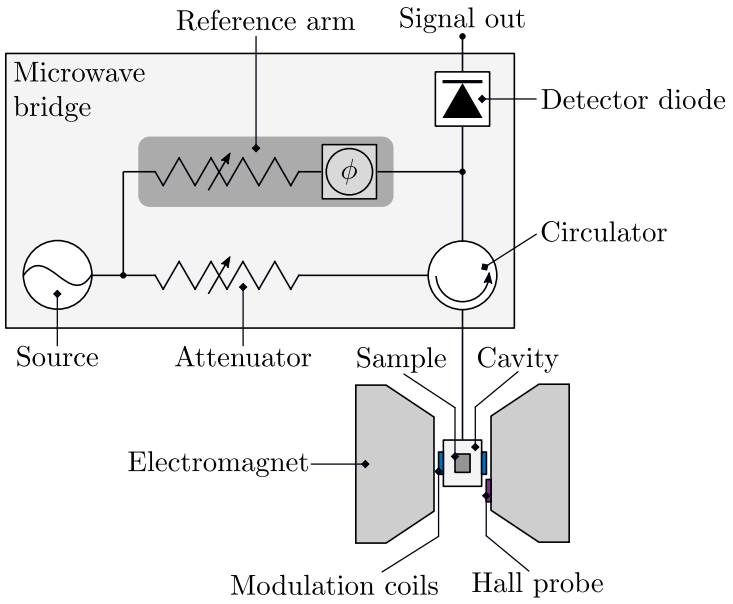

Figure 4-1 Schematic of the components of an EPR spectrometer (excluding the computer, console, and magnetic power supply). Figure adapted from [1].

to only extract signal that matches the frequency and phase of the applied field modulation.

The spectrometer is operated by having a fixed microwave frequency and sweeping the magnetic field, which is the common method for continuous wave EPR (CWEPR). CWEPR typically operates in a *slow passage* regime such that the time to sweep through an EPR transition is much longer than the spin relaxation times (T_1 and T_2) of a given defect. Alternatively, *rapid passage* EPR (RPEPR) may be employed, whereby the rate of change of the magnetic field is faster than the spin relaxation times of a give defect. In this regime the magnetisation is not steady state, and thus it is experimentally necessary to increase the microwave power and adjust the field modulation phase by 90° in order to observe RPEPR signal. The benefit of RPEPR is that, for defects with a long spin-lattice relaxation time (i.e. T_1), a higher signal-to-noise ratio is achieved (compared to CWEPR) such that quantitative measurements for concentrations < 1 ppm are possible [2]. For more rigorous descriptions of CWEPR and RPEPR (and pulsed EPR which is not utilised in this thesis) the reader is directed to various other texts [2–5].

The EPR experiments in this thesis were all performed at room temperature on a Bruker EMX-E EPR spectrometer, in conjunction with a Bruker ER041X X-band

(8–12 GHz) microwave bridge. Both a Bruker ER 4122SHQ spherical cavity and a Bruker ER 4119HS cylindrical cavity were utilised for the measurements. The sample orientation relative to the magnetic field was controlled by a dual-axis goniometer. The experimental parameters utilised are provided by Breeze [2].

An EPR signal is expected to scale in intensity with the number of spins in a system for a given set of acquisition parameters. The concentration may be quantified by comparing the EPR signal intensity of a reference sample with a known concentration of a defect (e.g. neutral substitutional nitrogen (N_S^0) as used in this thesis). Thus, with the subscripts s and r for sample and reference, respectively, the concentration of a defect X may be calculated by

$$[X]_s = [N_S^0]_r \frac{I_s c_s}{I_r c_r}, \tag{4-1}$$

where, I is the EPR integrated intensity of the defect spectrum, and the factor c accounts for numerous experimental parameters that affect the EPR signal. For the EPR measurements in this thesis, a sufficient description of c is given by

$$\frac{1}{c} = \sqrt{P} \cdot B_{\mathrm{mod}} \cdot Q \cdot \underbrace{[G \cdot N \cdot t]}_{\text{scan}} \cdot \underbrace{[g^2 \cdot S(S+1) \cdot m]}_{\text{sample}}, \tag{4-2}$$

where the parameters are:

- P – microwave power,
- B_{mod} – magnetic field modulation amplitude,
- Q – cavity quality factor,
- G – detector gain,
- N – number of scans taken,
- t – acquisition time at each data point,
- g – electron g-factor,
- S – effective spin of defect,
- m – diamond sample mass.

Analysis of EPR spectra is undertaken with an in-house program called EPRsimulator developed by Dale [6]. The spectrum of the reference sample (with known mass and concentration of N_S^0) is loaded into EPRsimulator and a simulation of N_S^0 is fitted—this enables the creation of a reference file that contains $[N_S^0]_r$, I_r and c_r. The sample spectrum is then loaded and a simulation of the defect of interest is fitted to the spectrum. By using the reference file and inputting the sample mass, the concentration of defect X is calculated by solving equations (4-1) and (4-2). The typical error for the EPR measurements performed in this thesis was empirically determined to be approximately 10% by Edmonds [4].

4.2 Optical spectroscopy

The optical spectroscopy measurements in this thesis were made with two types of spectrometers: dispersive [7] and Fourier transform [8].

The dispersive spectrometers employed may be further subcatagorised by whether the diffraction grating moves or is fixed during a measurement. With a movable diffraction grating (Figure 4-2a) a slit is utilised to monochromate the diffracted light, (before or) after interacting with the sample, for a spatial point detector (e.g. a photomultiplier tube). A spectrum over a large wavelength range may be measured by incrementally rotating the diffraction grating and acquiring the signal after each rotation. With a fixed diffraction grating (Figure 4-2b), a range of wavelengths are simultaneously measured on an array of detectors, such as a charged couple device (CCD).

In general, a moveable grating dispersive spectrometer may achieve high sensitivity and resolution but compromises with slow acquisition times; and in contrast, a fixed grating dispersive spectrometer can achieve faster acquisition times from recording multiple wavelengths simultaneously, but may have to compromise with lower sensitivity and resolution.

A Fourier transform infrared (FTIR) spectrometer creates an interferogram of a broadband source—typically with a Michelson inferferometer (Figure 4-3)—that is subsequently Fourier transformed into a frequency domain spectrum. The source

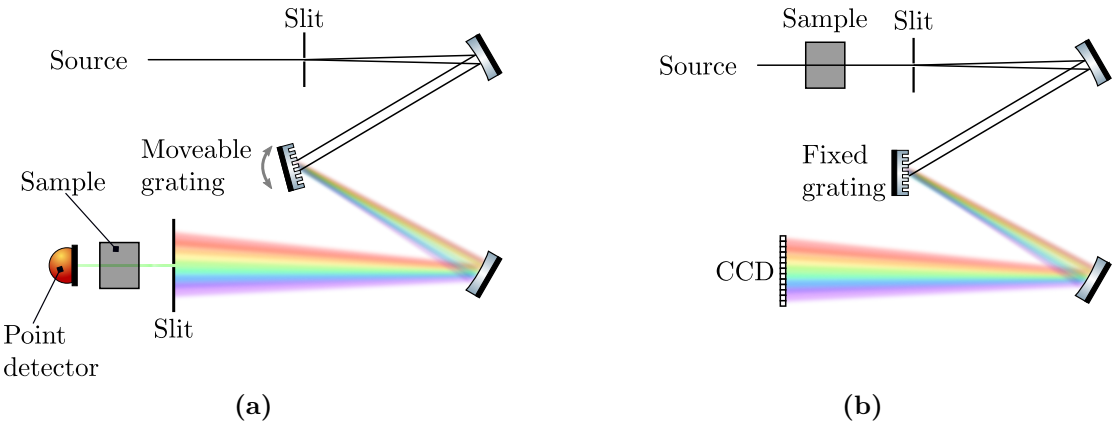

Figure 4-2 Schematic of two types of dispersive spectrometers. (a) A movable diffraction grating selects the wavelength of diffracted light that may pass through a slit onto a spatial point detector (e.g. a photomultiplier tube). (b) A fixed diffraction grating is used and a CCD detects over a range of wavelengths with spatially separated pixels.

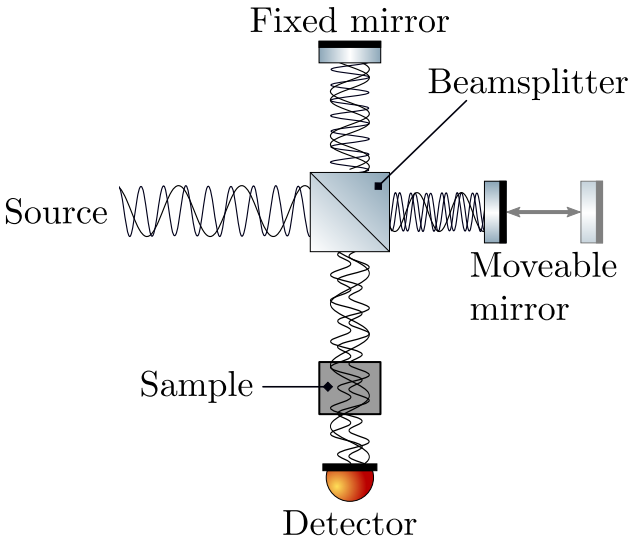

Figure 4-3 Schematic of a Michelson interferometer. Broadband light is split and directed towards one fixed mirror and one moveable mirror that varies the path length such that interference occurs at the beamsplitter upon recombination. This light is then passed through the sample before the interferogram is measured.

is split by a beamsplitter into two paths: towards a fixed mirror and towards a moveable mirror. The moveable mirror may change its path length to the beamsplitter, such that both constructive and destructive interference occurs at the beamsplitter upon recombination (with the fixed mirror path), resulting in the creation of an interferogram. The interferogram is then Fourier transformed into the frequency domain.

Compared to a dispersive spectrometer, a Fourier transform spectrometer (with a broadband source) offers several advantages [8]:

- **Multiplex (Fellgett's) advantage** – The acquisition time is typically smaller as all wavelengths are simultaneously measured.
- **Throughput (Jacquinot's) advantage** – The signal-to-noise ratio is better for a given acquisition time due to a greater energy throughput.
- **Accuracy (Connes') advantage** – An internal helium-neon (HeNe) laser accurately (and precisely) calibrates the wavelength, thereby improving the reproducibility.

However, a Fourier transform spectrometer may also possess disadvantages compared to a dispersive spectrometer [8]:

- **Multiplex (Fellgett's) disadvantage** – The simultaneous measurement of all source wavelengths also applies to the source noise. In the case of source noise-limited systems (e.g. a Fourier transform visible spectrometer), the noise is spread throughout the entire spectrum (thereby cancelling the multiplex (Fellgett's) advantage) and is not localised spatially as it would be for a dispersive spectrometer.
- **Sample photosensitivity** – Higher throughput may be undesirable if the sample is photosensitive (e.g. photo-chromic defects in diamond), and with higher energy/lower wavelength light (i.e. the UV-Vis range) the problem is exacerbated.
- **Atmospheric changes** – If a Fourier transform spectrometer is operated in single-beam mode, then any change in the atmospheric absorption between

the background spectrum and the sample spectrum will be observed in the final spectrum. A dual-beam dispersive spectrometer, with a reference arm and a sample arm, can actively compensate for any change in atmospheric absorption.

Therefore, upon consideration of the advantages and disadvantages, a Fourier transform spectrometer is typically utilised for IR absorption spectroscopy (mostly due to the multiplex disadvantage), whilst a dual-beam dispersive spectrometer is typically utilised for ultraviolet-visible (UV-Vis) absorption spectroscopy.

For all the techniques covered in this section, it is common practice to first record a background/reference spectrum with the spectrometer. The background/reference spectrum attempts to compensate for any unwanted signal that may arise from the source, the atmosphere, or the spectrometer components. By subtracting the background/reference spectrum from a spectrum recorded with the sample in the light path, the resultant spectrum will ideally only contain absorption/emission that originate from the sample.

4.2.1 Infrared absorption

The majority of IR absorption measurements in this thesis were obtained with a PerkinElmer Spectrum GX FTIR spectrometer, which may be operated with mid-infrared (MIR) and near-infrared (NIR) configurations (Table 4-1). All measurements were performed at a resolution of $1\,\mathrm{cm}^{-1}$.

For a room temperature measurement, the sample chamber contains a 5× beam condenser which creates a spot size diameter of approximately 1 mm (at a resolution of $1\,\mathrm{cm}^{-1}$) that is incident with the sample resting on a (changeable) aperture. The sample chamber is also subject to a constant flow of dry nitrogen gas in order to minimise absorption from atmospheric H_2O and CO_2. Evidence of atmospheric absorption is often still observed in both the background and sample spectra.

For experiments that require a polariser to investigate the preferential orientation of defects, a suitable MIR or NIR polariser was placed in the beam path before the sample, with the polarisation orientated either parallel or perpendicular to the

Spectrometer	Range (cm^{-1})	Source	Beamsplitter	Detector
Spectrum GX	MIR: 370–7800	Filament	KBr†	MIR-TGS‡
	NIR: 2700–15000	Tungsten-halogen lamp	Quartz	NIR-TSG‡
IFS 66	1000–10000	Tungsten-halogen lamp	CaF_2◇	DTGS⋆

Table 4-1 FTIR spectrometers utilised for IR absorption measurements and their configurations. All measurements were performed at a resolution of $1\,cm^{-1}$. † = Potassium bromide, ‡ = MIR/NIR optimised triglycine sulfate, ◇ = Calcium fluoride, ⋆ = Deuterated triglycine sulfate

growth direction. It is important to note that the background spectrum must also be obtained with the same polarisation direction, in order to compensate for any absorption (or other effects, such as reflection) from the polariser.

Low temperature measurements with the Spectrum GX were only performed in Chapter 7. The sample was supported within indium and positioned over an aperture at the end of a cold finger, which was itself placed inside a custom-built continuous flow cryostat (more detail is given by Glover [9]) with thallium bromide windows.

A Bruker IFS 66 FTIR spectrometer was also utilised solely for low temperature IR absorption measurements, in conjunction with uniaxial stress, in Chapter 6. The configuration of the IFS 66 is given in Table 4-1 and all measurements were also performed at a resolution of $1\,cm^{-1}$. Cryostat details are given in §4.4.

FTIR spectra are analysed with another in-house program called SpectrumManipulator which was also developed by Dale [6]. First, the spectrum is converted from absorbance (A) to absorption coefficient (cm^{-1}) by normalising to a pure IIa diamond reference spectrum with an absorption coefficient of $12.3\,cm^{-1}$ at an energy of $2000\,cm^{-1}$. Once normalised, a suite of in-house calibrated defect reference spectra [6] may be fitted to the spectrum in order to quantify defect concentrations (e.g. N_S^0, N_S^+, A centre (N_{2S}), B centre (N_4V), B_S^0).

4.2.2 Ultraviolet-Visible absorption

UV-Vis measurements were performed with a dual-beam, dispersive PerkinElmer Lambda 1050 spectrometer. The spectrometer contains two sources: a deuterium

lamp (175 nm < λ < 919.2 nm) and a tungsten-halogen lamp (319.2 nm < λ < 3300 nm). The source light is monochromated, masked, depolarised, and then directed either through the reference arm or sample arm via a rotating mirror, before reaching the detector. In this thesis (specifically in Chapter 7), UV-Vis measurements were only performed at room temperature between a wavelength range of 200–800 nm, thus only the photomultiplier tube detector was necessary. Analysis was also facilitated by SpectrumManipulator [6].

4.2.3 Photoluminescence (Renishaw 785–442 nm)

Several excitation wavelength were employed between two (commerical) dispersive Renishaw inVia Raman microscope spectrometers using a 441.6 nm (2.808 eV) helium-cadmium (HeCd) laser, a 514.5 nm (2.410 eV) argon ion (A^+) laser, and a 785.0 nm (1.579 eV) diode pumped solid state laser. The spectrometers are fitted with a motorised XYZ stage which allows for reproducible positioning (and large area mapping not utilised in this thesis).

Measurements with 441.6 nm and 514.5 nm excitation were performed at low temperature using a Linkam TMS600 stage. The sample is bonded to the stage with silver thermal paste (for improved thermal contact), baked for 5 min at 105 °C to remove water vapour from inside the stage, and then cooled down to approximately 80 K by liquid nitrogen. A 20× long working distance air objective (NA = 0.40) was utilised for these measurements.

Measurements with 785.0 nm excitation were also performed at low temperature, but only in conjunction with uniaxial stress (§4.4) for the results in Chapter 5.

4.2.4 Photoluminescence (NIR 1064 nm)

Photoluminescence spectroscopy on diamond is typically only concerned with emission below approximately 1000 nm, as non-radiative decay is expected to dominate at wavelengths further into the infrared [10]. It follows that only a maximum excitation wavelength near the red-end of the visible spectrum, such as 785.0 nm, is necessary to probe the majority of emissions up to 1000 nm.

However, the longest excitation wavelength available, on the Renishaw spectrom-

eters, of 785.0 nm was not sufficient for the project in Chapter 6 of this thesis, which concerns the investigation of a hydrogen-related defect that is commonly observed in nitrogen-doped CVD diamond by absorption *and* emission at 7354 cm^{-1}/1360 nm. Therefore, in order to investigate this defect further with PL spectroscopy (and applied uniaxial stress (§4.4)), a purpose-built PL spectrometer 1064 nm excitation was designed and constructed.

The schematic of the optical design of the 1064 nm PL spectrometer is presented in Figure 4-4, where the 1064 nm source is a continuous wave Elforlight I4-700-1064 diode pumped solid state laser, with an output power of 700 mW. In the source arm (red beam), a 1175 nm shortpass filter is used to avoid any unwanted source signal near the wavelength of interest in the PL experiments. The light is then passed through Keplerian-type telescope that produces a collimated beam of approximately 4 mm in diameter. As the system was built with the intention of investigating the effect of uniaxial stress on the 1360 nm defect, the polarisation of the input beam (normally vertical) may be adjusted with a 1064 nm half-wave plate, and the polarisation of the emission may be selected in the detection arm by a linear polariser. A 1100 nm dichroic shortpass beam splitter will then reflect the input beam towards the excitation arm (purple beam).

The flip mirror in the excitation arm selects between the uniaxial stress cryostat ($Cryo_1$), and the Linkam TMS600 stage cryostat ($Cryo_2$); in both cases an achromatic doublet is utilised to focus the laser onto the sample, and manual XYZ stages align the sample to the laser spot. Emission from the sample is collected by the achromatic doublet, passes through the dichroic beam splitter, and enters the detection arm (blue beam). A 1064 nm longpass filter removes any residual laser light that may still be in the output beam, after which the linear polariser (during uniaxial stress experiments) will select the desired polarisation. A flip mirror may direct the beam towards a CCD camera which aids with aligning the laser spot onto the sample. Finally, the emission is fibre-coupled by another achromatic double into a 105 µm multimode fibre that is connected to the Andor SR-303i-B dispersive spectrometer where an Andor iDus InGaAs CCD detector records the spectrum.

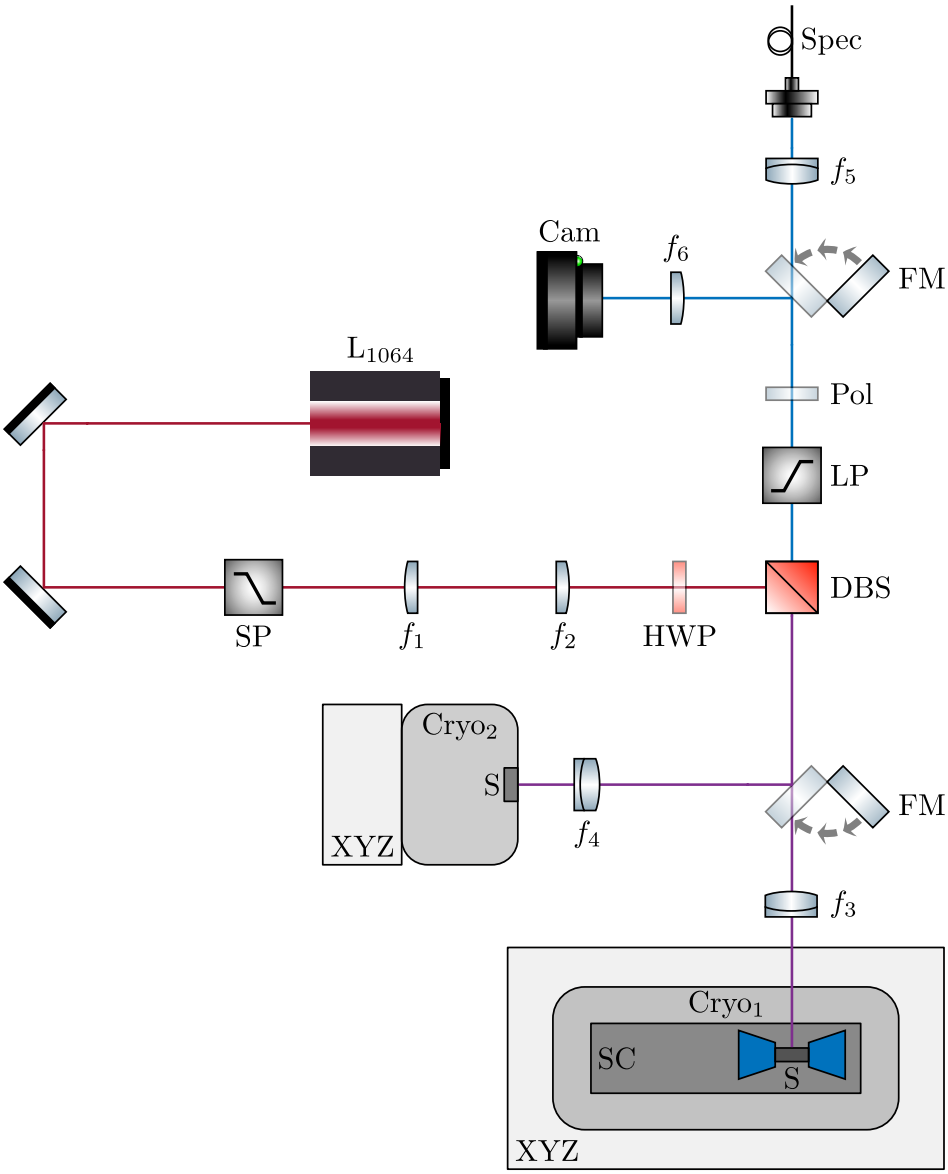

Figure 4-4 Schematic of the purpose-built 1064 nm photoluminescence spectrometer. L_{1064} = 1064 nm laser source, f_1 = 50 mm, f_2 = 100 mm, f_3 = 50 mm achromatic doublet, f_4 = 30 mm achromatic doublet, f_5 = 125 mm achromatic doublet, f_6 = 150 mm, FM = flip mirror, SP = 1175 nm shortpass filter (to clean laser output), LP = 1064 nm longpass filter, DBS = 1100 nm dichroic shortpass beam splitter, HWP = 1064 nm half-wave plate (optional), Pol = Linear polariser (optional), S = diamond sample, SC = stress cell with anvils (blue), $Cryo_1$ = Oxford Instruments Optistat, $Cryo_2$ = Linkham TMS600 stage, XYZ = manual XYZ stage, Cam = CCD camera, Spec = Fibre coupling to Andor spectrometer with an InGaAs detector.

Reference in Figure 4-5	Reference in thesis	[N] (ppm)	Other information
N-doped (very low)	—	< 0.005	—
N-doped (low)	B3 (Chapter 6)	3(0.5)	—
N-doped (high)	B1b (Chapter 6)	23(2)	—
HPHT annealed (2400 °C, low [N])	—	2(0.3)	2400 °C for 4 h
HPHT annealed (1600 °C, high [N])	—	23(2)	1600 °C for 24 h
Si-doped	—	< 0.001	[SiV] < 4 ppb
B-doped annealed (1500 °C)	C2 (Chapter 7)	< 0.001	1500 °C for 4 h, [B] ≥ 260 ppb
N/Si-doped	—	3(0.5)	[Si] ≥ 1 ppm

Table 4-2 Characterisation and treatment information of the CVD samples in Figure 4-5. Unless stated otherwise, all samples were in their as-grown state. The samples that are used elsewhere in this thesis have their relevant reference and chapter noted.

This system has predominately been used to study the 7354 cm^{-1}/1360 nm defect, but a characterisation survey on a variety of CVD diamonds has also been performed. The sample information is given in Table 4-2 and the PL spectra are presented in Figure 4-5. Other than the Raman line, the only notable feature in most samples is the 1360 nm defect, which is only observed in (low or high) nitrogen-doped samples that have not been annealed above 1600 °C. The boron-doped (annealed at 1500 °C for 4 h) and silicon-doped samples have effectively featureless spectra, along with the HPHT annealed (2400 °C, low [N]) sample that has been annealed at 2400 °C for 4 h.

The baseline of the Raman line in some of the PL spectra contains a selection of broad features. As the ratio of intensities between sp^3 and sp^2 bonded carbon, I_{sp^3}/I_{sp^2}, increases with shorter excitation wavelengths, these features are likely sp^2 bonded carbon that is more sensitive to long excitation in the IR range that is utilised here [11].

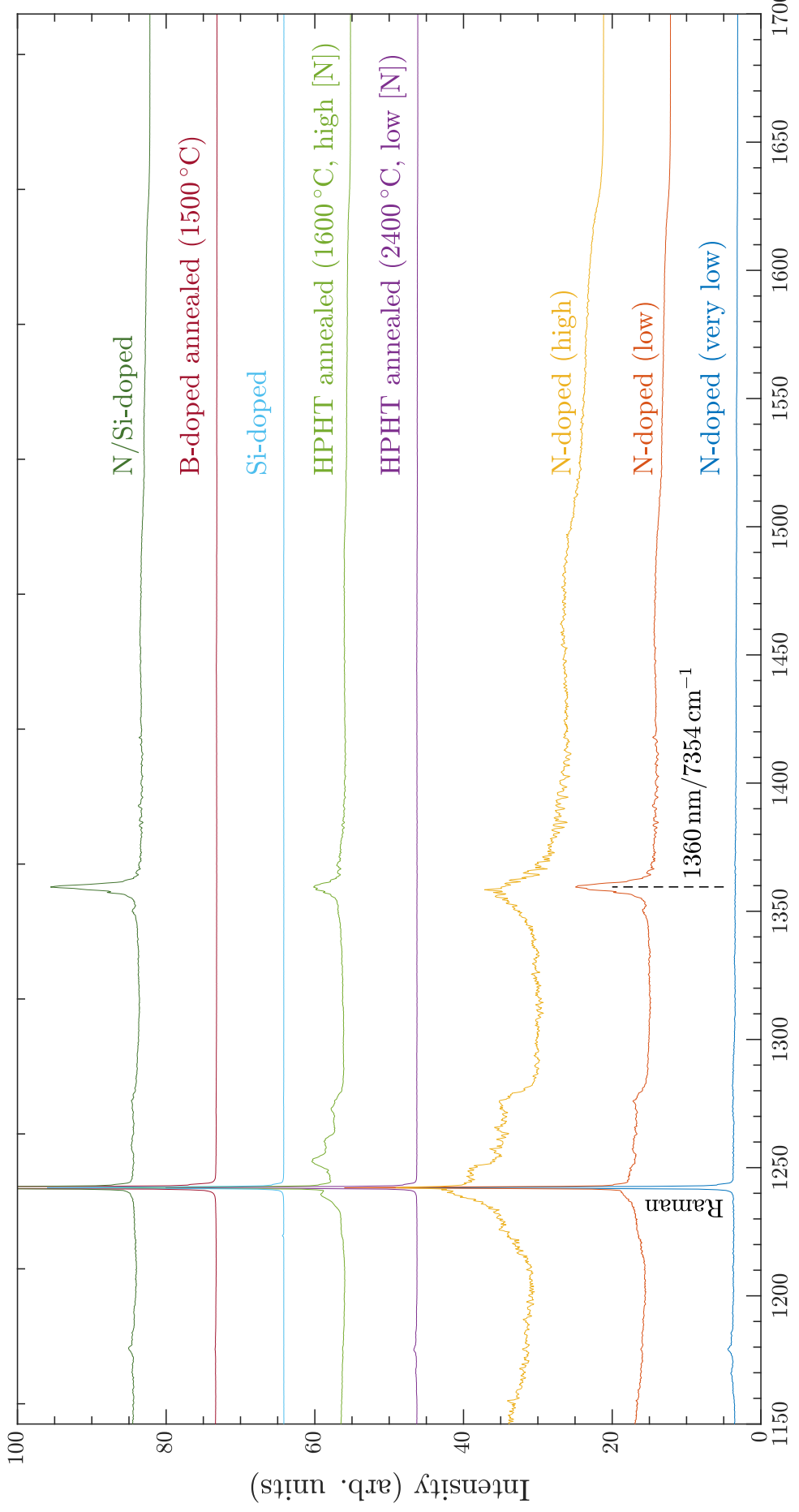

Figure 4-5 PL spectra with 1064 nm excitation on a variety of CVD diamond samples. Unless stated otherwise, all samples were in their as-grown state. Additional sample information may be found in Table 4-2. Spectra taken at 80 K.

4.3 Optical, birefringence, fluorescence and phosphorescence imaging

Optical and birefringence imaging is facilitated by a Leica DMI4000B optical microscope and Leica DFC310FX CCD camera through a 5× air objective (NA = 0.15), and a set of orthogonal polarisers (for the birefringence imaging only). The birefringence imaging will highlight areas of internal strain in the diamond that locally change the refractive index and therefore induce birefringence. As orthogonal polarisers are positioned after the source and before the detector, light may only be observed by the detector if the polarisation is changed by the diamond due to strain and birefringence. If the sample is larger than the field of view of the objective, then multiple (overlapping) images are recorded until the entire sample has been imaged. The post-process stitching of the images is performed by the readily available Image Composite Editor software from Microsoft.

Fluorescence and phosphorescence imaging is facilitated by a DiamondView™ instrument with a UV source emitting at $\lambda < 230\,\text{nm}$ (and near the band gap of diamond). With this source providing excitation, fluorescence is observed from surface and an image in recorded on the CCD camera; once the source is switched off, a time gated phosphorescence image is taken by the CCD. Amongst various controllable parameters, the exposure time and delay time may be adjusted to best suit the sample and defect(s) being studied.

4.4 Uniaxial stress

As discussed in §3.6, the splitting of optical transition lines by applied uniaxial stress may allow for the symmetry of the defect to be determining, along with the degeneracy of the associated states. The experimental considerations and apparatus of uniaxial stress will be discussed in this section.

Sample preparation is the first important consideration for an experiment with applied uniaxial stress. Specifically, the sample must not possess any cracks or inclusions that may become fracture sources, and at least two carefully polished

parallel sides with identical surface areas must be prepared. The area of the stressed faces are typically in the range of 1–2 mm^2; this compromises between having a small enough area to achieve the desired pressure, and having a large enough sample that is practical to prepare and measure with spectroscopy. The pressure P the sample experiences is inversely proportional to its area A, and may be related to the area of the piston pushing on it and the pressure the piston is experiencing from compressed (nitrogen) gas by

$$P_{\mathrm{sample}} = P_{\mathrm{piston}} \cdot \frac{A_{\mathrm{piston}}}{A_{\mathrm{sample}}} . \tag{4-3}$$

Thus, with the piston used having an area of 3805 mm^2, up to approximately 4000× amplification of pressure is possible with a sample of area 1–2 mm^2. As the piston pressure may reach up to 2 MPa, the pressure at the sample can easily reach several GPa.

The uniaxial stress probe utilised in experiments (Figure 4-6) was designed and constructed (out of grade 316 stainless steel and brass) by previous group members to be compatible with commercial cryostats [12–14]. The cylindrical chamber on the left contains a piston and a pre-tensioner which provides the necessary pressure on the piston to maintain the components in place before the experiment. The pre-tensioner does not form a vacuum seal so an equal pressure is always maintained throughout the chamber. The piston is in contact with a push rod, which itself is in contact with a sliding fit slug (ensuring a reproducible stress axis). The slug is in contact with an anvil, which holds the sample in place with the aid of another anvil at the end of the probe, where there is a removable end cap.

The anvil-diamond interfaces must be clean such that dirt does not lead to inhomogeneous stress or torque being applied to the sample. To further aid with ensuring homogeneous uniaxial stress, a thin aluminium foil gasket is inserted at each interface to account for small misalignments and imperfections between the sample and anvils, as the soft foil will readily fill any gaps under applied stress.

Once the stress probe is prepared, high press nitrogen gas may be supplied to the chamber via a fitting on the lid, which applies pressure on the piston and (by extension) each subsequent component and the sample. The gas pressure is regulated by a computer controlled Bronkhorst El-Press 602CV mass flow controller.

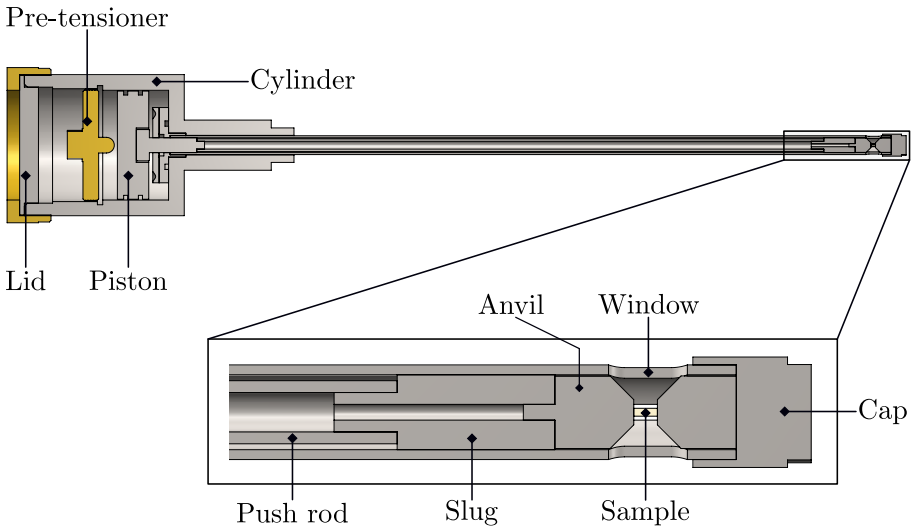

Figure 4-6 Cross section of the uniaxial stress probe and internal components. Figure adapted from [6].

For the low temperature experiments in this thesis, the stress probe was mounted inside an Oxford Instruments Optistat continous flow liquid helium cryostat. For low temperature absorption measurements with the Bruker IFS 66 FTIR spectrometer, a standard vacuum casing with a set of parallel windows was employed. The cryostat was mounted vertically onto an in-house three-axis stage positioned over the spectrometer [15]. The source light was polarised by a linear polariser before incident with the cryostat and sample.

For low temperature photoluminescence experiments with either the Renishaw inVia Raman microscope (with 785.0 nm excitation) or the purpose-built 1064 nm photoluminescence spectrometer, a modified vacuum casing that allows for the objective or lens to be closer to the sample was employed [14]. The cryostat was mounted horizontally on an aluminium plate and a heavy-duty XYZ stage, and the entire assembly was the mounted adjacent to the spectrometer on an aluminium frame [14]. Similar to the excitation and detection polarisation setup employed for the 1064 nm photoluminescence spectrometer (§4.2.4), the polarisation of the 785.0 nm excitation laser on the Renishaw microscope was selected by a suitable half-wave plate, and the detection polarisation was selected by a linear polariser.

4.5 Sample treatment

It is often useful to modify the defect concentrations in a sample via permanent (e.g. annealing) and/or temporary (e.g. charge transfer) treatments in order to aid with defect identification and characterisation.

4.5.1 Annealing

Annealing is the process of subjecting a diamond to heat in order to drive the migration, dissociation, and formation of defects. In this thesis, the technique is predominately employed for the annealing study (a series of repeat anneals on the same sample(s)) in Chapter 7, but no consideration is given to the specific chemical kinetics of the annealing process; the mechanics and formalism are therefore omitted, and a detailed review of the subject is provided by other authors [16, 17].

The annealing was facilitated by an Elite Thermal Systems horizontal tube furnace, with an upper temperature threshold of 1600 °C. Throughout any anneal, the interior of the alumina tube is continuously purged by a flow of nitrogen gas to ensure a non-oxidising atmosphere for the diamond samples. For annealing temperatures of and above 1000 °C, further protection against graphitisation is provided by burying the sample in a layer of sacrificial diamond grit.

4.5.2 Charge transfer

The charge transfer process has previously been discussed in §3.4, and comprises of reversible optical and thermal treatment processes. Optical treatment is facilitated by the DiamondView™ instrument providing 10 min of UV illumination to each face of the sample that will be subject to spectroscopy. Thermal treatment is facilitated by the same Elite Thermal Systems horizontal tube furnace employed for annealing, but the sample is only heated at a temperature of 550 °C for 15 min. It is important to keep the diamond in the dark after the thermal treatment in order to avoid any unwanted optical treatment from room lights or other sources of light.

References

1. G. R. Eaton *et al.*, *Quantitative EPR* (Springer, Vienna, 2010).
2. B. G. Breeze, PhD thesis, The University of Warwick, 2017.
3. J. A. Weil, J. R. Bolton, *Electron Paramagnetic Resonance* (John Wiley & Sons inc., Hoboken, NJ, 2nd, 2007).
4. A. M. Edmonds, PhD thesis, The University of Warwick, 2008.
5. B. L. Cann, PhD thesis, The University of Warwick, 2009.
6. M. W. Dale, PhD thesis, The University of Warwick, 2015.
7. W. Neumann, *Fundamentals of Dispersive Optical Spectroscopy Systems* (SPIE, Washington, 2014).
8. P. Griffiths, J. A. D. Haseth, *Fourier Transform Infrared Spectroscopy* (John Wiley & Sons, Hoboken, ed. 2, 2007).
9. C. Glover, PhD thesis, The University of Warwick, 2003.
10. L. Rogers, *Physics Procedia* **3**, 1557–1561 (2010).
11. S. Prawer, R. J. Nemanich, *Philosophical Transactions of the Royal Society of London. Series A: Mathematical, Physical and Engineering Sciences* **362**, 2537–2565 (2004).
12. R. Cruddace, PhD thesis, The University of Warwick, 2007.
13. S. Liggins, PhD thesis, The University of Warwick, 2010.
14. B. L. Green, PhD thesis, The University of Warwick, 2013.
15. H. E. Smith, PhD thesis, King's College London, 2004.
16. M. Lannoo, J. Bourgoin, *Point Defects in Semiconductors I* (Springer Berlin Heidelberg, Berlin, Heidelberg, 1981).
17. J. Bourgoin, M. Lannoo, *Point Defects in Semiconductors II* (Springer Berlin Heidelberg, Berlin, Heidelberg, 1983).

5

The neutral silicon vacancy centre in diamond

5.1 Introduction

Considerable efforts have been made to realise quantum bits for quantum applications in diamond via the utilisation of optical colour centres [1]. In particular, the negatively charged nitrogen vacancy (NV^-: 637 nm ZPL) centre [2, 3] and the negatively charged silicon vacancy (SiV^-: 737 nm ZPL) centre [4, 5] point defects have received significant attention due to their promising attributes as optically accessible single photon sources for quantum information processing [6].

In this regard, SiV^- possesses many advantages over NV^-. Greater than 70% of SiV^- luminescence is in the ZPL at room temperature (RT) [7] compared to the cryogenically-achieved ~3% for NV^- [8]. The RT ZPL is also extremely narrow at 0.7 nm [9], due to the inversion-symmetric $\mathscr{D}_{3d}$ symmetry of SiV^- resulting in a smaller electronic dipole moment that proves more insensitive to external electric fields [10, 11], in comparison to the non-inversion-symmetric $\mathscr{C}_{3v}$ symmetry of NV^- [12]. Single photon emission count rates of greater than 6 Mcps have been reported for SiV^- [13], whereas the highest NV^- count rate has been reported at only greater than 2 Mcps [14]—a corollary of the much shorter photoluminescence (PL) lifetime of 1–5 ns for SiV^- [7, 15] compared to 10–20 ns for NV^- [6, 16].

However, a major disadvantage for the SiV^- defect exists in its short spin-lattice relaxation time, which arises from strong spin-orbit coupling enabling phonon-assisted spin-state decoherence in the ground state [17, 18]. Reasonable spin lifetimes can only be achieved with prohibitive temperatures of $< 100\,\text{mK}$, where a $T_2 \approx 13\,\text{ms}$ has been reported [19]. In contrast, NV^- was observed to have the longest RT spin lifetimes observed in any solid state system (in a ^{13}C-enriched diamond) at $T_2 = 1.8\,\text{ms}$ [20]. More recently, this RT spin lifetime for the NV^- has been improved to $T_2 \approx 2.4\,\text{ms}$ by phosphorus-doping the host diamond crystal [21].

Whilst neither centre is currently ideal for quantum application, the challenges are slowly being addressed by careful engineering (e.g. strain tuning for SiV^- [22] and utilising optical cavities for NV^- [23]). Nevertheless, it would be preferable to identify a platform that does not inherently suffer from the respective shortcomings of SiV^- and NV^-: efforts are therefore also applied into researching other candidate colour centres that may be exploitable for quantum applications (including more obscure impurity-related centres such as nickel, chromium and xenon) [24]. One such promising candidate is the neutral silicon vacancy defect (SiV^0: 946 nm ZPL [25, 26]) as it potentially combines the ideal properties of SiV^- and NV^-. The defect emits greater than 90% of its emission into its ZPL whilst crucially demonstrating a long spin lifetime of $T_2 \approx 250\,\text{ms}$ at 15 K [27]. High-efficiency optical spin polarisation has also been demonstrated [25–27].

The SiV^0 centre has a promising combination of properties but realisation of quantum applications with this centre requires a more comprehensive understanding of its electric structure. The $\mathscr{D}_{3d}$ symmetry of the centre has been confirmed by electron paramagnetic (EPR) measurements [11] with the bond-centred silicon atom equidistant from two adjacent lattice-vacancy sites (the di-vacancy) as depicted in Figure 5-1a. The di-vacancy contains six nearest-neighbour carbon atoms that each possess a dangling bond.

A simple model for the molecular orbital (MO) configuration is depicted in Figure 5-1b. The MO configuration of the SiV^0 centre can be constructed as the interaction of orbitals from the constituent silicon atom and the di-vacancy [28].

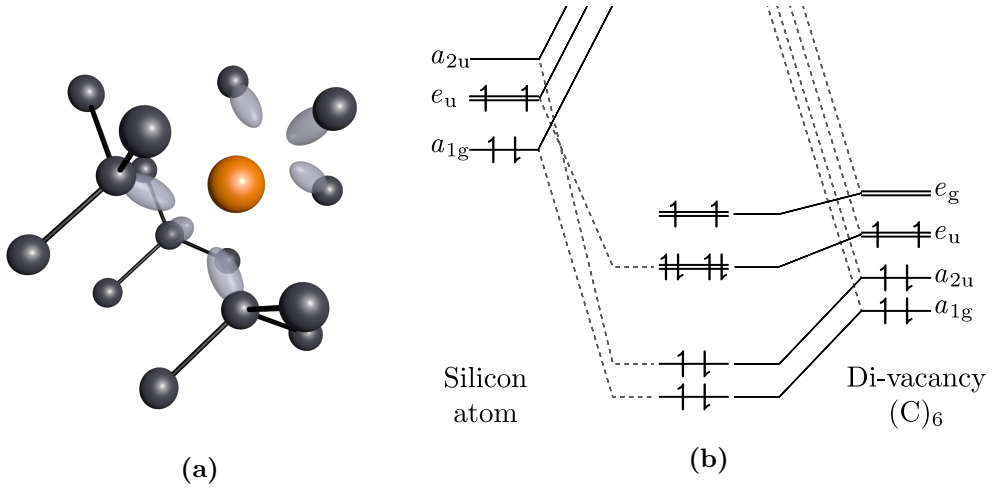

Figure 5-1 (a) Schematic of the silicon split-vacancy defect (SiV). The silicon atom (orange) is positioned equidistant from two adjacent lattice-vacancy sites; dangling bonds are highlighted by lobes (grey) on the six nearest-neighbour carbon atoms (black). (b) The irreducible representation of the molecular orbitals of the $\mathscr{D}_{3d}$ symmetric SiV^0 defect as a combination of the constituent silicon atom and di-vacancy/$(C)_6$ nearest-neighbour atoms. Arrows indicate electron orbital-position and (up/down) spin. Higher-energy molecular orbitals that form nearer the conduction band are not shown. Figure adapted from [28].

Whilst both the silicon atom and the di-vacancy donate electrons for the SiV^0 MOs (4 and 6 electrons, respectively), it is effectively only the MOs of the di-vacancy that are pulled down in energy to form the MOs of SiV^0 that are occupied by electrons, as the silicon atom is very weakly coupled to the lattice and its MOs are therefore pushed up in energy towards the conduction band [29].

In the electron picture, the ground state MO configuration of SiV^0 is $a_{1g}^2 a_{2u}^2 e_u^4 e_g^2$ and the equivalent hole picture (describing one-electron states that are *not* full) is e_g^2 as two additional electrons are required to completely fill the e_g orbital. As the two pictures are equivalent, the symmetry of resultant states that both pictures describe is identical: $^1A_{1g}$ + $^3A_{2g}$ + ^1E_g. This ground state description and the lowest-energy one-electron excited state of the SiV^0 centre, along with the symmetry of resultant states, is given in Table 5-1.

The lowest-energy excitation of one electron from e_u to e_g changes the electron picture to $a_{1g}^2 a_{2u}^2 e_u^3 e_g^3$ and equivalently the hole picture to $e_u^1 e_g^1$. The symmetry of resultant states for this configuration is $^1A_{1u}$ + $^1A_{2u}$ + ^1E_u + $^3A_{1u}$ + $^3A_{2u}$ + ^3E_u. Theoretically, the addition or removal of electrons at the e_g orbital should allow

One-electron excitation	Molecular orbital configuration		Symmetry of resultant states
	Electron picture	Hole picture	
Ground state	$a_{1g}^2 a_{2u}^2 e_u^4 e_g^2$	e_g^2	${}^1A_{1g} + {}^3A_{2g} + {}^1E_g$
Excited state	$a_{1g}^2 a_{2u}^2 e_u^3 e_g^3$	$e_u^1 e_g^1$	${}^1A_{1u} + {}^1A_{2u} + {}^1E_u +$ ${}^3A_{1u} + {}^3A_{2u} + {}^3E_u$

Table 5-1 Symmetry of resultant states of the molecular orbital configurations (given as equivalent electron and hole pictures) for the one-electron ground and excited states of SiV^0. Table adapted from [29].

ionisation of the SiV^0 centre up to values of charge 2±. The existence of SiV^- has been extensively discussed in this introduction and a tentative observation of the double-negatively charged silicon vacancy (SiV^{2-}) has been reported [30], however there have been no reports identifying either the positively or double-positively charged silicon vacancy centres.

Whilst the employment of group theory can predict all possible symmetry states of a given MO configuration, it is unable to predict the relative energy levels and ordering of the states; this challenge is taken up by theoretical and experimental investigation of the specific centre of interest. To that effect, the EPR measurements that confirmed the $\mathscr{D}_{3d}$ symmetry of the SiV^0 centre also indicated that the ground state of the centre is ${}^3A_{2g}$ [11]. Subsequent optical absorption measurements correlating the charge transfer between SiV^0 and SiV^- suggested the excited state of the SiV^0 946 nm ZPL is the ${}^3A_{1u}$ [31, 32]. Both the ground and excited state assignments were supported by density functional theory (DFT) calculations [28].

The predominant findings of this chapter, reported in Green *et al.* [33], show that the assignment of the SiV^0 excited state as ${}^3A_{1u}$ is incorrect and that the previous experimental and theoretical reports are therefore erroneous. The 946 nm ZPL excited state is instead assigned to ${}^3E_u$ and the presence of a ${}^3A_{2u}$ shelving state approximately 6.8 meV below the excited state is confirmed; the existence of this state has been previously indicated by variable temperature PL measurements [31]. Investigation and discussion of the SiV^0-related pseudo-local vibrational mode (pLVM) at 976 nm is also presented.

5.2 Experimental details

Sample A1 is the principal sample employed in this chapter and has orientations $\langle 1\,\bar{1}\,0\rangle$, $\langle 1\,1\,1\rangle$, $\langle 1\,1\,\bar{2}\rangle$; its details are presented in Table 5-2, along with the supplementary sample A2. Both samples were grown via MPCVD (by Element Six Ltd), though sample A1 was intentionally doped with approximately 90% ^{29}Si-enriched silicon, unlike sample A2 which was grown with natural abundance (approximately 92% ^{28}Si) silicon. The respective meta-stable state $^{28/29}\mathrm{SiV}^0$ concentrations were estimated by EPR: for sample A1 $[^{29}\mathrm{SiV}^0] \approx 70\,\mathrm{ppb}$ and for sample A2 $[^{28}\mathrm{SiV}^0] \approx 10\,\mathrm{ppb}$. Further characterisation on sample A1 with EPR and FTIR measured $[\mathrm{N_S^0}] < 15\,\mathrm{ppb}$ and $[\mathrm{B_S^0}] < 10\,\mathrm{ppb}$, respectively. Neither sample has been subject to post-growth treatment.

PL measurements with 785 nm (1.58 eV) excitation, in a backscatter configuration, were carried out at variable temperatures using unixaial stress (along $\langle 1\,1\,1\rangle$ and $\langle 1\,1\,0\rangle$) as a perturbation. For the stress direction $\boldsymbol{\sigma} \parallel \langle 1\,1\,1\rangle$, the parallel and perpendicular directions of the electric field vector are $[1\,\bar{1}\,\bar{1}]$ and $[1\,1\,0]$, respectively. Similarly for $\boldsymbol{\sigma} \parallel \langle 1\,1\,0\rangle$, the respective directions are $[1\,1\,0]$ and $[\bar{1}\,1\,\bar{2}]$. PL measurements were also performed on sample A2 to investigating the position of the 976 nm line in a natural abundance of silicon sample.

Sample	Silicon isotope	EPR $[\mathrm{SiV}^0]$ (ppb)	EPR $[\mathrm{N_S^0}]$ (ppb)	FTIR $[\mathrm{B_S^0}]$ (ppb)
A1	90% ^{29}Si	≈ 70 ($^{29}\mathrm{SiV}^0$)	< 15	< 10
A2	92% ^{28}Si	≈ 10 ($^{28}\mathrm{SiV}^0$)	–	–

Table 5-2 Samples employed for investigation of the SiV^0 centre. Characterisation measurements utilising EPR and FTIR have estimated the concentration of the appropriate isotope of $^{28/29}\mathrm{SiV}^0$, and for sample A1 only, the concentrations of $\mathrm{N_S^0}$ and $\mathrm{B_S^0}$.

5.3 Results

Any data presented that has the stress direction $\boldsymbol{\sigma} \parallel \langle 1\,1\,0 \rangle$ was acquired by B. L. Green whereas any data that has the stress direction $\boldsymbol{\sigma} \parallel \langle 1\,1\,1 \rangle$ was acquired by the author of this thesis.

5.3.1 The 946 nm SiV^0 ZPL

The validity of any state-to-state assignment of a transition can be interrogated by considering the maximum number of transitions that may be observed under uniaxial stress. For the proposed $A \leftrightarrow A$ assignment of the 946 nm SiV^0 ZPL in published work [28, 31], only one transition is possible per unique orientation between orbitally non-degenerate states. The stress directions of $\langle 1\,1\,1 \rangle$ and $\langle 1\,1\,0 \rangle$ lift the orientational degeneracy of a trigonal centre into two subensembles based on the angle between the principal axis to the stress axis—$\langle 1\,1\,1 \rangle$: 0°, 109° and $\langle 1\,1\,0 \rangle$: 35°, 90° (see §5.3.2 for more detail). Consequently, the maximum number of transitions possible for an $A \leftrightarrow A$ transition is two per stress axis.

Similarly, for the $E \leftrightarrow A$ case (orbital doublet-to-singlet) there are two transitions possible per unique orientation (owing to the degeneracy of the E state), which doubles to a maximum of four total transitions when considering the two subensembles per stress axis. The degeneracy of the E state is not lifted in the case of $\langle 1\,1\,1 \rangle$ stress on the orientation of the trigonal centre that has its principal axis parallel to the stress axis (i.e. the $[1\,1\,1]$ orientation of the axis). The symmetry of the trigonal centre is not changed so splitting of transitions will not occur (though they do still shift in energy). This reduces the maximum number of possible transitions to three for $\langle 1\,1\,1 \rangle$ stress applied to a trigonal centre.

Figure 5-2 presents the PL spectra of the stress-split 946 nm ZPL under applied stress along $\langle 1\,1\,1 \rangle$ and $\langle 1\,1\,0 \rangle$ at the respective pressures of 2.0 GPa and 2.1 GPa. The number of transitions for both stress axes are consistent with an $E \leftrightarrow A$ transition, and therefore the observations do not support the $A \leftrightarrow A$ proposal for the 946 nm ZPL transition. The stress-induced transitions that arise from the $E \leftrightarrow A$ model are labelled Γ_1^- and Γ_2^-, which are derived from the E state that

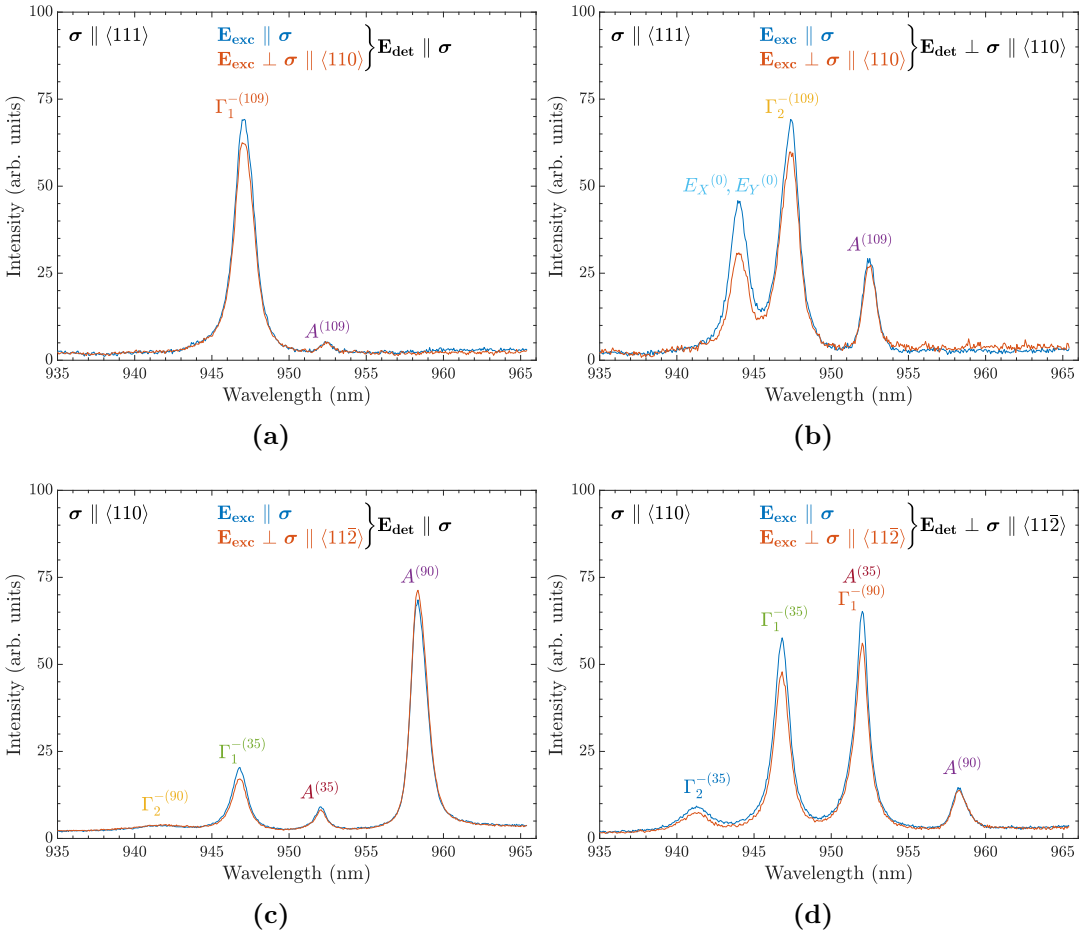

Figure 5-2 Polarisation dependence of SiV^0 at an applied stress ($\boldsymbol{\sigma}$) of (a) and (b) 2.0 GPa along ⟨1 1 1⟩, and (c) and (d) 2.1 GPa along ⟨1 1 0⟩. Spectra in blue (orange) represent measurements with the excitation electric field vector ($\mathbf{E_{exc}}$) polarised parallel (perpendicular) to the stress axis. The detection electric field vector ($\mathbf{E_{det}}$) is polarised parallel (in (a) and (c)) and perpendicular (in (b) and (d)) to the stress axis. Transitions are labelled according to the excited state they refer to (A and Γ_1^-, Γ_2^- for the E state) and the angle (in degrees) between the principal axis of the subensemble to the stress axis, as explained in §5.3.2. Data taken at 80 K.

has its degeneracy lifted by stress; the transitions are further subcatagorised by the relative angle (in degrees) of each principal axis of the defect to the stress axis (as previously discussed). As the degeneracy of the E state is not lifted by stress along ⟨1 1 1⟩ for the [1 1 1] orientation of the principal axis, the transition to this state is referred to as E_X, E_Y. Hence, Figures 5-2a and 5-2b, with stress axis $\boldsymbol{\sigma} \parallel \langle 1\,1\,1 \rangle$, have three transitions that originate from the 946 nm ZPL: $\Gamma_1^{-(109)}$, $\Gamma_2^{-(109)}$, and $E_X^{(0)}, E_Y^{(0)}$; and Figures 5-2c and 5-2d, with stress axis $\boldsymbol{\sigma} \parallel \langle 1\,1\,1 \rangle$, have four transitions that originate from the 946 nm ZPL: $\Gamma_1^{-(35)}$, $\Gamma_1^{-(90)}$, $\Gamma_2^{-(35)}$

and $\Gamma_2^{-(90)}$.

In addition to the E state transitions (Γ_1^-, Γ_2^-), both stress directions induce transitions that originate at approximately 951 nm at low applied stress, which subsequently increase in intensity with an increase of applied stress. A maximum of two transition are observed, which is consistent with the $A \leftrightarrow A$ model and they are therefore labelled as A transitions. Differentiating by angle again, as for the $E \leftrightarrow A$ transitions, one transition is observed with $\langle 1\,1\,1 \rangle$ stress ($A^{(109)}$) and two transition are observed with $\langle 1\,1\,0 \rangle$ stress ($A^{(35)}$, $A^{(90)}$).

Careful examination of Figure 5-2 reveals that a significant intensity of each A transition is only observed if the same subensemble of the Γ_2^- is also observed—this indicates that the A transition has the same symmetry as the Γ_2^- transition. Furthermore, measurements performed at static stress but variable temperatures (presented in §5.3.3) also showed these A transitions to increase in intensity, at the expense of the $E \leftrightarrow A$ transitions, with decreasing temperature; it is therefore inferred that these transitions originate from an A state near and coupled to the E state of the $E \leftrightarrow A$ transition.

Each subfigure of Figure 5-2 contains two spectra that represent either parallel (blue) or perpendicular (orange) excitation electric field vector ($\mathbf{E_{exc}}$) polarisation relative to the stress axis. In all cases, the observed spectra are effectively invariant to excitation polarisation. This invariance is believed to be a result of the 785 nm excitation laser being of higher energy (1.58 eV) than the ionisation energy of the SiV^0 defect (1.50 eV, from the valence band maximum), thereby resulting in a loss of the excitation polarisation information [31]. As there is only one degree of freedom for polarisation, the intensities will effectively behave as absorption intensities—a more detailed discussion is provided for the reader in §5.4.1.1. Consequently, the majority of future figures will only present spectra with $\mathbf{E_{exc}} \parallel \boldsymbol{\sigma}$ as the inclusion of both excitation polarisations does not provide any new information.

Whilst the number of transitions observed in Figure 5-2 is consistent with an $E \leftrightarrow A$ model that is coupled to an A state (for both stress directions), it does not solely provide conclusive proof. A fit to the uniaxial stress data, using a suitable

model, must be successfully applied before any conclusions are drawn.

5.3.2 The coupled $E \leftrightarrow A$ uniaxial stress model

The following model was derived by a co-author of the paper resulting from the work presented in this chapter: M. W. Doherty. The model builds on the work of the same author that focused on $E \leftrightarrow A_2$ (and $E \leftrightarrow A_1$) transitions at a non-inversion-symmetric $\mathscr{C}_{3v}$ trigonal centre, as presented by Rogers *et al.* [34]. Whilst the derivation of this model will be discussed, for a full derivation the reader is directed towards the Supplemental Material of the Green *et al.* paper [35].

The results in §5.3.1 suggest the SiV^0 centre ZPL consists of an $E \leftrightarrow A$ transition that is coupled to an A state. Given results from EPR that assign the ground state level of SiV^0 as $^3A_{2g}$ [11], the model may be updated to an $E \leftrightarrow A_2$ PL transition that is coupled to an A_2 state. The model was further updated upon consideration of all the results in this chapter (discussed in §5.4.1), so for completeness only the final version of the model will be presented here, along with labelling of states that accurately reflects their symmetry. Therefore, the proposed model for the SiV^0 centre with $\mathscr{D}_{3d}$ symmetry (i.e. an inversion-symmetric trigonal centre) is a $^3E_u \leftrightarrow {}^3A_{2g}$ PL transition coupled to another nearby and lower energy $^3A_{2u}$ level. All four possible orientations of the principal axis of any trigonal centre (noted as z) are given in Table 5-3, along with the orientations of the other axes of the centre (x, y). The three conventional stress directions of $\langle 0\,0\,1\rangle$, $\langle 1\,1\,1\rangle$ and $\langle 1\,1\,0\rangle$ are also depicted relative to the principal axes.

Stress along any of the three conventional directions on an inversion-symmetric $\mathscr{D}_{3d}$ centre is always parallel or perpendicular to a reflection place such that (in most cases) the symmetry is lowered to $\mathscr{C}_{2h}$ (also inversion-symmetric); the symmetry is not lowered if the stress axis is parallel to the principal axis. In the lower symmetry $\mathscr{C}_{2h}$ point group, the degeneracy of an E_u level is split into the irreducible representations of A_{1u} and A_{2u}. However, to avoid confusion with the coupled A_{2u} state that is not derived from the E_u level, they will be referred to by the equivalent Bethe notation [36] states of Γ_1^- and Γ_2^-, respectively.

Initially, an uncoupled $E_u \leftrightarrow A_{2g}$ transition at a centre with $\mathscr{D}_{3d}$ symmetry is

considered: the stress-induced shifts, splittings and absorption intensities for such a transition are presented in Table 5-4 for the three stress directions; the intensities in luminescence are given in Table 5-5.

For an uncoupled $E_u \leftrightarrow A_{2g}$ transition at a centre with $\mathscr{D}_{3d}$ symmetry the uncoupled stress Hamiltonian may be given as

$$\mathscr{H}_{\text{uncoupled}} = \begin{pmatrix} 0 & 0 & 0 \\ 0 & \alpha+\beta & \gamma \\ 0 & \gamma & \alpha-\beta \end{pmatrix}, \tag{5-1}$$

where, α, β, and γ describe the response to stress of the E_u state. The stress Hamiltonian describing the coupling interactions may then be given as

$$\mathscr{H}_{\text{coupled}} = \begin{pmatrix} W+\alpha' & \gamma^c & \beta^c \\ \gamma^c & 0 & 0 \\ \beta^c & 0 & 0 \end{pmatrix}, \tag{5-2}$$

where, W is the zero-stress energy separation of the coupled E_u and A_{2u} states, α' describes the response to stress of the A_{2u} state, and β^c and γ^c describe the coupling between the two states. The total Hamiltonian, $\mathscr{H} = \mathscr{H}_{\text{uncoupled}} + \mathscr{H}_{\text{coupled}}$, is therefore

$$\mathscr{H} = \begin{pmatrix} W+\alpha' & \gamma^c & \beta^c \\ \gamma^c & \alpha+\beta & \gamma \\ \beta^c & \gamma & \alpha-\beta \end{pmatrix}. \tag{5-3}$$

The functions $\alpha^{(\prime)}$, $\beta^{(c)}$ and $\gamma^{(c)}$ respond linearly to stress and comprise of state-dependent piezospectroscopic parameters, which are the energy shift parameters in Table 5-4.

As derived in the Supplemental Material [35], the eigenenergies ($\mathscr{E}$) of total Hamiltonian can be parameterised in the following form:

$$\begin{aligned} \mathscr{E}(A) &= \frac{1}{2}(\alpha+\Delta+W+\alpha') - \frac{1}{2}\left[(\alpha+\Delta-W-\alpha')^2+4\Omega^2\right]^{1/2} \\ \mathscr{E}(\Gamma_1^-) &= \alpha-\Delta \\ \mathscr{E}(\Gamma_2^-) &= \frac{1}{2}(\alpha+\Delta+W+\alpha') + \frac{1}{2}\left[(\alpha+\Delta-W-\alpha')^2+4\Omega^2\right]^{1/2} \end{aligned} \tag{5-4}$$

where, Δ is the splitting of the degenerate E_u level under stress without consideration of coupling to the A_{2u} level and Ω is the coupling between the E_u and

Index	Centre axes		
	x	y	z
①	$[1\,\bar{1}\,0]$	$[1\,1\,\bar{2}]$	$[1\,1\,1]$
②	$[\bar{1}\,1\,0]$	$[\bar{1}\,\bar{1}\,\bar{2}]$	$[\bar{1}\,\bar{1}\,1]$
③	$[1\,1\,0]$	$[1\,\bar{1}\,2]$	$[1\,\bar{1}\,\bar{1}]$
④	$[\bar{1}\,\bar{1}\,0]$	$[\bar{1}\,1\,2]$	$[\bar{1}\,1\,\bar{1}]$

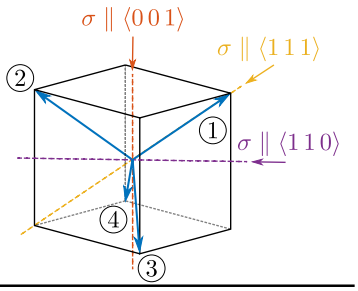

Table 5-3 Orientations of a trigonal centre, with a $\langle 1\,1\,1\rangle$ principal axis, in a $\mathscr{T}_\mathrm{d}$ lattice. Stress axis direction are also depicted relative to the principal axes.

Stress	Orientation	Symmetry	Energy shift parameters	Intensity in absorption	
				$\mathbf{E} \parallel \boldsymbol{\sigma}$	$\mathbf{E} \perp \boldsymbol{\sigma}$
$\langle 0\,0\,1\rangle$	54° ①, ②	E_X (Γ_2^-)	$A_1 + 2B$	0	2
	54° ③, ④	E_Y (Γ_1^-)	$A_1 - 2B$	$^8/_3$	$^2/_3$
$\langle 1\,1\,1\rangle$	0° ①	E_X, E_Y	$A_1 + 2A_2$	0	1
	109° ②, ③, ④	E_X (Γ_2^-)	$A_1 - \frac{2}{3}A_2 + \frac{4}{3}C$	0	$^3/_2$
		E_Y (Γ_1^-)	$A_1 - \frac{2}{3}A_2 - \frac{4}{3}C$	$^8/_3$	$^1/_6$
				$\mathbf{E} \parallel \langle 1\,1\,1\rangle$	$\mathbf{E} \parallel \langle 1\,1\,\bar{2}\rangle$
$\langle 1\,1\,0\rangle$	35° ①, ②	E_X (Γ_2^-)	$A_1 + A_2 - B + C$	0	2	$^2/_3$
		E_Y (Γ_1^-)	$A_1 + A_2 + B - C$	$^2/_3$	0	$^8/_9$
	90° ③, ④	E_X (Γ_2^-)	$A_1 - A_2 - B - C$	2	0	0
		E_Y (Γ_1^-)	$A_1 - A_2 + B + C$	0	$^2/_3$	$^{10}/_9$

Table 5-4 Stress-induced shifts, splittings and intensities in absorption for an $E_\mathrm{u} \leftrightarrow A_{2g}$ transition at a $\mathscr{D}_\mathrm{3d}$ symmetric centre. The orientation of each $\langle 1\,1\,1\rangle$ principal axis relative to the stress axis is given, along with the symmetry of the transition to that orientation, the energy shift parameters (stress-induced shifts are calculated by multiplying by the stress value) and intensity in absorption when detected parallel or perpendicular ($\parallel$ or $\perp$) to the stress axis. Intensity values have been calculated for the samples orientations relevant to this chapter. Table adapted from [34].

Stress	Orientation	Symmetry	Intensity in luminescence							
			$\mathbf{E_{exc}} \parallel \boldsymbol{\sigma}$				$\mathbf{E_{exc}} \perp \boldsymbol{\sigma}$			
			$\mathbf{E_{det}} \parallel \boldsymbol{\sigma}$	$\mathbf{E_{det}} \perp \boldsymbol{\sigma}$			$\mathbf{E_{det}} \parallel \boldsymbol{\sigma}$	$\mathbf{E_{det}} \perp \boldsymbol{\sigma}$		
$\langle 0\,0\,1\rangle$	54° { ①, ②, ③, ④ }	E_X (Γ_2^-)	0	2			0	$^{12}/_{5}$		
		E_Y (Γ_1^-)	$^{8}/_{3}$	$^{2}/_{3}$			$^{8}/_{3}$	$^{4}/_{15}$		
$\langle 1\,1\,1\rangle$	0° { ① }	E_X, E_Y	0	0			0	$^{6}/_{5}$		
	109° { ②, ③, ④ }	E_X (Γ_2^-)	0	$^{7}/_{5}$			0	$^{7}/_{5}$		
		E_Y (Γ_1^-)	$^{8}/_{3}$	$^{4}/_{15}$			$^{8}/_{3}$	$^{1}/_{15}$		
				$\mathbf{E_{det}} \parallel \langle 1\,1\,1\rangle$	$\mathbf{E_{det}} \parallel \langle 1\,1\,\bar{2}\rangle$		$\mathbf{E_{exc}} \parallel \langle 1\,1\,1\rangle$	$\mathbf{E_{exc}} \parallel \langle 1\,1\,\bar{2}\rangle$	$\mathbf{E_{det}} \parallel \langle 1\,1\,1\rangle$	$\mathbf{E_{det}} \parallel \langle 1\,1\,\bar{2}\rangle$
$\langle 1\,1\,0\rangle$	35° { ①, ② }	E_X (Γ_2^-)	0	$^{4}/_{5}$	$^{4}/_{11}$		0	0	$^{4}/_{3}$	$^{28}/_{45}$
		E_Y (Γ_1^-)	$^{4}/_{15}$	$^{4}/_{15}$	$^{16}/_{33}$		$^{16}/_{15}$	$^{28}/_{33}$	$^{4}/_{9}$	$^{112}/_{135}$
	90° { ③, ④ }	E_X (Γ_2^-)	$^{7}/_{5}$	0	0		$^{8}/_{5}$	$^{20}/_{11}$	0	0
		E_Y (Γ_1^-)	0	$^{8}/_{5}$	$^{20}/_{11}$		0	0	$^{8}/_{9}$	$^{164}/_{135}$

Table 5-5 Stress-induced shifts, splittings and intensities in luminescence for an $E_u \leftrightarrow A_{2g}$ transition at a $\mathscr{D}_{3d}$ symmetric centre. The orientation of each $\langle 1\,1\,1\rangle$ principal axis relative to the stress axis is given, along with the symmetry of the transition to that orientation, the energy shift parameters (stress-induced shifts are calculated by multiplying by the stress value) and intensity in absorption when detected parallel or perpendicular ($\parallel$ or $\perp$) to the stress axis. Intensity values have been calculated for the samples orientations relevant to this chapter. Table adapted from [34].

A_{2u} state. Whilst the A_{2u} state is also a Γ_2^- symmetry species, it labelled A for simplicity.

As presented in Figure 5-2, the excitation polarisation information was lost, so with only detection polarisation information the intensities will effectively behave as absorption intensities. Therefore, specifically for the PL data set presented in this chapter, the absorption intensity values in Table 5-4 are used with the model. The relative intensities (I_p), for each symmetry species, are then only given as a function of detection polarisation p:

$$\begin{aligned} I_p(A) &= Z^{-1} e^{-\mathscr{E}(A)/k_B T} I_{2p} \sin^2 \frac{\phi}{2} \\ I_p\left(\Gamma_1^-\right) &= Z^{-1} e^{-\mathscr{E}\left(\Gamma_1^-\right)/k_B T} I_{1p} \\ I_p\left(\Gamma_2^-\right) &= Z^{-1} e^{-\mathscr{E}\left(\Gamma_2^-\right)/k_B T} I_{2p} \cos^2 \frac{\phi}{2} \end{aligned} \tag{5-5}$$

where, I_{1p} and I_{2p} are the intensities of the Γ_1^- and Γ_2^- symmetries under p-polarisation, $\phi = \arctan \frac{2\Omega}{\alpha+\Delta-W-\alpha'}$ is the angle describing the coupling between the A_{2u} state and the $E_u(\Gamma_2^-)$ substate, and Z is the partition function that normalises for the total intensity of all symmetry species at any given temperature:

$$Z = e^{-\mathscr{E}(A)/k_B T} + e^{-\mathscr{E}\left(\Gamma_1^-\right)/k_B T} + e^{-\mathscr{E}\left(\Gamma_2^-\right)/k_B T}. \tag{5-6}$$

The piezospectroscopic parameterisation of the Hamiltonian parameters relating to equations (5-4) and (5-5) are presented in Table 5-6, for the subensembles of the $\langle 1\,1\,1\rangle$ and $\langle 1\,1\,0\rangle$ stress directions. Parameters are consolidated such that $\beta \equiv \Delta$, $\beta^c \equiv \Omega$, and the values of γ and γ^c equate to zero. The energies and intensities of the proposed model of the SiV^0 centre can now be fit against PL

Subensemble		α	$\beta \equiv \Delta$	γ	α'	$\beta^c \equiv \Omega$	γ^c
$\langle 1\,1\,1\rangle$	0°	$(A_1 + 2A_2)\sigma$	0	0	$(A_1' + 2A_2')\sigma$	0	0
	109°	$(A_1 - \frac{2}{3}A_2)\sigma$	$\frac{4}{3}C\sigma$	0	$(A_1' - \frac{2}{3}A_2')\sigma$	$\frac{4}{3}C^c\sigma$	0
$\langle 1\,1\,0\rangle$	35°	$(A_1 + A_2)\sigma$	$(-B + C)\sigma$	0	$(A_1' + A_2')\sigma$	$(-B^c + C^c)\sigma$	0
	90°	$(A_1 - A_2)\sigma$	$(-B - C)\sigma$	0	$(A_1' - A_2')\sigma$	$(-B^c - C^c)\sigma$	0

Table 5-6 Hamiltonian parameters for the uniaxial stress model of the SiV^0 centre. Substitution into equations (5-4) and (5-5) will provide fully parameterised energy and intensity equations for the model that can be used to fit data.

measurements under applied uniaxial stress to ascertain if the model accurately describes the behaviour of the SiV^0 centre and in turn calculate the values of the piezospectroscopic parameters.

5.3.3 Fitting the 946 nm SiV^0 ZPL

The model must be capable of predicting the energy and intensity of any transition for a given stress direction and pressure, excitation and detection polarisation, and temperature. The first experiment conducted involved uniaxial stress at a range of pressures and constant temperature (80 K). The energies of the stress-split transitions of the SiV^0 centre were extracted from the PL spectra for each stress direction and pressure; these data points are presented in Figure 5-3. Also presented in the same figure is the result of a least squares fit (lines) of the proposed ${}^3E_u \leftrightarrow {}^3A_{2g}$ model (presented in §5.3.2) to the data. In each subfigure, the data from both detection polarisations are combined, however a distinction in the polarisation is made with the model lines: dashed (dotted) lines indicate observation when parallel (perpendicular) to the stress direction and solid lines indicate observation with both polarisations.

In general the model proves a reliable fit of the experimental data and the piezospectroscopic parameter values derived from the fit to the data are given in Table 5-7. In Figure 5-3a, the model predicts the energy of the $A^{(0)}$ transition under $\langle 1\,1\,1\rangle$ stress but also predicts it has zero intensity; the lack of experimental observation of this transition is therefore unsurprising. The model miscalculates the relative ordering of the $\Gamma_2^{-(35)}$ and $\Gamma_2^{-(90)}$ transitions when under $\langle 1\,1\,0\rangle$ stress at high pressures in Figure 5-3b. Also for $\langle 1\,1\,0\rangle$ stress, the model overestimates the energy of the $\Gamma_1^{-(90)}$ transition.

A_1	A_2	B	C	A_1'	A_2'	B^c	C^c	W
-0.077	0.93	-1.0	-0.24	0.97	1.1	-4.7	-1.1	-6.8

Table 5-7 Experimentally determined piezospectroscopic parameters from fitting the SiV^0 centre as a ${}^3E_u \leftrightarrow {}^3A_{2g}$ transition coupled to an ${}^3A_{2u}$ level, at an inversion-symmetric trigonal center ($\mathscr{D}_{3d}$). Parameters are given in meV GPa^{-1}, except for W, which is given in meV.

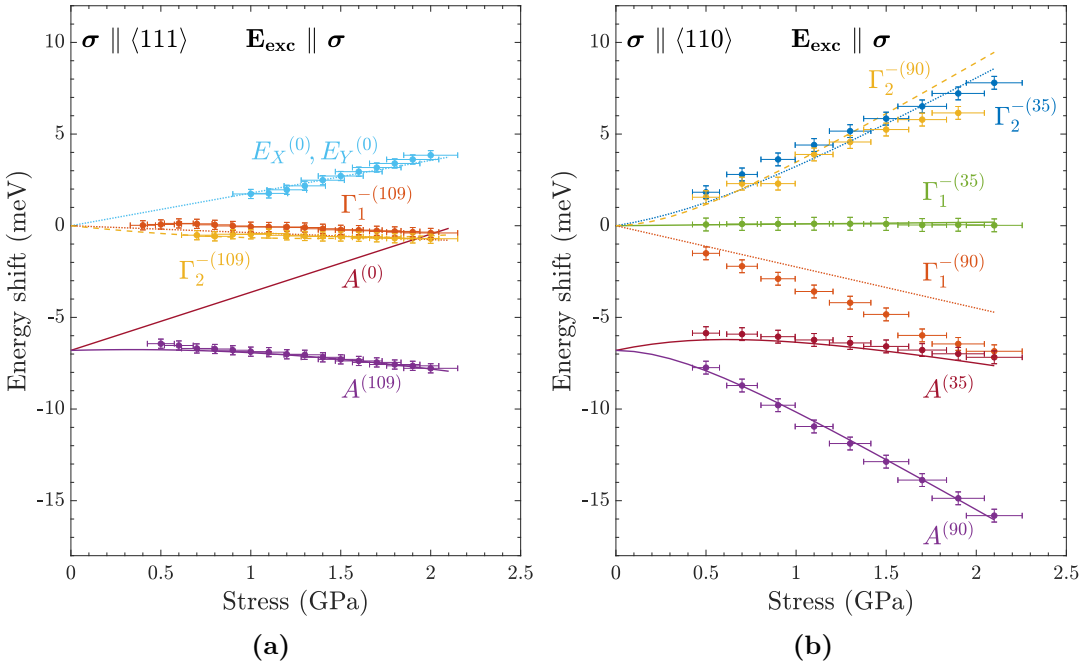

Figure 5-3 Comparison between experimental data (points) and analytical model (lines). The energy of all transitions are given as a function of applied stress ($\boldsymbol{\sigma}$) along (a) $\langle 1\,1\,1\rangle$ and (b) $\langle 1\,1\,0\rangle$. The excitation electric field vector ($\mathbf{E_{exc}}$) is polarised parallel to the stress axis. Dashed (dotted) lines indicate a transition only visible when parallel (perpendicular) to the stress direction. Solid lines indicates a transition visible in both polarisations. Transitions labelled as explained in Figure 5-2 and §5.3.2. For $\boldsymbol{\sigma} \parallel \langle 1\,1\,1\rangle$, $\mathbf{E_{det}} \perp \boldsymbol{\sigma} \parallel \langle 1\,1\,0\rangle$, and for $\boldsymbol{\sigma} \parallel \langle 1\,1\,0\rangle$, $\mathbf{E_{det}} \perp \boldsymbol{\sigma} \parallel \langle 1\,1\,\bar{2}\rangle$. Data taken at 80 K.

Further interrogation of the model and the parameters generated with its fit can be performed by testing its ability to handle the stress splitting under constant stress but variable temperature. Figure 5-4 presents the intensity of each transition (normalised to the most intense transition: $A^{(90)}$ when $\mathbf{E_{det}} \parallel \boldsymbol{\sigma}$) at an applied $\langle 1\,1\,0\rangle$ stress of 1.3 GPa, in the temperature range of approximately 30–80 K. The model intensity lines were calculated using parameters in Table 5-7.

Similarly for this experiment, the model predicts the intensity of the majority of transitions to a good degree of accuracy. In Figure 5-4a where $\mathbf{E_{det}} \parallel \boldsymbol{\sigma}$, the model does not predict any intensity for the $A^{(35)}$ transition that is observed, but does accurately predict the intensities of the other three transitions in that polarisation. For Figure 5-4b where $\mathbf{E_{det}} \perp \boldsymbol{\sigma} \parallel \langle 1\,1\,\bar{2}\rangle$, the observed $A^{(90)}$ transition is also predicted to not have any intensity by the model whilst transitions $A^{(35)}$ and $\Gamma_1^{-(90)}$ have their intensities overestimated by the model. The two other transitions have

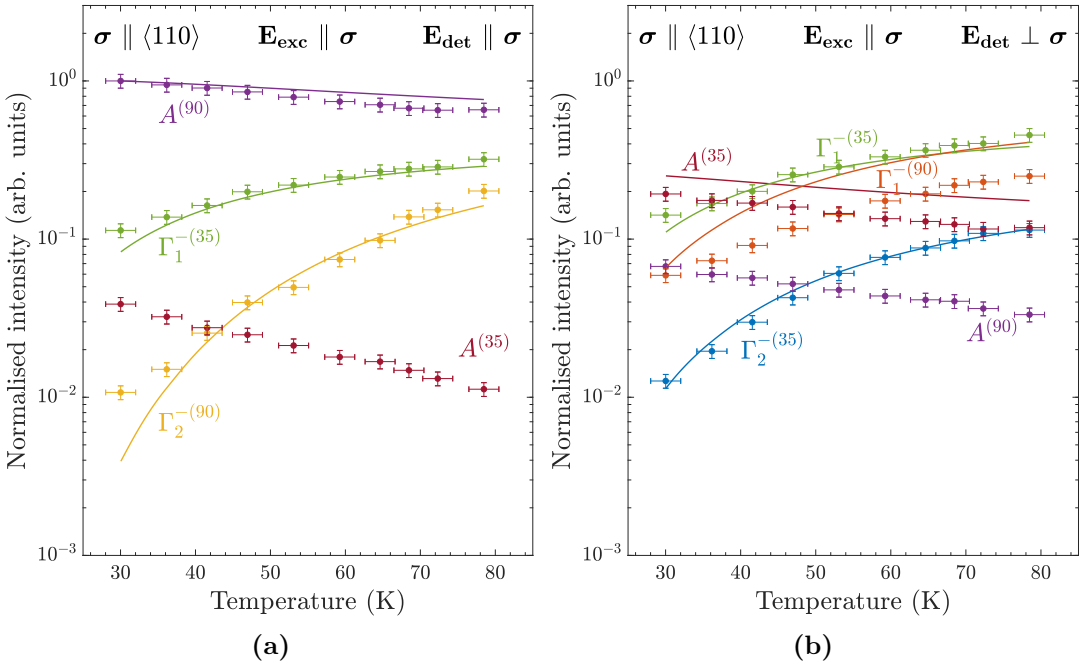

Figure 5-4 Temperature-dependent experimental (points) and theoretical (lines) transition intensities at an applied stress ($\boldsymbol{\sigma}$) of 1.3 GPa along ⟨1 1 0⟩. The excitation electric field vector ($\mathbf{E_{exc}}$) is polarised parallel to the stress axis. The detection electric field vector ($\mathbf{E_{det}}$) is polarised (a) parallel and (b) perpendicular to the stress axis. All intensities have been normalised to the most intense experimental transition ($A^{(90)}$ when $\mathbf{E_{det}} \parallel \boldsymbol{\sigma}$). Transitions labelled as explained in Figure 5-2 and §5.3.2. $\mathbf{E_{det}} \perp \boldsymbol{\sigma}$ corresponds to the direction $\langle 1\,1\,\bar{2} \rangle$.

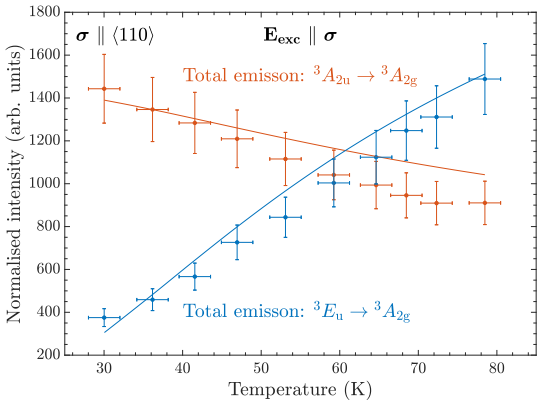

Figure 5-5 Total intensity of transitions observed from the ^3E_u and $^3A_{2u}$ states at an applied stress of 1.3 GPa along ⟨1 1 0⟩. The experimental data (points) and model lines are the summed values of the normalised data in Figure 5-4. The states are labelled according to discussion of the results in §5.4.1.

their intensities accurately predicted. Except for the case of the missing transition intensity predictions, the model correctly predicts the ordering and behaviour of all transitions such that the coupled ${}^3E_u \leftrightarrow {}^3A_{2g}$ model can be considered a reasonable description of the SiV^0 excited state.

The W parameter in Table 5-7, which describes the energy separation between the ${}^3E_u$ state and the coupled ${}^3A_{2u}$ state, suggests that the ${}^3A_{2u}$ state is below the ${}^3E_u$ state as the value is negative (−6.8 meV). This is supported by the observation that the transitions originating from the ${}^3E_u$ state decrease in intensity as the temperature is reduced in Figure 5-4, whilst the transitions related to the ${}^3A_{2u}$ state increase in energy as the temperature is reduced. This relationship is presented more clearly in Figure 5-5 where the data and model lines in Figure 5-4 have been summed to show the total intensity emissions from both states, as a function of temperature.

5.3.4 The 976 nm pseudo-LVM

A small SiV^0-related feature at 976 nm has been observed in the PL spectrum of SiV^0 [25, 31] but not in the absorption spectrum [31]. The response of this feature to uniaxial stress was also measured during the stress experiments of the 946 nm ZPL. The polarisation dependence of the 976 nm transition is presented in Figure 5-6 for all combinations of excitation and detection electric field vector polarisations; the 946 nm (and 951 nm) stress-split spectra are overlaid on each spectrum in blue.

As the 976 nm exhibits a near-identical response to stress in comparison to the 946 nm transition and the stress-induced transition at lower energy (i.e. 951 nm emission from ${}^3A_{2u}$), this indicates the 976 nm transition is a vibrational replica of the 946 nm transition, rather than an independent ZPL. Furthermore, as the 951 nm replica (observed in the splitting of the 976 nm transition) maintains the same relative splitting to the 976 nm transition as the actual 951 nm transition does to the 946 nm transition, this indicates that both the 951 nm and 946 nm transitions are connected to the same ground state.

An additional feature (indicated by black arrows) is present in some of the 976 nm

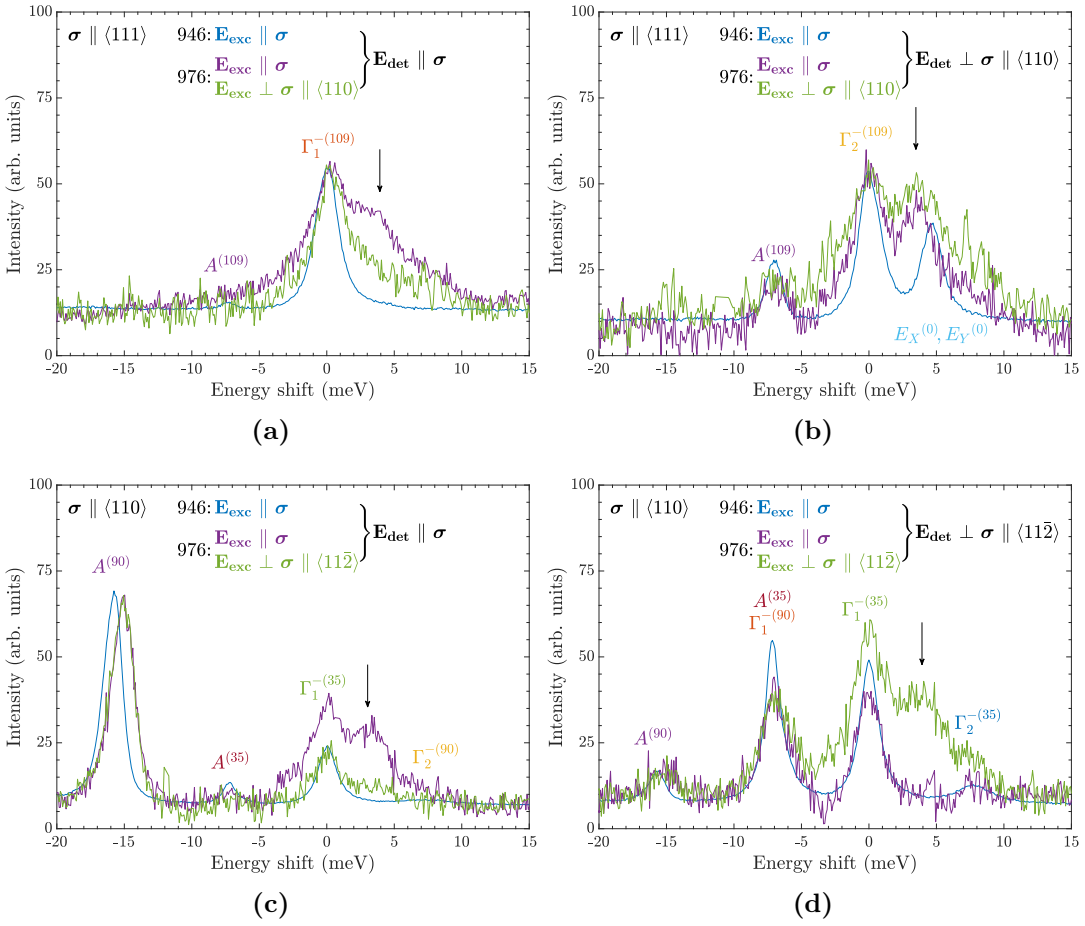

Figure 5-6 Polarisation dependence of 976 nm pLVM as a comparison to the SiV^0 ZPL under an applied stress ($\boldsymbol{\sigma}$) of (a) and (b) 2.0 GPa along ⟨1 1 1⟩, and (c) and (d) 2.1 GPa along ⟨1 1 0⟩. Spectra in blue represent measurements of the 946 nm ZPL with the excitation electric field vector ($\mathbf{E_{exc}}$) polarised parallel to the stress axis. Spectra in purple (green) represent measurements of the 976 nm pLVM with $\mathbf{E_{exc}}$ polarised parallel (perpendicular) to the stress axis. Black arrow highlights intensity of a feature unrelated to SiV^0. Transitions labelled as explained in Figure 5-2 and §5.3.2. For $\boldsymbol{\sigma} \parallel \langle 1\,1\,0\rangle$, $\mathbf{E_{exc}}$ or $\mathbf{E_{det}} \perp \boldsymbol{\sigma}$ corresponds to the direction $\langle 1\,1\,\bar{2}\rangle$. Data taken at 80 K.

stress-split spectra. The feature appears when the excitation and detection polarisations of the electric field vector are the same (i.e. both parallel or both perpendicular to the stress direction), except for the case of $\boldsymbol{\sigma} \parallel \langle 1\,1\,1\rangle$ and $\mathbf{E_{det}} \perp \boldsymbol{\sigma}$ when the feature is invariant to excitation polarisation. The feature clearly demonstrates polarisation dependence which is unlike any other SiV^0 features—this suggests the feature is unrelated to SiV^0 and coincidentally emits in the same spectral region.

The combination of characteristics suggest the 976 nm feature is a pseudo-local vibrational mode (pLVM). Whilst pLVMs are spatially localised in the lattice like

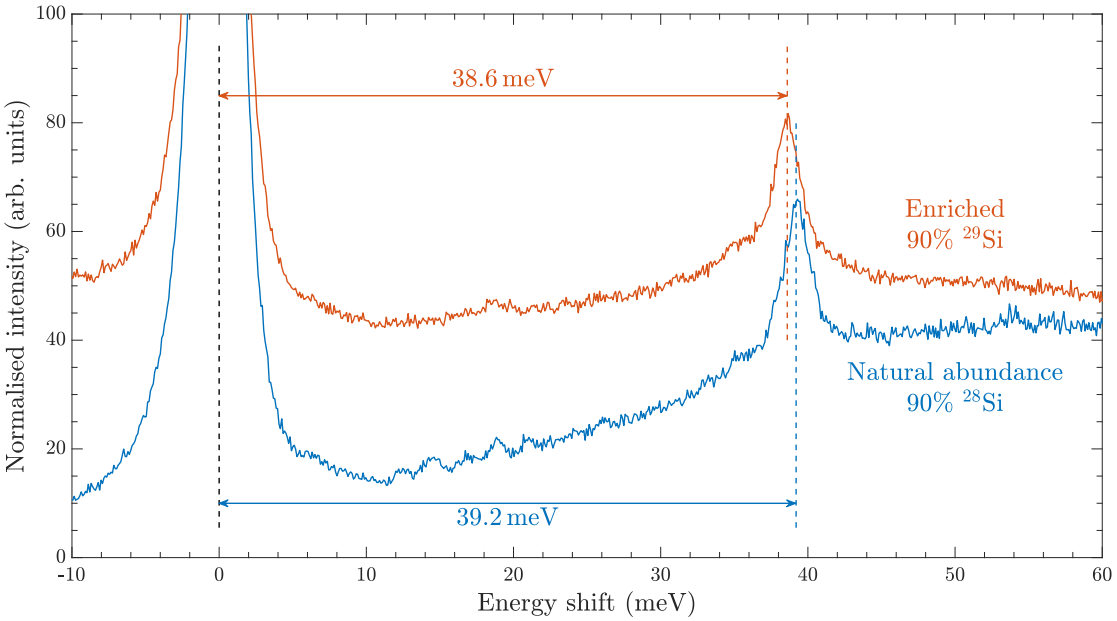

Figure 5-7 Energy shift of the 976 nm pLVM in PL with isotopic enrichment of (90%) ^{29}Si compared to a natural abundance (90% ^{28}Si) sample. The SiV^0 ZPLs have been fixed at zero for clarity. Data was measured at 80 K and taken by B. L. Green.

LVMs, their frequency localisation is below the Gamma (Γ) phonon frequency of the host lattice instead of above, where LVMs are situated [37]. The Γ phonon is the phonon frequency at the Γ point of the reciprocal lattice (1332 cm^{-1} for diamond) which is probed in Raman and FTIR spectroscopy. Consequently, they are challenging to detect in both Raman and FTIR spectroscopy but they can be appear as "replicas" of the ZPL in the phonon sideband of the ZPL in PL spectra [37]. Heavy impurities in semiconductors (compared to the host lattice element(s)) produce these low-frequency pLVMs [37, 38].

As diamond is the host lattice of this 976 nm pLVM, and given that a silicon impurity is much heavier than a carbon atom, the silicon atom in the SiV^0 centre is likely the cause of this pLVM. This hypothesis can be tested by comparing the PL spectra of the (90%) ^{29}Si enriched sample A1 to the natural abundance (92%) ^{28}Si sample A2—Figure 5-7 presents this comparison. With the ZPL of SiV^0 fixed at zero, the vibration frequency lowers from 39.2 meV in the natural abundance sample A2 to 38.6 meV in the ^{29}Si enriched sample A1.

Unsurprisingly, the sample with the heavier silicon isotope produces the lower frequency. This reduction in vibrational frequency due to isotopic enrichment can

also be modelled by treating the vibration as a simple harmonic oscillator, where the mode frequency of the isotopic enrichment Ω^*, is given by

$$\Omega^* = \Omega^0 \sqrt{\frac{m_0}{m^*}}, \tag{5-7}$$

where, Ω_0 is the mode frequency of the natural abundance sample, and m_0 and m^* are the effective masses of the natural abundance and isotopically enriched samples, respectively. The model predicts a reduction in vibration frequency to $\Omega^* = 38.6\,\text{meV}$ from a natural abundance mode frequency of $\Omega_0 = 39.2\,\text{meV}$, which is identical to the experimental behaviour observed in Figure 5-7.

5.4 Discussion

5.4.1 The 946 nm SiV^0 ZPL

The coupled ${}^3E_\text{u} \leftrightarrow {}^3A_{2\text{g}}$ model used to fit the 946 nm SiV^0 ZPL transition is an accurate qualitative description even though quantitatively the model is relatively poor. There are both experimental and theoretical considerations for why the fits to the data are not perfect. Any intrinsic inhomogeneous stress in the sample will produce a non-linear response to the applied external stress at low stress pressures—Figures 5-3 and 5-4 have low stress ($< 0.5\,\text{GPa}$) data omitted due to poor fits. Small misalignments or slightly non-parallel stress faces that lead to non-uniaxial stress will also adjust the response to applied external stress; the effect is made worse if the response is different for the two stress directions. The model itself does not consider Jahn-Teller interactions in the ${}^3E_\text{u}$ state or pseudo-Jahn-Teller interactions between the ${}^3E_\text{u}$ and ${}^3A_{2\text{u}}$ states that may be able to explain some of the inaccuracies of the fit. Investigating the existence of these interactions will require high-quality absorption data with applied stress that is not possible with sample A1 due to the low concentration of SiV^0.

Irrespective of the fit not being perfect, the data still allows for a convincing assignments of symmetries to the excited states. EPR measurements on the SiV^0 centre measured the spin of the ground state as $S = 1$ [11]: the ground state must therefore be ${}^3A_{2\text{g}}$ as no other spin-triplet symmetry state arise from the ground state e_g^2 hole picture configuration of SiV^0 (Table 5-1). Consequently, the previous

experimental [31] and theoretical [28] investigations that assigned the excited state of the 946 nm transition as $^3A_{1u}$ are incorrect as there are too many stress-split lines observed for an $A \leftrightarrow A$ transition to be responsible for the 946 nm ZPL. The excited state symmetry must therefore be degenerate and also a spin-triplet state in order to conserve spin, which from the lowest-energy one-electron hole picture of $e_u^1 e_g^1$ only leaves ^3E_u as the excited state of the 946 nm ZPL. Hence the assignment of a $^3E_u \leftrightarrow {}^3A_{2g}$ transition to the 946 nm ZPL, which also necessarily observes a change in parity along with the other selection rules.

The assignment of the stress-induced transition at approximately 951 nm can also be addressed. The transition is shown to be non-degenerate (i.e. an A state) as only two stress-split lines are observed with its transition with the $^3A_{2g}$ ground state of SiV^0. It must share a ground state with the SiV^0 ZPL in order for the 976 nm pLVM to produce a replica of the 951 nm with relative splitting that is identical to the splitting of the actual 951 nm transition relative to the SiV^0 ZPL (§5.3.4). The transition is allowed under stress, so only symmetry selection rules must prevent the transition and not spin (as spin is not changed under stress), which indicates a spin-triplet state. The $e_u^1 e_g^1$ hole picture of the excited states gives two options that fulfil the spin and degeneracy criteria: $^3A_{1u}$ and $^3A_{2u}$. A transition between $^3A_{2g}$ and $^3A_{1u}$ is allowed in a $\mathscr{D}_{3d}$ centre so the excited state of the 951 nm transition must be $^3A_{2u}$ as it is only observable under applied stress.

This $^3A_{2u}$ state is also recognised as the shelving state responsible for the intensity reduction of the 946 nm ZPL with decreasing temperature, in Figures 5-4 and 5-5, which is calculated at −6.8 meV below the ^3E_u excited state. Recent *ab initio* results support this assignment and energy separation [39]; the same study also supports the assignment of the ^3E_u state. However, recent experimental measurements on single SiV^0 centres do not indicate the presence of the $^3A_{2u}$ shelving state [27] and currently there is no obvious explanation for why this contradicts the qualitatively convincing coupled $E_u \leftrightarrow A_{2g}$ model proposed here. Further measurements are required.

5.4.1.1 Ionisation of SiV^0

The invariant behaviour towards excitation polarisation that the 946 nm ZPL system exhibits in Figure 5-2 (and similarly by extension the 976 nm system in Figure 5-6) is not due to the SiV^0 centre but is instead attributed to energy of the 785 nm (1.58 eV) excitation used during measurements. As the excited state of the 946 nm transition in SiV^0 is ~1.5 eV above the valence band [40], the laser has sufficient energy to excite an electron to the SiV^0 excited states from both the ground state of the centre and the valence band; the latter effectively results in a temporary ionisation of the SiV^0 centre by gaining an electron. Figure 5-8 provides a schematic of the SiV^0 valence-band-excitation process facilitated by the 785 nm laser.

In general, the purpose of exciting an ensemble of centres with polarised light is to deconvolve the proportional response of all orientations of that ensemble (specifically the dipole orientations) to the polarisation axis of the light. However, in the case of PL experiments, if an electron from an external source—such as the valence band—is excited to the excited level of a centre, the excitation polarisation is irrelevant (and the polarisation information is therefore lost) because all orientations of the centre will be excited equally by this process. It must be noted that whilst the laser will also excite electrons from the ground states of the centres and enable the desired polarisation-dependent emission, it is not possible to deconvolve this emission from a spectrum of all possible emissions.

There are two key corollaries from this process of excitation from the valence band: first, the detected response of the centres will be invariant to excitation polarisation (as noted for both the 946 nm ZPL and the 976 nm pLVM); and second, as the centres will only exhibit detection polarisation-dependence, this is effectively the same as observing an absorption measurement (i.e. one degree of freedom in terms of polarisation) and as such the emission intensities of any given transition will match the values given in absorption tables rather than luminescence tables. This is the reason why the absorption intensity values in Table 5-4, and not the luminescence intensity values in Table 5-5, were used to fit the intensity data in Figure 5-4. This result does however confirm the understanding that the position

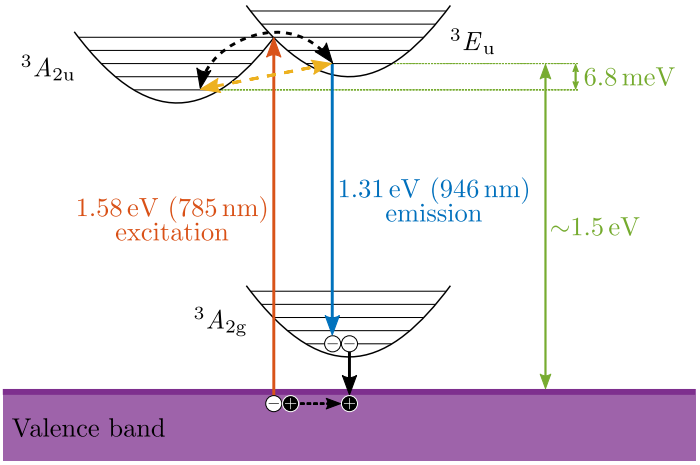

Figure 5-8 Schematic representation of the SiV^0 valence-band-excitation process facilitated by the 785 nm laser. At an energy of 1.58 eV, the laser can excite an electron directly from the valence band to the excited states of SiV^0 (orange arrow) situated ~1.5 eV above the valence band maximum (green arrow). The electron is excited into either the 946 nm ^3E_u vibronic band or the coupled non-radiative $^3A_{2u}$ vibronic band 6.8 meV below. Thermalisation between the two levels is possible in either direction (yellow-dashed arrow). A hole is generated in the valence band by the electron excitation and is subsequently trapped by the $^3A_{2g}$ ground state of SiV^0. If the electron reaches the lowest energy of the ^3E_u vibronic band and recombination occurs between the trapped hole and an electron in the $^3A_{2g}$ ground state, 946 nm ZPL emission (blue arrow) is possible from de-excitation of the electron in the ^3E_u level. Figure adapted from [31].

of the SiV^0 excited states must be < 1.58 eV above the valence band, and therefore the ground state is very close to the valence band.

Nevertheless, the lack of excitation polarisation-dependence is largely irrelevant to aims of this chapter, as the results of the numerical model are still convincing. Whilst using a more appropriate excitation wavelength would produce a complete set of polarisation-dependent spectra, the measurements were not repeated as no new information would be acquired about the SiV^0 centre. Were this experiment to be repeated, an excitation laser of energy 1.31–1.5 eV (946–827 nm) would allow for full polarisation-dependence of the SiV^0 centre from PL measurements to be observed.

5.4.2 Spin polarisation of SiV^0

The information learned from the uniaxial stress experiments about the electronic structure and symmetries of the excited state of SiV^0 incentivises a review of the

spin polarisation of SiV^0. Green *et al.* [25] and Rose *et al.* [27] have observed off-resonant (absorption from any absorption band energy) spin polarisation of the 946 nm ZPL transition; the latter also observed spin polarisation at 951.3 nm (see Figure S10 in the Supplemental Material [27]). Observation of spin polarisation is an indication of intersystem crossing (ISC, Figure 5-9a), whereby non-radiative phonon-facilitated transitions occur between states with different spin multiplicity, that can result in a preferentially populated spin state in electronic ground state—this is, for example, well documented for the NV^- centre [41]. The exact ISC mechanism for SiV^0 is currently unknown as neither the ISC rates to the spin-singlet states, or the relative ordering of the spin-singlet states are known.

The results in this chapter demonstrate the optical transition at approximately 951 nm is stress-induced. Observation of spin polarisation at this transition by Rose *et al.* [27] suggests the sample contained a strained ensemble of SiV^0 centres such that the symmetry forbidden transition between the $^3A_{2g}$ ground state (where the readout of the spin polarisation occurred) and the $^3A_{2u}$ excited state was allowed under strain (Figure 5-9a). At the experimental temperature of approximately 4 K, the thermal population of the ^3E_u ground state is negligible due to the phonon-assisted thermalisation into the $^3A_{2u}$ state. As the $^3A_{2u}$ state was the only significantly populated state, it must be directly involved in the spin polarisation mechanism of the 951 nm transition.

Consequently, it is inferred that the $^3A_{2u}$ state is also involved in the off-resonant spin polarisation mechanism of the 946 nm transition that excites into the ^3E_u state. In this scenario, the $^3A_{2u}$ will be also be populated via phonon relaxation from the ^3E_u state and therefore it is currently unclear if both states contribute to the mechanism via ISC or only the $^3A_{2u}$ state contributes (as discussed for the 951 nm transition). In either case, off-resonant optical spin readout resulting in the observation of optically detected magnetic resonance (ODMR) [42] via emission from the $^3A_{2u}$ state (under applied stress) will be expected and potentially also the ^3E_u state if it is involved in the spin polarisation mechanism. Realisation of ODMR in SiV^0 would allow the measurement of ISC rates for the spin states ($m_s = 0, \pm 1$) of the electron excited states, which are currently unknown elements

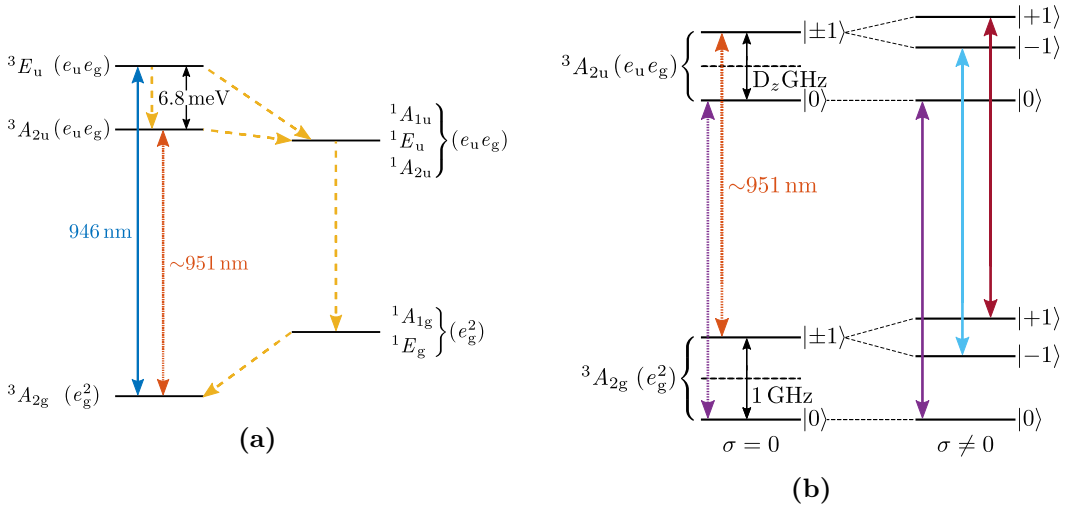

Figure 5-9 (a) The proposed electronic structure of SiV^0 based on the uniaxial stress results in this chapter. The relative energy ordering of the spin-singlet states are unknown. Yellow dashed arrows indicate phonon-enabled transitions that also allow intersystem crossing. (b) A proposed scheme for spin-dependent initialisation and readout of the 951 nm transition. Symmetry-forbidden transitions (short-dashed arrows) may become allowed (solid arrows) with a small applied stress. The value of D_z is unknown. Electronic configurations are presented in the hole picture.

of the spin polarisation mechanism. Off-resonant ODMR has been realised for the NV^- centre [43] and on-resonant (at the ZPL energy) ODMR has been realised for the SiV^- centre [44].

A proposed scheme for the spin-dependent initialisation and readout of the 951 nm transition is presented in Figure 5-9b. As discussed previously, the parity forbidden transition between the $^3A_{2g}$ ground state and the $^3A_{2u}$ excited state becomes allowed if applied stress can break the symmetry of the inversion-symmetric $\mathscr{D}_{3d}$ centre. Applied stress also has a secondary benefit of lifting the $m_s = \pm1$ spin degeneracy in the spin-triplet manifolds of the two states and potentially reducing the magnitude of magnetic field that would otherwise be required to lift the spin degeneracy. Spin-conserving optical transitions between the three m_s states are observable if the difference in zero-field splitting (ZFS) between the $^3A_{2g}$ and $^3A_{2u}$ states is greater than the inhomogeneous linewidth of the optical transitions themselves. The ZFS of the $^3A_{2g}$ ground state is known to be 1 GHz at 300 K [11] but the value of the ZFS (D_z) of the $^3A_{2u}$ excited state is currently unknown.

Given observation of the transitions, then spin-dependent initialisation and read-

out may be controlled: high-fidelity initialisation into $m_s = 0$ in the $^3A_{2g}$ ground state can be achieved through internal, off-resonant spin polarisation of SiV^0 [25, 27]. Population control between $m_s = 0$ and the non-degenerate $m_s = +1$, $m_s = -1$ states may be realised by coherent microwave frequency control at a low magnetic field. If the $m_s = \pm 1$ spin manifolds of the ground and excited states can demonstrate unique splitting energies—through different g-factors, or different responses to strain, or both—then control of spin populations is possible with only optical inputs. Manifestation of this scheme may lead to the realisation of a spin-photon entanglement protocol for the SiV^0 centre, as already realised for the NV^- centre [45].

5.4.3 The 976 nm pseudo-LVM

The 976 nm pLVM is predominantly due to oscillation of the Si atom within the di-vacancy, as supported by the isotopic enrichment observations and simple harmonic oscillator modelling. Given that the calculated reduction in frequency mode of the ^{29}Si-enriched sample (39.2 meV to 38.6 meV) was the same as the observed shift in Figure 5-7, the vibration appears to be weakly coupled to the bulk diamond lattice. Were the vibration more strongly coupled, the calculation would not be able to predict the frequency accurately as it does not take into account coupling effects; the frequency reduction would be smaller with stronger coupling.

Gali and Maze [28] provided DFT calculations that suggested the 976 nm transition is actually a parity forbidden electronic transition between the $^3A_{2g}$ ground state and a ^3E_g excited state (result from the $a_{1g}^1 e_g^1$ hole picture) that becomes optically active when the inversion symmetry of the centre is broken. The spectra provided in Figure 5-7 were not measured with samples subject to external stress; even if they were, stress along the three conventional stress directions of $\langle 0\,0\,1 \rangle$, $\langle 1\,1\,1 \rangle$ and $\langle 1\,1\,0 \rangle$ does not remove the inversion symmetry. Internal strain could theoretically break the inversion symmetry but the ^3E_g excited state would have to be coupled to an unrelated nearby A state that is 6.8 meV lower in energy in order to reproduce (as accurately as it does) the behaviour of the 946 nm ZPL under applied stress. This is very unlikely, and as no experimental evidence currently supports this

suggestion, the 976 nm transition is confidently identified as a pLVM.

The symmetry of the pLVM may also be considered given its similar response to applied stress in comparison to the 946 nm transition (Figure 5-6). For a purely electronic transition, such as the 946 nm ZPL, only the symmetry of the ground and excited electronic states (and also the dipole operator) are considered when calculating if a transition is allowed or forbidden (see §3.5). For the 976 nm pLVM, the symmetry of the phonon mode must also be considered as this is a vibronic transition. As the electronic 946 nm transition and the vibronic 976 nm transitions have near-identical polarisation behaviour under applied stress, it suggests symmetry of the phonon mode does not change the overall symmetry of the transition and only the totally symmetric irreducible representation of A_{1g} allows for this.

However, DFT calculations by Londero *et al.* [46] suggest only E_u and A_{2u} silicon vibration modes are responsible for pLVMs in SiV centres. Whilst incompatible with the experimentally suggested mode of A_{1g}, the modes proposed by Londero *et al.* are also incompatible with the symmetries of the SiV^0 centre. The overall mode symmetry from coupling either of the proposed vibrational modes (E_u or A_{2u}) to the electronic ground state through ${}^3A_{2g} \otimes \Gamma_{LVM}$ results in a state that is *ungerade* (uneven) and therefore vibronic transitions with either of the excited states (${}^3E_u$ or ${}^3A_{2u}$) are forbidden by parity (as only parity-flipping transitions are allowed). The A_{2u} mode can become compatible if the symmetry is lowered by, for example, (pseudo-)Jahn Teller distortions in the excited state that change the symmetry of the centre from $\mathscr{D}_{3d} \rightarrow \mathscr{C}_{3v}$. The vibrational mode would then transform from $A_{2u} \rightarrow A_1$, thereby allowing the transition. A sharp mode related to the E_u vibration of the silicon is not observed in SiV^0 (but it is observed in SiV^- [47]).

The complexities of understanding pLVM symmetries in SiV^0 are shared with its negatively charged analogue, SiV^-. Two pLVMs are identified in SiV^-, with energy shifts relative to the ZPL at 40 meV and 64 meV [47]. The energy shift of the 64 meV mode is accurately approximated by a simple harmonic oscillator model (such as that utilised for the 976 nm pLVM in §5.3.4) where effectively only the silicon atom need be considered in the oscillation [48]. Experimental results

on single-centres have assigned A_{2u} symmetry to the mode [48, 49] but the DFT calculations by Londero *et al.* disagree and assign E_u symmetry [46]; they also argue that the 40 meV is not a pLVM, in contradiction to the experimental observations. It is apparent that current experimental and theoretical investigations are irreconcilable and conclusive identification of the vibrational modes of both the neutral and negative SiV charge variants requires further work.

5.5 Conclusion

PL measurements at variable temperature with perturbing uniaxial stress have been performed on an ensemble of SiV^0 centres in order to better understand the electronic structure. The model proposes a qualitatively convincing description of the lowest-energy one-electron excited state of the SiV^0 centre as a ${}^3E_u \leftrightarrow {}^3A_{2g}$ ZPL transition, where the ${}^3E_u$ excited state is coupled to a ${}^3A_{2u}$ shelving state that is 6.8 meV lower in energy. Too many stress-split lines are observed from the 946 nm ZPL for the previous assignment of the excited as ${}^3A_{1u}$ to be correct.

Quenching of the SiV^0 946 nm ZPL occurs with lower temperatures, as Boltzmann populations shift from the ${}^3E_u$ to the ${}^3A_{2u}$ state. Under applied stress that lowers the $\mathscr{D}_{3d}$ symmetry, a transition between the ${}^3A_{2g}$ ground state and ${}^3A_{2u}$ excited state is observed (at approximately 951 nm), that otherwise is forbidden by symmetry. As spin polarisation of both the 946 nm and 951 nm transitions has been previously demonstrated, a scheme is proposed for spin-dependent initialisation and readout of the spin states in the 951 nm transition, but this has yet to be tested and should be a focus of future research.

A pseudo-LVM corresponding to the silicon atom in SiV^0 is identified at 976 nm that exhibits near-identical stress-inducing splitting as the 946 nm and 951 nm transitions. The energy shift of the pLVM with a change of silicon isotope concentrations is accurately estimated by a simple harmonic oscillator model. The inferred symmetry of the vibrational mode based on the experimental results is currently incompatible with DFT calculations and requires further work.

References

1. T. Schröder *et al.*, *Journal of the Optical Society of America B* **33**, B65–B83 (2016).
2. M. W. Doherty *et al.*, *Physics Reports* **528**, 1–45 (2013).
3. R. Schirhagl *et al.*, *Annual Review of Physical Chemistry* **65**, 83–105 (2014).
4. C. Hepp *et al.*, *Physical Review Letters* **112**, 036405 (2014).
5. C. J. Hepp, PhD, Saarland University, 2014.
6. M. Leifgen *et al.*, *New Journal of Physics* **16**, 023021 (2014).
7. A. Sipahigil *et al.*, *Physical Review Letters* **113**, 113602 (2014).
8. J. Wolters *et al.*, *Applied Physics Letters* **97**, 141108 (2010).
9. E. Neu *et al.*, *New Journal of Physics* **15**, 043005 (2013).
10. H. Sternschulte *et al.*, *Diamond and Related Materials* **4**, 1189–1192 (1995).
11. A. M. Edmonds *et al.*, *Physical Review B* **77**, 245205 (2008).
12. J. H. N. Loubser, J. A. van Wyk, *Reports on Progress in Physics* **41**, 1201–1248 (1978).
13. E. Neu *et al.*, *New Journal of Physics* **13**, 025012 (2011).
14. T. Schröder *et al.*, *New Journal of Physics* **13**, 055017 (2011).
15. C. Wang *et al.*, *Journal of Physics B: Atomic, Molecular and Optical Physics* **39**, 37–41 (2006).
16. A. Batalov *et al.*, *Physical Review Letters* **100**, 077401 (2008).
17. J. N. Becker *et al.*, *Nature Communications* **7**, 13512 (2016).
18. S. Meesala *et al.*, *Physical Review B* **97**, 205444 (2018).
19. D. D. Sukachev *et al.*, *Physical Review Letters* **119**, 223602 (2017).
20. G. Balasubramanian *et al.*, *Nature Materials* **8**, 383 (2009).
21. E. D. Herbschleb *et al.*, *Nature Communications* **10**, 3766 (2019).
22. Y. I. Sohn *et al.*, *Nature Communications* **9**, 2010 (2018).
23. D. Riedel *et al.*, *Physical Review X* **7**, 031040 (2017).
24. S. Pezzagna *et al.*, *New Journal of Physics* **13**, 035024 (2011).
25. B. L. Green *et al.*, *Physical Review Letters* **119**, 096402 (2017).
26. S. Mottishaw, PhD thesis, The University of Warwick, 2017.
27. B. C. Rose *et al.*, *Science* **361**, 60–63 (2018).

28. A. Gali, J. R. Maze, *Physical Review B* **88**, 235205 (2013).
29. C. A. Coulson, F. P. Larkins, *Journal of Physics and Chemistry of Solids* **30**, 1963–1972 (1969).
30. S. Häußler *et al.*, *New Journal of Physics* **19**, 063036 (2017).
31. U. F. S. D'Haenens-Johansson *et al.*, *Physical Review B* **84**, 245208 (2011).
32. U. F. S. D'Haenens-Johansson, PhD thesis, The University of Warwick, 2011.
33. B. L. Green *et al.*, *Physical Review B* **99**, 161112 (2019).
34. L. J. Rogers *et al.*, *New Journal of Physics* **17**, 013048 (2015).
35. Supplemental Material for B. L. Green *et al.*, *Physical Review B* **99**, 161112 (2019), found at http://link.aps.org/supplemental/10.1103/PhysRevB.99.161112.
36. H. A. Bethe, *Annalen der Physik* **3**, 133–206 (1929).
37. S. K. Estreicher *et al.*, *Physical Review Letters* **90**, 4 (2003).
38. S. K. Estreicher *et al.*, *Journal of Applied Physics* **115**, 012012 (2014).
39. G. Thiering, A. Gali, *npj Computational Materials* **5**, 18 (2019).
40. L. Allers, A. T. Collins, *Journal of Applied Physics* **77**, 3879–3884 (1995).
41. M. L. Goldman *et al.*, *Physical Review B* **91**, 165201 (2015).
42. J. J. Davies, *Contemporary Physics* **17**, 275–294 (1976).
43. A. Gruber *et al.*, *Science* **276**, 2012–2014 (1997).
44. B. Pingault *et al.*, *Nature Communications* **8**, 15579 (2017).
45. E. Togan *et al.*, *Nature* **466**, 730–734 (2010).
46. E. Londero *et al.*, *Physical Review B* **98**, 35306 (2018).
47. L. J. Rogers *et al.*, *Physical Review B* **89**, 235101 (2014).
48. A. Dietrich *et al.*, *New Journal of Physics* **16**, 113019 (2014).
49. L. J. Rogers *et al.*, *Physical Review Letters* **113**, 263602 (2014).

6

The 7354 cm^{-1} centre

6.1 Introduction

The near-infrared (NIR) absorption spectrum of nitrogen-doped single crystal CVD diamond often contains a strong 7354 cm^{-1} line decorated with other weaker (and potentially related) absorption lines [1–5]. Room temperature (RT) FTIR measurements by Glover [6] correlated the absorption peak sizes of the 6425 cm^{-1}, 7354 cm^{-1} and 8753 cm^{-1} lines as $5(1):1:20(8)$, respectively, leading to the set of lines being referred to as "the 7354 cm^{-1} system." Subsequent measurements by Glover [6] demonstrated that the lines shift in energy with temperature; consequently, the energies reported in literature and this chapter will vary slightly due to this temperature dependence.

These measurements also deduced the 6425 cm^{-1} line was an electronic transition originating from an excited state, as it disappeared below ~80 K suggesting its ground state population had thermalised out, and that the 8753 cm^{-1} line behaves as a local vibrational mode (LVM) of the 7354 cm^{-1} line. No observsation of these lines has been made in high pressure high temperature (HPHT) or natural diamond samples and as such they can be used as reliable indicators of the CVD synthetic origin of the diamond [4].

Since the first reports in 1995 by Fuchs *et al.* [1, 2], an expansive host of characterisation techniques have been employed in order to understand more about these

commonly observed lines. The RT full width at half maximum (FWFH) of the 7354 cm^{-1} line is typically ~50 cm^{-1}. Isotopic substitution with deuterium (^{2}D) caused a large negative shift of 42–44 cm^{-1} in the 7354 cm^{-1} feature, indicating that hydrogen is involved in the defect [1, 2, 7]. Specifically, the sample grown with an equal amount of hydrogen (^{1}H) and ^{2}D produced a spectrum that is the superposition of spectra of 100% ^{1}H and 100% ^{2}D grown samples, suggesting that only one hydrogen atom is involved in the defect. This does not, however, rule out the possibility that the 7354 cm^{-1} defect involves more than one hydrogen atom.

Isotopic substitution with ^{13}C produces a small positive shift of 12 cm^{-1} in the 7354 cm^{-1} peak; a similar positive shift of 8–12 cm^{-1} is observed when cooling to liquid helium temperatures (~10 K), along with a narrowing of the FWHM, which suggests the line originates from an electronic transition [1, 2]. Therefore, the 7354 cm^{-1} line is recognised as a zero-phonon line (ZPL) and (as shall be presented in this chapter) is also optically observable with 1064 nm excitation photoluminescnce (PL). No shift is observed from isotopic substitution with ^{15}N, thereby implying that nitrogen is not involved in this transition, and by extension is not bonded to hydrogen in the defect [6].

Isochronal annealing between 900–1500 °C in increments of 100 °C for 2 h, with a final anneal of 4 h at 1600 °C, was performed by Cruddace [7]. The 7354 cm^{-1} system begins to anneal-out at 1300 °C and is still weakly present (~5–10% of as-grown intensity) after the 1600 °C anneal. Charles *et al.* [5] report complete removal of the system after 1 h of HPHT annealing at 1900 °C. Given that the system is present in as-grown CVD diamond and begins to anneal-out at the relatively low temperature of 1300 °C, it implies the centre responsible for the system is "simple." Consequently, the structure of this centre is likely to be of (a diamond applicable [8]) high symmetry, i.e. tetrahedral, tetragonal or trigonal.

Initial uniaxial stress measurements in absorption performed by Glover [6] suggested the 7354 cm^{-1} line is an $E \leftrightarrow A$ transition at a trigonal centre with point group $\mathscr{C}_{3v}$. Whilst only a singular stress direction was investigated ($\boldsymbol{\sigma} \parallel \langle 0\,0\,1 \rangle$), the ground state was observed to thermalise at low temperatures, hence the labelling of the ground state as a doubly degenerate E state. Further uniaxial stress

measurements in absorption by Cruddace [7], this time along three stress directions $\boldsymbol{\sigma} \parallel \langle 0\,0\,1\rangle$, $\langle 1\,1\,1\rangle$ and $\langle 1\,1\,0\rangle$, suggested the 6425 cm^{-1} and 7354 cm^{-1} lines were $E \leftrightarrow E$ transitions from a trigonal centre with point group $\mathscr{D}_{3d}$, with the fit of the former line being much better than the latter. Whilst the symmetry was still not confidently identified, Cruddace also observed thermalisation in the ground state of the 7354 cm^{-1} line and therefore supported the assignment of a doubly degenerate E ground state. Unbeknownst at the time, and as shall be presented in this chapter, the 7354 cm^{-1} system exhibits preferential orientation with respect to the CVD growth direction, which could have potentially mislead the analysis of the optical absorption uniaxial stress experiments.

Whilst the defect responsible for the 7354 cm^{-1} line is currently unknown, one would be remiss to not briefly discuss the possible defects which could be responsible for the line, given the characterisation work described. The defect contains hydrogen (likely only one hydrogen atom) but may or may not contain nitrogen, and is of high symmetry due to having a degenerate E ground state. At the time of writing, isolated interstitial hydrogen has not been experimentally observed in diamond but theoretical investigations on defects which match the above criteria have been performed, with one such example being bond-centred interstitial hydrogen (H_{BC}) with point group $\mathscr{D}_{3d}$ [9–11]. The negative charge state H_{BC}^- of this theoretically stable defect is expected to be diamagnetic with an estimated C–H stretch LVM at ~2730 cm^{-1} [10]. A theoretically more stable defect than H_{BC} is the di-hydrogen interstitial H_2^* with point group $\mathscr{C}_{3v}$ [11, 12]. Hydrogen incorporation in other semiconductors, including other group IV semiconductors such as silicon, is much better understood than in diamond [13] so positive identification of these possible hydrogen interstitials (or other hydrogen-related defects) would satisfy a significant number of questions regarding hydrogen in CVD diamond.

Taking into consideration the previous work regarding the 7354 cm^{-1} system and the importance that this hydrogen-related defect may have on the understand of hydrogen in CVD diamond, the motivation for this chapter is as follows:

- What are the properties of the preferential orientation of the 7354 cm^{-1} system and what does the presence of preferential orientation inform about the

growth process?

- What is the degeneracy of the excited state of the 7354 cm^{-1} line and does it match the current suggestion of a degenerate E state such that the transition of the line is $E \leftrightarrow E$?
- What is the symmetry of the centre responsible for the 7354 cm^{-1} system and is it either of the previously suggested point groups in the trigonal family of $\mathscr{C}_{3v}$ or $\mathscr{D}_{3d}$?
- Ultimately, what is the hydrogen-related centre responsible for the 7354 cm^{-1} system?

6.2 Experimental details

The data presented in this chapter has been obtained from a suite of as-grown CVD diamonds containing the 7354 cm^{-1} system and hereby will be referred to as the set of samples B1-4. The concentrations of N_S^0, N_S^+ and the integrated intensities of the 7354 cm^{-1} line of these samples, measured by RT FTIR, are given in Table 6-1. Optical and DiamondView™ fluorescence images of these samples (except B4) are given in Figure 6-1. Figure 6-1a shows images of sample B1 before begin cut and polished into samples B1a and B1b. The lines going across the DiamondView™ fluorescence images, parallel to ⟨1 1 0⟩, originate from the step-flow growth of CVD diamond [14]—the growth direction is approximately 90° to these lines, i.e. ⟨0 0 1⟩. Consequently, all samples (including B4) have orientations ⟨0 0 1⟩ (the growth

Sample	$[N_S^0]$ (ppm)	$[N_S^+]$ (ppm)	7354 cm^{-1} (cm^{-2})	Grower
B1a	8.2(5)	14.3(8)	2100(100)	ME†
B1b	8.2(5)	14.3(8)	2100(100)	ME†
B2	27.8(9)	3.1(3)	1000(50)	E6‡
B3	2.0(2)	0.6(1)	300(10)	AD⋄
B4	7.2(5)	1.5(2)	210(10)	E6‡

Table 6-1 Samples investigated regarding the 7354 cm^{-1} system. Absorption lines were measured by RT FTIR. Note sample B4 is ^{15}N-doped and also silicon-doped. All samples were grown on {0 0 1}-oriented substrates. † = Microwave Enterprises Ltd, ‡ = Element Six Ltd, ⋄ = Apollo Diamond Inc.

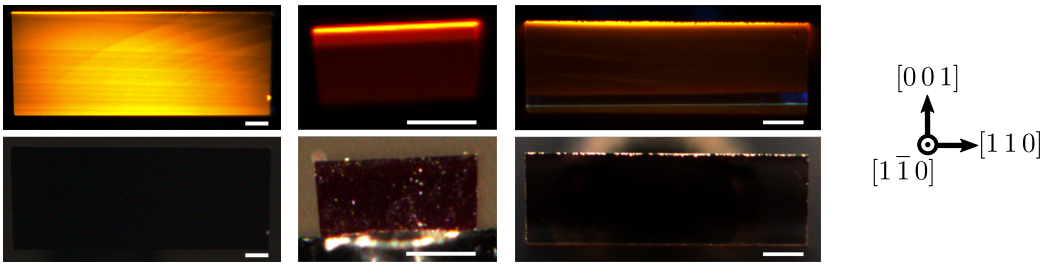

(a) Sample B1 (B1a/b) **(b)** Sample B2 **(c)** Sample B3 **(d)** Orientations

Figure 6-1 Optical (bottom) and DiamondView™ flourescence (top) imaging of the suite of samples containing the 7354 cm^{-1} system. (a) Sample B1 imaged before begin cut and polished into samples B1a and B1b, (b) sample B2, and (c) sample B3. Scale bar = 0.5 mm.

direction), $\langle 1\,1\,0\rangle$ and $\langle 1\,\bar{1}\,0\rangle$. It is worth noting that the 7354 cm^{-1} system is observable in a variety of nitrogen-doped diamonds, with colours varying from entirely black (samples B1a/b), to purple-coloured (sample B2), and to light grey (sample B3).

Samples B1a and B1b (both as-grown) were used for absorption uniaxial stress measurements with FTIR due to their high integrated intensity of the 7354 cm^{-1} line, compared to the other samples. Whilst useful for the absorption uniaxial stress measurements, they were not used for PL uniaxial stress measurements because when tested they produced broad 7354 cm^{-1} lines. This may be observed in the PL spectrum of samples B1a/b, which can be found in §4.2.4 under the label "N-doped (high)." Therefore, a different sample (B3) was employed for the set of 1064 nm PL uniaxial stress measurements in this chapter, even though its integrated intensity of the 7354 cm^{-1} line is lower. The details of the uniaxial stress measurements for both FTIR absorption and the purpose-built 1064 nm PL system are described in §4.2.4.

Samples B2, B3 and B4 were used to investigate the charge transfer and preferential orientation properties of the 7354 cm^{-1} system with FTIR absorption. Sample B1a also underwent preferential orientation measurements with FTIR in its as-grown state and after being annealed at 1500 °C for 4 h—this is the only set of data in this chapter that was performed on a sample that was not as-grown.

6.3 Results

Absorption spectra typically report line positions in units of wavenumber (cm^{-1}) whereas photoluminescence spectra typically report line positions in units of wavelength (nm). The figures in this chapter comprise of both of the aforementioned spectra and as such the position of all lines are given (where appropriate) in both units of wavenumber and wavelength. For simplicity and readability the text of this chapter will default to wavenumber values, if possible.

A comparison of spectra of the 7354 cm^{-1} system, as measured by RT 1064 nm PL and RT IR absorption, is given in Figure 6-2. The 7354 cm^{-1} line and the four lines to left (6861.2 cm^{-1}, 6953.7 cm^{-1}, 7183.6 cm^{-1} and 7224.8 cm^{-1}) are present in both spectra, although weakly in the case of the 6861.2 cm^{-1} and 6953.7 cm^{-1} lines. The 6426.5 cm^{-1} line is strong in absorption yet absent in PL. The broad line at 7825.4 cm^{-1} is also relatively strong in absorption and not obviously visible in PL, however the PL spectrum has a raised baseline between the 7354 cm^{-1} line and Raman line (1239.7 nm) which may be obscuring the broad line. The LVM at 8750.7 cm^{-1} should have its PL counterpart at 1678.6 nm (red dashed lines) but no line in present in PL. The lack of detection is most likely due to the technical reason of the iDus InGaAs detector measuring up to 1700 nm but having a rapidly reducing quantum efficiency (QE) [15] above 1600 nm ($QE_{1678.6\,nm} \approx 20\%$) [16].

6.3.1 Preferential orientation and charge transfer

The preferential orientation and charge transfer behaviour of the 7354 cm^{-1} system, in as-grown samples B2 and B3, is shown in Figure 6-3. The 7354 cm^{-1} line is clearly preferentially orientated in the samples such that incident light polarised perpendicular to the growth direction ($\mathbf{E} \parallel [1\,1\,0]$) is absorbed by a factor of 2.2(2)–3.0(2) greater than incident light polarised parallel to the growth direction ($\mathbf{E} \parallel [0\,0\,1]$). The lines at 7183.6 cm^{-1}, 7224.8 cm^{-1}, 7825.4 cm^{-1} and 8750.7 cm^{-1} (indicated by red dashed lines) also exhibit the same preferential orientation whilst all the other labelled lines are indifferent to incident light polarisation.

Similarly, Figure 6-4 shows the preferential orientation behaviour of the 7354 cm^{-1}

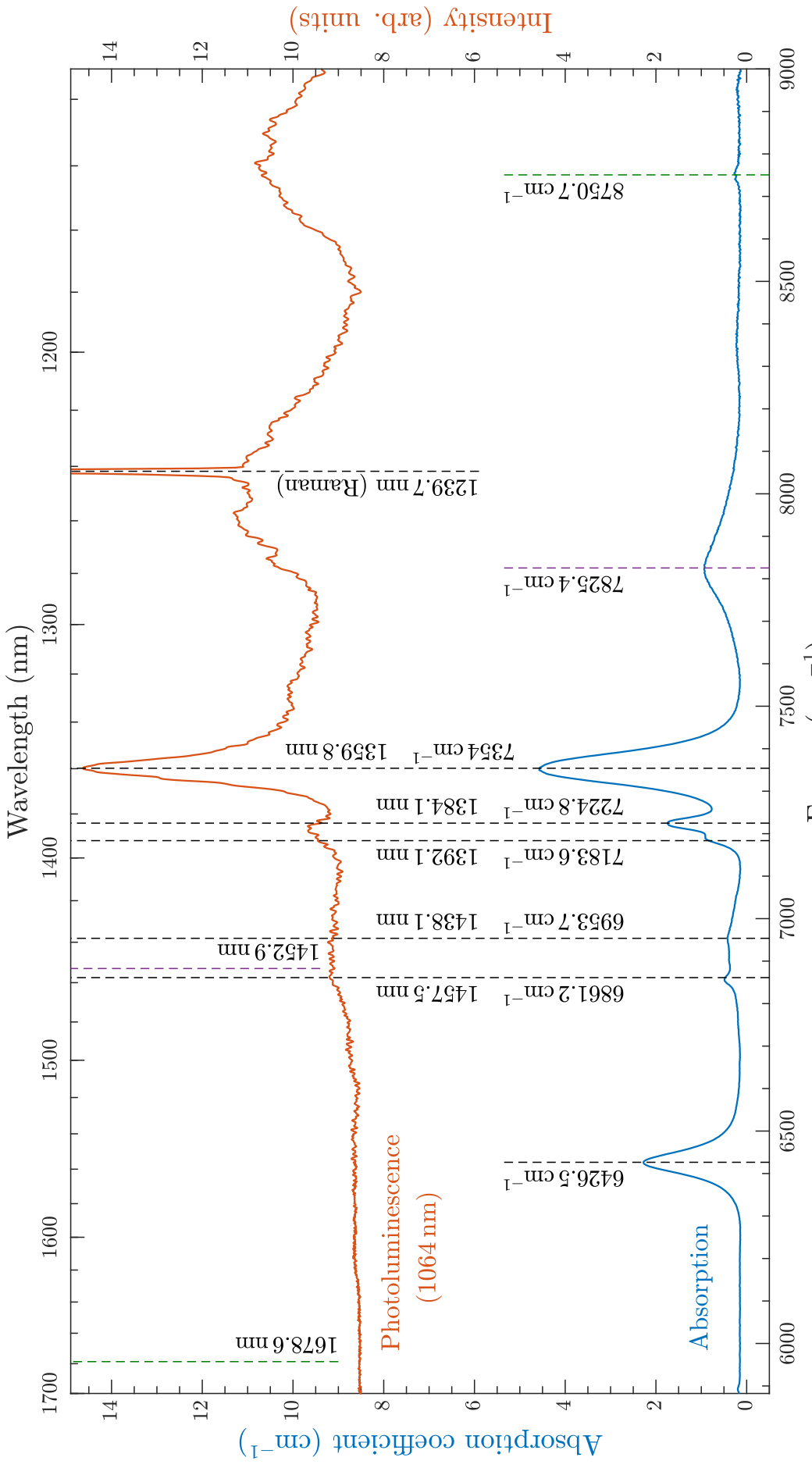

Figure 6-2 Comparison of the 1064 nm photoluminescence (orange, above) and absorption (blue, below) spectra taken at room temperature of the 7354 cm^{-1} system in sample B2. Absorption/emission lines in either spectrum are labelled with a dashed line dissecting at the given wavenumber/wavelength. The pairs of coloured dashed lines (green and purple) show the positions of the local vibrational modes in the absorption spectrum and their corresponding position in the photoluminescence spectrum. Spectra offset for clarity.

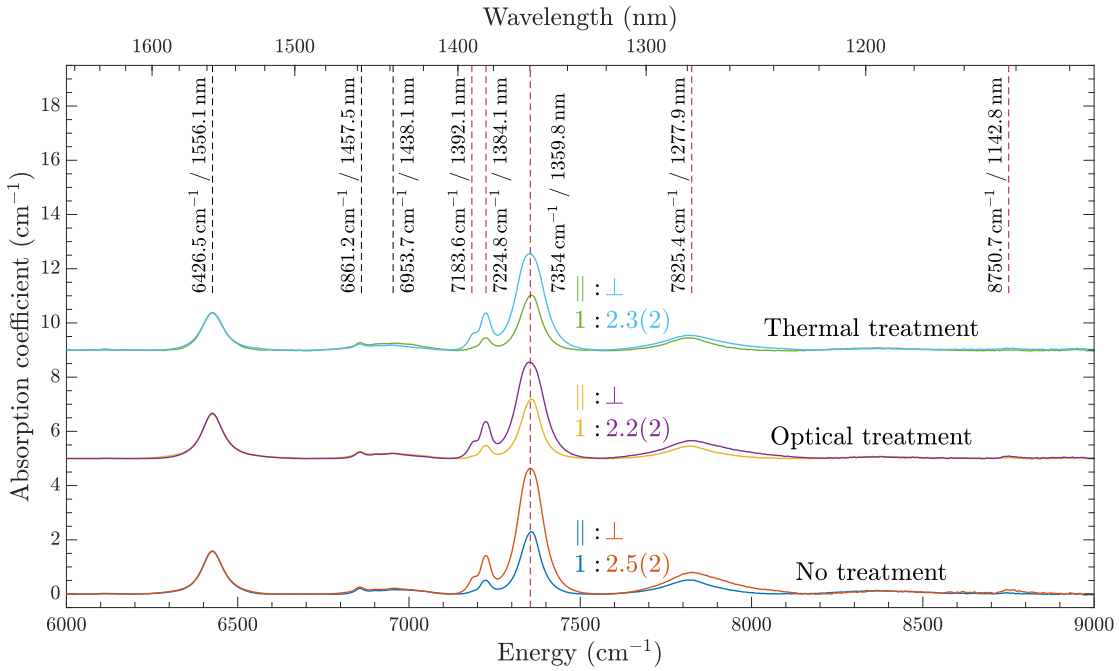

(a) Sample B2

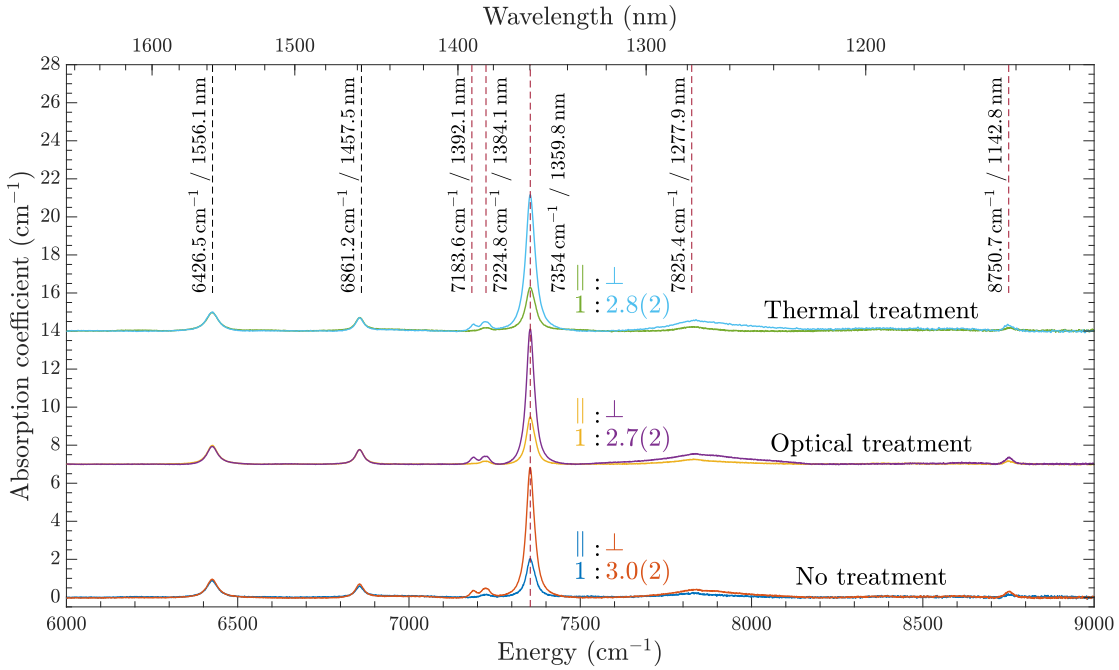

(b) Sample B3

Figure 6-3 IR absorption spectra showing preferential orientation and charge transfer behaviour of the 7354 cm^{-1} system. For (a) Sample B2, and (b) Sample B3, spectra labelled with ∥ indicate incident light polarised parallel to the growth direction (**E** ∥[0 0 1]), whereas spectra labelled with ⊥ indicate incident light polarised perpendicular to the growth direction (**E** ∥[1 1 0]). Additionally, spectra recorded after thermal, optical or no treatment are also indicated. The ratio of integrated intensity of the 7354 cm^{-1} line for ∥:⊥ for each charge transfer state is stated. Red dashed lines indicated lines affected by incident light polarisation. Spectra offset for clarity.

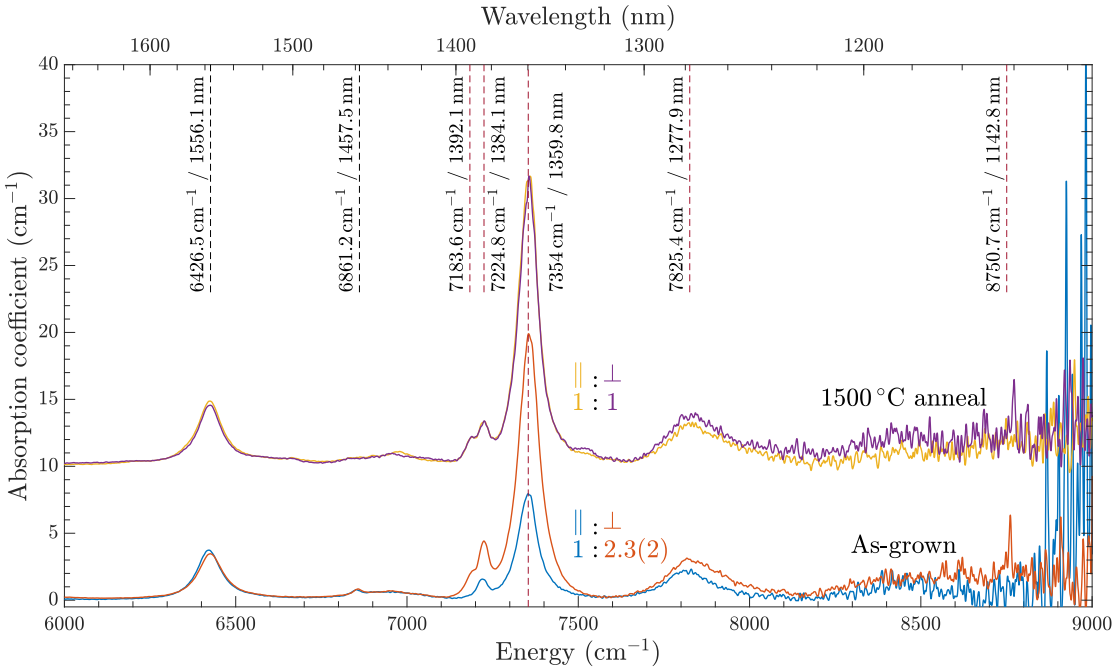

Figure 6-4 IR absorption spectra showing the effect of annealing on the preferential orientation behaviour of the 7354 cm^{-1} system in sample B1a as-grown and after annealing at 1500 °C for 4 h. Spectra offset for clarity.

system in sample B1a in its as-grown state and after annealing at 1500 °C for 4 h. The clear preferential orientation observed in the as-grown sample is removed upon annealing, such that the same intensity of absorption is observed from the 7354 cm^{-1} line with both polarisation directions.

Charge transfer treatments result in much smaller changes to the integrated intensity of the lines, and specifically the 7354 cm^{-1} line (Table 6-2). Sample B2 has approximately the same integrated intensity (within error) of the 7354 cm^{-1} line after optical and thermal charge transfer treatments (regardless of polarisation with respect to growth direction). Sample B3 has a more significant result

Sample	Optical : Thermal	
	∥	⊥
B2	1 : 0.94(5)	1 : 1.00(5)
B3	1 : 1.15(5)	1 : 1.18(5)

Table 6-2 IR absorption integrated intensity ratios of charge transfer treatments of the 7354 cm^{-1} line. Polarisations parallel (∥, where **E** ∥[0 0 1]) and perpendicular (⊥, where **E** ∥[1 1 0]) are with respect to growth direction of the sample.

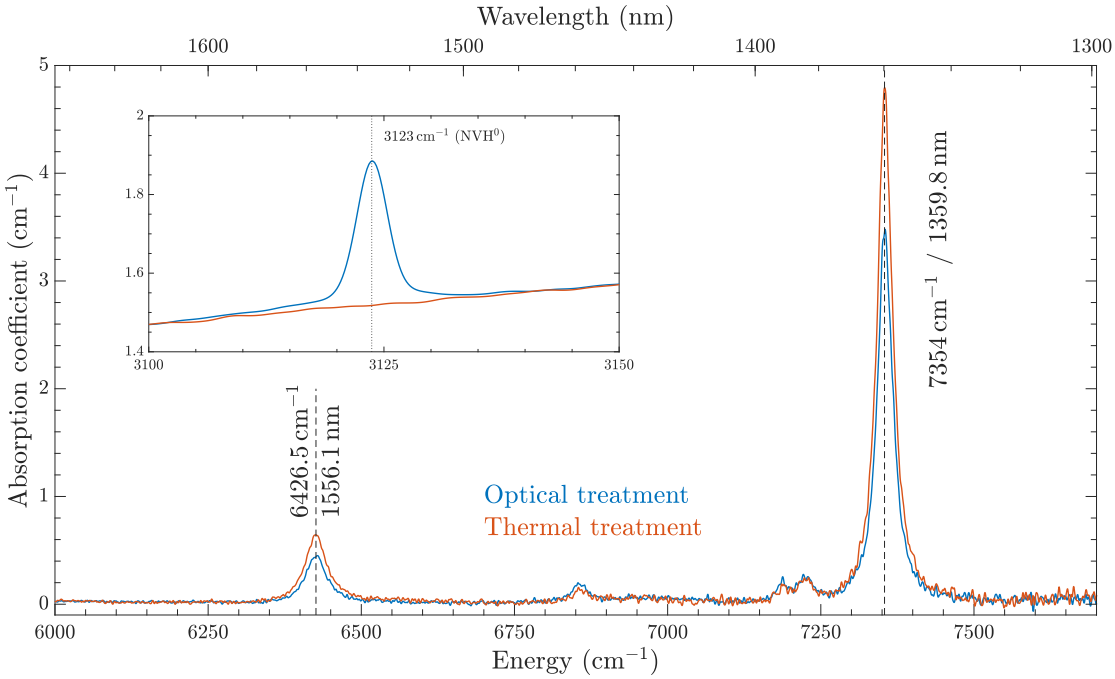

Figure 6-5 IR absorption spectra showing the charge transfer behaviour of the 7354 cm^{-1} line and the NVH^0 line at 3123 cm^{-1} in sample B4.

in that thermal treatment produces an integrated intensity of the 7354 cm^{-1} line of factor 1.15(5)–1.18(5) greater than the optical treatment produces (depending on polarisation with respect to growth direction).

The effect of charge transfer treatment on sample B4 is much more obvious (Figure 6-5). Upon thermal treatment the integrated intensity of the 7354 cm^{-1} line increases to 240(20) cm^{-2}, whilst the intensity of the 3123 cm^{-1} decreases to zero. Conversely, upon optical treatment the integrated intensity of the 7354 cm^{-1} line decreases to 160(20) cm^{-2}, and the concentration of NVH^0 measured is approximated 660(60) ppb (using the 3123 cm^{-1} calibration coefficient of 330(30)ppb cm^{-2} [17]). The 6426.5 cm^{-1} line is exhibiting similar changes of intensity as the 7354 cm^{-1} line during the charge transfer treatments. There are various other line changing in intensity with charge transfer treatments in this sample, such as SiV^0 and SiV$^-$, along with other unknown lines.

6.3.2 Uniaxial stress

The response of the 7354 cm^{-1} line to uniaxial stress, whilst observed by PL, has not been previously reported. The centre that emits at 7354 cm^{-1} demonstrates

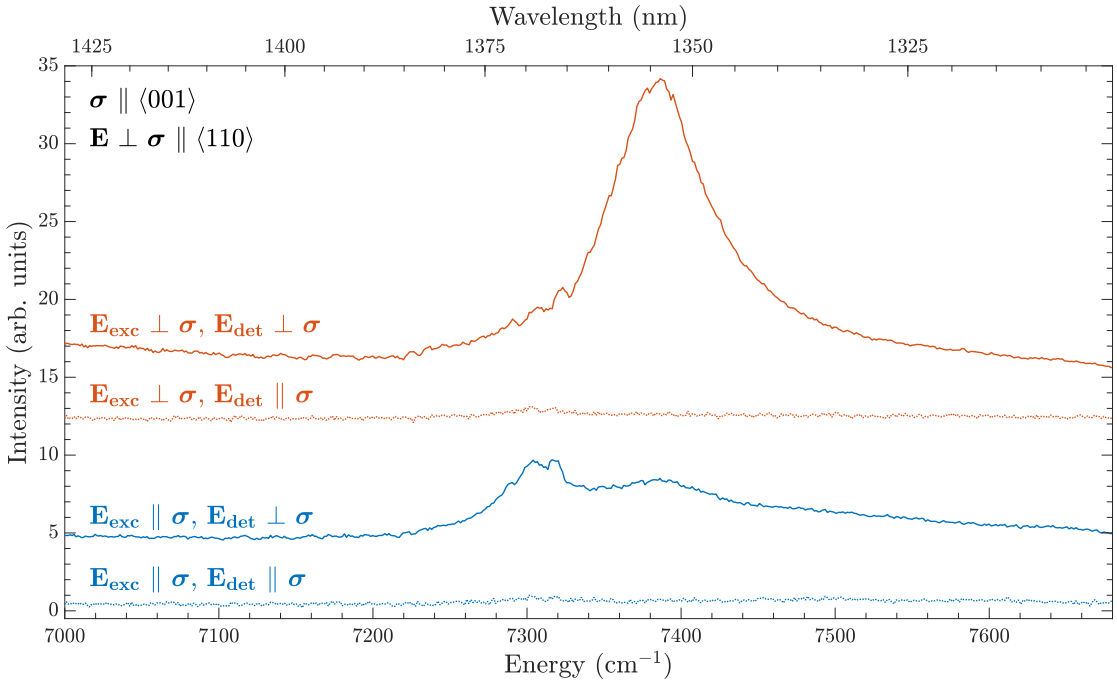

Figure 6-6 Detection polarisation dependence of the 7354 cm^{-1} line in photoluminescence in sample B2. Irrespective of the polarisation of the excitation electric field vector ($\mathbf{E_{exc}}$), significant emission from the 7354 cm^{-1} centre is only observed with the detection polarisation ($\mathbf{E_{det}}$) perpendicular to the stress axis. Data taken with $\boldsymbol{\sigma} \parallel \langle 0\,0\,1 \rangle$ at 3.2 GPa and at a temperature of 80 K. Spectra offset for clarity.

a PL detection polarisation dependence, and is effectively invariant to excitation polarisation. Figure 6-6 shows that under an applied stress of 3.2 GPa along $\langle 0\,0\,1 \rangle$, significant emission is only observed with the detection electric field vector polarised perpendicular to the stress axis. Consequently, only PL spectra with $\mathbf{E_{det}} \perp \boldsymbol{\sigma}$ are presented in the uniaxial stress results of this chapter.

6.3.2.1 Degeneracy of the excited state

As demonstrated by Glover [6] and Cruddace [7], the degeneracy of the ground state of the 7354 cm^{-1} transition line can be investigated by inducing a splitting of the line via uniaxial stress, and then varying the temperature and observing any change in the integrated intensity of the split-out peaks in absorption. Figure 6-7a is a reproduction of the figure in the PhD thesis of Cruddace [7], which demonstrates thermalisation in the IR absorption spectra under uniaxial stress of σ = 2.7 GPa. Note the 30 K and 180 K spectra in the figure by Cruddace [7] are believed to be mislabelled, and so in Figure 6-7a they have been swapped. This

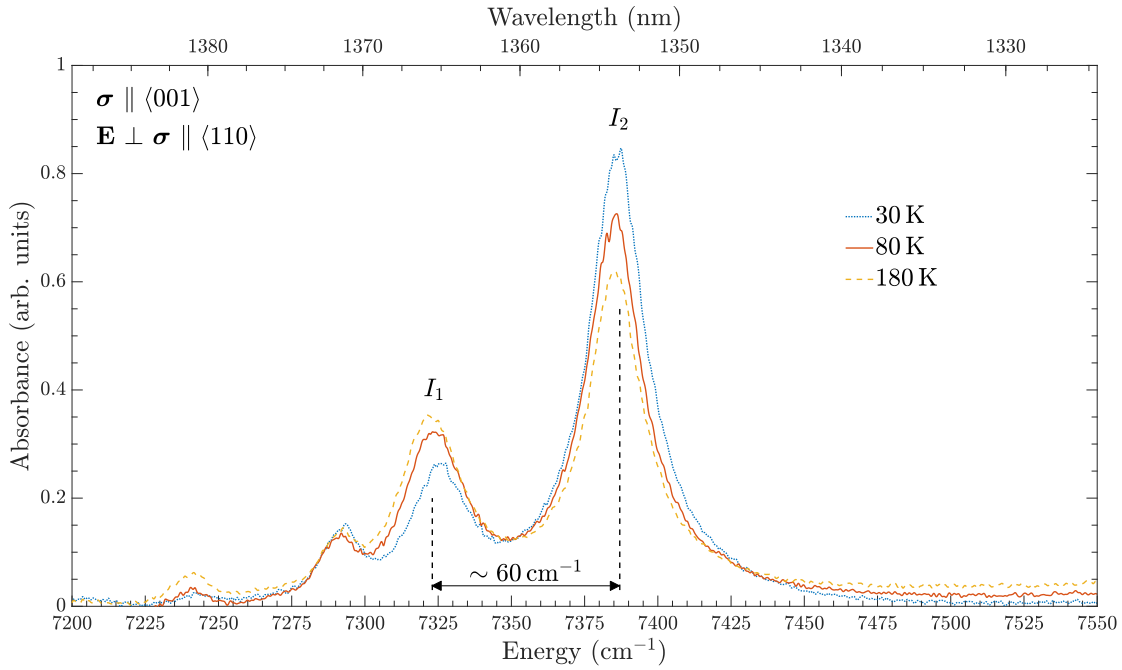

(a) IR absorption spectra

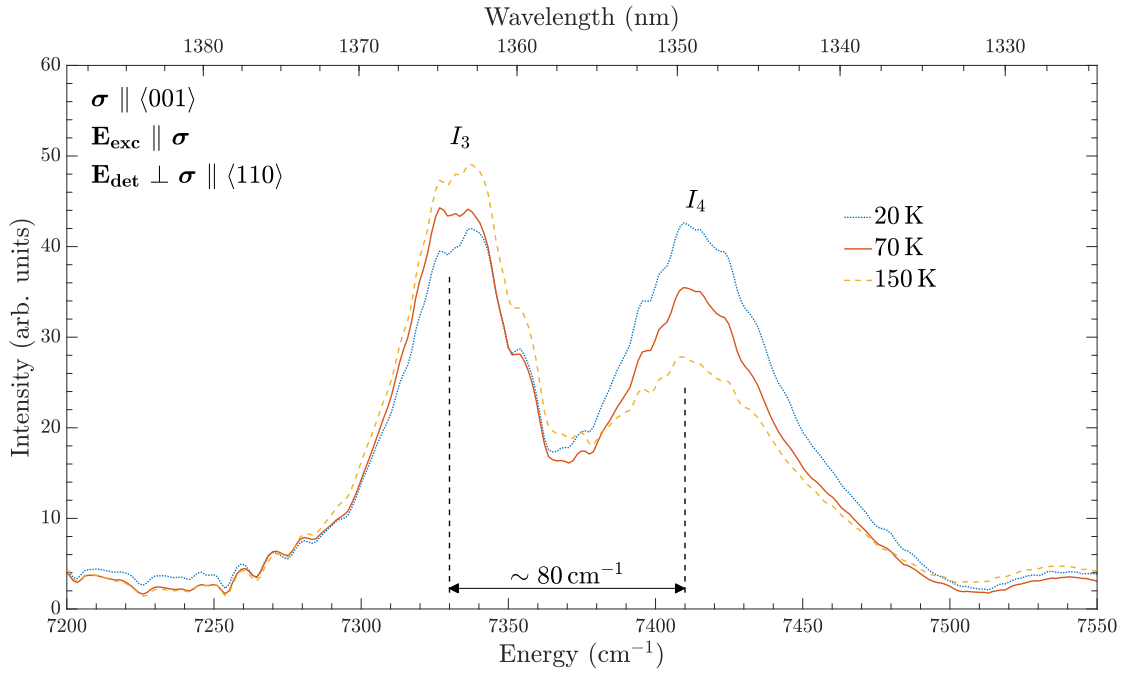

(b) PL spectra

Figure 6-7 Both sets of spectra demonstrate thermalisation between two stress-split lines at a variety of temperatures. (a) IR absorption spectra demonstrating thermalisation in the ground state of the 7354 cm^{-1} line under applied stress σ = 2.7 GPa, between the lines I_1 and I_2. Reproduced from Cruddace [7]. (b) PL spectra of sample B2 demonstrating thermalisation in the excited state of the 7354 cm^{-1} line under applied stress σ = 3.2 GPa, between the lines I_3 and I_4.

investigation led to the result that the ground state of the 7354 cm^{-1} transition line is (at least) a doubly degenerate E state. By changing the optical spectroscopy method from absorption to (1064 nm) photoluminescence, the same methodology and analysis of data can be applied to probe the degeneracy the excited state of the 7354 cm^{-1} transition line.

The excited state of the 7354 cm^{-1} transition line shows similar thermalisation behaviour to that of the ground state. Figure 6-7b shows the thermalisation behaviour of sample B2 under applied stress of σ = 3.2 GPa along $\langle 0\,0\,1\rangle$, when probed with excitation polarisation $\mathbf{E_{exc}} \parallel \langle 0\,0\,1\rangle$ and observed through the detection polarisation $\mathbf{E_{det}} \parallel \langle 1\,1\,0\rangle$. The two lines labelled I_3 and I_4 show simultaneous and opposite changes in intensity as the temperature is varied between 20 K, 70 K and 150 K. With this result, the excited state can now also be labelled as (at least) a doubly degenerate E state and therefore the 7354 cm^{-1} line is (at least) an $E \leftrightarrow E$ transition. Furthermore, the intensity changes are consistent between the IR absorption and PL spectra, as the lower energy lines (I_1 and I_3) decrease in intensity with a reduction of temperature whilst the higher energy lines (I_2 and I_4) increase in intensity with a reduction of temperature.

The thermalisation behaviour can be described using a partition function model with intensity I described as

$$I = A \exp\left(-\frac{E_{\text{level}}}{k_B T}\right), \tag{6-1}$$

where the constant A relates the number of absorbing centres to the absorption strength, E_{level} is the energy of the level, k_B is the Boltzmann constant in the relevant units (cm^{-1} in this chapter), and T is the temperature. Once the integrated intensities of I_3 and I_4 (at each temperature measured) are determined by fitting the spectra, their changing intensities may be independently modelled by equation (6-1), as shown in Figure 6-8a.

Further information about the system may be calculated by comparing the two sets of data. The energy separation between the two levels of the excited E state, ΔE, can be parameterised by the ratio of the two partition functions:

$$\frac{I_4}{I_3} = B \exp\left(-\frac{\Delta E}{k_B T}\right), \tag{6-2}$$

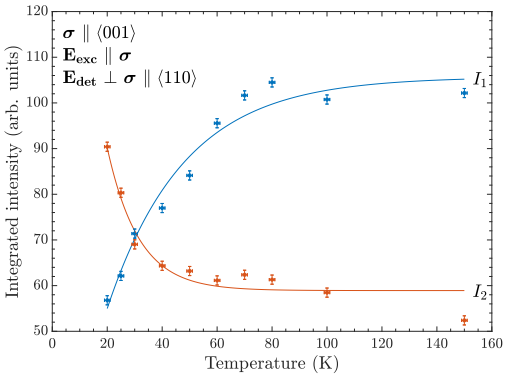

(a) Integrated intensities of stress split lines I_3 and I_4 varying with temperature. The curves through each data set are fits using a standard partition function model.

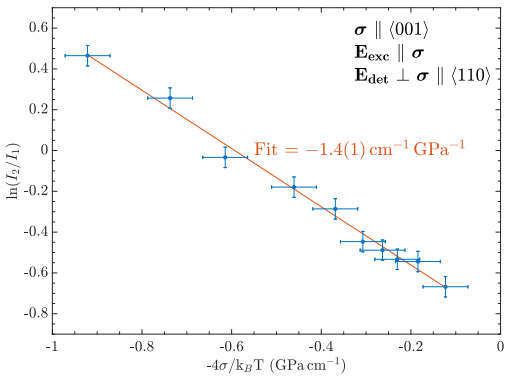

(b) The ratio of intensities of the stress split lines I_3 and I_4, as a function of reciprocal temperature. The data has a linear fit of gradient $-1.4(1)\,\mathrm{cm}^{-1}\,\mathrm{GPa}^{-1}$ = B^e, the stress splitting parameter.

Figure 6-8 (a) and (b) represent analysis of 1064 nm PL spectra of sample B2 under applied stress σ = 3.2 GPa, but varying temperature.

where B is the ratio of original partition function constants (A_4/A_3). For $\boldsymbol{\sigma} \parallel \langle 0\,0\,1\rangle$, the basis functions of the degenerate excited state (θ^e/ϵ^e) of an $E \leftrightarrow E$ transition at a trigonal centre are $\theta^e : A_1^e + 2B^e$ and $\epsilon^e : A_1^e - 2B^e$ [18], where A_1^e and B^e are piezospectroscopic parameters that describe the response of the levels to applied stress (also given later in Table 6-3). Under a given value of applied stress (σ), the energy separation between the two levels may be described as

$$\Delta E = |\theta^e - \epsilon^e|\sigma = 4B^e\sigma\,. \tag{6-3}$$

Substitution of equation (6-3) into equation (6-2), followed by rearrangement, allows for the ratio of intensities of the two degenerate excited state energy levels to be described linearly as a function of stress and reciprocal temperature (where C is a constant):

$$\ln\left(\frac{I_4}{I_3}\right) = \frac{-4\sigma}{k_B T}B^e + C\,. \tag{6-4}$$

Figure 6-8b shows the thermalisation data plotted in the form of equation (6-4). As stress was kept constant at 3.2 GPa, the gradient of the line only represents the value of the parameter: $B^e = -1.4(1)\,\mathrm{cm}^{-1}\,\mathrm{GPa}^{-1}$.

A similar procedure conducted by Cruddace [7] with the data in Figure 6-7a found the value of the parameter $B^g = 2.2(1)\,\mathrm{cm}^{-1}\,\mathrm{GPa}^{-1}$, which similar to B^e describes the energy separation response of the ground E state to applied stress. In fact,

ΔE for the ground state has the same form as equation (6-3), except that B^e is replaced by B^g. Thus, the energy separation of both the ground (ΔE_{GS}) and excited (ΔE_{ES}) state under any applied stress may now be given as

$$\begin{aligned} \Delta E_{\mathrm{GS}}(\mathrm{cm}^{-1}) &= 4 \times 2.2(1) \times \sigma(\mathrm{GPa}) \,, \\ \Delta E_{\mathrm{ES}}(\mathrm{cm}^{-1}) &= 4 \times 1.4(1) \times \sigma(\mathrm{GPa}) \,. \end{aligned} \tag{6-5}$$

6.3.2.2 Trigonal centre with an $E \leftrightarrow E$ transition

Uniaxial stress along stress axes $\langle 0\,0\,1 \rangle$ and $\langle 1\,1\,0 \rangle$ has been utilised during both FTIR absorption and photoluminescence measurements. For $\boldsymbol{\sigma} \parallel \langle 1\,1\,0 \rangle$, the direction perpendicular to the stress axis for absorption measurements is $\langle 0\,0\,1 \rangle$ whilst for the PL measurements the direction is $\langle 1\,\bar{1}\,0 \rangle$.

Figure 6-9 shows the absorption spectra ((a) and (b)) and PL spectra ((c) and (d)) of the 7354 cm^{-1} line with no stress applied and under applied stress along $\langle 0\,0\,1 \rangle$ and $\langle 1\,1\,0 \rangle$ at 3.2 GPa. Two spectra are supplied for each stress pressure in each subplot that corresponds to parallel (blue) and perpendicular (orange) electric field vector polarisations. The black lines that correspond to predicted energies and intensities of stress-split lines will be address later in this section of results.

The spectra have been fitted to extract the energy of each stress-split component from the range of spectra acquired during the experiments. Due to the large linewidths of the majority of stress-split lines, deconvolution of stress-split components could only be confidently achieved from the relatively high stress spectra. The energy shifts of these components from the 7354 cm^{-1} line are presented in Figure 6-10, where the layout of the subplots matches that in Figure 6-9. Given the investigations of Glover [6] and Cruddace [7] that suggest the 7354 cm^{-1} centre is of trigonal symmetry with a degenerate E ground state, and the thermalistion behaviour in §6.3.2.1 indicating the excited state also has E degeneracy, the stress split lines were subject to a least squares fit to a trigonal $E \leftrightarrow E$ model.

The stress-induced shifts and splittings for an $E \leftrightarrow E$ transition at a trigonal centre are given in Table 6-3, along with the intensities in absorption; intensities in luminescence are given in Table 6-4. The simultaneous degeneracy of the ground

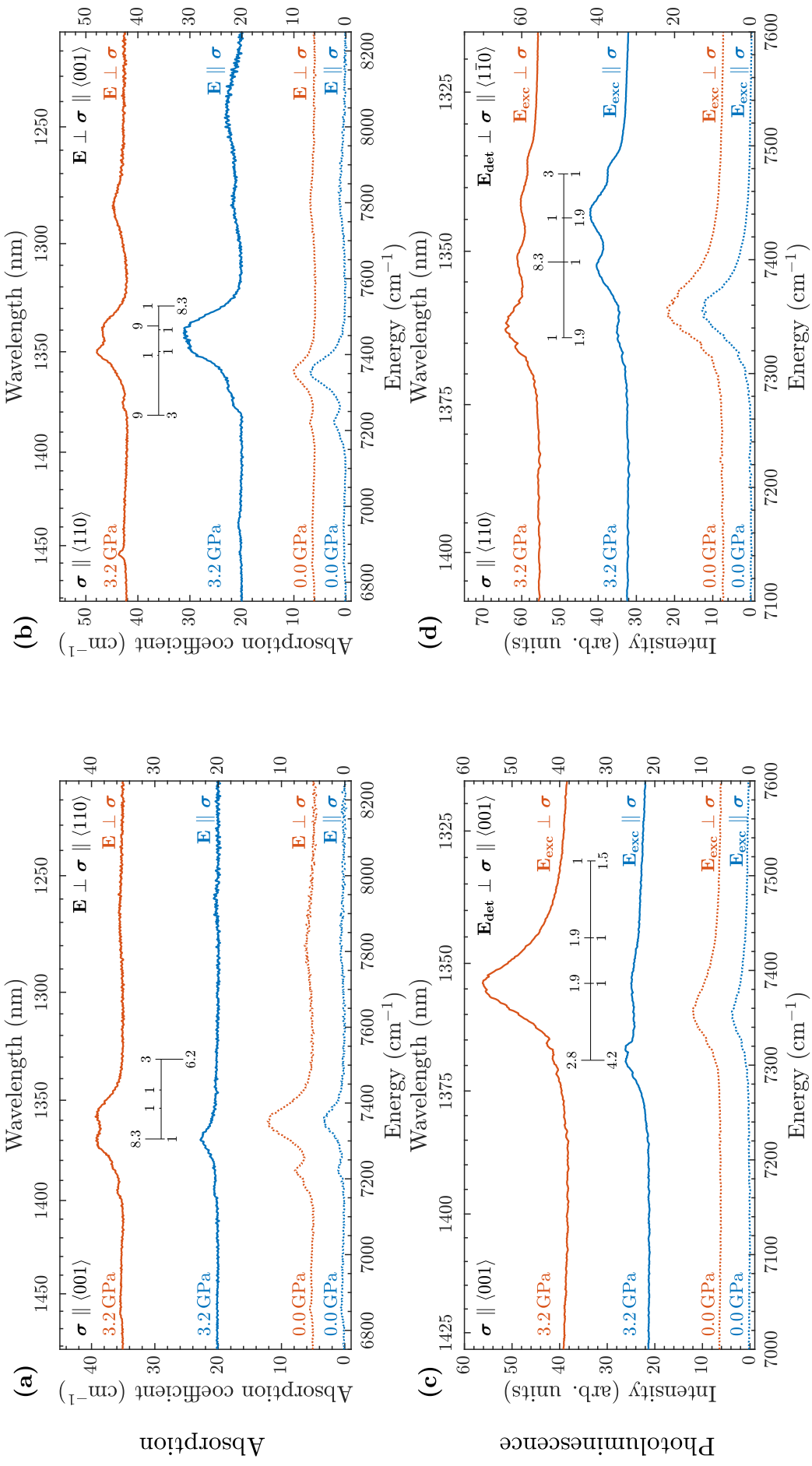

Figure 6-9 Uniaxial stress spectra in absorption and photoluminescence. (a) Sample B1a, (b) sample B1b, and (c) and (d) sample B2. Electric field vector directions (**E**) are given as parallel or perpendicular ($\parallel$ or $\perp$) to the stress axis $\boldsymbol{\sigma}$. All spectra were measured at 80 K at either 0.0 GPa or 3.2 GPa. Theoretical positions of stress split peaks for an $E \leftrightarrow E$ transition at a trigonal centre are shown via vertical black lines labelled with the relative magnitude. Lines below (above) the horizontal line indicated parallel (perpendicular) to the stress direction. Spectra offset for clarity.

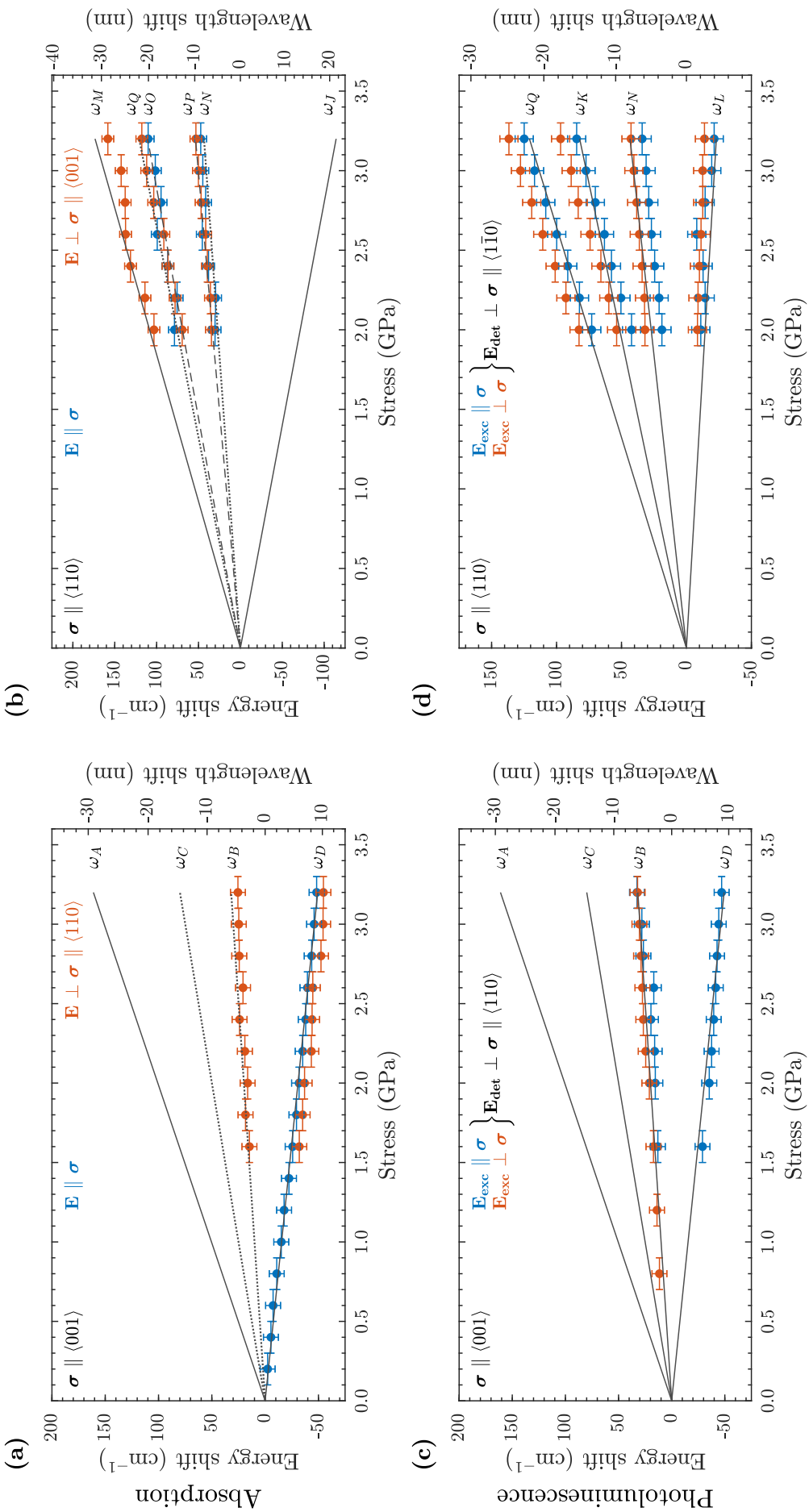

Figure 6-10 Uniaxial stress splitting in absorption and photoluminescence. (a) Sample B1a, (b) sample B1b, and (c) and (d) sample B2. Electric field vector directions ($\mathbf{E}$ for absorption, $\mathbf{E}_{\mathbf{exc}}$ and $\mathbf{E}_{\mathbf{det}}$ for photoluminescence) are given as parallel or perpendicular ($\parallel$ or $\perp$) to the stress axis $\boldsymbol{\sigma}$. Theoretical fits to the data (black lines) and labels are given for an $E \leftrightarrow E$ transition at a trigonal centre using parameters in Tables 6-3. Dashed (dotted) lines indicate a transition only visible when parallel (perpendicular) to the stress direction. Solid lines indicate a transition visible in both polarisations.

Stress axis	Ground state	Excited state	Energy shift	Intensity in absorption		
				$\mathbf{E} \parallel \boldsymbol{\sigma}$	$\mathbf{E} \perp \boldsymbol{\sigma}$	
$\langle 0\,0\,1 \rangle$	$\theta^g : A_1^g + 2B^g$	$\theta^e : A_1^e + 2B^e$	$(\theta^e - \theta^g)\sigma = \omega_A$	$(2D + \sqrt{2}d)^2$	$(\sqrt{2}d - D)^2$	
		$\epsilon^e : A_1^e - 2B^e$	$(\epsilon^e - \theta^g)\sigma = \omega_B$	0	$3D^2$	
	$\epsilon^g : A_1^g - 2B^g$	$\theta^e : A_1^e + 2B^e$	$(\theta^e - \epsilon^g)\sigma = \omega_C$	0	$3D^2$	
		$\epsilon^e : A_1^e - 2B^e$	$(\epsilon^e - \epsilon^g)\sigma = \omega_D$	$(2D - \sqrt{2}d)^2$	$(\sqrt{2}d + D)^2$	
$\langle 1\,1\,1 \rangle$	$\begin{matrix}\theta^g \\ \epsilon^g\end{matrix} : A_1^g + 2A_2^g$	$\begin{matrix}\theta^e \\ \epsilon^e\end{matrix} : A_1^e + 2A_2^e$	$\begin{bmatrix}\theta^e & \theta^g \\ \epsilon^e & \epsilon^g\end{bmatrix}\sigma = \omega_E$	$2d^2$	$2D^2$	
	$\theta^g : A_1^g - \frac{2}{3}A_2^g + \frac{4}{3}C^g$	$\theta^e : A_1^e - \frac{2}{3}A_2^e + \frac{4}{3}C^e$	$(\theta^e - \theta^g)\sigma = \omega_F$	$(\sqrt{8/3}D - \sqrt{1/3}d)^2$	$(\sqrt{1/6}D + \sqrt{4/3}d)^2$	
		$\epsilon^e : A_1^e - \frac{2}{3}A_2^e - \frac{4}{3}C^e$	$(\epsilon^e - \theta^g)\sigma = \omega_G$	0	$3D^2/2$	
	$\epsilon^g : A_1^g - \frac{2}{3}A_2^g - \frac{4}{3}C^g$	$\theta^e : A_1^e - \frac{2}{3}A_2^e + \frac{4}{3}C^e$	$(\theta^e - \epsilon^g)\sigma = \omega_H$	0	$3D^2/2$	
		$\epsilon^e : A_1^e - \frac{2}{3}A_2^e - \frac{4}{3}C^e$	$(\epsilon^e - \epsilon^g)\sigma = \omega_I$	$(\sqrt{8/3}D + \sqrt{1/3}d)^2$	$(\sqrt{1/6}D - \sqrt{4/3}d)^2$	
$\langle 1\,1\,0 \rangle$					$\mathbf{E} \parallel \langle 1\,\bar{1}\,0 \rangle$	$\mathbf{E} \parallel \langle 0\,0\,1 \rangle$
	$\theta^g : A_1^g + A_2^g - B^g + C^g$	$\theta^e : A_1^e + A_2^e - B^e + C^e$	$(\theta^e - \theta^g)\sigma = \omega_J$	$(\sqrt{2}D - 2d)^2$	0	$(2D + \sqrt{2}d)^2$
		$\epsilon^e : A_1^e + A_2^e + B^e - C^e$	$(\epsilon^e - \theta^g)\sigma = \omega_K$	0	$6D^2$	0
	$\epsilon^g : A_1^g + A_2^g + B^g - C^g$	$\theta^e : A_1^e + A_2^e - B^e + C^e$	$(\theta^e - \epsilon^g)\sigma = \omega_L$	0	$6D^2$	0
		$\epsilon^e : A_1^e + A_2^e + B^e - C^e$	$(\epsilon^e - \epsilon^g)\sigma = \omega_M$	$(\sqrt{2}D + 2d)^2$	0	$(2D - \sqrt{2}d)^2$
	$\epsilon^g : A_1^g - A_2^g + B^g + C^g$	$\epsilon^e : A_1^e - A_2^e + B^e + C^e$	$(\epsilon^e - \epsilon^g)\sigma = \omega_N$	0	$(\sqrt{2}D + 2d)^2$	$(2D - \sqrt{2}d)^2$
		$\theta^e : A_1^e - A_2^e - B^e - C^e$	$(\theta^e - \epsilon^g)\sigma = \omega_O$	$6D^2$	0	0
	$\theta^g : A_1^g - A_2^g - B^g - C^g$	$\epsilon^e : A_1^e - A_2^e + B^e + C^e$	$(\epsilon^e - \theta^g)\sigma = \omega_P$	$6D^2$	0	0
		$\theta^e : A_1^e - A_2^e - B^e - C^e$	$(\theta^e - \theta^g)\sigma = \omega_Q$	0	$(\sqrt{2}D - 2d)^2$	$(2D + \sqrt{2}d)^2$

Table 6-3 Stress-induced shifts, splittings and intensities in absorption for an $E \leftrightarrow E$ transition at a trigonal centre. For each stress axis direction, the degenerate (θ/ϵ) basis functions for the ground (g) and excited (e) states are given along with the stress-induced (σ) energy shift equations of all possible transitions (ω_X). The relative intensities of transitions in absorption are given with electric vector $\mathbf{E}$ parallel or perpendicular ($\parallel$ or $\perp$) to the stress axis ($\boldsymbol{\sigma}$) direction (or the specific directions given for $\boldsymbol{\sigma} \parallel \langle 1\,1\,0 \rangle$). Table adapted from [18] and [19].

Stress axis	Energy shift	Intensity in luminescence			
		$\mathbf{E_{exc}} \parallel \boldsymbol{\sigma}$		$\mathbf{E_{exc}} \perp \boldsymbol{\sigma}$	
		$\mathbf{E_{det}} \parallel \boldsymbol{\sigma}$	$\mathbf{E_{det}} \perp \boldsymbol{\sigma}$	$\mathbf{E_{det}} \parallel \boldsymbol{\sigma}$	$\mathbf{E_{det}} \perp \boldsymbol{\sigma}$
$\langle 0\,0\,1\rangle$	ω_A	$\frac{4}{9}(2D+\sqrt{2}d)^2(2D^2+d^2)$	$\frac{2}{9}(\sqrt{2}d-D)^2(2D^2+d^2)$	$\frac{4}{9}(2D+\sqrt{2}d)^2(2D^2+d^2)$	$\frac{2}{3}D^2(\sqrt{2}D-2d)^2$
	ω_B	0	$\frac{4}{3}D^2(2D^2+d^2)^2$	0	$\frac{4}{3}D^2(D^2+2d^2)^2$
	ω_C	0	$\frac{4}{3}D^2(2D^2+d^2)^2$	0	$\frac{4}{3}D^2(D^2+2d^2)^2$
	ω_D	$\frac{4}{9}(2D-\sqrt{2}d)^2(2D^2+d^2)$	$\frac{2}{9}(\sqrt{2}d+D)^2(2D^2+d^2)$	$\frac{4}{9}(2D-\sqrt{2}d)^2(2D^2+d^2)$	$\frac{2}{3}D^2(\sqrt{2}D+2d)^2$
$\langle 1\,1\,1\rangle$	ω_E	$4d^4$	$4D^4d^2$	$4D^2d^2$	$4D^4$
	ω_F	$\frac{2}{9}(\sqrt{8/3}D-\sqrt{1/3}d)^2(8D^2+d^2)$	$\frac{1}{27}(D+2\sqrt{2}d)^2(8D^2+d^2)$	$\frac{2}{9}(\sqrt{8/3}D-\sqrt{1/3}d)^2(5D^2+4d^2)$	$\frac{1}{27}(D+2\sqrt{2}d)^2(7D^2+2d^2)$
	ω_G	0	$\frac{1}{3}D^2(8D^2+d^2)$	0	$D^2(D^2+2d^2)$
	ω_H	0	$\frac{1}{3}D^2(8D^2+d^2)$	0	$D^2(D^2+2d^2)$
	ω_I	$\frac{2}{9}(\sqrt{8/3}D+\sqrt{1/3}d)^2(8D^2+d^2)$	$\frac{1}{27}(D-2\sqrt{2}d)^2(8D^2+d^2)$	$\frac{2}{9}(\sqrt{8/3}D+\sqrt{1/3}d)^2(5D^2+4d^2)$	$\frac{1}{27}(D-2\sqrt{2}d)^2(7D^2+2d^2)$
			$\mathbf{E_{det}} \parallel \langle 1\bar{1}0\rangle$	$\mathbf{E_{det}} \parallel \langle 0\,0\,1\rangle$		$\mathbf{E_{det}} \parallel \langle 1\bar{1}0\rangle$	$\mathbf{E_{det}} \parallel \langle 0\,0\,1\rangle$
$\langle 1\,1\,0\rangle$	ω_J	$\frac{2}{9}(\sqrt{2}D-2d)^2(D^2+2d^2)$	0	$\frac{2}{9}(2D+\sqrt{2}d)^2(D^2+2d^2)$	$\frac{2}{3}D^2(\sqrt{2}D-2d)^2$	0	$\frac{2}{3}D^2(2D+\sqrt{2}d)^2$
	ω_K	0	$\frac{4}{3}D^2(D^2+2d^2)$	0	0	$\frac{4}{3}D^2(2D^2+d^2)$	0
	ω_L	0	$\frac{4}{3}D^2(D^2+2d^2)$	0	0	$\frac{4}{3}D^2(2D^2+d^2)$	0
	ω_M	$\frac{2}{9}(\sqrt{2}D+2d)^2(D^2+2d^2)$	0	$\frac{2}{9}(2D-\sqrt{2}d)^2(D^2+2d^2)$	$\frac{2}{3}D^2(\sqrt{2}D+2d)^2$	0	$\frac{2}{3}D^2(2D-\sqrt{2}d)^2$
	ω_N	0	$\frac{2}{3}D^2(\sqrt{2}D+2d)^2$	$\frac{2}{3}D^2(2D-\sqrt{2}d)^2$	0	$\frac{2}{9}(\sqrt{2}D+2d)^2(2D^2+d^2)$	$\frac{2}{9}(2D-\sqrt{2}d)^2(D^2+2d^2)$
	ω_O	$4D^4$	0	0	$\frac{4}{3}D^2(D+2d^2)$	0	0
	ω_P	$4D^4$	0	0	$\frac{4}{3}D^2(D+2d^2)$	0	0
	ω_Q	0	$\frac{2}{3}D^2(\sqrt{2}D-2d)^2$	$\frac{2}{3}D^2(2D+\sqrt{2}d)^2$	0	$\frac{2}{9}(\sqrt{2}D-2d)^2(2D^2+d^2)$	$\frac{2}{9}(2D+\sqrt{2}d)^2(D^2+2d^2)$

Table 6-4 Stress-induced intensities in luminescence for an $E \leftrightarrow E$ transition at a trigonal centre. Extended from Table 6-3, for each stress axis direction and stress-induced energy shift equation of all possible transitions (ω_X), the relative intensities of transitions in luminescence are given. The electric vector ($\mathbf{E_{exc}}$) of exciting light and the polarised electric vector ($\mathbf{E_{det}}$) of the detected luminescence is parallel or perpendicular ($\parallel$ or $\perp$) to the stress axis ($\boldsymbol{\sigma}$) direction (or the specific directions given for $\boldsymbol{\sigma} \parallel \langle 1\,1\,0\rangle$). For $\boldsymbol{\sigma} \parallel \langle 1\,1\,0\rangle$, the intensities given for $\mathbf{E_{det}} \parallel \boldsymbol{\sigma}$ are valid for $\mathbf{E_{exc}} \parallel \langle 1\bar{1}0\rangle$; for $\mathbf{E_{exc}} \parallel \langle 0\,0\,1\rangle$ replace $\frac{2}{3}D^2(\sqrt{2}D \pm 2d)^2$ with $\frac{2}{9}(2D^2+d^2)^2(\sqrt{2}D \pm 2d)^2$. Table adapted from [19].

$A_1^e - A_1^g$	A_2^g	A_2^e	B^g	B^e	C^g	C^e	d/D $(D \neq 0)$
17.5	4.1	−4.1	∓10.1	±6.4	±20.6	∓7.9	$\mp 2\sqrt{2}$

Table 6-5 Experimentally determined values of piezospectroscopic parameters from fitting the 7354 cm^{-1} line as an $E \leftrightarrow E$ transition at a trigonal center. Parameters are given in units of cm^{-1} GPa^{-1}, except for the dimensionless d/D parameter. The sign of some parameters are undetermined since changing between the two sets of signs produces the same stress splitting pattern [20].

and excited states results in up to four transitions for $\boldsymbol{\sigma} \parallel \langle 0\,0\,1 \rangle$ and up to eight transitions for $\boldsymbol{\sigma} \parallel \langle 1\,1\,0 \rangle$, all of which are labelled as ω_X, where X is a letter from A–Q. As there are more possible transitions than observed transitions, the initial challenge is to assign the correct ω_X transition(s) to the correct stress split component. Even once discounting the transitions that have zero intensity for a given stress axis and polarisation, there are still ~10^8 combinations of matching the transitions to the observed stress split components across all the data sets.

To avoid the computational bottleneck this may cause by trying to simultaneously fit all of the data sets, the computation was performed in stages and independently for absorption and PL. Initially, the data set of the stress axis with the most transitions, $\boldsymbol{\sigma} \parallel \langle 1\,1\,0 \rangle$, was subject to a least squares fit for all combinations of matching transitions to components. Based on the quality of the fit, the best N (typically $N < 200$) combinations were chosen. The data for $\boldsymbol{\sigma} \parallel \langle 1\,1\,0 \rangle$ and $\boldsymbol{\sigma} \parallel \langle 0\,0\,1 \rangle$ were then simultaneously subject to a least squares fit, using all combinations of matches for $\boldsymbol{\sigma} \parallel \langle 0\,0\,1 \rangle$ but only the N subset of combination for $\boldsymbol{\sigma} \parallel \langle 1\,1\,0 \rangle$. Again, based on the quality of the fits, the best N combinations were chosen for the absorption and PL data sets. A final least squares fit was performed on the combined data sets of absorption and PL, using the two subsets of combinations to find the best set of transitions that match the stress split components. This process produced a good fit of the stress split components and the experimentally determined values of the piezospectroscopic parameters are given in Table 6-5.

A fit of the data was found by not constraining the B^e parameter to the value of 1.4(1) cm^{-1} GPa^{-1} measured in §6.3.2.1, or the B^g parameter to the value of 2.2(1) cm^{-1} GPa^{-1} as measured by Cruddace [7]. All possible permutations of which parameters to constrain were tested: fit with only B^e constrained, fit with

Technique	$\boldsymbol{\sigma} \parallel \langle 0\,0\,1 \rangle$		$\boldsymbol{\sigma} \parallel \langle 1\,1\,0 \rangle$	
	$\mathbf{E} \parallel \boldsymbol{\sigma}$	$\mathbf{E} \perp \boldsymbol{\sigma}$	$\mathbf{E} \parallel \boldsymbol{\sigma}$	$\mathbf{E} \perp \boldsymbol{\sigma}$
Absorption	$\omega_A = 0 \Rightarrow {}^{d}/_{D} = -\sqrt{2}$	$\omega_A = 0 \Rightarrow {}^{d}/_{D} = {}^{1}/_{\sqrt{2}}$ $\omega_C = 0 \Rightarrow D = 0$	$\omega_J = 0 \Rightarrow {}^{d}/_{D} = {}^{1}/_{\sqrt{2}}$	$\omega_J = 0 \Rightarrow {}^{d}/_{D} = -\sqrt{2}$
PL	$\omega_A = 0 \Rightarrow {}^{d}/_{D} = -\sqrt{2}$ $\omega_C = 0 \Rightarrow D = 0$	$\omega_A = 0 \Rightarrow {}^{d}/_{D} = {}^{1}/_{\sqrt{2}}$ $\omega_C = 0 \Rightarrow D = 0$	All lines observed	

Table 6-6 Deduced values for parameters d and D required to predict the intensities of transitions not observed in the experimental data in Figure 6-10 as zero by considering the intensity equations in Tables 6-3 and 6-4 for absorption and luminescence, respectively.

only B^g constrained, and fit with both B^e and B^g constrained—they all produced extremely poor fits of the data and are therefore not presented.

An accurate value of the d/D parameter, that contains the two parameters of d and D that predict the intensity of stress-split transitions, could not be found. The value given $(2\sqrt{2})$ was chosen such that a non-zero intensity is predicted for all observed transitions, at the expense of predicting intensity for unobserved transitions and predicting the relative intensities incorrectly.

A careful comparison between the experimental data in Figure 6-10 and the intensity equations in Tables 6-3 and 6-4 results in contradictory deductions for the values of d and D. For every transition that is not observed and has a non-zero intensity equation, the value of d and D required for the intensity equation to equal zero, is given in Table 6-6. As an example, transition ω_A is not observed in either polarisation for $\boldsymbol{\sigma} \parallel \langle 0\,0\,1 \rangle$ during absorption measurements, but in order for the transition to not be observed when $\mathbf{E} \parallel \boldsymbol{\sigma}$, $d/D = -\sqrt{2}$, and for the transition to not be observed when $\mathbf{E} \perp \boldsymbol{\sigma}$, $d/D = 1/\sqrt{2}$. Similarly contradictory results are also found for transition ω_A for PL measuremnts with $\boldsymbol{\sigma} \parallel \langle 0\,0\,1 \rangle$ and absorption measurements with $\boldsymbol{\sigma} \parallel \langle 1\,1\,0 \rangle$ for transition ω_J. The deduction that $D = 0$ in order for ω_C to not be observed cannot be correct either: if $D = 0$, then several absorptions transitions that are observed, would be expected to have zero intensity (ω_B, ω_O and ω_P); similarly, most PL transitions would have an expected intensity of zero when clearly they are present. No value of d and D can therefore be found that satisfies the intensities for all observed and unobserved transitions. It therefore appears that at least some unobserved transmission are in fact missing

and should be observed, which would also explain why the intensities cannot be accurately predicted either.

6.4 Discussion

6.4.1 Preferential orientation

The data presented in Figures 6-3 and 6-4 provide the first documented evidence of the 7354 cm^{-1} centre exhibiting preferential orientation relative to the growth direction, in samples grown on {0 0 1}-orientated substrates. For all samples with a [0 0 1] growth direction, light polarised along the perpendicular direction of [1 1 0] produces the larger absorption intensity. Furthermore, the preferential orientation can be removed by annealing at a temperature of at least 1500 °C, as demonstrated in Figure 6-4.

As all the samples studied in this chapter have the same growth direction, they cannot inform about the preferential orientation of samples grown on different orientation substrates. However, Chapter 7 reports on the study of sample C1, which was grown on a {1 1 0}-oriented substrate and contains the 7354 cm^{-1} line. The figure demonstrating the preferential behaviour of the 7354 cm^{-1} in sample C1 from that chapter is reproduced here as Figure 6-11. The small as-grown concentration of the 7354 cm^{-1} line in that sample exhibits preferential orientation parallel to the growth direction of [1 1 0] compared to perpendicular direction of [1 $\bar{1}$ 0], at an approximate ratio of 2:1. After the first anneal at 1000 °C (and each subsequent anneal in the annealing study), the 7354 cm^{-1} line no longer exhibits preferential orientation in that sample. It appears that the temperature required to reorientate the defect may be as low as 1000 °C.

Based on the current evidence it appears that, for samples with a [0 0 1] growth direction the intensity of the 7354 cm^{-1} line is larger when light is polarised perpendicular to the growth direction; and for samples with a [1 1 0] growth direction the intensity of the 7354 cm^{-1} line is larger when light is polarised parallel to the growth direction. An attempt can be made to reconcile the preferential orientation results of samples with different growth directions by calculating the relative

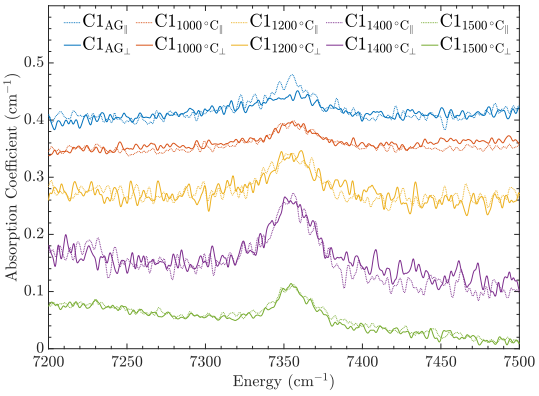

(a)

Figure 6-11 IR absorption spectra showing the preferential orientation behaviour of the 7354 cm^{-1} line in sample C1. ∥ (⊥) indicates parallel (perpendicular) to the growth direction. Reproduced from Figure 7-12b in Chapter 7.

intensities of absorption for each dipole moment relative to the polarisation directions. For linearly polarised light, this can be calculated by $|\mathbf{p} \cdot \mathbf{E}|^2$, where $\mathbf{p}$ is the dipole moment, and $\mathbf{E}$ is a electric field vector of the light. Table 6-4 presents the expected intensities, based on the assumptions that the 7354 cm^{-1} centre has trigonal symmetry (as suggested by the uniaxial stress results) with dipole orientations that are along the $\langle 1\,1\,1 \rangle$ symmetry axes. The intensities suggest that preferential orientation into the $[1\,1\,1]$ and $[\bar{1}\,\bar{1}\,1]$ sites will allow for the preferential behaviour observed in both samples, but care must be taken with this interpretation.

For growth on a $\{1\,1\,0\}$-oriented substrate, this result is consistent with preferential orientation results of other trigonal defects in diamond, where preferential orientation of the two directions that are out-of-plane of the $(1\,1\,0)$ growth surface ($[1\,1\,1]$ and $[\bar{1}\,\bar{1}\,1]$) is observed. Both the nitrogen vacancy (NV) centre with $\mathscr{C}_{3v}$ symmetry [21] and the silicon vacancy (SiV) centre with $\mathscr{D}_{3d}$ symmetry [22] have exhibited this behaviour. Whilst the NV centre can form by a substitutional nitrogen impurity trapping a vacancy, it is believed that the NV centre can also grow in as a unit during CVD growth. A nitrogen atom incorporated into the surface is energetically unlikely to bond to a carbon atom above it due to the N–C antibonding orbital; this increases the probability of creating a vacancy above the nitrogen such that the NV points out of the $(1\,1\,0)$ surface [21]. A similar process is postulated for the creation of SiV centres, that finishes with the silicon atom

Site	Dipole axis	Samples B1-3		Sample C1	
		$\mathbf{E}_{\parallel} = [0\,0\,1]$	$\mathbf{E}_{\perp} = [1\,1\,0]$	$\mathbf{E}_{\parallel} = [1\,1\,0]$	$\mathbf{E}_{\perp} = [1\,\bar{1}\,0]$
1	$[1\,1\,1]$	1/4	1/2	1/2	0
2	$[\bar{1}\,\bar{1}\,1]$	1/4	1/2	1/2	0
3	$[1\,\bar{1}\,\bar{1}]$	1/4	0	0	1/2
4	$[\bar{1}\,1\,\bar{1}]$	1/4	0	0	1/2

Table 6-7 Relative intensities for different sites of a trigonal defect with $\langle 1\,1\,1\rangle$ dipole orientations, with electric field vectors that parallel or perpendicular ($\mathbf{E}_{\parallel}$ or $\mathbf{E}_{\perp}$) to the growth directions of samples B1-3 and C1 (Chapter 7).

relaxing into the more energetically favourable position between its initial lattice position and the vacancy [22]. It is therefore entirely possible that if the 7354 cm^{-1} centre is of trigonal symmetry, it may also grow in as a unit on a $\{1\,1\,0\}$-oriented substrate.

However, for growth on a $\{0\,0\,1\}$-oriented substrate, the result is not consistent for a bulk IR absorption measurement of a potential trigonal defect. It is true that growth on a $\{0\,0\,1\}$-oriented substrate can also preferentially grow the NV centre in the same manner as $\{1\,1\,0\}$-oriented growth, but only locally onto risers that contain $(1\,1\,0)$ facets, which form during the step-flow process of CVD diamond [23]. Other $\{1\,1\,0\}$ facets will preferentially grow different trigonal orientations compared to $(1\,1\,0)$ facets, such that a bulk ensemble measurement will included all of the $\{1\,1\,0\}$ facets (and also other non-$\{1\,1\,0\}$ facets) resulting in an averaged measurement that will not show any preferential orientation.

An example is provided in Figure 6-12, where the step-flow growth process on a $\{0\,0\,1\}$-orientated substrate with $\{0\,1\,1\}$ risers is considered (Figure 6-12a). Relative to the $(0\,\bar{1}\,1)$ riser that is formed, $[\bar{1}\,1\,\bar{1}]$ and $[\bar{1}\,\bar{1}\,1]$ are the out-of-plane orientations (Figure 6-12b), whereas on the $(0\,1\,1)$ riser, the two other orientations of $[\bar{1}\,1\,1]$ and $[1\,1\,1]$ are out-of-plane (Figure 6-12b). Thus, only a local measurement on one of these risers would produce a preferential orientation result, but as inevitably both would be observed in a bulk IR absorption measurement, then the overall result would show no preferential orientation.

The NV centre is also observed to preferentially grow along the $[1\,1\,1]$ direction

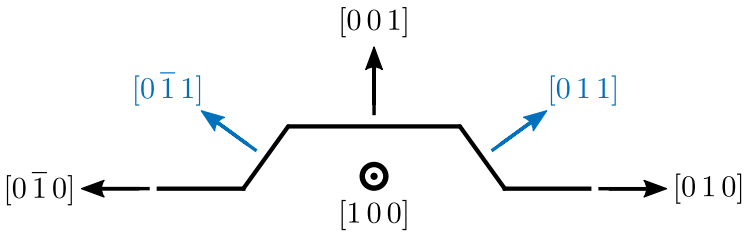

(a) Step-flow growth on a {0 0 1}-oriented substrate, with ⟨0 1 0⟩ layer flow directions and (0 1 1) risers.

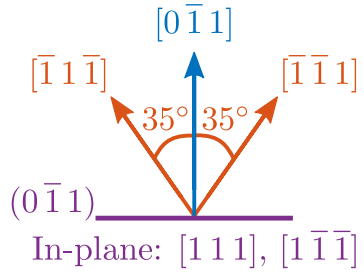

(b) On the (0 $\bar{1}$ 1) riser, the [$\bar{1}$ 1 $\bar{1}$] and [$\bar{1}$ $\bar{1}$ 1] orientations are out-of-plane.

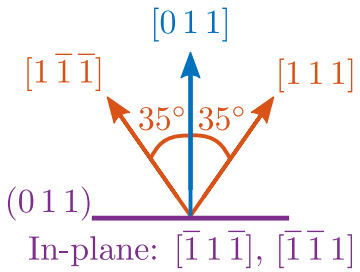

(c) On the (0 1 1) riser, the [1 $\bar{1}$ $\bar{1}$] and [1 1 1] orientations are out-of-plane.

Figure 6-12 Local preferential orientation of a trigonal defect arising from step-flow growth on a {0 0 1}-oriented substrate.

in diamond grown on {1 1 1}-oriented substrates [24], but this has yet to be investigated for the 7354 cm^{-1} centre as no suitable samples are currently available.

The observed "reorientation" behaviour of the 7354 cm^{-1} centre, in sample C1, at a temperature of 1000 °C is lower than the 1300 °C annealing-out temperature of the centre [7]. Other defects in diamond have exhibited similar reorientation to an equilibrium of orientations through annealing, without being annealed-out: the neutral ⟨0 0 1⟩-split self interstitial ($C^0_{I_{001}}$) with $\mathscr{D}_{2d}$ symmetry [25], N^0_S with $\mathscr{C}_{3v}$ symmetry [26], and more recently the NV centre at a temperature of 1050 °C [27, 28]. The exact mechanism for the reorientation of the NV centre is currently unknown, although both authors suggest it is a mobile-vacancy-facilitated process [27, 28].

6.4.2 Charge transfer

Samples B2 and B3 demonstrate little-to-no change in integrated intensity of the 7354 cm^{-1} line during charge transfer experiments. Sample B4 however, demonstrates a significant increase in intensity of the 7354 cm^{-1} line (and the 6426.5 cm^{-1}

line) after thermal treatment, and similarly a decrease upon optical treatment. The main difference between these samples is that sample B4 has an obvious concentration of acceptors (i.e. NVH^0 and SiV^0), which reduce in concentration upon thermal treatment. As there are many unknown lines in the absorption spectra of sample B4 that change with charge transfer (not presented), a charge transfer equation with the 7354 cm^{-1} centre cannot be confidently given. This charge transfer behavour of the 7354 cm^{-1} line (and the 6426.5 cm^{-1} line) has previously been reported by Cann [29], in a sample that also contained a notable concentration of the NVH^0 acceptor.

Furthermore, the 7354 cm^{-1} centre in the brown boron-doped sample C1 (Chapter 7) is also believed to undergo charge charge transfer. In sample C1 the 7354 cm^{-1} centre appears to anneal-in, but this is not previously observed behaviour [7]; instead it is argued that the increase in intensity after annealing is due to charge transfer through a change of relative concentrations of acceptors and donors caused by the annealing—a more detailed explanation is given in Chapter 7. This boron-doped sample naturally contains a notable concentration of the B_S^0 acceptor.

It appears that the 7354 cm^{-1} centre exhibits charge transfer the presence of a notable concentration of acceptors. The corollary of these observations suggests the 7354 cm^{-1} centre is the charge analogue of a centre that has already donated an electron to an acceptor. The line at 7354 cm^{-1} would most likely relate to a centre of neutral or positive charge (0/+), that increases in concentration upon thermal treatment, but decreases in concentration through optical treatment that would maximise the negative or neutral charge state (−/0).

Confirmation of the charge transfer behaviour of the 7354 cm^{-1} centre will require further investigation. The charge analogue the 7354 cm^{-1} centre charge transfers to upon optical treatment is currently unknown, but it may be observable with optical spectroscopy. Furthermore, as the 7354 cm^{-1} centre is not observable in EPR it may be considered as diamagnetic [7]; the charge analogue it charge transfers into should be paramagnetic (if only one electron is donated) and therefore should be observable in EPR.

6.4.3 Uniaxial stress

The uniaxial stress measurements presented build on the previous work of Glover [6] and Cruddace [7], and show that the 7354 cm^{-1} line arises from a transition between degenerate states through the thermalisation behaviour in Figure 6-7. This thermalisation behaviour may be explained with the aid of Figure 6-13, which depicts the energy level structure of the 7354 cm^{-1} centre, with E ground and excited states, under applied stress. A total of four transitions, labelled T_{n} where $\mathrm{n} = 1, 2, 3, 4$, may occur under applied stress.

In Figure 6-7, both the IR absorption and PL thermalisation spectra depict the higher energy lines (I_2 and I_4) increasing in intensity with reducing temperature, whilst the lower energy lines (I_1 and I_3) are decreasing. Based on the uniaxial stress Tables 6-3 and 6-4, and the electric field vector polarisations in the IR absorption and PL thermalisation spectra (Figure 6-7), all four T_{n} transitions may have non-zero intensities and thus the thermalisation lines can be expressed as combinations of the transitions:

$$\begin{aligned} I_1 &= T_3 + T_4\,, \\ I_2 &= T_1 + T_2\,, \\ I_3 &= T_2 + T_4\,, \\ I_4 &= T_1 + T_3\,. \end{aligned} \tag{6-6}$$

With regards to thermalisation observed by IR absorption in Figure 6-7a, a reduction in temperature causes a Boltzmann population shift in the stress-split E ground state (E_{GS}) from the higher energy level to the lower energy level. Consequently, as there are more electrons in the lower energy level of E_{GS}, the I_1 thermalisation line increases in absorption intensity as both the T_1 and T_2 transitions originate from the lower level. It follows that the reduction in absorption intensity of the I_1 thermalisation line is a direct consequence of the electron population in the higher energy level being reduced, seeing as the T_3 and T_4 transitions originates from the higher level.

With regards to thermalisation observed by photoluminescence in Figure 6-7b, the populations of the stress-split E excited state (E_{ES}) are relevant to the ob-

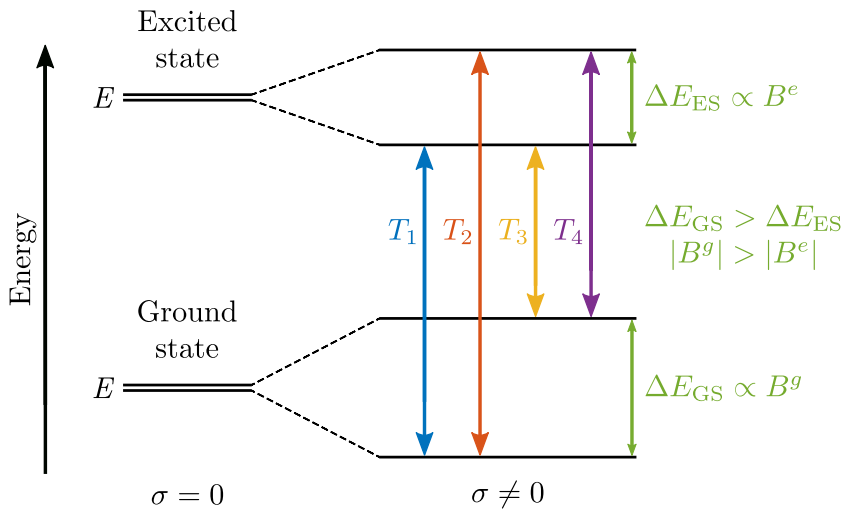

Figure 6-13 Electronic structure of the 7354 cm^{-1} centre. Under applied stress, a total of four transitions (T_n where n = 1, 2, 3, 4) are possible for this $E \leftrightarrow E$ system. The thermalisation behaviour indicates that the energy separation of the ground state is greater than the energy separation of the excited state, under applied stress, such that $\Delta E_{GS} > \Delta E_{ES}$ which by extension implies for the piezospectroscopic parameters that $|B^g| > |B^e|$.

servations. If an electron is excited to the lower level of E_{ES}, then decay most likely occurs via the I_4 emission (ignoring non-radiative decay), which comprises of transitions T_1 and T_3. Similarly, if an electron is excited to the higher level of E_{ES}, then the expected decay is the I_3 emission (comprised of transitions T_2 and T_4). However, if the electron thermally decays from the higher level of E_{ES} to the lower level (before it undergoes radiative decay via the two I_3 transitions), then it may only undergo radiative decay by the two I_4 transitions instead. The probability of thermal decay increases with a reduction in temperature, thus an increase in the intensity of I_4 is observed with a reduction in temperature.

The thermalisation data also informs on the relative response to stress that each E state exhibits. In order for I_2 and I_4 to increase in intensity with a reduction in temperature, E_{GS} must undergo a larger energy split when its degeneracy is broken by a given amount of applied stress, compared to E_{ES}. Thus, for $\sigma \neq 0$, $\Delta E_{GS} > \Delta E_{ES}$ and by extension equation (6-3) implies that $|B^g| > |B^e|$. The experimental results support this statement about the piezospectroscopic parameters, as from Cruddace [7], $B^g = -2.2(1)\,\text{cm}^{-1}\,\text{GPa}^{-1}$ and from §6.3.2.1, $B^e = -1.4(1)\,\text{cm}^{-1}\,\text{GPa}^{-1}$.

The values of B^g and B^e determined from thermalisation measurements do not match the values determined from fitting the uniaxial stress data. There are clearly unobserved transitions missing in the uniaxial stress data (Figure 6-10), so the fit was performed on an incomplete data set that does not accurately reflect the behaviour of the 7354 cm^{-1} line under applied stress, hence the parameter values generated are inconsistent with the thermalisation experiments. Thus, the assignment of the 7354 cm^{-1} line originating from an $E \leftrightarrow E$ transition at a trigonal centre is not proven by the fit to the incomplete data.

Naturally, it follows that the reason why no suitable values of intensity-related parameters d and D are found, is as a direct consequence of attempting to yet again fit an incomplete data set. If the structure of the 7354 cm^{-1} centre in Figure 6-13 is correct, then the missing transitions likely arise from the inability to resolve and/or deconvolve the T_n transitions in stress-split spectra of the 7354 cm^{-1} centre. Further investigation of the symmetry and states of the 7354 cm^{-1} centre will require an approach that overcomes this challenge.

Additionally, the detection polarisation dependence and excitation polarisation invariance of the 7354 cm^{-1} line in PL (Figure 6-6) is also challenging to explain. The behaviour is observed under an applied stress of 3.2 GPa but the spectra taken at zero applied stress during the same experiment demonstrates a similar effect, as shown in Figure 6-14. The difference in intensity between the two excitation polarisations is unrelated to this effect as it is due to the preferential orientation of the 7354 cm^{-1} centre that was observed in the absorption spectra in §6.3.1. Observation of the behaviour at zero applied stress therefore implies the dependence is not stress-related. It may be possible for the absorption and emission dipoles to operate at different orientations as a result of a stress-induced reorientation, but there is no obvious reason why this would be the case at zero stress. This phenomenon currently remains unexplained.

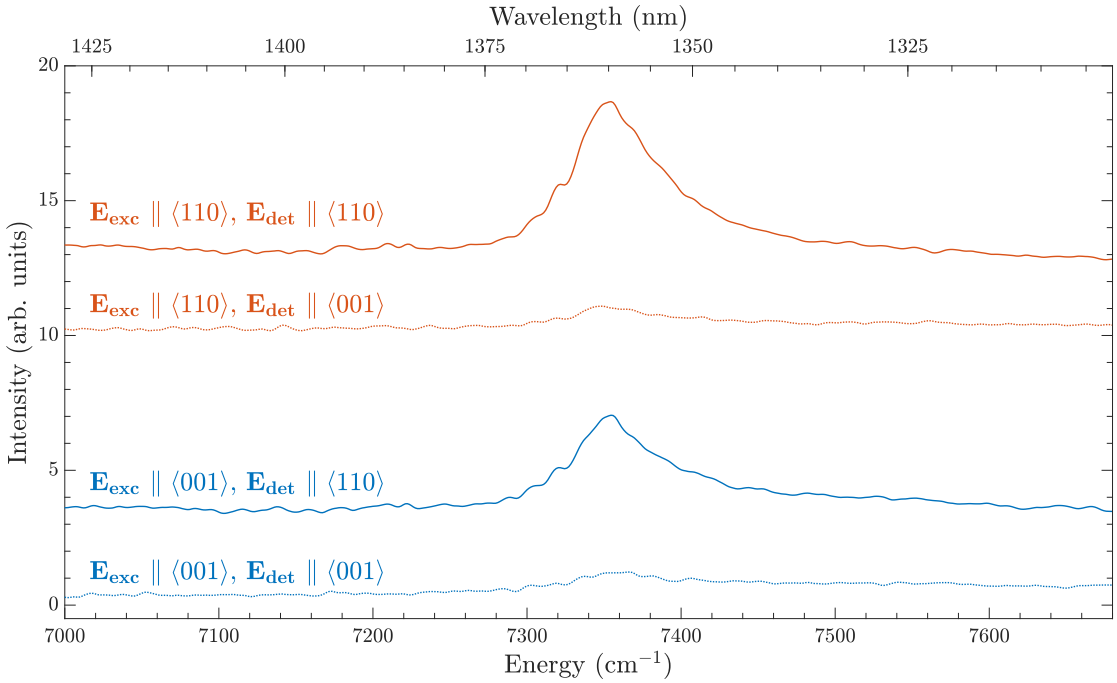

Figure 6-14 Detection polarisation dependence of the 7354 cm^{-1} line in photoluminescence at zero stress in sample B2. Irrespective of the polarisation of the excitation electric field vector ($\mathbf{E_{exc}}$), significant emission from the 7354 cm^{-1} centre is only observed with the detection polarisation ($\mathbf{E_{det}}$) perpendicular to the crystal axis $\langle 0\,0\,1 \rangle$. Spectra taken at 80 K and offset for clarity.

6.5 Conclusions

The 7354 cm^{-1} centre is reported to exhibit preferential orientation, when grown on $\{0\,0\,1\}$- and $\{1\,1\,0\}$-orientated substrates, relative to the growth direction. The absorption intensity of the 7354 cm^{-1} line is greater when light is polarised perpendicular to the $[0\,0\,1]$ growth direction, or parallel to the $[1\,1\,0]$ growth direction. The preferential orientation is lost upon annealing the sample at a temperature of at least 1000 °C.

In the presence of a sufficient concentration of acceptors (e.g. B_S^0, NVH^0, SiV^0) the 7354 cm^{-1} will exhibit charge transfer. The intensity of the 7354 cm^{-1} line increases upon thermal treatment and decreases upon optical treatment, thereby suggesting the centre is of neutral or positive charge (0/+). The 6426.5 cm^{-1} line exhibits similar charge transfer behaviour, but unlike the 7354 cm^{-1} line it does not demonstrate any preferential orientation.

Observation of thermalisation during PL measurements has confirmed that the

excited state of the 7354 cm^{-1} centre is also degenerate and likely an E state. The 7354 cm^{-1} line is therefore believed to originate from at least an $E \leftrightarrow E$ transition, although the exact symmetry has yet to be conclusively determined. If an $E \leftrightarrow E$ transition is the correct assignment of the 7354 cm^{-1} line, then there must be unresolved overlapping transitions in the unixial stress data (in both IR absorption and PL measurements). This may explain why the fit to the data, as an $E \leftrightarrow E$ transition at a trigonal centre, can only estimate the splitting and shift rates of the lines but not the intensities of the line. The parameter values generated by the fit are also not consistent with the parameter values calculated from the thermalisation results. As the symmetry of the 7354 cm^{-1} centre has not been conclusively determined, it is premature to speculate on the defect composition and structure.

During PL measurements, and under both zero and non-zero applied stress, the 7354 cm^{-1} line exhibits a dependence on the detection polarisation but is effectively invariant to the excitation polarisation.

Further work should include more detailed investigation of the charge transfer behaviour of the 7354 cm^{-1} centre. Ideally, a suitable nitrogen-doped sample, with a sufficient concentration of NVH^0 to induce charge transfer of the 7354 cm^{-1} centre, can be acquired for study. Given that all the defects that are likely to undergo charge transfer in such a sample can be assayed (i.e. N_S^0, N_S^+, NVH^0, NVH^-, and even NV^0 and NV^-—see Chapter 2), it should be possible to estimate the calibration coefficient of the 7354 cm^{-1} line. Consequently, the species the 7354 cm^{-1} centre charge transfers into upon optical treatment may also be observed by optical and/or EPR spectroscopies.

In addition, further work should also focus on resolving the overlapping transitions of the 7354 cm^{-1} centre under applied stress. Progress may be achieved if a sample with a much narrower 7354 cm^{-1} line is acquired for uniaxial stress experiments and/or if higher stress pressures are utilised to induce larger splittings of the lines.

References

1. F. Fuchs *et al.*, *Applied Physics Letters* **66**, 177–179 (1995).
2. F. Fuchs *et al.*, *Diamond and Related Materials* **4**, 652–656 (1995).
3. W. Wang *et al.*, *Gems & Gemology* **39**, 268–283 (2003).
4. P. M. Martineau *et al.*, *Gems & Gemology* **40**, 2–25 (2004).
5. S. J. Charles *et al.*, *physica status solidi (a)* **201**, 2473–2485 (2004).
6. C. Glover, PhD thesis, The University of Warwick, 2003.
7. R. Cruddace, PhD thesis, The University of Warwick, 2007.
8. J. Walker, *Reports on Progress in Physics* **42**, 1605–1659 (1979).
9. J. Goss *et al.*, *physica status solidi (a)* **186**, 215–220 (2001).
10. J. P. Goss *et al.*, *Physical Review B* **65**, 115207 (2002).
11. J. P. Goss, *Journal of Physics: Condensed Matter* **15**, R551–R580 (2003).
12. J. D. Holbech *et al.*, *Physical Review Letters* **71**, 875–878 (1993).
13. V. Kolkovsky *et al.*, *Physica B: Condensed Matter* **404**, 5080–5084 (2009).
14. N. Davies *et al.*, *Journal of Physics: Conference Series* **281**, 012026 (2011).
15. J. G. Rarity, K. D. Ridley, P. R. Tapster, *Applied Optics* **26**, 4616 (1987).
16. Oxford Instruments, *iDus 1.7μm InGaAs*, 2019, https://andor.oxinst.com/products/idus-spectroscopy-cameras/idus-1-7-ingaas (Retrieved 11/09/2019).
17. S. Liggins, PhD thesis, The University of Warwick, 2010.
18. G. Davies, M. H. Nazaré, *Journal of Physics C: Solid State Physics* **13**, 4127–4136 (1980).
19. K. Mohammed, G. Davies, A. T. Collins, *Journal of Physics C: Solid State Physics* **15**, 2779–2788 (1982).
20. G. Davies, *Journal of Physics C: Solid State Physics* **5**, 2534–2542 (1972).
21. A. M. Edmonds *et al.*, *Physical Review B* **86**, 35201 (2012).
22. U. F. S. D'Haenens-Johansson *et al.*, *Physical Review B* **84**, 245208 (2011).
23. L. M. Pham *et al.*, *Physical Review B* **86**, 121202 (2012).
24. C. Osterkamp *et al.*, *Scientific Reports* **9**, 5789 (2019).
25. M. W. Dale, PhD thesis, The University of Warwick, 2015.
26. B. G. Breeze, PhD thesis, The University of Warwick, 2017.

27. H. Ozawa *et al.*, *physica status solidi (a)* **215**, 1800342 (2018).

28. S. Chakravarthi *et al.*, arXiv: 1907.07793 (2019).

29. B. L. Cann, PhD thesis, The University of Warwick, 2009.

7

An annealing study of brown boron-doped diamond

7.1 Introduction

Boron and nitrogen are the two most common impurities in both natural and synthetic diamond. Characteristics of substitutional boron and nitrogen have already been discussed in Chapter 2, along with a variety of nitrogen-related complexes that may form in CVD diamond. Therefore, in this chapter the discussion will instead pertain to the simultaneous co-doping with boron and nitrogen in microwave plasma (MP) CVD diamond, in addition to the consideration of boron-related complexes.

It has been shown that both impurities exhibit preferential incorporation into {1 1 1} growth sectors approximately one order of magnitude more efficiently than into {0 0 1} sectors, under certain growth conditions during MPCVD growth [1]. In both cases boron incorporation is at least three orders of magnitude more efficient than nitrogen [2]. For HPHT growth, the modified Kanda diagrams by Burns *et al.* [3] and more recently Diggle [4], describe the sector dependence of boron and nitrogen in detail.

Nitrogen-induced growth rate enhancement of MPCVD diamond is well-known [5, 6]. However, as reported by Sartori *et al.* [7, 8] this effect can be completely

suppressed by the addition of trace amounts of boron to the gas phase plasma (a sole boron atom is capable of suppressing the efforts of 1000 nitrogen atoms). This finding has since been supported by more recent investigation by Croot [9], and whilst the phenomenon is well documented, the mechanisms are as yet not well understood.

Other consequences of co-doping are also well documented, such as the suppression of boron-related electrical conductivity by nitrogen incorporation: $N_S^0 + B_S^0 \rightarrow N_S^+ + B_S^-$ [10–12]. However, much less is known about potentially new point defects that may form in B/N co-doped CVD diamond, and in general boron-related complexes.

The ⟨0 0 1⟩-split BN^+ interstitial

To the author's knowledge, the only unambiguous identification of a boron- and nitrogen-related defect is the ⟨0 0 1⟩-split BN^+ interstitial (in HPHT diamond), that was identified with electron paramagnetic resonance (EPR) [13]. This defect is structurally similar to the di-nitrogen ⟨0 0 1⟩-split interstitial (N_{2I}) [14], except for the substitution of a nitrogen atom for a boron atom. Given this arguably intuitive substitution of similar-sized dopants, it is perhaps surprising that no other observations of defects where N_S is replaced by B_S have been reported.

The B_S–H complex (in silicon)

When investigating a defect in diamond, it is often useful to consult what is known about the defect in identically-structured crystalline silicon. In silicon, experimental and theoretical studies have identified the substitutional boron-hydrogen (B_S–H) complex, where the hydrogen is positioned at a bond-centred site between a silicon atom and the boron atom [15]. The associated hydrogen-related vibration at 1875–1880 cm^{-1} (at room temperature) is a local vibrational mode (LVM) and may be observed by both absorption and Raman scattering. The position of the LVM varies with temperature, although a comparison between hydrogen- and deuterium-doped samples demonstrates a constant isotope shift of 1.371 at all temperatures [16]. A similar comparison between ^{10}B (19.8% natural abundance) and ^{11}B (80.2% natural abundance) demonstrates a relatively small isotopic shift,

which indicates that the hydrogen atom is predominately bonded to the silicon atom, and that a small but non-zero bonding interaction exists between the hydrogen atom and the boron atom. The hydrogen atom can easily move a small amount off the B–Si axis, and even at a temperature of 100 K the hydrogen can easily move around the boron atom as the barrier to thermal activated motion is 0.3 eV; the binding energy of the B_S–H complex is 0.6 eV [16].

The B_S–H complex (in diamond)

An *ab initio* study by Breuer and Briddon [17] predicted that the structure of the B_S–H complex in diamond is different to that in silicon, with the hydrogen atom positioned in a $\langle 0\,0\,1 \rangle$ direction relative to the boron atom. Additionally, the vibrational frequency of the B_S–H stretch mode is predicted to be between 2540–2655 cm^{-1} [17], and isotopic substitution with ^{10}B or ^{11}B is anticipated to produce a small shift in frequency [18]. Whilst the dipole axis of B_S–H is expected to be along $\langle 0\,0\,1 \rangle$, reorientation between equivalent $\langle 0\,0\,1 \rangle$ directions is also expected to be easy, thereby eliminating any expectation of preferential orientation. The proposal that boron may trap two deuterium atoms to form a shallow donor has been disproved and assigned to erroneous experimental interpretation [19]. However, given that the suggested dissociation energy (= binding energy + H-migration barrier) of B_S–H is 2.5 eV [18], it is unlikely that the B_S–H complex would be stable at the CVD diamond growth temperatures.

Boron-vacancy(-hydrogen) complexes

The binding energy of the boron vacancy centre (BV: a substitutional boron atom adjacent to a lattice vacancy) is predicted at approximately 1.8 eV [19]. Formation of the centre during growth is not expected due to instability at CVD growth temperatures; formation by annealing to facilitate vacancy migration (migration energy, E_m = 2.2 eV) and capture at a B_S atom is also not expected as the BV centre would dissociate. It is therefore unsurprising that no charge state of the BV centre—be it BV^0 or BV^- with predicted paramagnetic ground states, or BV^+ with a predicted diamagnetic ground state—have been observed in diamond.

However, as the addition of hydrogen to the nitrogen vacancy (NV) centre is

known to stabilise the defect such that the annealing-out temperature of NVH is higher than NV [20], it is worth considering boron-vacancy-hydrogen complexes of the form BVH_n (n = 1, 2, 3). Consequently, it is reasonable to expect that a hydrogen atom would bond to one of the carbon dangling bonds of BV, and that the hydrogen would probably tunnel between different carbon sites as observed with the NVH centre (see Chapter 2).

Goss *et al.* [19] predict all three complexes—BVH, BVH_2, and BVH_3—would give rise to mid-gap acceptor states, but only the former two would also give rise to donor levels near the valence band maximum (as all the carbons are fully bonded in BVH_3). Additionally, all three complexes are expected to be thermally stable, with BVH_3 having a much lower hydrogen binding energy in comparison to the other two complexes. If BVH is formed during CVD synthesis, then an associated hydrogen vibration akin to a C–H stretch would be expected, and the defect would have a static $\mathscr{C}_{1h}$ symmetry and a time-averaged $\mathscr{C}_{3v}$ symmetry.

Boron-interstitial(-hydrogen) complexes

Goss *et al.* [19] also considered two boron-related interstitials: a ⟨0 0 1⟩-split self interstitial ($C_{I_{001}}$) with a nearest-neighbour substitutional boron atom, and the previously discussed ⟨0 0 1⟩-split BN interstitial decorated with a hydrogen atom. Both complexes are predicted to have high formation energies, with the former being the lower energy configuration, such that they would be stable at CVD diamond growth temperatures. However, it is unclear if the high formation energy would prevent the complexes being grown into boron-doped CVD diamond. For both complexes, the preferred hydrogen bonding site is a carbon dangling bond with an approximated binding energy of 4.5 eV [19].

Clearly the understanding of the point defects in B/N co-doped CVD diamond, and boron-related complexes in general, is incomplete and there would be benefit to further investigation. Annealing studies are a productive means of acquiring a wealth of information about defects in diamond, and also highlight which features merit further immediate investigation and characterisation. This chapter will therefore focus on an annealing study of two brown-coloured boron-doped samples

which aims to understand where the brown-colouration originates from in samples that otherwise were not intentionally doped with any other impurities. Brown-colouration is typically observed in nitrogen-doped diamond, so a comparison to features expected in only nitrogen-doped diamond will also be presented.

In addition, a polarised IR absorption study has also been performed on both samples in order to assess if any of the defects exhibit non-equilibrium population, i.e. if they are preferentially orientated. For a statically oriented defect, the probability of the defect being aligned along all equivalent directs is equal. However, a defect may grow with non-equilibrium population, as discussed in §3.6 where several examples may also be found.

7.2 Experimental details

The brown boron-doped CVD samples studied, labelled C1 and C2, were grown by Element Six Ltd and are presented in Figure 7-1. Sample C1 was grown on a {1 1 0}-orientated substrate that is still attached and identifiable as the clear region in the bottom half of the diamond. The birefringence imaging of the sample shows dislocation bundles in the substrate are directed towards the surface of the sample: the substrate is therefore also a CVD diamond [21]. Sample C2 was grown on a {0 0 1}-oriented substrate and also has its CVD substrate attached. Confirmation of the CVD-origin on both substrates is provided from the results in this chapter. Both samples have a brown region where the boron-doped layer was grown. Sample C1 has a notable lateral growth section where the boron uptake is much higher than the nitrogen uptake, thereby resulting in its label as the lateral growth region. The approximate boundaries between the regions in both samples are marked by yellow dashed lines in Figure 7-1c.

The samples are clearly inhomogeneous in their brown regions as reflected by the gradients of brown-colouration, so a method to repeatedly measure the same parts of the samples throughout the variety of treatments was deemed necessary. Figure 7-1c shows the locations on both samples where apertures for Fourier transform infrared (FTIR) and ultraviolet-visible (UV-Vis) absorption measurements were placed, as indicated with a blue circle on each sample. The aperture placement

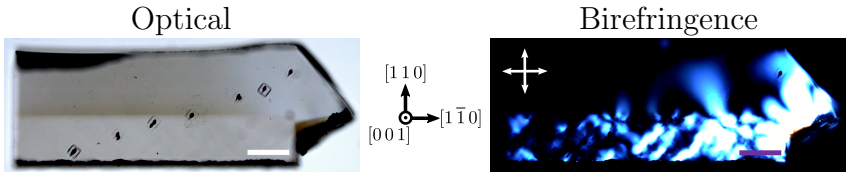

(a) Sample C1

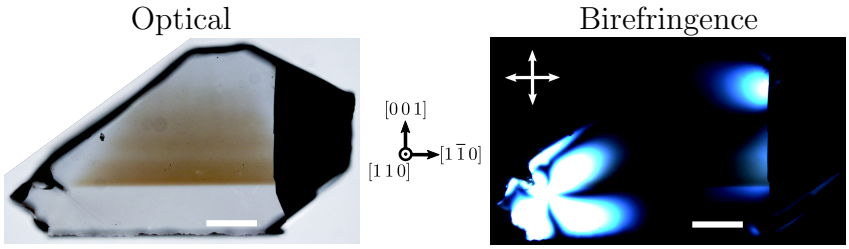

(b) Sample C2

FTIR/UV-Vis:
0.5 mm aperture
PL: 1 – Substrate region
PL: 2 – Brown region
PL: 3 – Lateral growth region

FTIR/UV-Vis:
1.0 mm aperture
PL: 1 – Substrate region
PL: 2 – Brown region

(c) FTIR/UV-Vis & PL experiment locations

Figure 7-1 Optical and birefringence (cross polarisation orientation marked) imaging of the brown boron-doped samples (a) C1 and (b) C2 in their as-grown state. (c) Measurement locations are marked on the samples where an aperture was placed for FTIR/UV-Vis measurements (blue circles) and where PL measurements were focused (orange points) in the 1 – substrate, 2 – brown, and 3 – lateral growth regions, with the approximate boundaries between the regions marked by yellow dashed lines. Scale bar = 0.5 mm.

was aligned by eye, so inevitably there will be some small misalignment error between all the measurements performed in this chapter.

Photoluminescence (PL) measurements were made at the locations indicated by orange points. These position were more accurately reproducible than the absorption measurements by using identification markers and moving the sample with the piezoelectric stage on the spectrometer. Using the third pit on sample C1 as a marker (Figure 7-2): point 1 is 200 µm below the pit, point 2 is 500 µm above

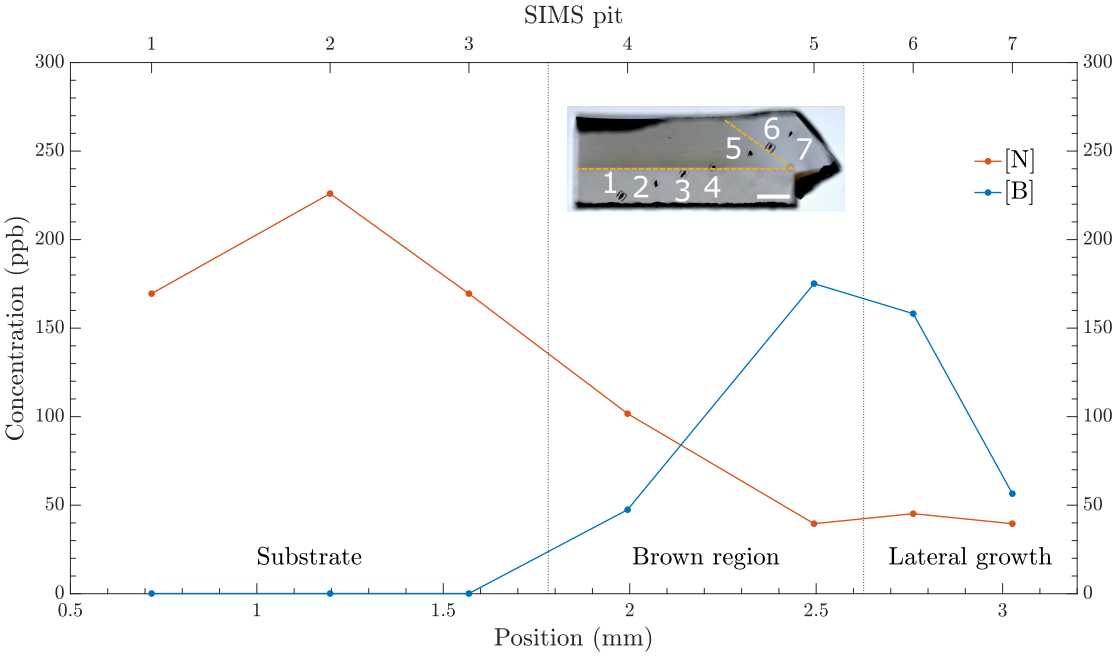

Figure 7-2 SIMS measurements of the [N] and [B] in sample C1. The SIMS pits are numbered. The substrate, brown region, and lateral growth region boundaries are approximately highlighted by yellow dashed lines on the optical image of sample C1. Data provided by De Beers Technologies, UK. Scale bar = 0.5 mm.

the pit, and point 3 is 250 µm above and 1200 µm to the right of the pit. Using the corner directly above the two points on sample C2 as a marker: point 1 is 1650 µm below the corner and point 2 is 825 µm below the corner.

Sample C1 also has a series of seven pits resulting from secondary ion mass spectrometry (SIMS) in its three regions where the total concentrations of boron and nitrogen were measured. Figure 7-2 presents these results, which were provided by De Beers Technologies, UK. The SIMS results suggest that the substrate only contains ~150–225 ppb of nitrogen; the brown region contains ~50–100 ppb of nitrogen and ~50–175 ppb of boron; and that the lateral growth region has < 50 ppb of nitrogen and ~50–150 ppb of boron. Errors for the measurements are not provided, but given that the boron and nitrogen concentrations estimated are below the SIMS detection limits for nitrogen and boron in diamond (stated in published literature at ~10^{17} cm^{-3} (~500 ppb) [22, 23]), it would be reasonable to suggest the SIMS measurement may have a significant error attached to them.

The boron-doped samples were subject to a variety of characterisation techniques in their as-grown state and also after each isochronal anneal of 4 h at temperatures

Annealing temperature (°C)	Characterisation performed
As-grown	Optical & DiamondView™ imaging CT & PO FTIR (RT) UV-Vis (RT) PL with 442 nm & 514 nm excitation (80 K) RPEPR (RT) In-situ CT FTIR (variable temperatures)
4 h at 1000, 1200, 1400, and 1500	Optical & DiamondView™ imaging PO FTIR (RT) UV-Vis (RT) PL with 442 nm & 514 nm excitation (80 K)

Table 7-1 Annealing treatments and characterisation performed on the boron-doped samples. CT: charge transfer. PO: preferential orientation. RT: room temperature.

1000 °C, 1200 °C, 1400 °C and 1500 °C, with a summary of provided in Table 7-1. Details of the FTIR characterisation variations performed are:

- CT FTIR: Charge Transfer (CT) FTIR measurements after optical (UV illumination) treatment and thermal treatment at 550 °C as described in §4.5.2;
- PO FTIR: Preferential orientation (PO) FTIR measurements with an appropriate mid- or near-infrared (MIR/NIR) polariser (depending on the spectral range being measured) aligned either parallel or perpendicular to the growth direction of the sample; and
- In-situ CT FTIR: FTIR measurements utilising a cryostat for variable temperatures. Infrared (IR) light was passed through pair of thallium bromoiodide windows and a 450 nm diode laser at 970 mW provided in-situ charge transfer through a perpendicular quartz window.

7.3 Results

The majority of IR absorption figures presented in this chapter show only sections of the one- and three-phonon regions of the spectra and omit the intrinsic diamond (two-phonon) region entirely [24]. This has been done in order to focus on the

features of interest in the one- and three-phonon regions within one figure, and because there are no features of interest in the two-phonon regions of the samples studied. The figures where the two-phonon region has been removed have a clear break in the x-axis and the spectra. The data points either side of the break have been offset in the y-axis to be at the same horizontal position on the figure.

7.3.1 Pre-annealing characterisation

Initial characterisation of the as-grown brown boron-doped samples involved RPEPR and FTIR in order to assay any known defects; the results from these measurements are presented in Table 7-2. The N_S^0 concentration was measured to the same value in both samples (within error) at ~35–40 ppb by RPEPR, but it is important to note that this measurement also include the substrates. No other RPEPR signals were obviously present. The 3123 cm^{-1} line is an LVM produced by NVH^0 [25], and is only observed in the brown region of sample C1 at a very low concentration of approximately 23(5) ppb.

The B_S^0 concentration could only reliably be measured by FTIR in sample C1 (20(5) ppb), as demonstrated by the boron feature at 2802 cm^{-1} only observed in sample C1 in Figure 7-3. Whilst the feature is not present in the spectrum of sample C2 in Figure 7-3, other as-grown FTIR spectra of sample C2 in this chapter will show a clear B_S^0 feature at 2802 cm^{-1}: this is attributed to aperture misalignment when performing the measurement and inhomogeneity in the brown region of the sample. A B_S^0 concentration of < 1 ppb represents the smallest measurement in any of the acquired as-grown FTIR spectra of sample C2. The N_S^0 feature at

Sample	EPR (ppb)		FTIR (ppb)		
	$[N_S^0]$	$[NVH^-]$	$[N_S^+]$	$[NVH^0]$	$[B_S^0]$
C1	40(10)	< 1	< 1	23(5)	20(5)
C2	35(10)	< 1	< 1	< 1	< 1
Reference	1600(160)	290(3)	1600(160)	300(3)	< 1

Table 7-2 As-grown characterisation of quantifiable defects in the studied samples and the as-grown brown nitrogen-doped CVD diamond reference. Characterisation of reference sample is provided in the PhD thesis of C. B. Hartland [26], where the reference is referred to as GC3.

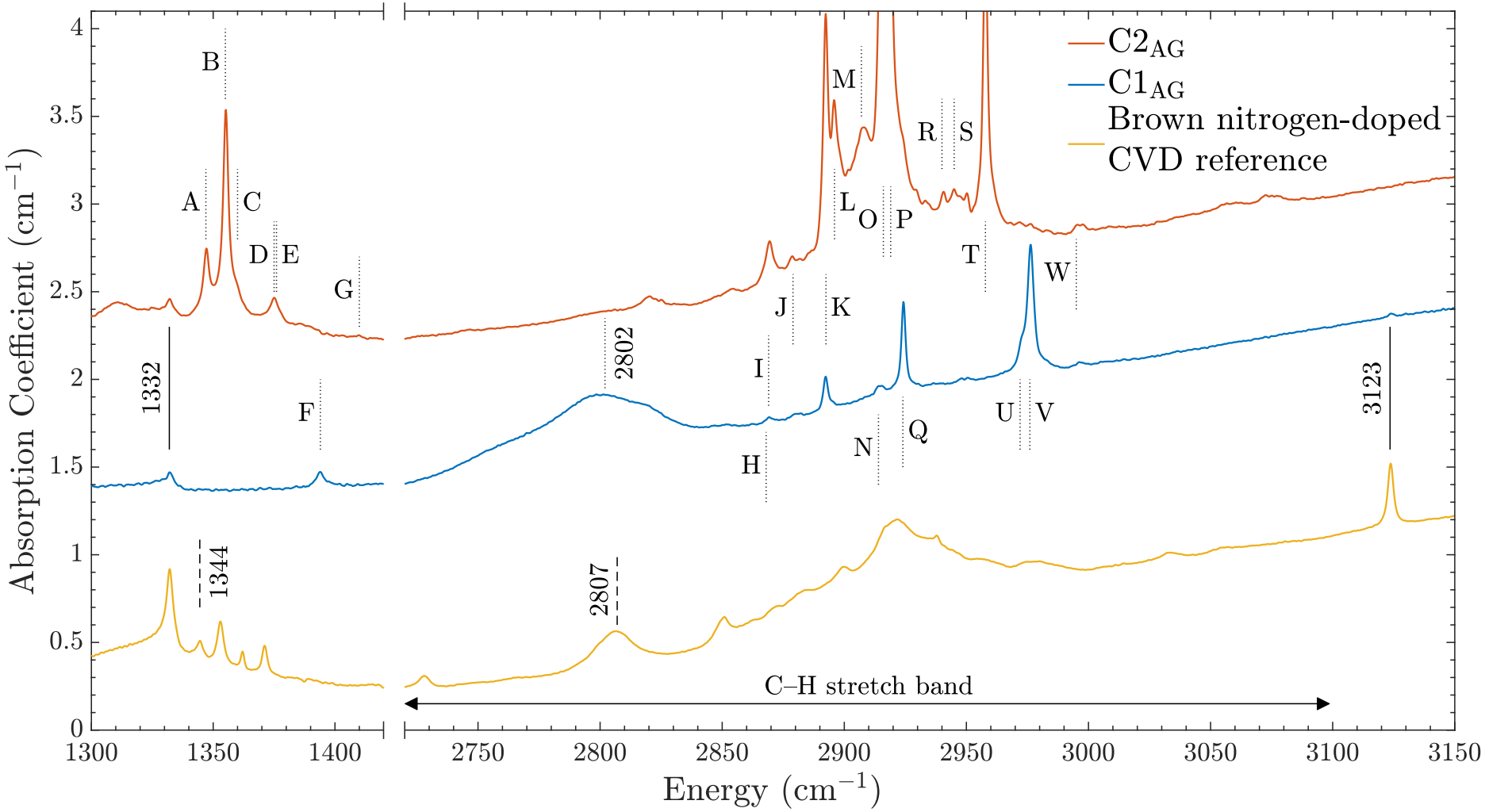

Figure 7-3 IR absorption spectra of the as-grown boron-doped samples ($C1_{AG}$/$C2_{AG}$) and a typical nitrogen-doped brown-coloured CVD reference. Dotted (dashed) lines indicate features in the boron-doped samples (brown CVD reference). Solid lines indicate features in both types of diamond (3123 cm^{-1} is not observed in sample C2). Brown nitrogen-doped CVD reference obtained by C. B. Hartland [26].

1344 cm^{-1} [27] (and related features) could not be confidently deconvolved from the IR absorption spectrum and therefore no estimation of the N_S^0 concentration can be offered from these spectra.

Both samples produced an atypical FTIR spectrum when compared to spectra recorded from as-grown brown-coloured nitrogen-doped CVD diamond. Figure 7-3 showcases the differences observed in the one- and three-phonon regions of the IR absorption spectra of the boron-doped samples and nitrogen-doped CVD diamond reference. Characterisation of the reference is provided in Table 7-2 and more information is provided in the PhD thesis of C. B. Hartland [26], where this reference sample is referred to as GC3. The unreported features in the boron-doped spectra (indicated by dotted lines) have been labelled alphabetically from A–W in order of energy (cm^{-1})—their behaviour is described in this section and also in §7.3.2.2 of this chapter.

Commonly observed features that are only observed in the brown CVD diamond reference (indicated with dashed lines) include the 1344 cm^{-1} line produced by N_S^0 [27]; the broad 2807 cm^{-1} line (which is not boron-related, unlike the broad 2802 cm^{-1} line in the boron-doped samples); and a notably broad band of C–H stretches (~2720–3100 cm^{-1}) that is part of the general C–H stretch region (~2600–3500 cm^{-1}). Only two features (indicated by solid lines) are clearly observed in both types of diamond: the defect-induced line at 1332 cm^{-1} and the NVH^0-related line at 3123 cm^{-1}. For both lines, the concentration measured in the brown CVD diamond reference are much higher than in the boron-doped samples.

7.3.1.1 Charge transfer

The room temperature charge transfer behaviour of the features in the as-grown boron-doped samples is presented in Figure 7-4. In both figures, features which are solely observed in sample C1 are indicated with dotted lines whereas features which are solely observed in sample C2 are indicated with dashed lines. Features present in both samples are indicated with solid lines. For each sample, a difference spectrum (thermal – optical) is provided for a comparison between the different states of charge transfer.

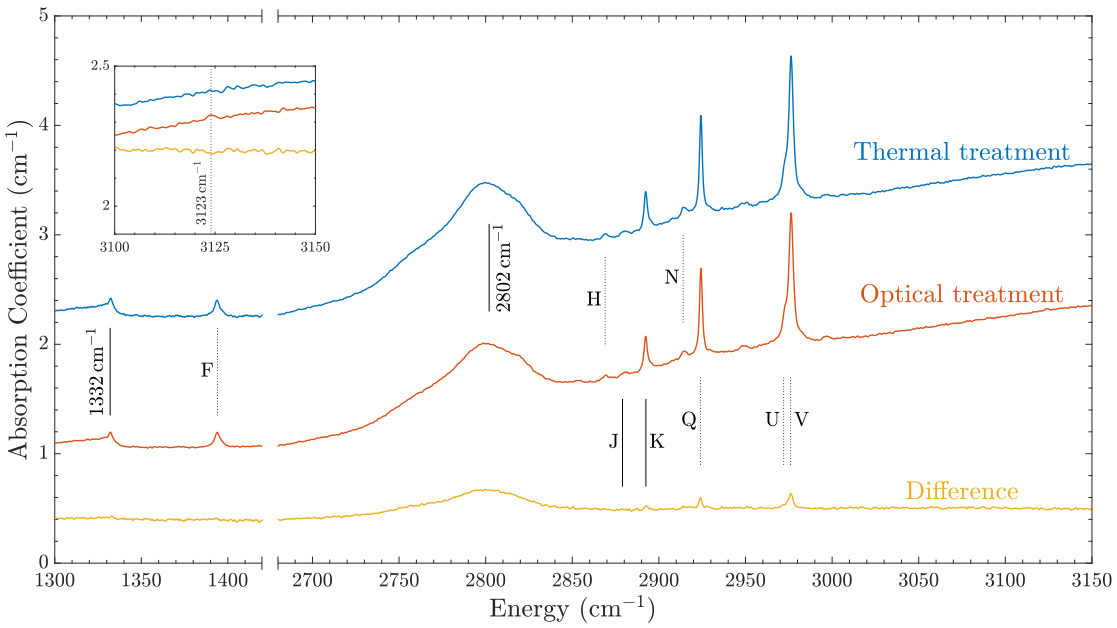

(a) Sample C1

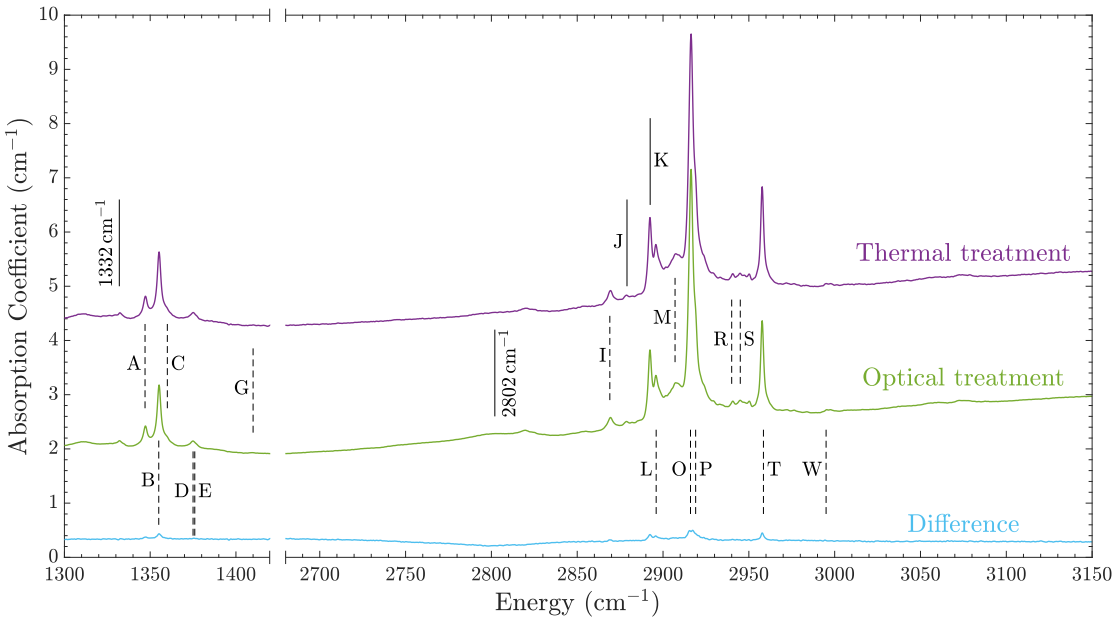

(b) Sample C2

Figure 7-4 Charge transfer IR absorption spectra at room temperature of as-grown samples (a) C1 and (b) C2. Difference spectra (thermal – optical) for each sample are also shown. Dotted (dashed) lines indicate features in sample C1 (C2). Solid lines indicate features in both boron-doped samples. Spectra have been offset for clarity.

The charge transfer difference spectra show very small changes in integrated intensity of any feature. Such small variation could be explained by inhomogeneity in the samples and misalignment of the aperture during measurements. Another possible explanation involves the substitutional boron impurities in these samples counteracting the effects of charge transfer treatment. Photo-generation of holes in the valence band, which arise from the electrically active B_S^0, will occur under illumination of energy > 0.37 eV. Similarly, holes may also be thermally-generated if the activation energy of B_S^0 is reached. Consequently, in order to at least combat the thermal generation of holes, an in-situ charge transfer IR absorption experiment at variable temperatures was performed in order limit the post-charge transfer effect boron may be having on the charges, whilst not adjusting the aperture position on the samples; details and results are found in §7.3.1.2.

7.3.1.2 In-situ charge transfer IR absorption

Further IR absorption experiments were therefore performed, with in-situ charge transfer and at both cryogenic and room temperatures. The sample was cooled to a temperature of 105 K and an FTIR spectrum was taken without any driven charge transfer. Still at 105 K, a 450 nm diode laser at 970 mW was utilised to drive charge transfer, and with the laser remaining active another FTIR spectrum was measured. Still with the laser active, the sample was warmed to 295 K and then another FTIR spectrum was measured. Finally, the laser was switched off and the final FTIR spectrum was measured at the same temperature of 295 K.

Both samples have only one set of polished faces, through which all light is passed during absorption measurements. The 450 nm laser providing charge transfer was therefore passed through the unpolished non-flat sides of the diamond (Figure 7-1). Given this, it is unlikely the 450 nm laser light was able to penetrate fully through the length of the samples.

Figure 7-5 shows an example of fitting the FTIR spectra, using a spectrum of sample C1 at 105 K with the laser diode switched on ($C1_{on}$). Each spectrum had the IIa reference removed along with a suitable uncompensated boron reference, resulting in a residual that (mostly) does not contain features from B_S^0 or intrinsic

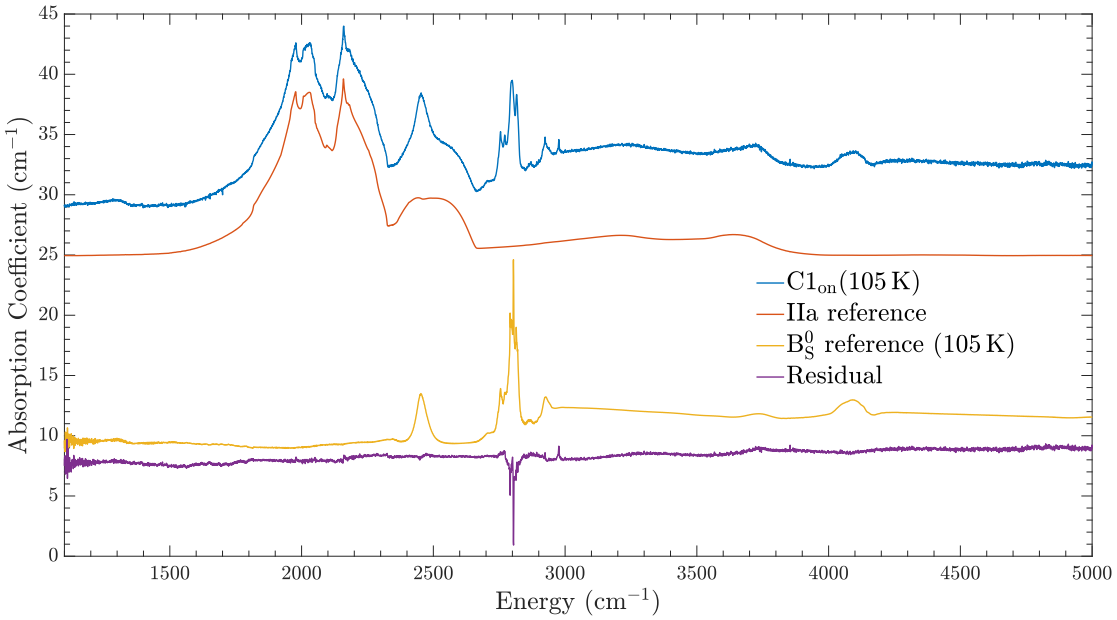

Figure 7-5 Example fit of uncompensated boron (B^0_S) in the IR absorption spectrum of sample C1, taken at 105 K, with the 450 nm laser providing in-situ charge transfer. The B^0_S reference was also necessarily acquired at 105 K.

Temperature (K)	$[B^0_S]$ (ppb)	
	C1	C2
105 (laser off)	70(10)	70(10)
105 (laser on)	150(10)	190(20)
295 (laser on)	20(10)	40(10)
295 (laser off)	30(10)	40(10)

Table 7-3 $[B^0_S]$ measured from in-situ charge transfer IR absorption at variable temperatures, where a 450 nm laser at 970 mW provided in-situ charge transfer.

diamond. The boron reference used to calculate the B^0_S concentration at the given conditions of the sample was also necessarily acquired at the same temperature of 105 K as the B^0_S absorption features change with temperature [28, 29]. However, the linewidth of the B^0_S absorption features also vary with concentration [3, 30], hence the large residual features at approximately 2700 cm^{-1}.

The uncompensated boron concentrations measured during the experiment are presented in Table 7-3. By cooling the samples from 295 K to 105 K, the concentration of B^0_S approximately doubles without any in-situ charge transfer. At 105 K the $[B^0_S]$ more than doubles in each sample once the laser is switched on. The laser has no effect on $[B^0_S]$ at 295 K.

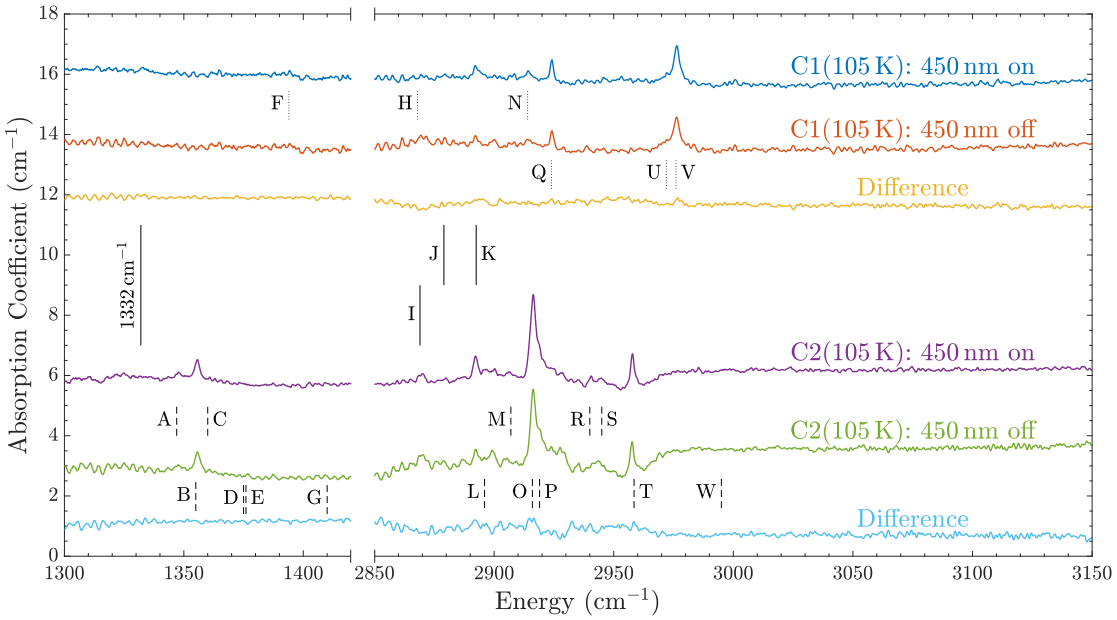

Figure 7-6 IR absoprtion spectra taken at 105 K with the 450 nm laser either switched on or off. Difference spectra (laser on – laser off) for each sample are also shown. Dotted (dashed) lines indicate features in sample C1 (C2). Solid lines indicate features in both boron-doped samples.

The residuals acquired from fitting spectra taken at 105 K with the diode laser on and off are given for each sample in Figure 7-6, along with the difference spectra (laser on – laser off). The features of interest show little-to-no change in the difference spectra of both samples.

7.3.1.3 Polarised IR absorption study

The room temperature dependence of the IR absorption features to linearly polarised light, in the as-grown samples, is presented in Figure 7-7. Measurements were made for polarisation directions parallel ($\parallel_{\text{growth}}$) and perpendicular ($\perp_{\text{growth}}$) to the growth direction of each sample, without moving the sample as only the polariser requires rotating—this removes any inhomogeneity concerns between the two measurements. Features that are solely observed in sample C1 are indicated with dotted lines whereas features that are solely observed in sample C2 are indicated with dashed lines. Features present in both samples are indicated with solid lines. For each sample, a difference spectrum ($\perp_{\text{growth}} - \parallel_{\text{growth}}$) is provided for a comparison between the different orientations of the polariser relative to the growth direction. Table 7-4 provides a summary of the results.

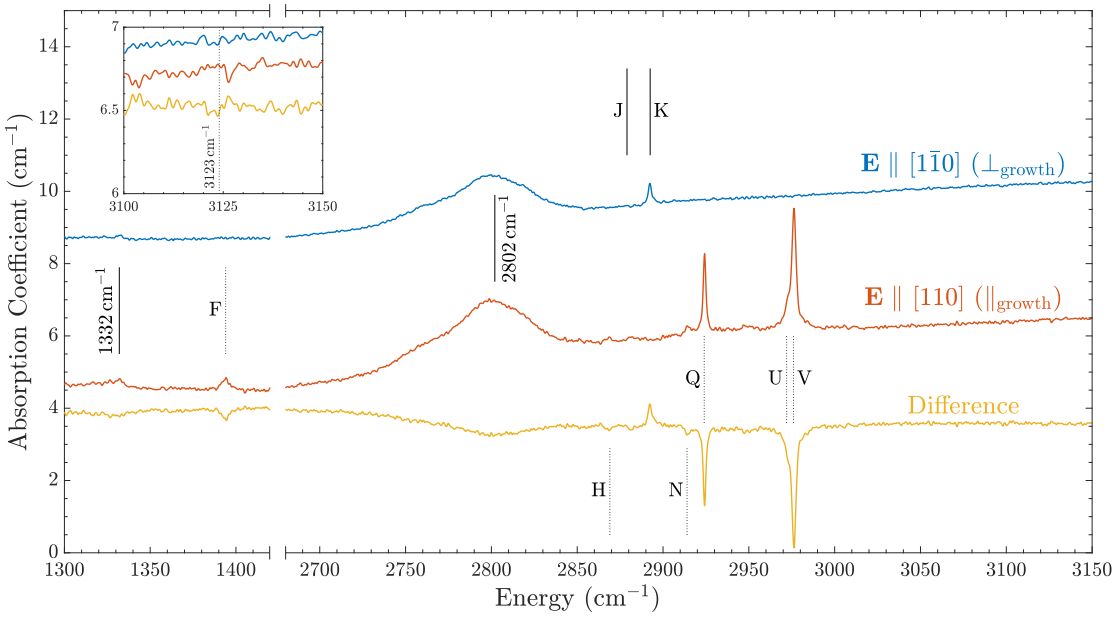

(a) Sample C1

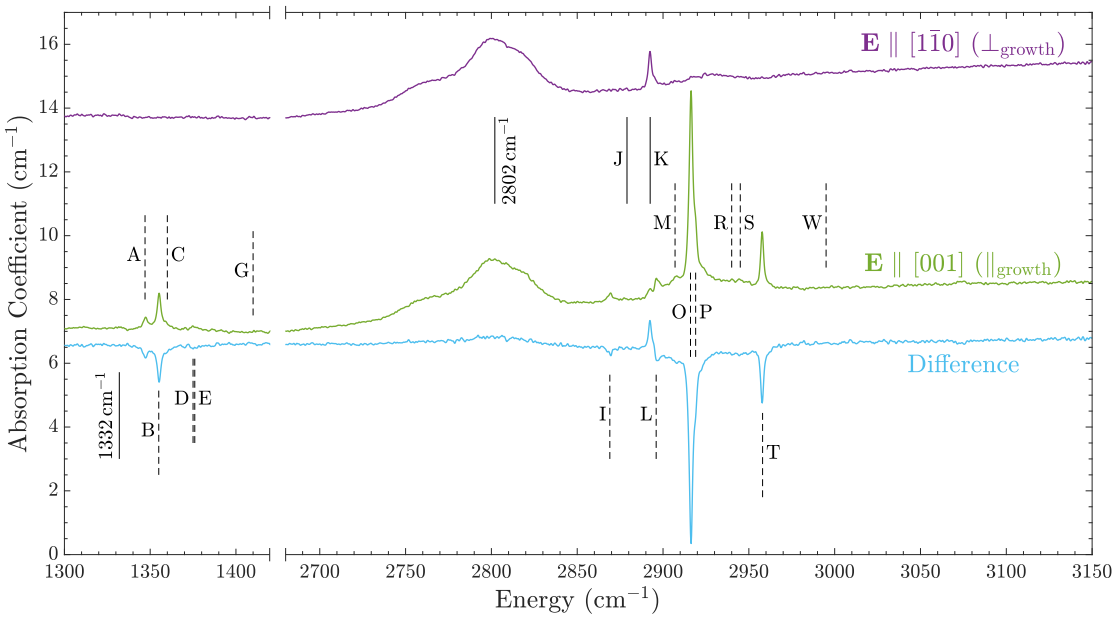

(b) Sample C2

Figure 7-7 Preferential orientation ($\|_{\text{growth}}$ ($\perp_{\text{growth}}$) indicating parallel (perpendicular) to the growth direction) IR absorption spectra at room temperature of (a) sample C1 and (b) sample C2 as-grown brown boron-doped samples. Difference spectra ($\perp_{\text{growth}} - \|_{\text{growth}}$) for each sample are also shown. Dotted (dashed) lines indicate features in sample C1 (C2). Solid lines indicate features in both boron-doped samples. Spectra have been offset for clarity.

Feature (cm^{-1})		Sample		Preferential orientation (%)	
				$\parallel_{growth}$	$\perp_{growth}$
N_S^+	: 1332	C1	C2	$\parallel_{growth} > \perp_{growth}$	
A	: 1347		C2	100	0
B	: 1355		C2	100	0
C	: 1360		C2	100	0
D	: 1375		C2	100	0
E	: 1376		C2	100	0
F	: 1394	C1		100	0
G	: 1410		C2	100	0
B_S^0	: 2802	C1		$\parallel_{growth} > \perp_{growth}$	
			C2	$\parallel_{growth} < \perp_{growth}$	
H	: 2868	C1		100	0
I	: 2870		C2	100	0
J	: 2879	C1	C2	100	0
K	: 2892	C1		0	100
			C2	15	85
L	: 2896		C2	100	0
M	: 2907		C2	0	100
N	: 2914	C1		100	0
O	: 2916		C2	100	0
P	: 2919		C2	100	0
Q	: 2924	C1		100	0
R	: 2940		C2	100	0
S	: 2945		C2	100	0
T	: 2958		C2	100	0
U	: 2972	C1		100	0
V	: 2976	C1		100	0
W	: 2995		C2	0	0
NVH^0	: 3123	C1		0	0

Table 7-4 Integrated intensity behaviour of IR absorption features, indicated by their defect/line label and energy, in the as-grown boron-doped samples under preferential orientation. $\parallel_{growth}$ ($\perp_{growth}$) indicates parallel (perpendicular) to the growth direction.

It is apparent from Figure 7-7 that the intensities of the majority of absorption features in the C–H stretch region clearly depend on the orientation of the linearly polarised incident light. A defect with all symmetry-related orientations present and equally populated would not show any change in intensity to the orientation of the incident light. The spectra in Figure 7-7 therefore provide compelling evidence that the defects responsible for these feature are preferentially orientated. As expected, there is effectively no change in intensity for B_S^0 (in either sample), as

its $\mathscr{C}_{3v}$ symmetry is only a very small distortion off $\mathscr{T}_d$ symmetry [31].

In the case of other features that are observed in both samples, there are some interesting findings. Features J is present in both samples and exhibits 100% parallel PO, even though the two samples are grown on differently orientated substrates (see Figure 7-1).

Feature K is also observed in both samples and presents the most interesting behaviour for a variety of reasons. When observed in sample C1, the feature shows 100% PO when incident light is polarised perpendicular to the growth direction, unlike the majority of the other features in sample C1 for which the opposite is true. When observed in sample C2, the feature shows a split PO with approximately 15% intensity with incident light polarised parallel to the growth direction and approximately 85% with perpendicular polarisation.

7.3.2 Post-annealing characterisation

7.3.2.1 Optical, fluorescence, and phosphorescence imaging

Figure 7-8 shows the optical, DiamondView™ fluorescence (0.5–1.0 s exposure time) and (with 0.05 s delay) phosphoresence imaging performed on the boron-doped samples in their as-grown states and also after each isochronal (4 h) anneal. The as-grown imaging has been previously shown in Figure 7-1 and is reproduced here for convenience with comparing to the post-annealing imaging.

The optical imaging shows the as-grown brown-colouration, in the boron-doped region of both samples, is gradually removed throughout the annealing stages with a particularly notable loss of colour after the 1200 °C anneal. After the 1500 °C anneal the colour of the samples is significantly reduced even though only a modest annealing temperature has been used. Whilst the B_S^0 concentration is measurable by optical absorption in both samples (as shown in §7.3.2.2 and §7.3.2.4), the concentration is not high enough for a noticeable blue colouration after the annealing presented here.

The lateral growth sector of sample C1 emits a notable blue-coloured fluorescence and phosphorescence at all stages of the annealing study that is most likely due to

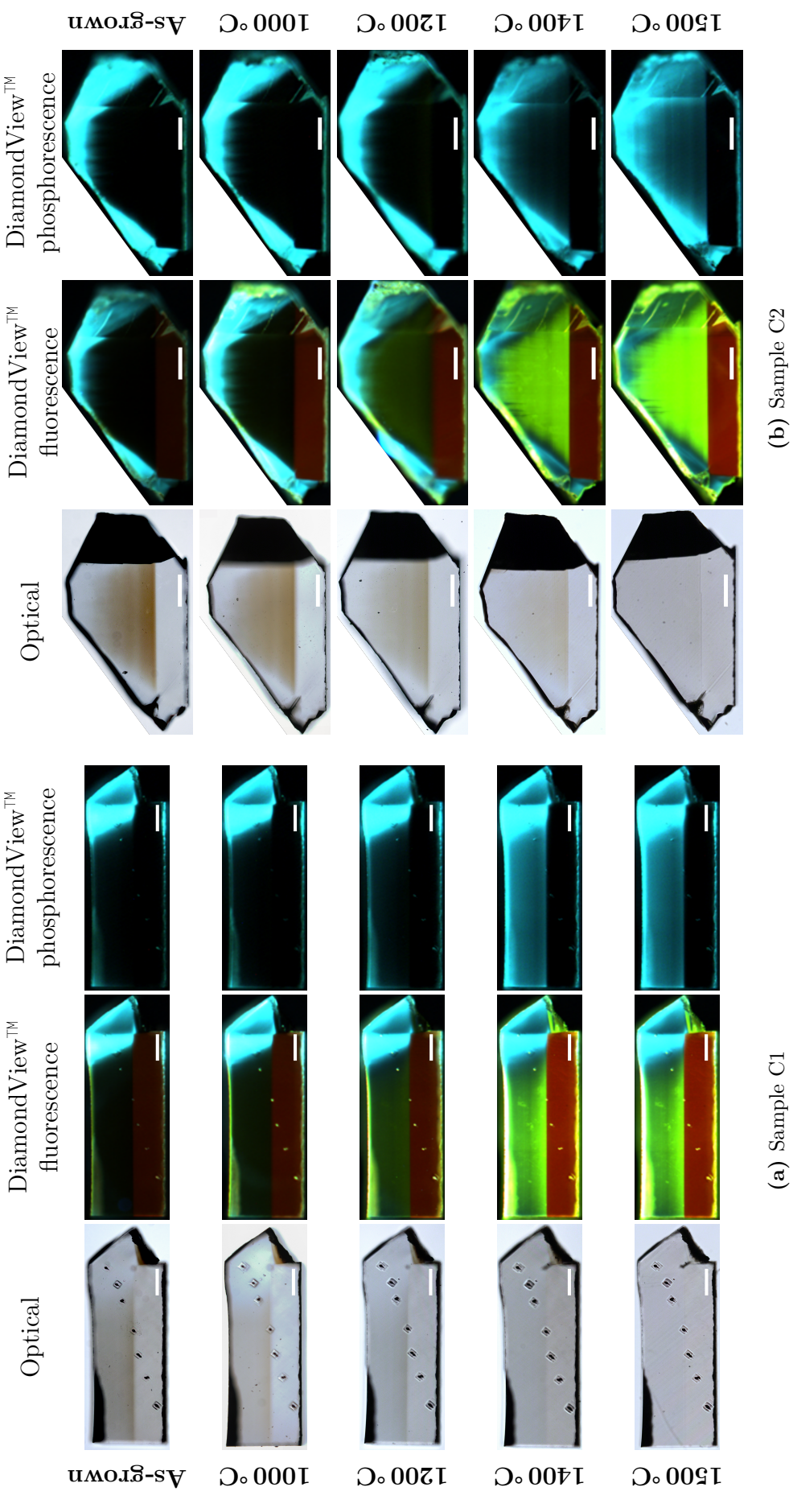

Figure 7-8 Optical, and DiamondView™ fluorescence (0.5–1.0 s exposure time) and (with 0.05 s delay) phosphoresence imaging of (a) sample C1 and (b) sample C2, as-grown and after each isochronal (4 h) anneal. The DiamondView™ UV source was set to full power. The exposure time of the 1500 °C fluorescence imaging was reduced by 30% to avoid saturation. Scale bar = 0.5 mm.

donor-acceptor pair-recombination [32]. Sample C2 similarly emits blue-coloured fluorescence and phosphorescence at all stages, but the emission is localised to the rough edges of the sample.

Both samples have their substrates still attached and both substrates fluoresce with an orange colour that is indicative of NV^0 [33]. The presence of as-grown NV defects is indicative of nitrogen-doped CVD diamond. No phosphorescence is observed from the substrates.

In their as-grown states, the fluorescence in the boron-doped region of both samples is initially very weakly green. The green fluorescence increases throughout the annealing and becomes particularly strong after the 1400 °C anneal. Similarly, the phosphorescence in the boron-doped region of both samples presents very weakly blue and then increases throughout the annealing, with a notable increase in intensity after the 1400 °C anneal.

7.3.2.2 IR absorption

A room temperature unpolarised IR absorption spectrum of each boron-doped sample was measured after each anneal; these spectra are shown in Figure 7-9 with features of interest indicated with dashed lines. The 2802 cm^{-1} line (a B_S^0 feature) undergoes the most notable change throughout the annealing study and the $[B_S^0]$ measured from this and other boron-related features are given in Table 7-5. Initially the 1000 °C and 1200 °C anneals only increase the B_S^0 by a few tens of ppb, but much larger increases are observed after the 1400 °C and particularly the 1500 °C anneals.

Annealing Temperature (°C)	$[B_S^0]$ (ppb)	
	C1	C2
As-grown	20(5)	< 1
1000	50(5)	15(5)
1200	75(5)	35(5)
1400	120(10)	180(10)
1500	260(20)	270(20)

Table 7-5 $[B_S^0]$ as measured from room temperature IR absorption spectra from (a) sample C1 and (b) sample C2 as-grown and after each anneal.

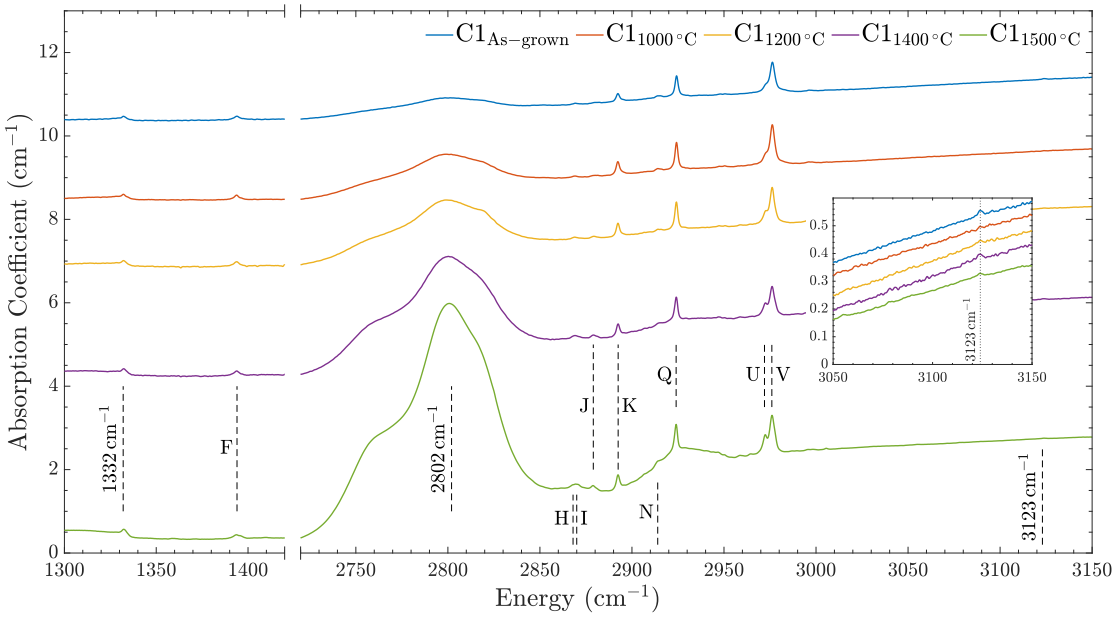

(a) Sample C1

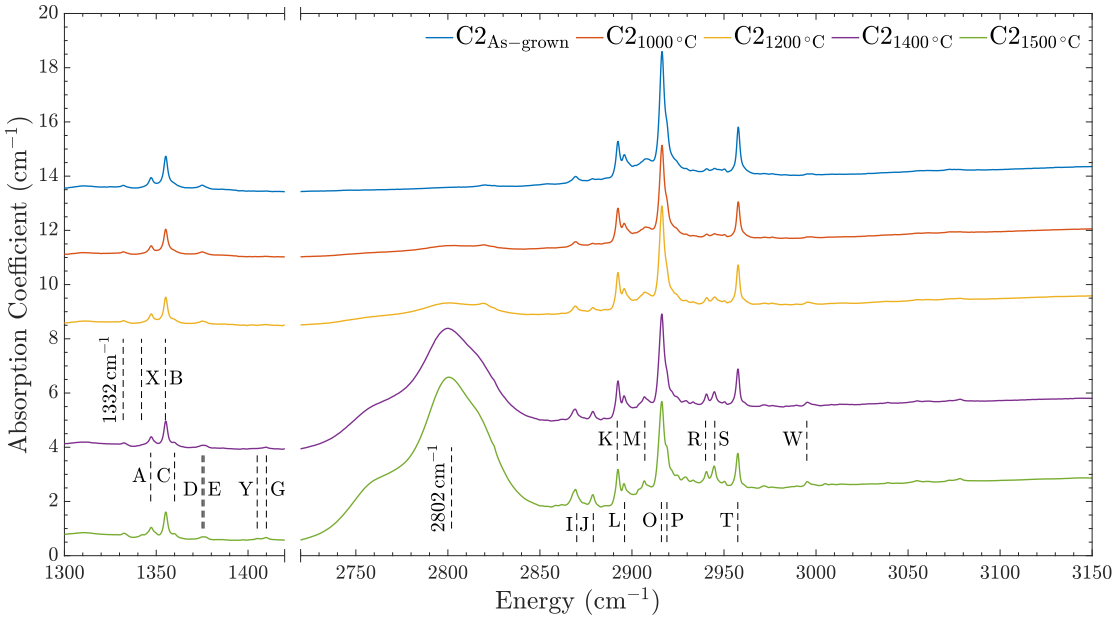

(b) Sample C2

Figure 7-9 IR absorption spectra at room temperature of (a) sample C1 and (b) sample C2 as-grown and after each anneal. The spectra were not subject to polarisation. Features of interest are indicated with dashed lines. Spectra have been offset for clarity.

In order to assist with analysing the remaining features in the one- and three-phonon regions of the boron-doped samples, difference spectra between each annealing stage relative to the previous stage (or to the as-grown state for the 1000 °C anneal) for each sample are provided in Figure 7-10. The B_S^0 feature at 2802 cm^{-1} is not shown in the three-phonon part of the subfigures. A summary of integrated intensity behaviour of these features after each anneal is also presented in Table 7-6. The sets of markers that describe the same behaviour of integrated intensity of the features have been highlighted with the same colour; there are a total of six different sets of common markers. Any set of markers that is not highlighted is unique within this annealing study.

The marker sets highlighted in blue increase in intensity after each anneal and comprise of features H, J, K (C2 only), L, M, R, S, U, and also 1332 cm^{-1} and B_S^0 at 2802 cm^{-1}. The marker sets highlighted in green behave near identically to those highlighted blue, except that they lose intensity after the first anneal at 1000 °C. The green-highlighted features are I, O, P, and T.

The marker sets highlighted in orange decrease in intensity after the first anneal, increase after the next two anneals, and again decrease after the final anneal. Only three features are observed to have this behaviour: B and C (both C2 only), and NVH^0 (C1 only); unfortunately by appearing in different samples they cannot be obviously related.

The marker sets highlighted in purple show no change in intensity after the first anneal but an increase after each subsequent anneal; the only two features with a purple highlight (both in C2) are G : 1410 cm^{-1} and W : 2995 cm^{-1}. Their relative energy separation and identical annealing behaviour suggest they could be a related bend and stretch mode, respectively, of a C–H bond. The integrated intensity correlation between these two features at each part of the annealing study, as shown in Figure 7-11a, is of good agreement. The gradient implies that the relative integrated intensity of the feature G is 62(1)% of the integrated intensity of the feature W.

The marker sets highlighted in yellow increase in intensity after the first anneal, decrease after the next two anneals, and again increase after the final anneal. As

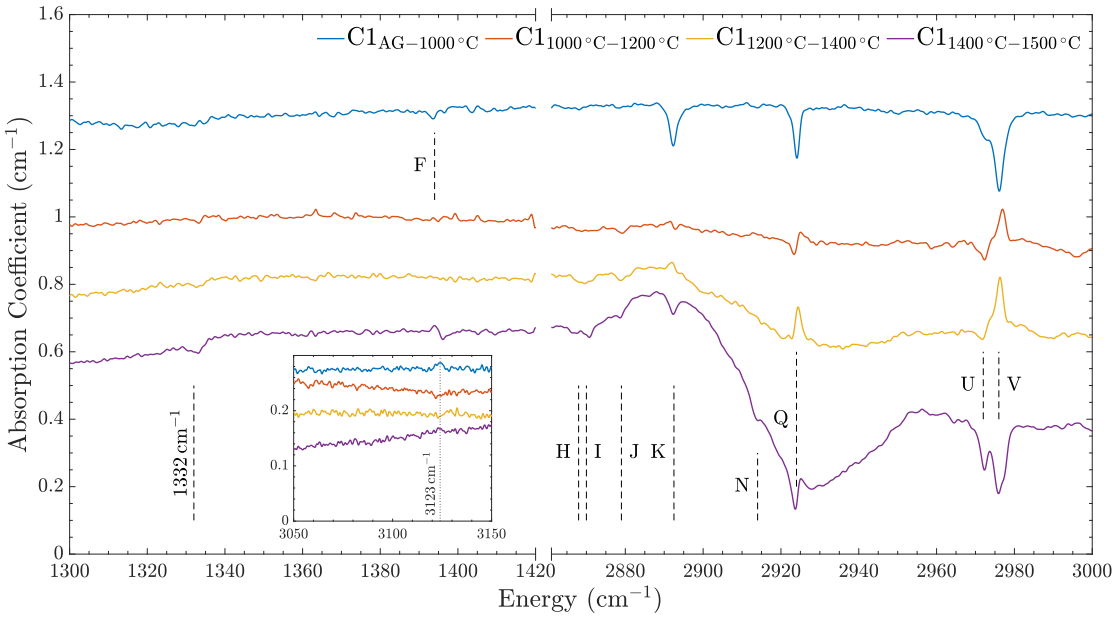

(a) Sample C1

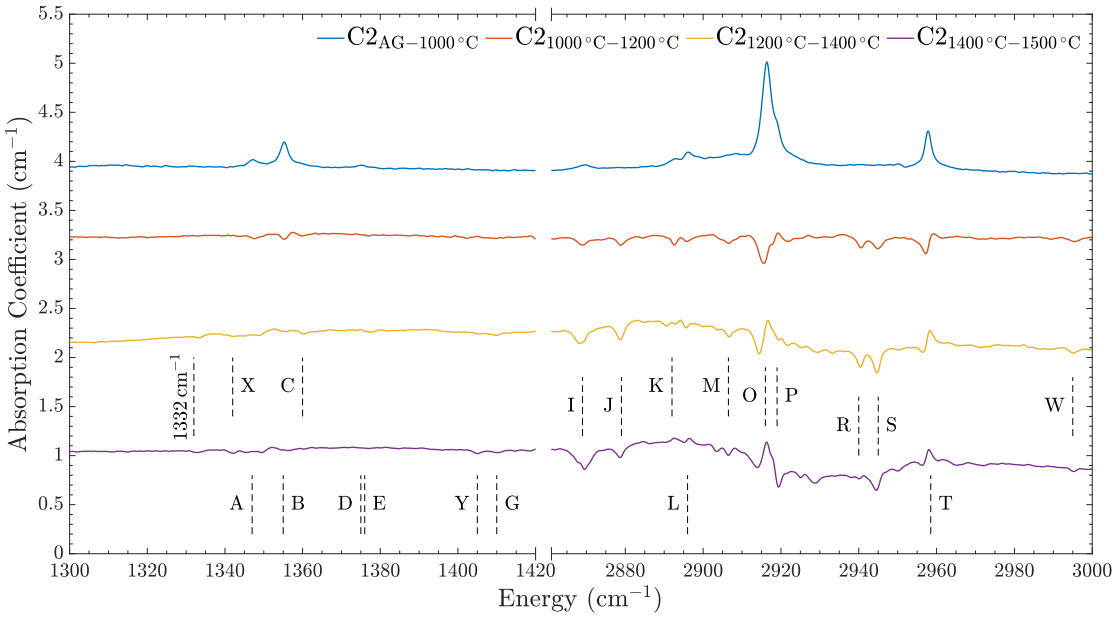

(b) Sample C2

Figure 7-10 Differences between each annealing stage relative to the previous stage (or to the as-grown (AG) state for the 1000 °C anneal) for (a) sample C1 and (b) sample C2. Features showing positive (negative) change of intensity have decreased (increased) in intensity relative to the previous state of the samples. Features of interest are indicated with dashed lines. Spectra taken at room temperature.

Feature (cm^{-1})	Sample		Annealing temperature (°C)			
			1000	1200	1400	1500
N_S^+ : 1332	C1		↑	↑	↑	↑
		C2	–	–	–	–
A : 1347		C2	↑	↓	–	–
B : 1355		C2	↓	↑	↑	↓
C : 1360		C2	↓	↑	↑	↓
D : 1375		C2	↑	–	↑	↑
E : 1376		C2	–	↑	↑	–
F : 1394	C1		↑	↓	↓	↑
G : 1410		C2	–	↑	↑	↑
B_S^0 : 2802	C1	C2	↑	↑	↑	↑
H : 2868	C1		↑	↑	↑	↑
I : 2870	C1				↑	↑
		C2	↓	↑	↑	↑
J : 2879	C1	C2	↑	↑	↑	↑
K : 2892	C1		↑	↑	–	–
		C2	↑	↑	↑	↑
L : 2896		C2	↑	↑	↑	↑
M : 2907		C2	↑	↑	↑	↑
N : 2914	C1		↑	↓	↑	↑
O : 2916		C2	↓	↑	↑	↑
P : 2919		C2	↓	↑	↑	↑
Q : 2924	C1		↑	↑	↓	↑
R : 2940		C2	↑	↑	↑	↑
S : 2945		C2	↑	↑	↑	↑
T : 2958		C2	↓	↑	↑	↑
U : 2972	C1		↑	↑	↑	↑
V : 2976	C1		↑	↓	↓	↑
W : 2995		C2	–	↑	↑	↑
NVH^0 : 3123	C1		↓	↑	↑	↓
X : 1342		C2			↑	↑
Y : 1405		C2				↑

Table 7-6 Integrated intensity behaviour of IR absorption features, indicated by their defect/line label and energy, at each annealing stage relative to the previous stage (or to the as-grown state for the 1000 °C anneal). Features I (for C1 only), X and Y anneal-in after 1400 °C, 1400 °C and 1500 °C, respectively, with a blank cell indicating no integrated intensity is measurable before those anneals. ↑ (↓) indicates an increase (decrease) in integrated intensity. – indicates no change in integrated intensity. Features with the same intensity behaviour throughout the annealing study have their intensity change markers highlighted with the same colour. Features with unique intensity behaviour do not have their intensity change markers highlighted.

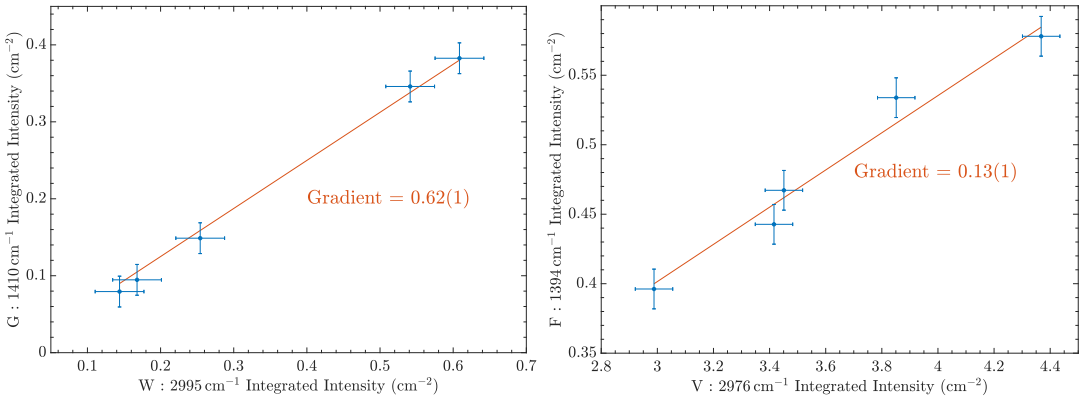

(a) G : 1410 cm^{-1} and W : 2995 cm^{-1} **(b)** F : 1394 cm^{-1} and V : 2976 cm^{-1}

Figure 7-11 Integrated intensity correlation of IR absorption lines (a) G : 1410 cm^{-1} and W : 2995 cm^{-1} and (b) F : 1394 cm^{-1} and V : 2976 cm^{-1} at each stage of the annealing study. The linear fits have been constrained to go through the origin.

in the case of the purple-highlighted features, there are again only two features with a yellow highlight (this time both in C1) at F : 1394 cm^{-1} and V : 2976 cm^{-1}, which similarly suggests a potentially related bend and stretch mode, respectively. The integrated intensity correlation of features F and V in Figure 7-11b is of good agreement (though not quite as good as the agreement for features G and W in Figure 7-11a). The gradient implies that the relative integrated intensity of the feature F is 13(1)% of the integrated intensity of the feature V.

The marker sets highlighted in red appear after the 1400 °C anneal and increase in intensity after the 1500 °C anneal. These features are I : 2870 cm^{-1}, for sample C1 only as feature I was present in the as-grown sample C2, and X : 1342 cm^{-1} (C2 only). It is of note that the annealing behaviour of feature I in sample C2 also increases in intensity after the latter two anneals, as it does in sample C1. It is possible that these features could also be related bend and stretch modes, but the very weak intensities and lack of data points for feature X does not invite further investigation at this point.

7.3.2.3 The 7354 cm^{-1} centre

The 7354 cm^{-1} line is a hydrogen-related centre that is commonly observed in nitrogen-doped CVD diamond (see Chapter 6 for more information) and is also

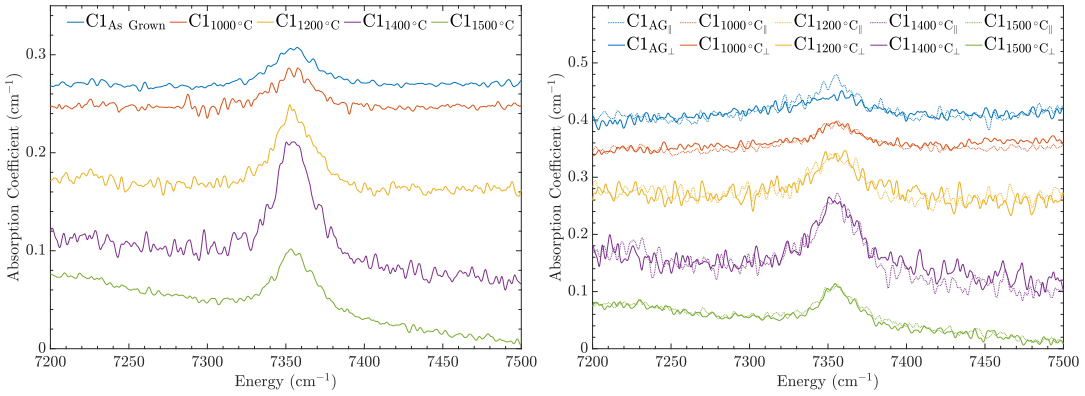

Figure 7-12 (a) Annealing and (b) preferential orientation behaviour of the 7354 cm^{-1} line, that is only observable in sample C1, throughout the annealing study. ∥ (⊥) indicates parallel (perpendicular) to the growth direction.

observed in sample C1. The line appears to anneal-in after each anneal up to 1400 °C and only begin to anneal-out after the 1500 °C anneal as shown in Figure 7-12a. This is contradictory to the previously observed annealing behaviour where the 7354 cm^{-1} line did not anneal-in at any temperature and began to anneal-out after a 2 h anneal at 1300 °C [20]. It is believed the lack of sufficient acceptors in the sample utilised by Cruddace [20] is the reason for the differences (see §7.4.5).

Additionally, the preferential orientation behaviour of the line relative to the growth direction of the sample, at each annealing stage, is presented in Figure 7-12b. Apart from the as-grown IR absorption preferential orientation measurements, there is no observable difference in the intensity of the 7354 cm^{-1} line when IR light is polarised parallel or perpendicular to the growth direction, which for sample C1 is [1 1 0].

7.3.2.4 UV-Vis absorption

The UV-Vis absorption spectra of the boron-doped samples at each stage of the annealing study are presented in Figures 7-13a and 7-13b. For clarity, the spectra have been offset such that the absorption coefficient value of each spectrum at 800 nm is the same arbitrary value.

A typical UV-Vis spectrum of brown-coloured nitrogen-doped CVD diamond includes the N_S^0 component at approximately 270 nm [34]. Additionally, two bands

at approximately 350–365 nm and 510–520 nm, and a "ramp" with the strength of absorption increasing with shorter wavelengths, are also typically observed [25, 35–37]. The origin of the two bands and the ramp are unknown but it has been suggested by Mäki *et al.* [38] and Jones [39] that they are all potentially related and caused by vacancy cluster defects in brown-coloured CVD diamond. Support of this argument is supplied by Khan *et al.* [25] through observation of positive correlations between the relative absorption strengths of the 350–365 nm band and the ramp, and the absorption strength of the 510–520 nm band and the ramp in relation to the brown-colouration of CVD diamond. It should be noted that in the same paper, Khan *et al.* also observe similar annealing behaviour between the 510–520 nm band and NVH^0, however they explain there is no obvious reason for the NVH^0 acceptor at 0.6–1.2 eV above the valance band to be responsible for the 510–520 nm (~2 eV) optical absorption feature.

In a 2006 patent [37], the approximate empirical form of the ramp is stated as

$$r_f \times \lambda[\mu\text{m}]^{-3}, \tag{7-1}$$

where, the ramp factor $r_f < 0.2$ and is therefore a proxy for ramp absorption strength, and the wavelength of light (in microns) λ is scaled to the negative third power. The ramp, along with the 270 nm, 350–365 nm and 510–520 nm components were applied to the UV-Vis spectra of the brown boron-doped samples to see what effects boron-doping has on what otherwise appear to be typical brown-coloured CVD diamonds. The B_S^0 absorption component that caused more absorption at longer wavelengths also merits consideration so a boron-doped HPHT diamond (of known boron concentration) was utilised to create a boron reference absorption spectrum for the UV-Vis data.

The 2006 patent [37] prescribes the fitting order to be the N_S^0/270 nm component initially, followed by the ramp and then the residual of this fit should be composed of the final two bands at 350–365 nm and 510–520 nm. The procedure was followed for the data presented here, after the boron reference was scaled to the specified B_S^0 concentrations (determined by IR absorption) in Table 7-5 and removed from the spectrum. An example component fit on the C2 UV-Vis spectrum after the 1400 °C anneal ($C2_{1400\,°C}$) is presented in Figure 7-13c. The N_S^0 feature was not

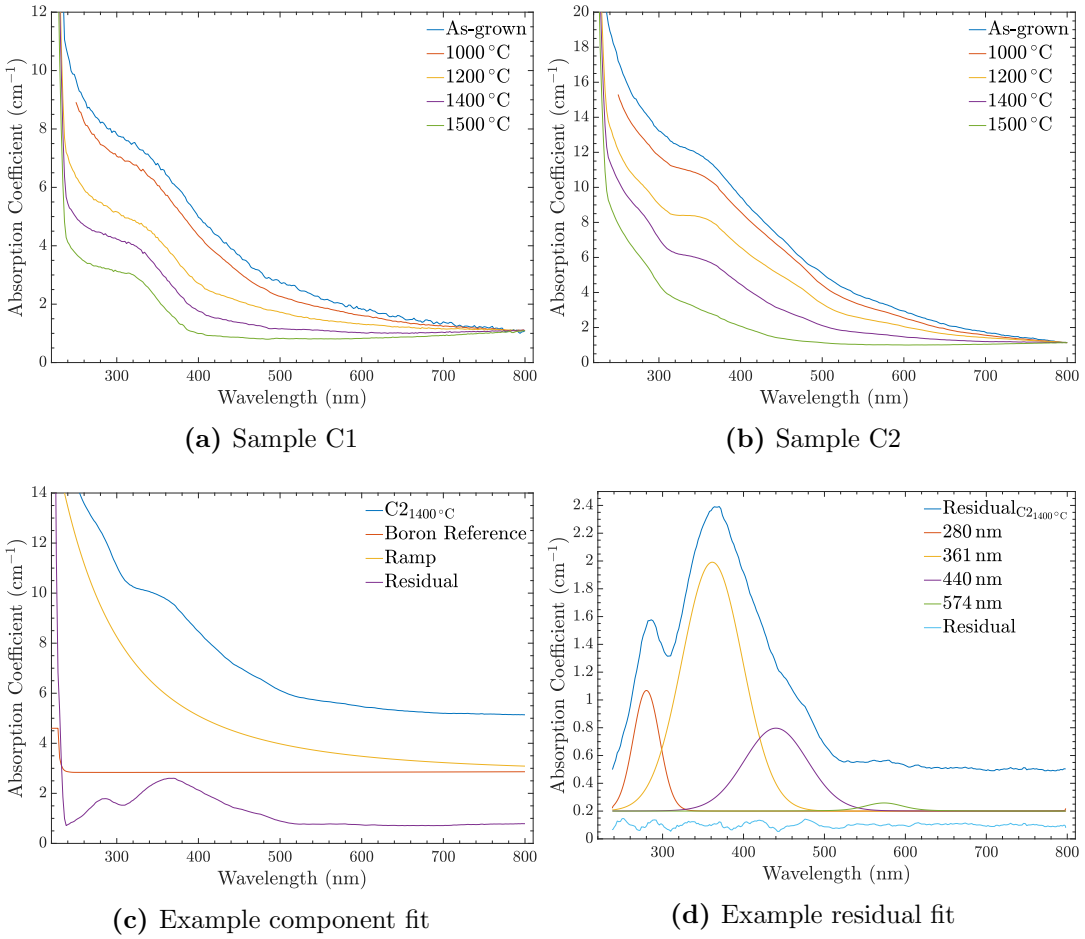

(a) Sample C1 **(b)** Sample C2

(c) Example component fit **(d)** Example residual fit

Figure 7-13 UV-Vis absorption spectra of (a) sample C1 and (b) sample C2 as-grown and after each anneal. (c) An example of fitting the components of a UV-Vis absorption spectrum. (d) An example of fitting the residual from (c). Spectra have been offset for clarity.

present in any of the spectra and therefore was not included in the fit.

The r_f values for each boron-doped UV-Vis spectrum along with associated B_S^0 concentration (from Table 7-5) are presented in Figure 7-14. A 2004 patent [36] reports substantial reduction in the ramp intensity with annealing temperatures of 1400 °C and higher. This behaviour is observed for sample C2 but sample C1 measures substantial reduction one annealing stage earlier with the 1200 °C anneal. It is clear that as the $[B_S^0]$ increases in each sample, the r_f value after each anneal decreases. The rate of change of the r_f for sample C1 is faster than sample C2, as the linear fits show in Figure 7-14.

Complete fitting of the UV-Vis spectra concludes with fitting any observable features in the residual of the component fit. An example of the residual fitting is

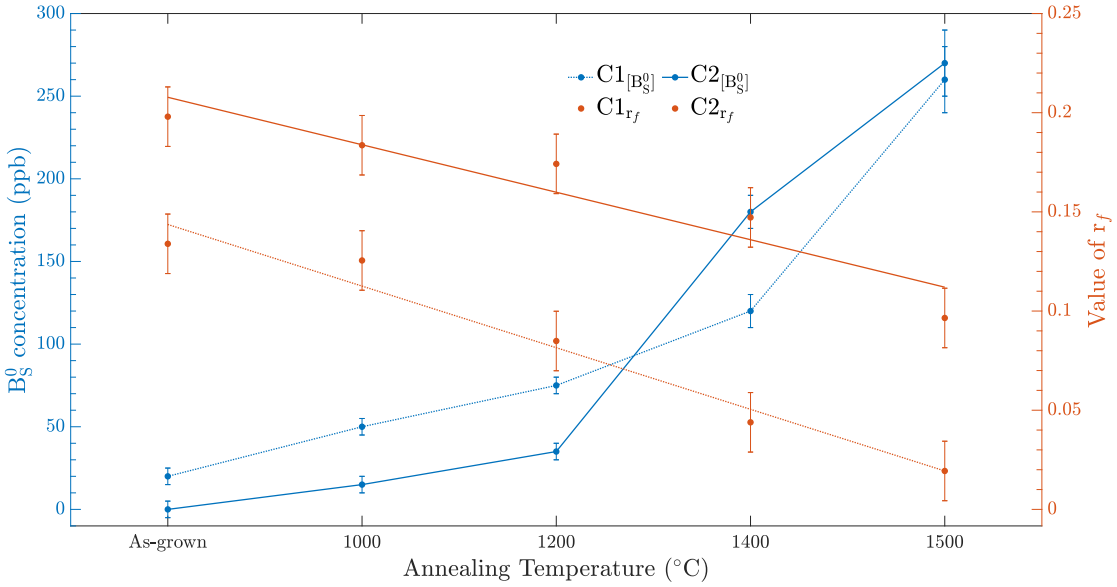

Figure 7-14 B^0_S concentrations of the boron-doped samples as given in Table 7-5 and ramp factor (r_f) values from fitting all the spectra in Figures 7-13a and 7-13b as demonstrated in Figure 7-13c. Dotted (solid) lines indicates sample C1 (C2).

presented in Figure 7-13d with the specific residual from the example component fit of the $C2_{1400\,°C}$ spectrum in Figure 7-13c. For this specific spectrum, a total of four features were identified and their spectral positions are noted in the legend.

The number of features, and the spectral positions of those feature, varies between all the spectra of both samples. The average spectral position of the features was calculated for each sample and the integrated intensity of each feature is presented in Figures 7-15a and 7-15b for samples C1 and C2, respectively. The errors on the spectra position of the features was calculated from the range of positions acquired during the fitting of the residuals.

Whilst neither of the expected bands (350–365 nm and 510–520 nm) are present in the sample C1 residual fits, all of the observed features at 332(8) nm, 438(13) nm, and 536(10) nm significantly decrease in intensity after each anneal. This behaviour is similar to the $C1_{r_f}$ values, hence they strongly correlate with the brown-colouration of the sample.

Sample C2 has one feature at 357(4) nm that falls in-range of the expected 350–365 nm band. The three other observed residual fit features are located at 285(6) nm, 433(18) nm and 567(9) nm. In general, all of the residual fit features correlate with

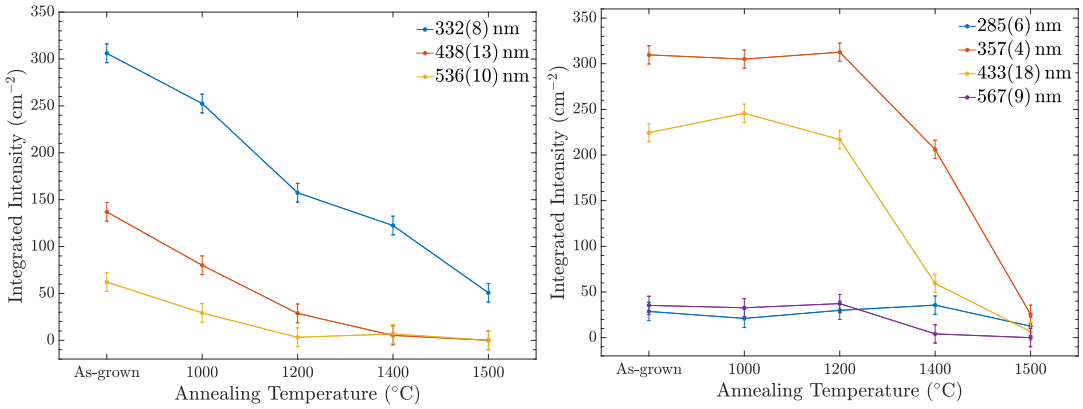

(a) Sample C1 residual fits

(b) Sample C2 residual fits

Figure 7-15 Integrated intensities of the average spectral position of observed features in the residuals of UV-Vis absorption spectra for (a) sample C1 and (b) sample C2 as demonstrated in Figure 7-13d.

the $C2_{r_f}$ values, in that significant reductions in intensity begin after the 1400 °C anneal and therefore—similar to the residual fit features and r_f values of sample C1—also strongly correlate with brown-colouration of the sample.

7.3.2.5 Photoluminescence

The PL spectra in this subsection have all been acquired at 80 K and with a 20× long working distance objective (NA = 0.40). The excitation power was adjusted to maximise the number of counts without saturating the detector. Spectra have been normalised to the same intensity of the first order Raman line. As a reminder, spectra of the substrate, brown, and lateral growth regions were acquired at specific points on each sample (Figure 7-1c).

The PL spectra of the brown regions, acquired with 442 nm and 514 nm excitation, are presented in Figure 7-16. A plethora of sharp peaks are observed in both samples throughout the annealing study. Two main points will be focused on: a comparison to commonly observed features in nitrogen-doped diamond, and the features observed with both 442 nm and 514 nm excitation. Helpfully in this instance, the substrates attached to the boron-doped samples not only provide suitable as-grown nitrogen-doped CVD references, which are readily available for comparison, but they were inescapably also isochronally annealed under identical conditions, and thus can also be useful annealing behaviour references.

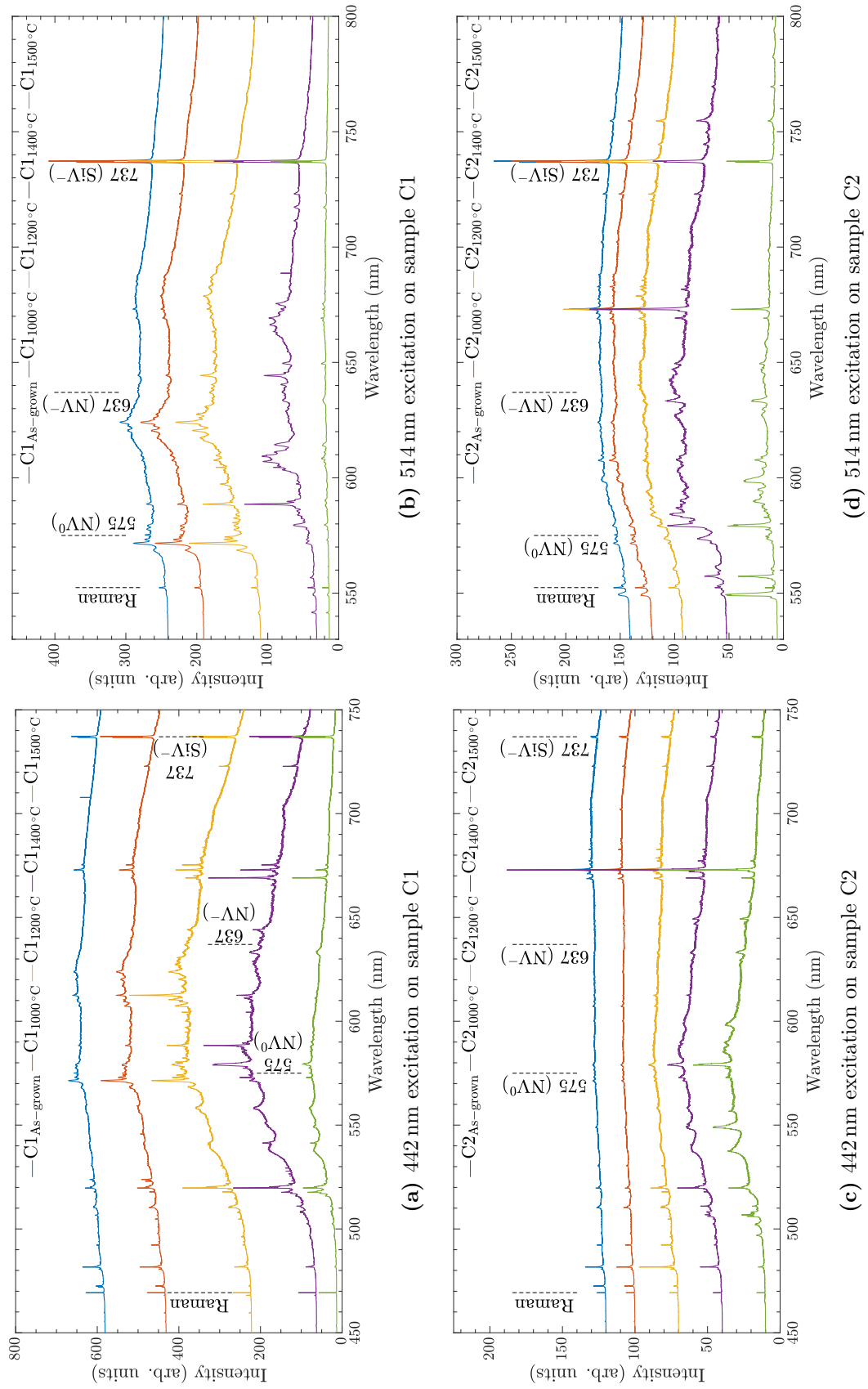

(a) 442 nm excitation on sample C1

(b) 514 nm excitation on sample C1

(c) 442 nm excitation on sample C2

(d) 514 nm excitation on sample C2

Figure 7-16 PL spectra (taken at 80 K) at the brown region point (see Figure 7-1c), with an excitation of 442 nm on (a) sample C1, (b) sample C2, and with an excitation of 514 nm on (c) sample C1, and (d) sample C2. Spectra are normalised to the same intensity of the first order Raman line. Features of interest are indicated with dashed lines. Spectra have been offset for clarity.

Two commonly observed features in nitrogen-doped diamond are NV^0 with its ZPL at 575 nm, and NV^- with its ZPL at 637 nm, as evident in the PL spectra of the substrate regions of the boron-doped samples in Figure 7-17. Excitation with 442 nm will efficiently photoionise NV^-, such that only NV^0 is observable, but with 514 nm excitation both NV^0 and NV^- are observable. Whilst PL spectroscopy is not a quantitative technique, both NV analogues clearly produce strong emissions in these substrates. The intensity of the phonon side bands of the analogues throughout the annealing study indicates that the concentration of NV^0 is increasing whilst the concentration of NV^- is decreasing.

The SiV^- defect ZPL at 737 nm can also be observed with very weak emission in most of the substrate spectra. During growth of any CVD diamond, the silicon-containing components of the CVD reactor (e.g. the quarts window(s)) are etched by the plasma which can result in unintentional silicon-doping [40, 41]. Additionally, a small peak at approximately 503 nm is observed in the substrates of both samples after the 1500 °C anneal. This peak is most likely produced by the N_2V^0 centre [42], as it is known to anneal-in from 1400 °C [43]. An interstitial-related centre called 3H also has a ZPL at approximately 503 nm, but this is unlikely to have formed in the substrates as 3H is typically produced through irradiation [44].

Whilst a plethora of sharp features are present in the brown region PL spectra of the boron-doped samples in Figure 7-16, the NV^0 and NV^- ZPLs at 575 nm and 637 nm, respectively, are not observed. Weak features are observed near their positions, but these are unlikely to be related to the NV analogues as the excitation wavelengths employed will efficiently excite the NV centre so even a small concentration of either analogue should be clearly visible. However, the same cannot be said for the SiV^- ZPL (doublet) at 737 nm which is notably stronger in intensity in the brown regions of both boron-doped samples in comparison to their substrates.

Figure 7-18 compares the common brown region features between the as-grown and post-1500 °C anneal spectra in Figure 7-16. The most intense features that are observed with both 442 nm and 514 nm excitation are indicated with dashed lines. A summary of the annealing behaviour of theses lines (as shown in Figure 7-16) is provided in Table 7-7.

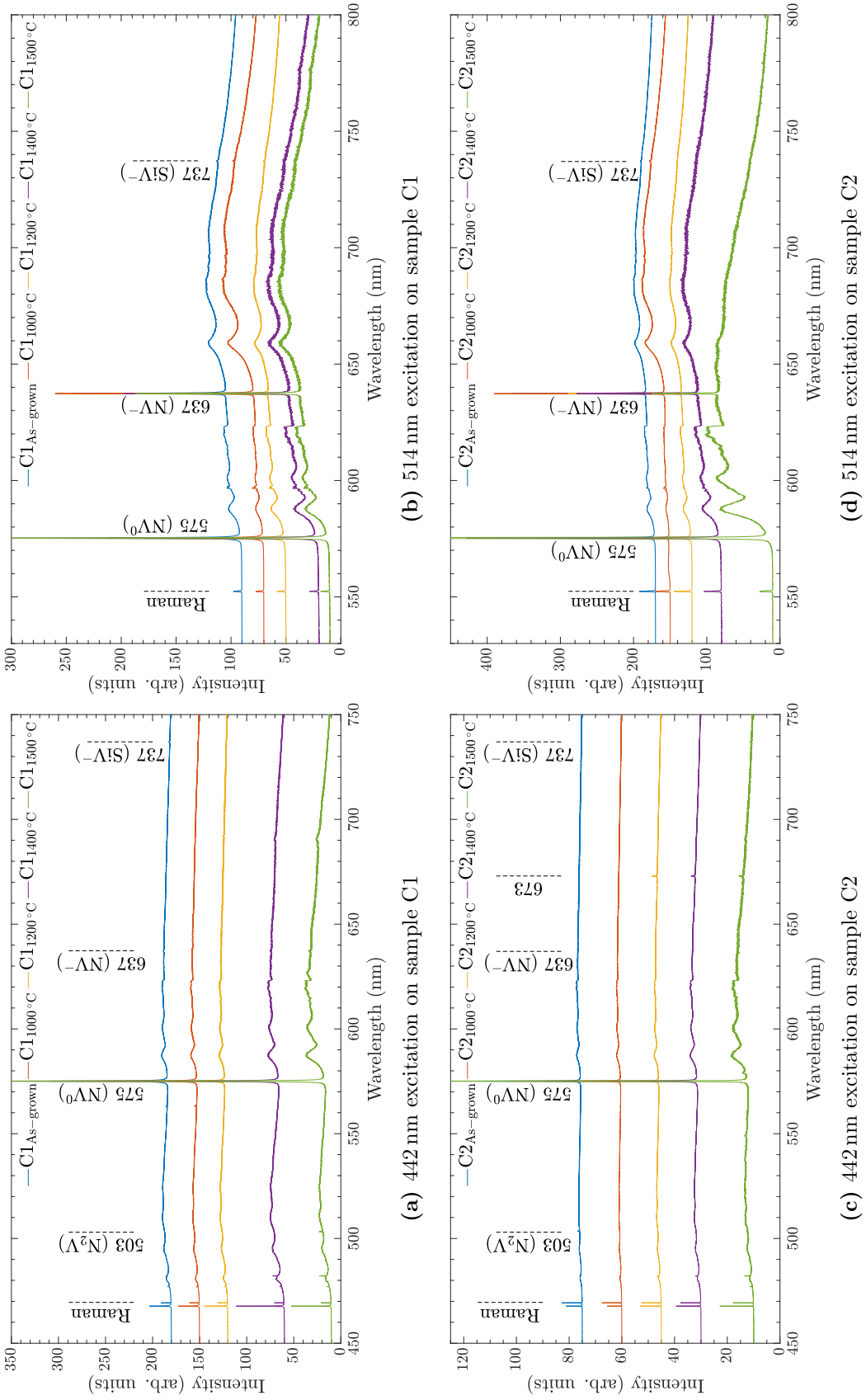

(a) 442 nm excitation on sample C1

(b) 514 nm excitation on sample C1

(c) 442 nm excitation on sample C2

(d) 514 nm excitation on sample C2

Figure 7-17 PL spectra (taken at 80 K) at the substrate region point (see Figure 7-1c), with an excitation of 442 nm on (a) sample C1, (b) sample C2, and with an excitation of 514 nm on (c) sample C1, and (d) sample C2. Spectra are normalised to the same intensity of the first order Raman line. The Raman line of $C2_{1500\,°C}$ in (d) appears smaller than the other Raman lines in that subfigure, but the FWHM is the same. Features of interest are indicated with dashed lines. Spectra have been offset for clarity.

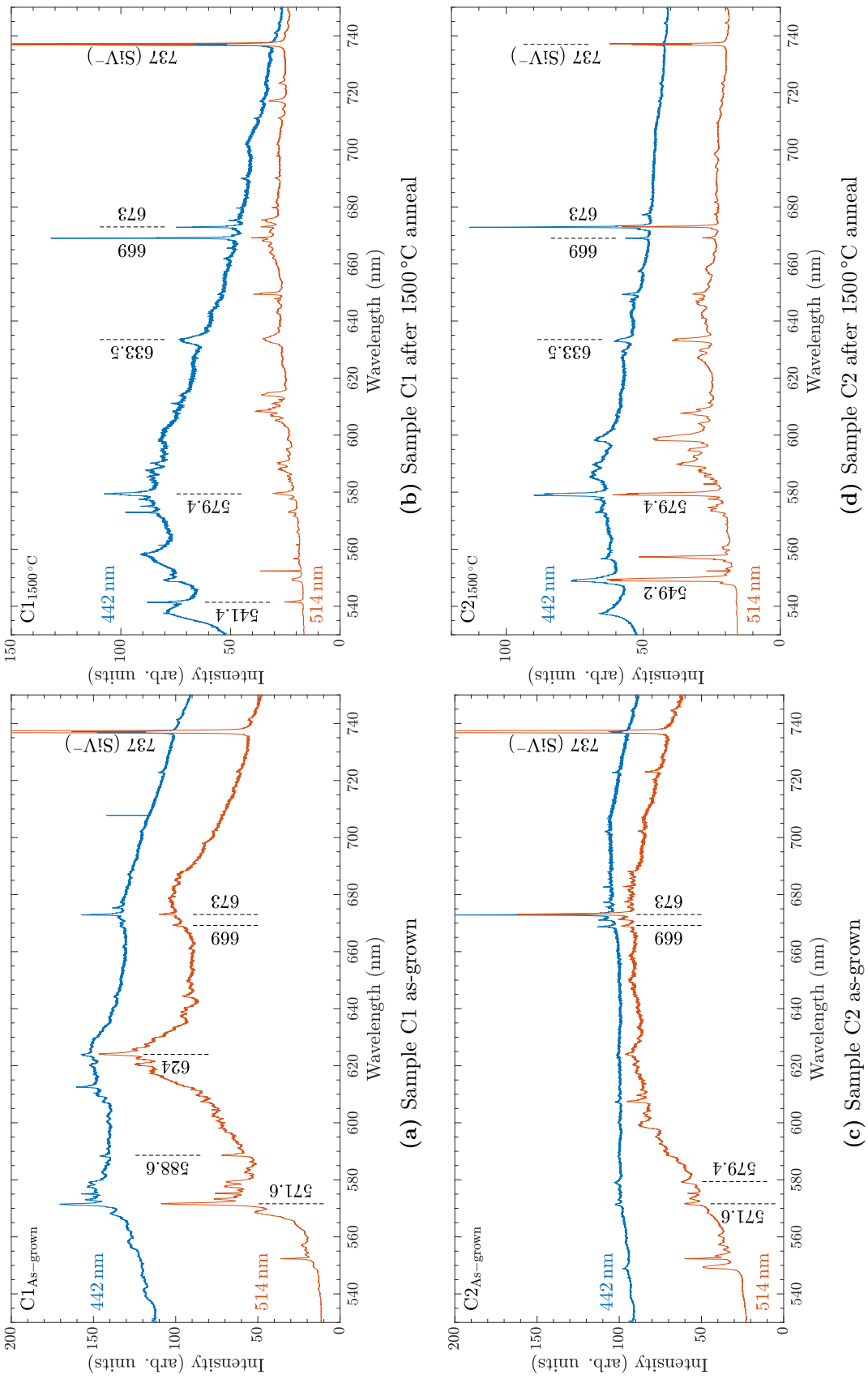

(a) Sample C1 as-grown **(b)** Sample C1 after 1500 °C anneal **(c)** Sample C2 as-grown **(d)** Sample C2 after 1500 °C anneal

Figure 7-18 Comparison of similar features in the PL spectra (taken at 80 K) from 442 nm and 514 nm excitation at the brown region point (see Figure 7-1c) of (a) sample C1 as-grown, (b) sample C1 after the 1500 °C anneal, (c) sample C2 as-grown, and (d) sample C2 after the 1500 °C anneal. Spectra are normalised to the same intensity of the first order Raman line. Features of interest are indicated with dashed lines. Spectra have been offset for clarity.

Feature (nm)	Sample		Annealing temperature (°C)			
			1000	1200	1400	1500
541.4	C1		↑	↑	↑	↓
549		C2			↑	↑
571.6	C1	C2	↑	↑	↓	↓
579.4	C1		–	↑	↑	↓
		C2	–	↑	↑	↑
588.6	C1		↑	↑	↑	↓
624	C1		↑	↑	↑	↓
633.5	C1		–	↑	↑	↓
		C2	–	↑	↑	↑
669	C1	C2	–	↑	↑	↓
673	C1	C2	↑	↑	↑	↓

Table 7-7 Intensity behaviour of PL features, indicated by their wavelength, at each annealing stage relative to the previous stage (or to the as-grown state for the 1000 °C anneal). A blank cell indicates no intensity is measurable after the anneals. ↑ (↓) indicates an increase (decrease) in intensity. – indicates no change in intensity. Features with the same intensity behaviour throughout the annealing study as the IR absorption features in Table 7-6 have their intensity change markers highlighted with the same colour.

Several features: 571.6 nm, 579.4 nm, 633.5 nm, 669 nm and 673 nm are observed in both samples. The annealing behaviour of the features is the same in both samples, except for the features at 579.4 nm and 633.5 nm which differ in intensity change after the final anneal. In sample C2, the features do not change in intensity after the first anneal, but increase after each anneal thereafter: the intensity change markers are therefore highlighted purple as they match the pattern shown by the purple-highlighted features observed in IR absorption (Table 7-6). Similarly, the feature at 549 nm is highlighted in red as its intensity change markers match the red-highlighted markers of the features observed in IR absorption. The intensity changes of the other features do not directly match with any IR absorption features, so are not highlighted.

The lateral growth region of sample C1 was also characterised with excitation wavelengths 442 nm and 514 nm during the annealing study (Figure 7-19). Similarly to the brown region of sample C1, the SiV^- centre is observed in this region, but dissimilar the brown region, the NV^0 and NV^- ZPLs are observed through all of the annealing study PL spectra in this region.

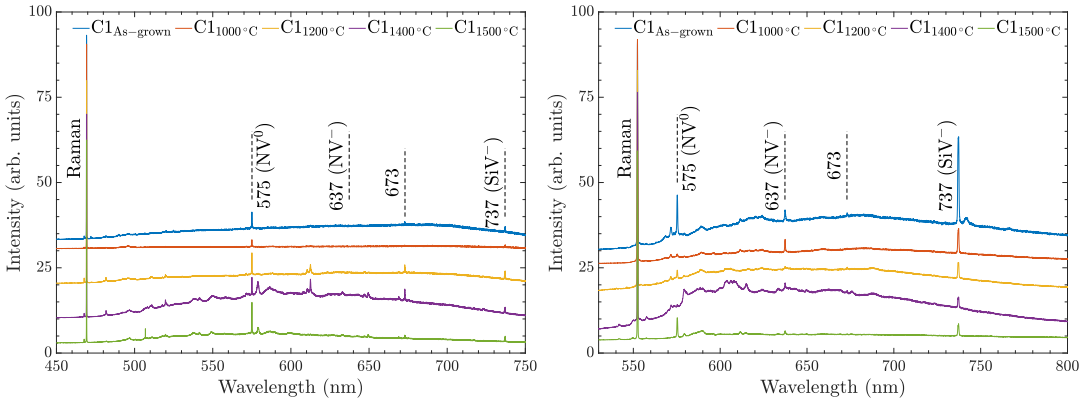

(a) 442 nm excitation **(b)** 514 nm excitation

Figure 7-19 PL spectra (taken at 80 K) at the lateral growth region point of sample C1 (see Figure 7-1c), with an excitation of (a) 442 nm and (b) 514 nm. Spectra are normalised to the same intensity of the first order Raman line. Features of interest are indicated with dashed lines. Spectra have been offset for clarity.

7.4 Discussion

7.4.1 Charge transfer

Neither the room temperature nor variable temperature in-situ charge transfer spectra demonstrated any significant change in absorption in the features of interest labelled A–W. As previously mentioned, changes in absorption from room temperature charge transfer are likely to be unstable because of photo-excited carriers (i.e. B_S^0). However, it is surprising to not observe any change in the features of interest with the in-situ charge transfer experiment as there is clear evidence of charge transfer occurring with the changing B_S^0 concentration at 105 K.

At the experimental temperature of 105 K, the concentration of B_S^0 more than doubles in both samples when comparing the first measurement of the laser switched off to the second measurement of the laser switched on. This indicates a relatively large concentration of compensated boron (i.e. B_S^-) was present in the sample. The mechanism for this charge transfer is not immediately obvious.

For the typical case where $[N_S] \gg [B_S]$, charge transfer between acceptor X and donor N_S^0 in CVD diamond would behave as explained in §3.4:

$$X^{+/0} + N_S^0 \underset{\text{Optical}}{\overset{\text{Thermal}}{\rightleftharpoons}} X^{0/-} + N_S^+ \,. \tag{7-2}$$

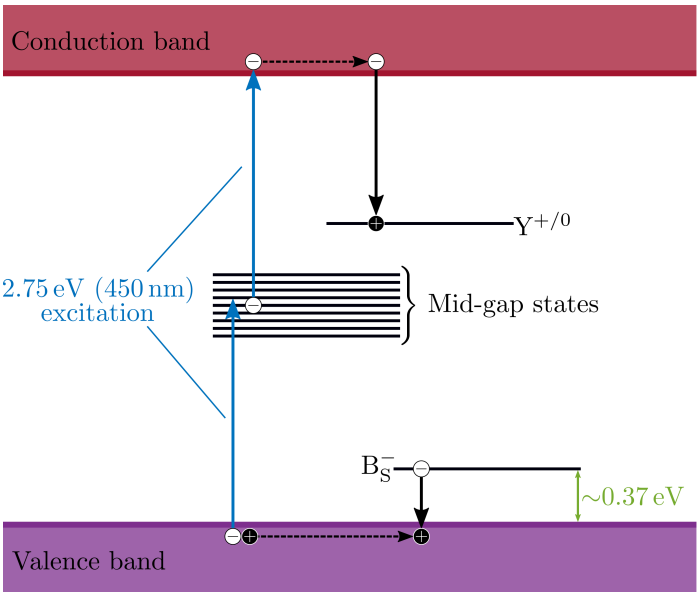

Figure 7-20 Mid-gap state facilitated charge transfer between substitutional boron and nitrogen. Optical excitation at 450 nm (2.75 eV) excites an electron from the valence band to a mid-gap state which simultaneously creates a hole in the valence band. The hole travels through the valence band and is captured by a compensated B_S^- defect which is then charge transferred to an uncompensated B_S^0 defect. The electron at a mid-gap state can be excited again with 2.75 eV such that it reaches the conduction band. Similar to the hole in the valence band, the electron travels through the conduction band and is captured by a defect ($Y^{+/0}$) with an energy level closer to the conduction band than the mid-gap states.

However, this is likely not the case for the boron-doped samples as there is very little evidence of substitutional nitrogen in these samples (see §7.4.3). Instead, it suggests there are mid-gap states, created by other defects, that help facilitate the charge transfer observed in the boron-doped samples.

Figure 7-20 shows the process of how this charge transfer process can occur with the mid-gap states. An electron in the valence band can be excited by the 2.75 eV laser to a mid-gap state and then excited again by the 2.75 eV laser such that it reaches the conduction band; two excitations of 2.75 eV can bridge the ~5.5 eV band gap of diamond. The electron in the conduction band can be captured by some defect with a nearby level. The excitation of the electron from the valence band creates a hole in the valence band, which similarly can be captured by a compensated boron defect that results in the charge transfer to B_S^0.

Equation (7-2) can therefore be modified for the boron-doped samples, for which

$[B_S] \gg [N_S]$ and charge transfer occurs between the B_S^0 acceptor and a donor Y:

$$B_S^0 + Y^{0/-} \underset{\text{Optical}}{\overset{\text{Thermal}}{\rightleftharpoons}} B_S^- + Y^{+/0} \,. \tag{7-3}$$

7.4.2 Preferential Orientation

To aid with the discussion of the preferential orientation data, Figure 7-21 illustrates the crystal axes of both samples along with the directions where the electric field vector is parallel ($\mathbf{E}_\parallel$) and perpendicular ($\mathbf{E}_\perp$) to the growth direction. Furthermore, the expected relative absorption intensity (for equal populations of defect orientations) between any given dipole moment $\mathbf{p}$ and linearly polarised electric field vector of light $\mathbf{E}$ may be calculated by $|\mathbf{p} \cdot \mathbf{E}|^2$. Table 7-8 presents the relative intensities, for electric field vector directions pertinent to samples C1 and C2, for a variety of point group symmetries such that dipoles moments of $\langle 0\,0\,1 \rangle$, $\langle 1\,1\,1 \rangle$, and $\langle 1\,1\,0 \rangle$ directions are considered.

There are few common features in the IR absorption spectra of the two boron-doped CVD samples which were grown on $\{0\,0\,1\}$- and $\{1\,1\,0\}$-orientated substrates (samples C2 and C1, respectively). Absorption from the neutral substitutional boron acceptor and weak absorption from the $1332\,\mathrm{cm}^{-1}$ line is present in both samples, but the intensity of both features is independent of the linear polarisation of the incident light.

The relatively weak feature K : $2892\,\mathrm{cm}^{-1}$ is one of the few common to both samples, and is characteristic of a hydrogen stretch vibration X–H (where the H atom is bonded to an atom X, which could be C, B, N or another atom). The intensity of the line is strongest when the light is polarised perpendicular to the growth direction in both samples (i.e. $\mathbf{E} \parallel [1\,\bar{1}\,0]$) and very weak or entirely absent when the light is polarised parallel to the respective $[0\,0\,1]$ or $[1\,1\,0]$ growth directions. Assuming the dipole moment is along the X–H bond direction, then this result is inconsistent with an X–H stretch vibration along a $\langle 1\,1\,1 \rangle$ or $\langle 0\,0\,1 \rangle$ direction, and may only be explained for a dipole orientation along a $\langle 1\,1\,0 \rangle$ direction that is perpendicular to the growth direction. Thus, for sample C2 with a $[0\,0\,1]$ growth direction, the $2892\,\mathrm{cm}^{-1}$ defects would be required to incorporate with an absorption dipole along $[1\,1\,0]$ and $[1\,\bar{1}\,0]$, and for sample C1 with a $[1\,1\,0]$ growth

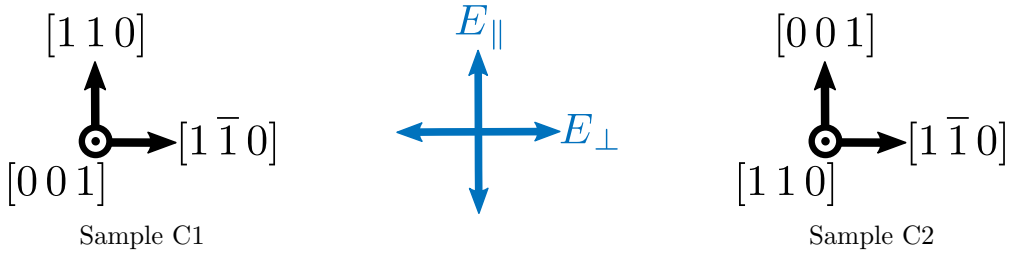

Figure 7-21 Crystal axes of the boron-doped samples and electric field vector measurement orientations parallel ($\mathbf{E}_{\parallel}$) and perpendicular ($\mathbf{E}_{\perp}$) to the growth direction.

Symmetry	Site	Dipole axis	Sample C1		Sample C2	
			$\mathbf{E}_{\parallel}$ = [1 1 0]	$\mathbf{E}_{\perp}$ = [1 $\bar{1}$ 0]	$\mathbf{E}_{\parallel}$ = [0 0 1]	$\mathbf{E}_{\perp}$ = [1 $\bar{1}$ 0]
$\mathscr{D}_{2d}$	1	[0 0 1]	0	0	1	0
	2	[1 0 0]	1/2	1/2	0	1/2
	3	[0 1 0]	1/2	1/2	0	1/2
$\mathscr{C}_{3v}$ or $\mathscr{D}_{3d}$	1	[1 1 1]	1/2	0	1/4	0
	2	[$\bar{1}$ $\bar{1}$ 1]	1/2	0	1/4	0
	3	[1 $\bar{1}$ $\bar{1}$]	0	1/2	1/4	1/2
	4	[$\bar{1}$ 1 $\bar{1}$]	0	1/2	1/4	1/2
$\mathscr{C}_{2v}^{\langle 1\,1\,0\rangle}$	1	[1 1 0]	1/2	0	0	0
	2	[$\bar{1}$ 1 0]	0	1/2	0	1/2
	3	[0 1 1]	1/8	1/8	1/4	1/4
	4	[0 1 $\bar{1}$]	1/8	1/8	1/4	1/4
	5	[1 0 1]	1/8	1/8	1/4	1/4
	6	[$\bar{1}$ 0 1]	1/8	1/8	1/4	1/4

Table 7-8 Relative intensities of the different sites of: a $\mathscr{D}_{2d}$ defect, a trigonal defect, and a $\mathscr{C}_{2v}$ defect with $\langle 1\,1\,0\rangle$ dipoles with the electric field vectors that parallel or perpendicular ($\mathbf{E}_{\parallel}$ or $\mathbf{E}_{\perp}$) to the growth directions of samples C1 and C2. The sum of intensities for any given sample direction have been normalised to unity.

direction, incorporation with an absorption dipole along [1 $\bar{1}$ 0] would be required. For this to be correct, it requires that only 2892 cm^{-1} defects with a preferred orientation were incorporated.

In sample C2 ({0 0 1}-oriented substrate), there are a pair of relatively strong absorption lines in the hydrogen stretch region at O : 2916 cm^{-1} (with a shoulder at P : 2919 cm^{-1}) and T : 2958 cm^{-1}, which are only observed with light polarised parallel to the [0 0 1] growth direction. The relative intensities are approximately

3:1 (2958 cm^{-1} being the weaker feature), which removes the possibility that the features are B–H stretches from ^{11}B and ^{10}B isotopes, respectively (the expected intensity ratio is 4:1). These features are not observed in sample C1, which was grown on a {1 1 0}-oriented substrate. If a simple X–H stretch vibration is again considered, this result may be explained by a defect with an X–H bond orientated along a ⟨0 0 1⟩ direction but with only the [0 0 1] orientation incorporated. Such a preferential orientation has previously been observed (the WAR2 defect reported by Cann [45]), and similarly it is also possible that if these lines correspond to defects that are a result of a growth error on a {0 0 1} growth surface, then the defects may be unique to {0 0 1}-oriented CVD diamond growth.

As these IR absorption features in sample C2 have not been previously reported in nitrogen-doped CVD diamond, it is tempting to associate one or both to B–H stretch modes. The substitutional boron-hydrogen complex (B_S–H) is predicted to have a bond orientation along a ⟨0 0 1⟩ direction, but it appears implausible that either feature is associated to B_S–H as the expected barrier to reorientation is small (and therefore no preferential orientation is expected); the modest binding energy implies the defect should not survive the 1500 °C anneal (although both lines are observed after this anneal); and the expected vibrational frequency (2540–2655 cm^{-1}) is much lower than the observed lines.

Also in sample C2 there are two lines at A : 1347 cm^{-1} and B : 1355 cm^{-1}, that are also only observed with light polarised parallel to the [0 0 1] growth direction. These lines bear some resemblance to a pair of hydrogen-related abosprtion lines at 1353 cm^{-1} and 1371 cm^{-1} in nitrogen-doped CVD diamond, which were reported by Cruddace [20]. The uniaxial stress experiments performed by Cruddace suggested that the 1353 cm^{-1} line has $\mathscr{D}_{2d}$ symmetry and the 1371 cm^{-1} line has $\mathscr{C}_{2v}$ symmetry.

In sample C1 ({1 1 0}-oriented substrate), there are a pair of relatively strong absorption lines in the hydrogen stretch region at Q : 2924 cm^{-1} and V : 2976 cm^{-1} (with a shoulder at U : 2972 cm^{-1}), that are only observed with light polarised parallel to the [1 1 0] growth direction. These features are not observed in sample C2, which was grown on a {0 0 1}-oriented substrate. By considering a simple

X–H stretch vibration again, this result may be explained by a defect with an X–H bond orientated along a ⟨1 1 0⟩ direction but with only the [1 1 0] orientation incorporated. Whilst it may again be tempting to correspond these lines to B–H stretch vibrations, as they have only been observed in boron-doped diamond, there is no reason to speculate. Given the discussion on boron-vacancy complexes and boron-interstitial complexes, it is more likely that they are C–H vibrations at either boron-related complexes, or positive charge states of other defects (with substitutional boron acting as the acceptor).

7.4.3 Substitutional boron and nitrogen, and the brown-colouration

After annealing both samples at temperatures up to 1500 °C, the brown-colouration markedly decreased and the concentration of substitutional boron increased. The most logical explanation is that the defects giving rise to an assortment of mid-gap states, which are responsible for the brown colour, are being removed by annealing and that some of these defects act as donors and compensate the boron. There is no clear evidence in the IR absorption spectra that any of the presumed hydrogen-related features are annealing-out, indicating that the defects corresponding to these features do not act as donors or contribute to the brown colour.

The IR absorption measurements of the B_S^0 concentration call into question the validity of the SIMS measurements of total boron concentration (estimated at [B] < 175 ppb), as they are much lower than the B_S^0 concentration in sample C1 after the 1500 °C anneal ($[B_S^0]$ = 260(20) ppb). Further study on the matter is required, especially as there are several reasons why SIMS measurements may underestimate the total boron concentration (e.g. calibration error), particularly at the low levels reported here.

There is no conclusive evidence of N_S incorporation in the boron-doped samples. No observation of N_S^0 is convincingly made through IR or UV-Vis absorption measurements, and the small concentration of N_S^0 (~35–40 ppb) measured by RPEPR is consistent with attributing the entire N_S^0 concentration to the substrates. By inspection approximately 30–40% of the volume of each sample is their

substrate, which implies the N_S^0 concentration in the substrates is approximately 100–120 ppb—this is typical for a CVD diamond grown with a small addition of nitrogen to the gas phase. Furthermore, this implies the SIMS measurements may have a baseline offset error of approximately 50 ppb, as there is negligible nitrogen incorporation (as N_S or nitrogen-related complexes) in the boron-doped part of the sample.

The 1332 cm^{-1} absorption lines in Figure 7-3, with an intensity of ~0.1 cm^{-1} in both samples, may be attributed to B_S^0 rather than N_S^+: according to the in-house B_S^0 IR absorption reference 200 ppb of B_S^0 contributes approximately 0.1 cm^{-1} absorption intensity at 1332 cm^{-1}. Some nitrogen-related defects are observed by IR absorption (e.g. NVH^0), but their concentrations are very low.

7.4.4 Annealing behaviour of FTIR features

The intensity of the FTIR features labelled A–W demonstrated no significant change in intensity during the annealing study. Any small changes observed could potentially be attributed to inhomogeneity and aperture misalignment errors due to the samples requiring remounting several times during the measurements. It appears that the annealing temperatures used are too low to observe any significant annealing-out of the defects responsible for these features, and a better understanding of the annealing behaviour of theses features would be achieved by annealing at higher temperatures through HPHT annealing.

With regards to the intensity correlation of potentially related bend and stretch modes in Figure 7-11, no assignment for the set of modes G : 1410 cm^{-1} and W : 2995 cm^{-1} is offered, but the modes at F : 1394 cm^{-1} and V : 2976 cm^{-1} merit some discussion. Features F and V were only observed in sample C1, and their annealing behaviour is exactly opposite to NVH^0 (also in sample C1). Furthermore, the energies of feature F and V agree (within error) with the theoretical estimates for the bend and stretch modes of NVH^+ provided by Peaker [46]: 1330(67) $cm^{-1}$and 2950(30) cm^{-1}, respectively. The line at 2976 cm^{-1} may therefore correspond to NVH^+.

In order to assess the validity of this assignment, the linear fit of gain in NVH^0 con-

centration compared to loss of integrated intensity of the 2976 cm^{-1} line throughout the annealing study was performed. The fit is very poor and not presented, but it suggested that the calibration coefficient of the 2976 cm^{-1} line is 10(1) ppb cm^2. The calibration coefficient of NVH^+ (and other charge analogues of NVH^0) are expected to be similar as the environments of the respective C–H bonds in the analogues are also similar. Thus, the calculated calibration coefficient of 2976 cm^{-1} being a factor of ~33 times smaller than NVH^0 (330(30) ppb cm^2 [14]) does not support the assignment of NVH^+ to the 2976 cm^{-1} LVM.

7.4.5 The 7354 cm^{-1} centre

The previously unobserved annealing behaviour of the 7354 cm^{-1} line in sample C1 can be explained as being a consequence of the previously discussed donor defects (which also give rise to mid-gap states) being annealed-out. It is proposed that charge transfer towards the charge state of the defect responsible for the 7354 cm^{-1} line is occurring, rather than entirely new defect centres of the 7354 cm^{-1} line are formed by the annealing. As presented in Chapter 6, charge transfer with the 7354 cm^{-1} centre is possible in the presence of sufficient acceptors, which in this case is B_S^0. The centre should begin to anneal-out after the 1400 °C anneal [20] but it increases again, which indicates that charge transfer to the 7354 cm^{-1} centre was the dominant process compared to dissociation by annealing. Only after the 1500 °C anneal does the 7354 cm^{-1} centre anneal-out more rapidly than it can be charge transferred into, therefore resulting in an overall loss of intensity. The unusual annealing behaviour is unlikely to be related to inhomogeneity as the preferential orientation measurements (Figure 7-12b) show the same relative changes between anneals, and the sample was remounted between the unpolarised and polarised IR absorption measurements.

The preferential orientation behaviour of the line is also somewhat unusual in sample C1 compared to previous measurements. In samples with a [0 0 1] growth direction (see Chapter 6), the intensity of the 7354 cm^{-1} line is a factor of ~2–3 stronger with linear light polarised perpendicular to the growth direction (i.e. $\mathbf{E} \parallel [1\,1\,0]$). Sample C1 has a [1 1 0] growth direction, so whilst greater intensity of

the 7354 cm^{-1} line (in the as-grown spectra) is observed with linear light polarised parallel to the growth direction, the actual direction relative to the crystal axes is still the same (i.e. $\mathbf{E} \parallel [1\,1\,0]$). The more curious behaviour is that the preferential orientation of the 7354 cm^{-1} line entirely disappears after the first anneal and does not return. This is also previously unreported behaviour and has been attributed to the sample reorientating to equal populations of orientations—more explanation and evidence is provided in Chapter 6.

7.4.6 Comparison of FTIR results to features reported in published work

Due to the majority of the features labelled A–W appearing in feature-rich regions of diamond FTIR spectra, references to many of these features can be found in published work, including in the encyclopaedic collection of diamond-related optical features by Zaitsev [47].

Feature B : 1355 cm^{-1} was observed by Fuchs *et al.* as a weak line in some of the CVD diamonds they measured that were not boron-doped [48]. It may be a coincidence that these features are observed at the same energy in different types of diamond; too many questions remain unanswered presently to offer any clear analysis for such types of reference of the observed features.

Feature C : 1360 cm^{-1} (sample C2 only) has been observed by various authors in boron-doped CVD diamond and has been tentatively attributed to a B–H vibration [49]. As discussed in the introduction of this chapter, substitutional boron theoretically may form energetically favourable bonds with hydrogen atoms to produce vibrations in the one-phonon region.

Feature V : 2976 cm^{-1} (sample C1 only) has been observed in CVD diamond (including boron-doped) grown on $\{1\,1\,0\}$-orientated substrates by various authors [50–52]. Sample C1 was also grown on a $\{1\,1\,0\}$-orientated substrate, whilst sample C2 was not which could explain why the feature is not observed in sample C2. However, the 2976 cm^{-1} line is sometimes observed as a doublet with an associated line at 3025 cm^{-1}—no observation of this line is made in sample C1. The feature(s) are attributed to olefinic sp^2 CH_2 configuration of C–H stretches [50].

7.4.7 UV-Vis absorption

The significant reduction in the brown colour of both samples C1 and C2 throughout the annealing study occurs in tandem with the reduction of ramp factor values and absorption intensity of the broad unknown features. As previously discussed, the defect(s) responsible for the brown-colouration are also believed to give rise to mid-gap states. Given that only two samples have been studied, it is unwise to speculate on the nature of the defects responsible for these features.

There are, however, notable similarities to the annealing of brown nitrogen-doped CVD diamond, where the colour is believed to arise from hydrogenated vacancy clusters and incorporated non-diamond material [25]. Investigation of the nature of the ramp and the unknown features relative to brown-colouration of the boron-doped samples would benefit from further annealing studies on multiple samples with varying levels of brown-colouration and growth directions.

7.4.8 Photoluminescence

There is no evidence of NV centres of any charge state in the brown regions of the boron-doped samples. It appears that the incorporation of boron has either suppressed the formation of NV centres entirely, or the defect is only present as NV^+ and not (obviously) detected by the PL measurements.

There is a clear emission from both NV^0 and NV^- in the lateral growth section of sample C1 and the intensities of both ZPLs exhibit erratic annealing behaviour. Their presence indicates there are sufficient donors compared to acceptors in that region of sample C1, unlike in the brown region where there are clearly more acceptors. Given the crystal axes of sample C1, the lateral growth direction is a $\langle 0\,0\,1 \rangle$ direction (specifically $[0\,1\,0]$), where substitutional boron incorporation into CVD diamond in known to be low compared to other sectors [1, 2]. As incorporation of the main acceptor is low, then it is reasonable to suggest the total concentration of donors is higher than acceptors.

The substrates behave as expected for nitrogen-doped CVD diamond. They contain both of the expected charge states of the NV centre, and after annealing at

sufficiently high temperatures N_2V^0 formation is believed to have occurred with observation of the 503 nm ZPL in the PL spectra [43, 53]. As previously discussed, the interstitial-related 3H defect (formed by irradiation treatment [44]) with a ZPL at approximately 503 nm is not expected to have formed in these unirradiated substrates. Furthermore, low nitrogen-doped CVD diamond have almost no acceptors, so they do not produce phosphorescence which these substrates also lack as expected.

It is interesting to note that the negative charge state of the SiV centre is observed in these samples, even though they contain B_S^0 which should accept electrons from SiV^- centres such that only $SiV^{0/+}$ centres are present. Co-doping with boron and silicon is in fact utilised to preferentially produce SiV^0 centres [54]. The observation of SiV^- centres could be explained by the excitation wavelengths used resulting in optically driven charge transfer of $SiV^{0/+}$ centres during the measurements process, with the extra electron(s) originating from other centres or the valence band [55].

7.5 Conclusion

Characterisation of two brown-coloured boron-doped CVD samples (with different growth directions) has been performed throughout all stages of an annealing study. Many unreported features were identified in the IR absorption spectra of both samples. The features exhibited little-to-no charge transfer but most showed 100% preferential orientation either parallel or perpendicular to the specific growth direction of the sample. Charge transfer to B_S^0 was observed with a 450 nm laser in-situ at cryogenic temperatures that is believed to be facilitated by mid-gap states.

Throughout the annealing study in both samples the B_S^0 concentration increases as the brown-colouration is annealed-out. The destruction of donors (that are likely responsible for the mid-gap states) by annealing changed the relative concentration of acceptors and donors in the samples such that the concentration of B_S^0 increased. The features identified by UV-Vis absorption correlate with the loss of brown-colouration in the samples, indicating that they are related.

The IR absorption features showed little change from annealing, indicating that the defects responsible for the features are stable. A relative change in charge carriers is proposed as the explanation for the unusual annealing behaviour of the hydrogen-related 7354 cm^{-1} line in sample C1. Two sets of potentially related bend and stretch modes were correlated from the integrated intensities of the IR absorption features. The set labelled F : 1394 cm^{-1} and V : 2976 cm^{-1} fall within theoretical estimates for bend and stretch modes of the NVH^+ centre, but a comparison of the integrated intensities of NVH^0 and the 2976 cm^{-1} feature does not support this assignment.

Evidence of small amounts of nitrogen incorporation in both samples is shown in the PL spectra, through NV^0 and NV^-. Several unidentified ZPLs are reported from the brown regions of both samples.

Further work should include performing higher temperature anneals with HPHT annealing in order to understand the annealing-out behaviour of the IR absorption features and potentially observe any new lines annealing-in. It would also be beneficial to study more brown-coloured boron-doped CVD samples so that a more comprehensive understanding of these types of samples can be acquired.

References

1. R. Samlenski *et al.*, *Applied Physics Letters* **67**, 2798 (1995).
2. R. Samlenski *et al.*, *Diamond and Related Materials* **5**, 947–951 (1996).
3. R. Burns *et al.*, *Journal of Crystal Growth* **104**, 257–279 (1990).
4. P. L. Diggle, PhD thesis, The University of Warwick, 2019.
5. C.-S. Yan *et al.*, *Proceedings of the National Academy of Sciences of the United States of America* **99**, 12523–5 (2002).
6. S. Dunst, H. Sternschulte, M. Schreck, *Applied Physics Letters* **94**, 224101 (2009).
7. A. F. Sartori *et al.*, *physica status solidi (a)* **209**, 1643–1650 (2012).
8. A. F. Sartori, M. Schreck, *physica status solidi (a)* **211**, 2290–2295 (2014).
9. A. Croot, PhD thesis, University of Bristol, 2018.
10. R. Locher *et al.*, *Materials Science and Engineering: B* **29**, 211–215 (1995).
11. S. Sonoda *et al.*, *Applied Physics Letters* **70**, 2574–2576 (1997).
12. V. I. Polyakov *et al.*, *Diamond and Related Materials* **10**, 593–600 (2001).
13. J. Isoya, H. Kanda, Y. Morita, *Physical Review B* **56**, 6392–6395 (1997).
14. S. Liggins, PhD thesis, The University of Warwick, 2010.
15. A. D. Marwick, G. S. Oehrlein, N. M. Johnson, *Physical Review B* **36**, 4539–4542 (1987).
16. C. P. Herrero, M. Stutzmann, A. Breitschwerdt, *Physical Review B* **43**, 1555–1575 (1991).
17. S. J. Breuer, P. R. Briddon, *Physical Review B* **49**, 10332–10336 (1994).
18. J. P. Goss *et al.*, *Physical Review B* **68**, 235209 (2003).
19. J. P. Goss *et al.*, *Physical Review B* **69**, 165215 (2004).
20. R. Cruddace, PhD thesis, The University of Warwick, 2007.
21. H. Pinto, R. Jones, *Journal of Physics: Condensed Matter* **21**, 364220 (2009).
22. E. H. Hauri *et al.*, *Chemical Geology* **185**, 149–163 (2002).
23. M. N. Drozdov *et al.*, *Technical Physics Letters* **44**, 297–300 (2018).
24. R. P. Mildren, in *Optical Engineering of Diamond*, ed. by R. P. Mildren, J. R. Rabeau (John Wiley & Sons, Ltd, 2013), chap. 1, pp. 1–34.

25. R. U. A. Khan *et al.*, *Journal of Physics: Condensed Matter* **21**, 364214 (2009).
26. C. B. Hartland, PhD thesis, The University of Warwick, 2014.
27. A. T. Collins, M. Stanley, G. S. Woods, *Journal of Physics D: Applied Physics* **20**, 969–974 (1987).
28. K. Thonke, *Semiconductor Science and Technology* **18**, S20–S26 (2003).
29. J. Walker, *Reports on Progress in Physics* **42**, 1605–1659 (1979).
30. A. T. Collins *et al.*, *Physical Review* **140**, A1272–A1274 (1965).
31. J. P. Goss, P. R. Briddon, *Physical Review B* **73**, 085204 (2006).
32. B. Dischler *et al.*, *Diamond and Related Materials* **3**, 825–830 (1994).
33. J. E. Shigley, C. M. Breeding, *Gems & Gemology* **49**, 107 (2013).
34. R. M. Chrenko, H. M. Strong, R. E. Tuft, *Philosophical Magazine* **23**, 313 (1971).
35. P. M. Martineau *et al.*, *Gems & Gemology* **40**, 2–25 (2004).
36. D. J. Twitchen, P. M. Martineau, G. A. Scarsbrook, WO 2004/022821 A1 (2004).
37. S. D. Williams *et al.*, WO 2006/136929 A2 (2006).
38. J. M. Mäki *et al.*, *Physica B: Condensed Matter* **401-402**, 613–616 (2007).
39. R. Jones, *Diamond and Related Materials* **18**, 820–826 (2009).
40. L. H. Robins *et al.*, *Physical Review B* **39**, 13367 (1989).
41. J. Barjon *et al.*, *physica status solidi (a)* **202**, 2177–2181 (2005).
42. G. Davies, *Physica B: Condensed Matter* **273-274**, 15–23 (1999).
43. M. W. Dale, PhD thesis, The University of Warwick, 2015.
44. J. Walker, *Journal of Physics C: Solid State Physics* **10**, 3031–3037 (1977).
45. B. L. Cann, PhD thesis, The University of Warwick, 2009.
46. C. V. Peaker, PhD thesis, Newcastle University, 2018.
47. A. M. Zaitsev, *Optical Properties of Diamond* (Springer, Berlin, Heidelberg, Berlin, 2001).
48. F. Fuchs *et al.*, *Diamond and Related Materials* **4**, 652–656 (1995).
49. L. J. Bellamy *et al.*, *Journal of the Chemical Society (Resumed)*, 2412–2415 (1958).
50. B. Dischler *et al.*, *Physica B: Condensed Matter* **185**, 217–221 (1993).

51. G. Janssen *et al.*, *Surface and Coatings Technology* **47**, 113–126 (1991).

52. G. Janssen *et al.*, *Diamond and Related Materials* **1**, 789–800 (1992).

53. H. Pinto *et al.*, *physica status solidi (a)* **209**, 1765–1768 (2012).

54. B. C. Rose *et al.*, *Science* **361**, 60–63 (2018).

55. U. F. S. D'Haenens-Johansson *et al.*, *Physical Review B* **84**, 245208 (2011).

8

Summary

This thesis has employed a number of spectroscopic and uniaxial stress techniques in order to identify and characterise point defects in chemical vapour deposition (CVD) grown diamond. The electronic structure of the neutral silicon vacancy centre (SiV^0) has been investigated with photoluminescence (PL) measurements whilst under applied stress (Chapter 5). It was necessary to develop a purpose-built PL spectrometer equipped with 1064 nm excitation to investigate a hydrogen-related feature at 7354 cm^{-1}/1360 nm in the near-infrared (NIR) spectrum of nitrogen-doped diamond (Chapter 6). An extensive annealing study has been performed on brown-coloured boron-doped diamond which has revealed a large number of unreported features in infrared (IR) absorption, ultraviolet-visible (UV-Vis) absorption, and PL spectra (Chapter 7).

In addition, throughout all of the chapters electron paramagnetic resonance (EPR) and IR absorption spectroscopies have been used to assay the concentrations of defects. Charge transfer treatments have also been routinely employed to temporarily change the concentrations of defects.

8.1 The neutral silicon vacancy centre in diamond

Chapter 5 concerns the electronic structure of SiV^0 and the associated 946 nm zero-phonon line (ZPL). PL measurements at variable temperatures with perturbing uniaxial stress were performed on an ensemble of SiV^0 centres, that resulted in the ZPL assigned to a ${}^3E_u \leftrightarrow {}^3A_{2g}$ transition, where the ${}^3E_u$ excited state is coupled to a ${}^3A_{2u}$ shelving state 6.8 meV lower in energy. There were too many stress-split lines observed from the 946 nm ZPL (under applied stress) for the previous assignment of the excited state as ${}^3A_{1u}$ [1, 2] to be correct.

The 946 nm ZPL was found to quench with lower temperatures under constant applied stress, which is explained by a Boltzmann population shift occurring from the ${}^3E_u$ to the ${}^3A_{2u}$ state. In addition, under applied stress that lowers the $\mathscr{D}_{3d}$ symmetry of SiV^0, a normally symmetry-forbidden transition at approximately 951 nm is observed between the ${}^3A_{2u}$ excited state and the ${}^3A_{2g}$ ground state. Given that high-efficiency spin polarisation of the 946 nm and 951 nm transitions has already been demonstrated [3, 4], a scheme is proposed for spin-dependent initialisation and readout of the spin states in the 951 nm transition (under small non-zero applied stress). However, as little is known about the position and ordering of the other energy levels of the SiV^0 centre and their role in intersystem crossing (ISC) that facilitates the spin polarisation, there is much further work required to realise such a scheme.

Furthermore, whilst under applied stress, a line at 976 nm exhibited near-identical stress-induced splitting and shifts as the 946 nm ZPL and 951 nm forbidden transition. These results indicate that the 976 nm transition is a vibrational replica of the 946 nm ZPL and is assigned to a pseudo-local vibrational mode (pLVM). It was then determined from PL measurements that the 976 nm pLVM arises from the silicon atom in SiV^0 as an isotopic shift of the 976 nm line was observed in a ${}^{29}Si$-enriched sample. The silicon atom appears to be very weakly coupled to the di-vacancy in SiV^0 as a simple harmonic oscillator model can accurately predict the isotopic shift of the 976 nm pLVM. However, the inferred symmetry of the

vibrational mode based on the experimental results is currently incompatible with theory and requires further work.

8.2 The 7354 cm^{-1} centre

In Chapter 6, the properties and electronic structure of the 7354 cm^{-1} line are investigated. The 7354 cm^{-1} line is often observed in nitrogen-doped CVD diamond and is believed to be hydrogen-related [5, 6]. Previously unreported preferential orientation behaviour of the 7354 cm^{-1} line is observed (through IR absorption and PL measurements) with samples grown on {0 0 1}- and {1 1 0}-oriented substrates. Relative to the [0 0 1] growth direction, light with perpendicular polarisation produces the greater absorption intensity of the 7354 cm^{-1} line. Relative to the [1 1 0] growth direction, light with parallel polarisation produces the greater absorption intensity. The preferential orientation is lost upon annealing at a temperature of at least 1000 °C.

From the suite of samples investigated, it has been determined that the 7354 cm^{-1} centre will only exhibit charge transfer in the presence of a sufficient concentration of acceptors (e.g. B_S^0, NVH^0, SiV^0). Upon thermal treatment the IR absorption intensity of the 7354 cm^{-1} line increases, whilst optical treatment results in a decrease of intensity, thereby suggesting the 7354 cm^{-1} centre has donated an electron to an acceptor and is of neutral or positive charge (0/+). A potentially related line at 6426.5 cm^{-1}, which is often observed with the 7354 cm^{-1} line, exhibits similar charge transfer behaviour but it does not demonstrate any preferential orientation.

Previous work has determined the ground state of the 7354 cm^{-1} centre is at least an E state through the observation of thermalisation during IR absorption measurements whilst under applied stress [7, 8]. Observation of thermalisation with PL measurements (using the 1064 nm PL spectrometer) whilst under applied stress similarly determined that the excited state of the 7354 cm^{-1} centre is also at least an E state. The 7354 cm^{-1} line must therefore be at least an $E \leftrightarrow E$ transition.

The previous work also suggested the 7354 cm^{-1} centre is of trigonal symmetry [7, 8]. The uniaxial stress data of the 7354 cm^{-1} line (acquired from both IR ab-

sorption and PL measurements) was therefore fit to an $E \leftrightarrow E$ transition at a trigonal centre, but the exact symmetry of the 7354 cm^{-1} centre cannot be confidently determined from this fit. There appear to be transitions missing from the uniaxial stress data, that the fit performed suggests should have non-zero intensity but they are not observed. Thus, whilst the fit can estimate the splitting and shift rates of the lines, it does not estimate the intensities of the lines with any degree of accuracy. The uniaxial stress data is believed to be incomplete due to the inability to resolve/deconvolve the missing transitions from the stress-split lines. Consequently, this is believed to be the reason why the piezospectroscopic parameter values generated by the fit are incompatible with the same parameter values calculated from the thermalisation results.

The 7354 cm^{-1} line also exhibited polarisation dependence during PL measurements that is currently unexplained. Under both zero and non-zero applied stress, a significant intensity of the 7354 cm^{-1} line is only observed when the polarisation of the detection electric field vector is aligned perpendicular to the $\langle 0\,0\,1 \rangle$ crystal axis, whilst the line is effectively invariant to the polarisation of the excitation electric field vector.

Further work should include estimating the calibration coefficient of the 7354 cm^{-1} line through charge transfer experiments with a suitable nitrogen-doped sample that contains a sufficient concentration of the NVH^0 acceptor. In such a sample, all the defects that should be present and exhibit charge transfer are assayable (i.e. N_S^0, N_S^+, NVH^0, NVH^-, and even NV^0 and NV^-). This may also lead to identifying the charge analogue the 7354 cm^{-1} centre charge transfers into upon optical treatment through optical and/or EPR spectroscopy.

It would also be of benefit to resolve the missing transitions of the 7354 cm^{-1} centre whilst under applied stress. Possible avenues to explore include acquiring a sample with a much narrower 7354 cm^{-1} line and/or subjecting the stress samples to higher stress pressures so that larger splittings of the lines are induced.

8.3 An annealing study of brown boron-doped diamond

An annealing study of two brown-coloured boron-doped diamonds (with different growth directions) is reported in Chapter 7. Throughout all stages of the annealing study between temperatures of 1000–1500 °C, IR absorption, UV-Vis absorption, and PL spectroscopies have been employed to characterise the samples.

There are a large number of unreported features identified in the IR absorption spectra of the samples. The features exhibited negligible changes in intensity from charge transfer treatment but most showed 100% preferential orientation either parallel or perpendicular to the growth direction of the sample. Such preferential orientation behaviour allows for restrictions to be placed on the possible orientations and symmetries of the defects responsible for some of these lines, based on the assumption they are X–H stretches (where the H atom is bonded to the X atom, which could be C, B, N or another atom). IR absorption spectroscopy did observe charge transfer to B_S^0, upon in-situ optical treatment with a 450 nm laser at cryogenic temperatures, that is believed to be facilitated by mid-gap states.

In both samples throughout the annealing study, the B_S^0 concentration increases in conjunction with the brown-colouration and several unidentified UV-Vis absorption features that are annealing-out (thereby indicating they are related). It is argued that the destruction of donors (which are likely responsible for the mid-gap states) by annealing changes the relative concentrations of acceptor and donors such that the B_S^0 concentration increases.

The IR absorption features also showed little change from annealing, which indicates the features responsible for those defects are stable with strong bonds. From the annealing behaviour of IR absorption features, two sets of potentially related bend and stretch modes were identified and a correlation of integrated intensities between each potential bend and stretch mode produced a good fit. One of these sets of lines, at 1394 cm^{-1} and 2976 cm^{-1}, agree tolerably well with theoretical estimates for the bend and stretch modes of the NVH^+ defect (1330(67) cm^{-1} and 2950(30) cm^{-1}, respectively [9]). However, this assignment is not supported by a

comparison of integrated intensities between NVH^0 and the 2976 cm^{-1} feature.

There is little evidence of nitrogen incorporation in these samples, although the PL measurements do observe some NV^0 and NV^- centres in the lateral growth region of sample C1. The PL measurements also observe several unidentified ZPLs in these samples.

Further work should including continuing the annealing study to higher temperatures with HPHT annealing so that an understanding of the annealing-out behaviour of the IR absorption features may be obtained. Higher temperature annealing may also produce new defects and spectroscopic lines. As this annealing study only comprises of two samples, it would be beneficial to study other brown-coloured boron-doped CVD diamond samples in order to develop a more comprehensive understanding of these types of samples.

References

1. U. F. S. D'Haenens-Johansson *et al.*, *Physical Review B* **84**, 245208 (2011).
2. A. Gali, J. R. Maze, *Physical Review B* **88**, 235205 (2013).
3. B. L. Green *et al.*, *Physical Review Letters* **119**, 096402 (2017).
4. B. C. Rose *et al.*, *Science* **361**, 60–63 (2018).
5. F. Fuchs *et al.*, *Applied Physics Letters* **66**, 177–179 (1995).
6. F. Fuchs *et al.*, *Diamond and Related Materials* **4**, 652–656 (1995).
7. C. Glover, PhD thesis, The University of Warwick, 2003.
8. R. Cruddace, PhD thesis, The University of Warwick, 2007.
9. C. V. Peaker, PhD thesis, Newcastle University, 2018.